Expanding the Scope of Impedance Spectroscopy for the Analysis of Adherent Cells: Electrode Material, Electrode Design, and Data Analysis

DISSERTATION

zur Erlangung des Doktorgrades
der Naturwissenschaften (Dr. rer. nat.)
der Fakultät für Chemie und Pharmazie
der Universität Regensburg

vorgelegt von
Christian Götz
aus Regensburg

2017

Die vorliegende Arbeit wurde in der Zeit von Januar 2013 bis Oktober 2017 unter der Gesamtleitung von Prof. Dr. Joachim Wegener am Lehrstuhl für Analytische Chemie, Chemo- und Biosensorik der Universität Regensburg angefertigt.

Prüfungsgesuch eingereicht am: 13. Oktober 2017

Tag der mündlichen Prüfung: 05. Dezember 2017

Prüfungsausschuss: Vorsitzender: Prof. Dr. Hubert Motschmann
                       Erstgutachter: Prof. Dr. Joachim Wegener
                       Zweitgutachter: PD Dr. Rainer Müller
                       Drittprüfer: Prof. Dr. Antje Bäumner

"For a successful technology reality must take precedents over public relations for nature cannot be fooled."

—Richard Feynman

to Thea and my family

OUTLINE

TABLE OF CONTENTS

I   INTRODUCTION

1   Adherent Cells as Physiological *In Vitro* Model

1.1 Label-Free Whole-Cell Biosensors

The development of a new drug from its first synthesis until the introduction into the market is difficult, costly, and time-consuming. Out of every 5000 to 10000 newly synthesized potential drugs only 9 reach the clinical trial phase, and 1 enters the market. Including all developmental and clinical phases, this leads to an estimated cost for one new drug that gets successfully launched of about 1.8 billion US-Dollars. This high cost has led to a decline of the number and quality of innovative, cost-effective new drugs over the last years. One of the major challenges and opportunities for pharmaceutical research and development is the identification of bad candidates in the early phase of drug discovery. Lack of efficacy and 'off-target' toxicity that surface not until one of the highly expensive clinical stages are among the main reasons for late phase attrition, i.e. dropout of a potential compound. Shifting the identification of compounds with inappropriate drug-like properties to an earlier phase would significantly reduce the cost and improve the efficiency and productivity of the drug development process.[1-2]

Analytical tools that are both *label-free* and based on *whole-cell* biosensor techniques exhibit several advantages compared to classical methods to tackle that problem. Conventional *ligand affinity assays* mainly address the binding affinity between a ligand and a receptor or the inhibition of an enzyme.[3-4] The respective biomolecules are usually immobilized on the surface of multi-well plates or microbeads. Readout methods include radiometric as well as colorimetric and fluorimetric techniques. *Whole-cell* biosensors on the other hand use cells as recognition element and thus reveal functional information about the impact of a stimulus on a living system. They are not limited to a single event like receptor-ligand interaction, but mirror

the complexity of the signal pathway of a whole cell. As a consequence, the measurements may elucidate signal transduction pathways and drug mechanisms, and provide information on the effectiveness, selectivity, and cytotoxicity of an analyte. In addition, it opens the possibility to discover new off-target signaling pathways involved in a drug response during the screening.[5-6] In the recent years, *label-free* technologies have gained increasing importance in the field of cell-based drug discovery and high throughput screening. Reduced cost, improved throughput, increased sensitivity, and more sophisticated data analysis have led to more acceptance in research and industry.[7] Traditionally, tags, dyes, or genetically engineered cell lines are employed in label-based whole-cell assays. However, they have been criticized to compromise the outcome of the measurements due to cross-reactions and altered cell behavior. The labeled approaches are mostly end-point assays that contain no information on the kinetics, so that critical data may be missed. Moreover, waste disposal and health hazard issues have to be considered, especially when using radioactive probes or potentially cancerogenic DNA-binding labels. By contrast, label-free assays – as per definition – do not require tags or labeling, and in addition support time-resolved measurements. Generally speaking, label-free whole-cell assays provide a biologically more relevant environment and are a good trade-off between research on whole organisms, which raises ethical as well as financial challenges, and biochemical *in vitro* assays.[8]

On the other hand, whole-cell sensors are often considered to be a "black box" as only an overall response of the cell is transmitted.[7] Detailed mechanistic studies about the molecular processes inside the cell can – if at all – only be performed with considerable effort and exhaustive controls. This is why research in that field is often complemented with classical microscopy and fluorescence labeling. Despite substantial improvements over the last years, cost of instruments and plates, as well as low throughput are still the most substantial obstacles to comprehensive use of label-free technology in drug screening, as conveyed in a survey from 2010.[7] Consequently, these technologies are rarely used for high throughput screening, but rather during the subsequent *hit to lead* optimization. The hit to lead phase is an early stage during drug discovery where hits from the primary screening phase are verified, evaluated, and further optimized.[9]

Some of the most relevant label-free techniques are summarized in Tab. I-1.[10] Different sensor techniques address different features of a cell and must be chosen accordingly. **SPR** (surface plasmon resonance) and **RWG** (resonant waveguide grating) use the dependence of surface plasmons (electron oscillations) on a metal surface on the refractive index in the adjacent medium as sensor principle. The evanescent field generated by the surface plasmons has a

penetration depth of about 200 nm. It is, therefore, able to detect changes of the refractive index at the bottom of adherent cells, caused for example by a rearrangement of the cytoskeleton or other cellular components. The term *dynamic mass redistribution* has been established for these rearrangements inside the cell.[11-12] The detection method of a **QCM** (quartz crystal microbalance) is based on the principle that the resonance frequency and the amplitude of shear wave oscillations of a piezoelectric quartz crystal depend on the mass and viscoelasticity of the material deposited on the quartz. Changes in the cytomechanical properties of the cell can thus be monitored with high sensitivity.[13-14] Some semiconductor based biosensors have been developed that employ the same principles as a MOSFET (metal oxide field-effect transistor). In an **ISFET** (ion-selective field-effect transistor) the gate consists of an ion-selective membrane that is electrically connected to a reference electrode via the electrolyte. At constant gate and drain voltage, the concentration of the ions specified by the selective layer modulates the drain current. The main application of this method is the monitoring of changes in the extracellular p*H* value.[15] Transistors have also been used to examine the voltage peaks caused by neuronal action potentials.[16] Non-electrogenic cells could be studied by analysis of the thermal noise caused by cells growing on top of a MOSFET.[17] This eventually led to the development of the relatively new **CAN** (cell adhesion noise) spectroscopy, that is yet to be commercially established. By quantitative interpretation of the thermal noise in the cell-substrate junctions, a silicon chip consisting of an array of several thousand transistors with sub-cellular dimensions is used to produce time-resolved images of cells adhered on its surface.[18]

In **EIS** (electrochemical impedance spectroscopy) an alternating voltage is applied between two coplanar film-electrodes immersed in an electrolyte. The alterations in the impedance caused by cells growing on top of the electrodes is analyzed in a frequency dependent manner. EIS is the most versatile of these methods as numerous electrode layouts exist to address different aspects of cell analysis. Especially the widely-used ECIS™ (electric cell-substrate impedance sensing) method allows for a detailed analysis of the cell-cell junctions, the cell-substrate contacts, and the cell membrane. This is due to its defined electrode layout with a small working electrode and a larger counter electrode, as well as the in-depth mathematical model developed by Giaever and Keese (cf. II.1.4 for more details).[19-20] Based on this pioneering work, several other technologies have emerged. The xCelligence system by ACEA Biosciences uses arrays with interdigitated electrodes that are designed to cover a uniquely large portion of the well area. Thus, the impedance signal is averaged over a greater number of cells and may consequently show less well-to-well variations.[21] Their system is promoted with an emphasis

on the analysis of beating cardiac cells because of its particularly fast data acquisition rate (Real Time Cell Electric Sensing, RT-CES).[22] Molecular Devices has released a 384-well cell analysis system with strong focus on high throughput. The corresponding measurement technique is termed CDS (cellular dielectric spectroscopy).[6]

Tab. I-1: Label-free biosensing techniques used to monitor cell-based assays (SPR = surface plasmon resonance, RWG = resonant waveguide grating, QCM = quartz crystal microbalance, ISFET = ion-selective field-effect transistor, CAN = cell adhesion noise spectroscopy, EIS = electrical impedance spectroscopy).

technique	transduction	readout
SPR, RWG	optical	dynamic mass redistribution
QCM	piezoelectric	cytomechanics
ISFET	potentiometric	charged cell metabolites
CAN	thermal voltage noise	cell-substrate contact zone
EIS	impedimetric	cell morphology

1.2 Immobilizing Cell Monolayers on Transducer Surfaces

Aside from the measurement technique the choice of the cell line needs to be considered for compound testing. Immortalized cell lines are cell populations that proliferate indefinitely due to natural or artificial mutation. They are cheap, easy to grow, and reproducible. Primary cells, taken directly from living tissue, represent the respective biological systems more accurately, but require significantly more effort to grow and keep in culture.[8] For this reason, immortalized cells are often preferred over primary cells. Depending on the target of the drug or the analyte under test there are cell lines derived from the targeted tissue that are used as model systems. Tab. I-2 shows exemplarily some immortalized epithelial cell.

Tab. I-2: Selected immortalized cell lines and typical applications as model system (HUVEC = Human Umbilical Vein Endothelial Cells, Caco = adenocarcinoma of the colon, MDCK = Madin-Darby Canine Kidney, NRK = Normal Rat Kidney).

cell line	origin	model system for	source
HUVEC	human vein endothelium[a]	vascular inflammation	[23]
Caco-2	human colon epithelium	intestinal drug absorption	[24]
MDCK	canine kidney epithelium	epithelial water and solute transport	[25]
NRK	rat kidney epithelium	nephrotoxicity	[26]

Epithelia are a type of interfacial tissue that lines all inner and outer surfaces of the body. Epithelial tissues serve as protective barrier (skin), take up nutrients (intestine), control the transport of ions, metabolites, and proteins (blood vessel, intestine, kidney), or perform sensory tasks[27] (retinal pigment epithelium, auditory hair cells, olfactory epithelium). Growing in two-dimensional cell monolayers, they are particularly well suited for *in vitro* analyses. It is generally assumed that the interactions of cells with the surrounding tissue *in vivo* and technical *in vitro* surfaces rely on the same principles. When a cell suspension is placed inside a well, the cells sediment and get close to the surface, where they establish molecular contact with proteins immobilized on the surface. These proteins can be either artificially deposited on the surface or be excreted by the cells themselves. Especially positively charged polymers like poly-L-lysine facilitate surface adhesion due to electrostatic attraction between the polymer and the overall negatively charged membrane surface of cells. Proteins contained in physiological cell growth buffers or media also adsorb quickly on hydrophilic surfaces and support cell adhesion. Once the initially spherically shaped cells have *adhered* (or *attached*) to the substrate, they start to spread out and increase the contact area, followed by the formation of cell-cell contacts with their neighboring cells.[28-29]

In a fully established cell monolayer several proteins and other biopolymers are involved in keeping its functional and structural properties intact (Fig. I-1). Between the cells and the substrate is the subcellular cleft with the extracellular matrix (ECM). The average distance between cell and substrate is between 25 nm and 200 nm, depending on the cell type and the substrate coating. The ECM is a highly heterogeneous macromolecular network of proteins, carbohydrates, proteoglycans, glycoproteins, and other biomolecules. The cells are anchored to the ECM via surface receptor proteins that recognize certain amino acid sequences in ECM proteins. The most common surface receptor proteins are the *integrins*. They are transmembrane

---

[a] Endothelial cells are a subtype of epithelial cells lining the blood vessels.

proteins that are linked to the cytoskeleton via adapter proteins on the intracellular side and, for example, to the ECM protein fibronectin with its well-known RGDS amino acid sequence on the extracellular side of the membrane. This provides adhesive strength and prevents the anchorage proteins from being torn out of the cell membrane when the cell is exposed to mechanical stress.[28-29]
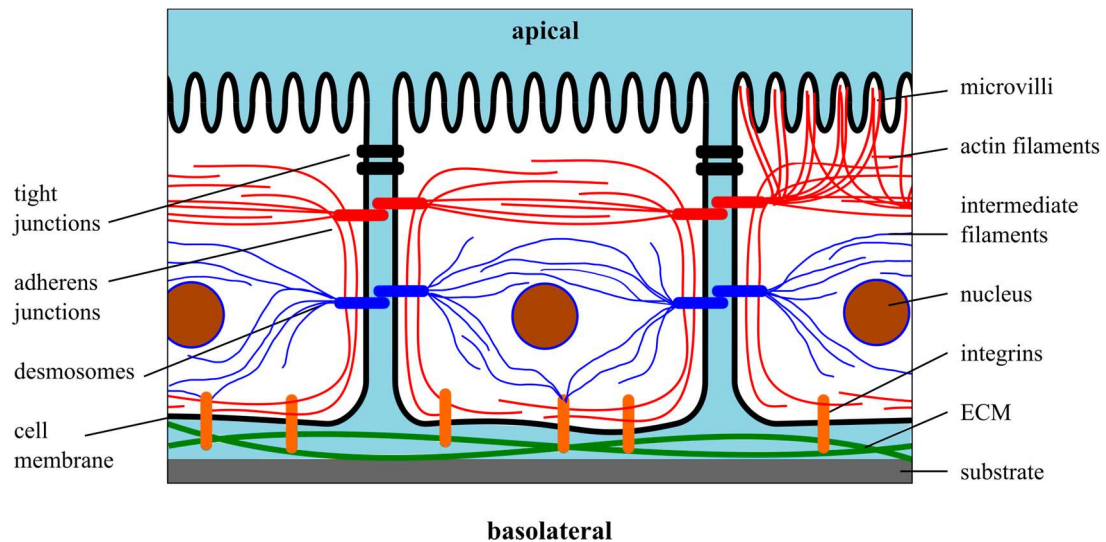
Fig. I-1: Schematic of epithelial cells growing as confluent two-dimensional monolayer (not drawn to scale). The cytoskeletons of individual cells are joined via adherens junctions and desmosoms, and linked to the ECM (extracelluar matrix) via transmembrane proteins called integrins. This provides mechanical stability and adhesion strength. The cytoskeleton – consisting of intermediate filaments (blue), actin filaments (red), and microtubuli (not shown) – defines the overall shape of the cells and supports also the microvilli (only shown in the right cell). The tight junctions ensure the polarity of the cell (fence function) and prevent molecules from crossing the cell layer on the paracellular pathway (gate function).[29]

In a similar fashion, the cytoskeletons of adjacent cells are interconnected via transmembrane proteins of the *cadherin* family. One usually distinguishes between the *adherens junctions*, that link the actin filaments, and the *desmosomes*, that connect the intermediate filaments of neighboring cells. Both have very distinct functions related to cell shape and tensile strength. The cytoskeleton continuously extends across the whole epithelium, thus providing a particularly high mechanical stability.[28-30]

The uptake or release of nutrients, ions, or metabolites through an epithelium is firmly regulated by the cells via transport proteins. The establishment of chemical and electrochemical gradients across the cell layer allows the active control of the transport processes required for the functionality of the cell layer. One example is the transport of glucose from the gut into the intestinal epithelium, driven by a Na^+-gradient, before it is further passed on to the underlying tissue. It is therefore highly important to prevent free diffusion across the cell layer on the paracellular pathway, i.e. through the intercellular cleft. This is accomplished by the *tight*

junctions, barrier proteins that are located close to the apical pole of the cell which seal the intercellular cleft (*gate function*, Fig. I-1). The second purpose of the tight junctions is that proteins integrated in the membrane cannot diffuse from the basal membrane side to the apical membrane side or vice versa (*fence function*). Thereby, the functional polarity of the cell is preserved.[29-30]

2 Conducting Polymers − Beginnings and Recent Advances in Biosensing

2.1 Short History of Conducting Polymers

Polymers are not simply electrically non-conducting insulators, but cover the whole spectrum between insulating materials and plastics with metal-like behavior. In 2000 Shirakawa, Heeger, and MacDiarmid received the Nobel prize for the "discovery and development of electrically conductive polymers".[31] Based on Kekulé's discovery of the electron structure of benzene around 1860 with its delocalized π-system, the idea had come up that electrons could be delocalized not only in cyclic molecules but also in polyconjugated organic chains, which should lead to electrical conductivity. The simplest polymer exhibiting such a structure is polyacetylene (Fig. I-2).
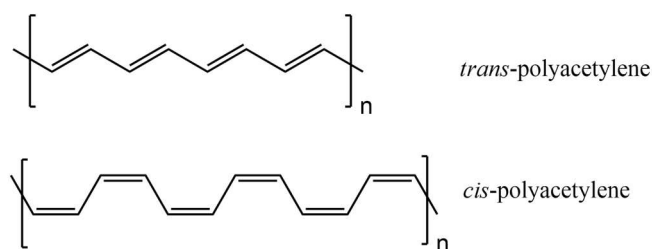
Fig. I-2: Chemical structures of *trans*- and *cis*-polyacetylene

Polyacetylene was first synthesized by Natta in 1958 as black, air-sensitive, insoluble, and infusible powder which did not attract much attention. [32] Even after Shirakawa was capable of controlling film formation and *cis/trans*-configuration of the polymer in the 1970s, its conductivity was still in the range of an insulator in case of *cis*-polyacetylene and in the range of a poor semiconductor in case of *trans*-polyacetylene.[32] It was not until 1977 when Heeger and MacDiarmid discovered that by modifying polyacetylene with halogens its conductivity could be increased by several orders of magnitude.[33] This process, called *doping*, leads to partial oxidation of the double bonds and is essential for the conductivity of the polymer. By mechanically stretching polyacetylene films its conductivity could even be increased to match that of silver or copper.[34] However, as doped PA loses its conductivity upon exposure to oxygen in ambient air, it has barely any significance nowadays.[35] Instead, other polymers like polypyrrole, polyaniline, or polythiophene and its derivative, poly(3,4-ethylenedioxythio-

phene) (PEDOT), have attracted much interest and are widely used in research and industrial applications (Fig. I-3).
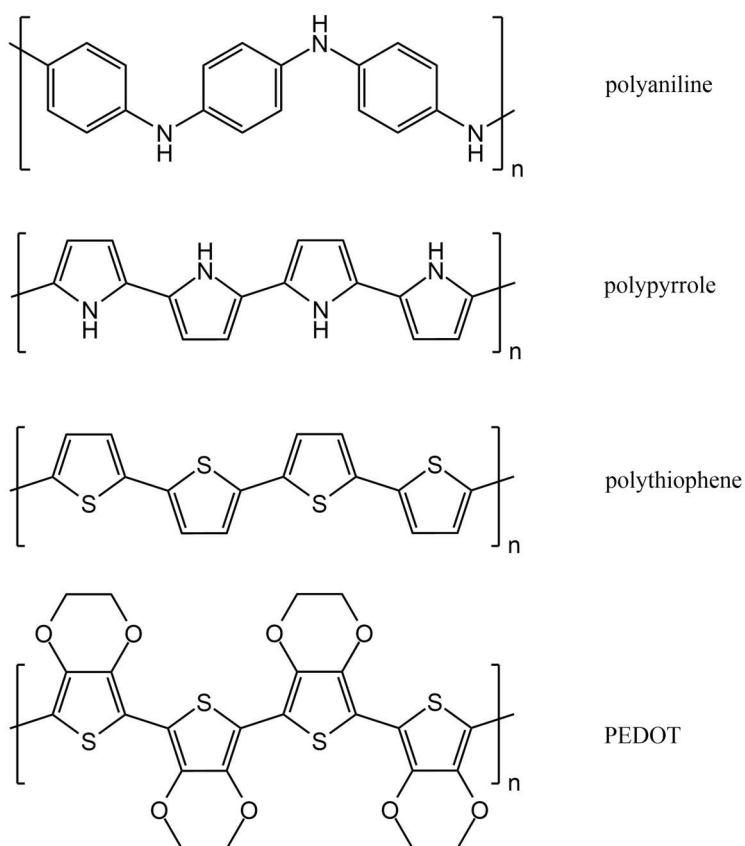
Fig. I-3: Chemical structures of the most relevant conducting polymers: polyaniline, polypyrrole, polythiophene, and PEDOT. PEDOT exhibits high electrochemical stability due to the blocked 3- and 4-positions of the thiophene ring by a dioxyethylene bridging group.

PEDOT for example has been used as antistatic[36] and sensor material[37], as hole injection layer in electroluminescent devices[38], and in photovoltaic cells[39-41]. Organic conducting polymers combine the electrical properties of metals and semiconductors with the mechanical properties and processability of polymers. Moreover, they can be derivatized to modify their mechanical, chemical, electrical, or optical properties.[42-43] Derivatization can either be accomplished via synthetic chemistry at the monomer itself or by choice and concentration of the dopant. The best example is PEDOT. Conductive polymers are usually quite insoluble in any solvent and thus difficult to handle. By doping with the negatively charged copolymer poly(styrene sulfonate) (PSS) PEDOT gets dispersed in the aqueous reaction solution during polymerization. PEDOT:PSS is commercially available as an aqueous dispersion which can easily be coated onto any substrate. The researchers initially developed PEDOT to be a water soluble polymer with blocked β-positions to prevent undesired cross-couplings. However, PEDOT itself was

found to be an insoluble polymer and exhibited a high conductivity (300 S/cm), stability, and visible light transmittance in thin films. Dispersability was finally achieved with the afore mentioned PEDOT:PSS, exhibiting good conductivity (10 S/cm), next to excellent degradation stability and transparency for visible light.[44-45] In the recent years the conductivity of PEDOT:PSS has been enormously increased by certain additives or processing techniques that lead to morphological changes within the polymer structure (Tab. I-3, cf. II.2.2 for more details). PEDOT:PSS shows properties of a supercapacitor as it forms a swollen hydrogel in aqueous solutions, hence generating a huge effective surface area.[46] This makes it particularly interesting for applications where the electrode-electrolyte interface plays an important role, like for example in biosensors.
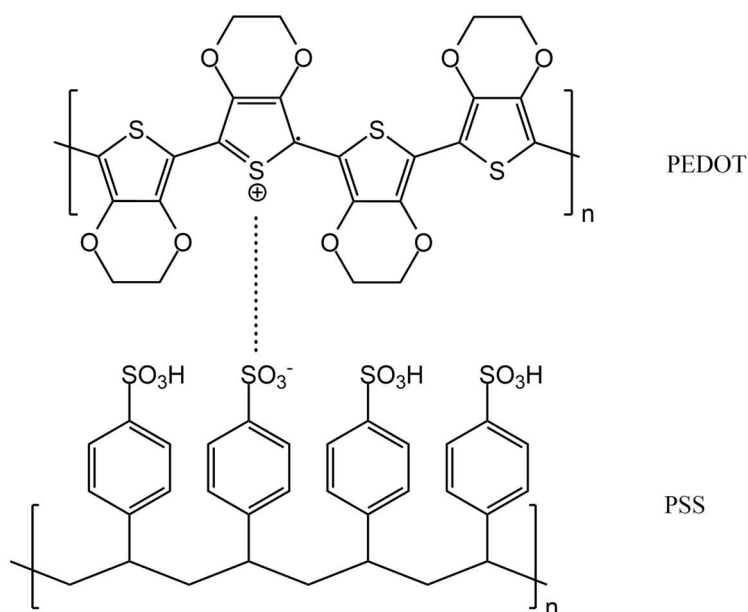
Fig. I-4: Chemical structure of PEDOT:PSS. PEDOT gets positively (p-) doped during the polymerization and PSS is bound as the respective counter anion.

Tab. I-3: Conductivity κ of PEDOT:PSS in comparison with selected metals and semiconductors under ambient conditions. The conductivity of metals and semiconductors strongly depends on impurities present in the lattice. ITO (indium tin oxide) conductivity varies with the processing technique. The conductivity of pristine PEDOT:PSS covers a wide range as it can be increased by several orders of magnitude by secondary doping (cf. II.2.2).

material	κ / S/cm	source
silver	$6.3 \cdot 10^5$	[47]
copper	$6.0 \cdot 10^5$	[47]
gold	$4.5 \cdot 10^5$	[47]
stainless steel	$1.3 \cdot 10^5 - 1.5 \cdot 10^5$	[48]
ITO	$6.3 \cdot 10^1 - 1.4 \cdot 10^4$	[49]
germanium	$2.2 \cdot 10^{-2}$	[47]
silicon	$4.0 \cdot 10^{-6}$	[47]
PEDOT:PSS	$1 \cdot 10^{-1} - 4.6 \cdot 10^3$	[50-51]

2.2 Conducting Polymers in Biosensing

Conducting polymers have been widely used as electrochemical transducers in biosensors. Mostly amperometric, but also plenty of potentiometric and conductometric sensors exist.[52-53] When using conducting polymers as a transducer, mediators and biorecognition elements like enzymes can be directly entrapped in the polymer matrix. The charge transfer between enzyme and conducting polymer is facilitated due to its low ionization energy, high electron affinity, and high surface area (Fig. I-5).[53] Electrochemical immobilization was identified as the most prominent method for the incorporation of enzymes in conducting polymers. Thereby, the respective monomer is polymerized by electrochemical oxidation on a metal electrode in the presence of the enzyme. Electrostatic interactions lead to an entrapment of the enzyme molecules between the polymer chains. This method is straightforward and very reproducible. The layer thickness and, therefore, the number of enzymes located in the polymer can be easily controlled by the amount of charge passed through the electrode during polymerization.[54] In terms of commercial availability, however, disposable screen printed electrodes have been more successful as environmental sensors and biosensors due to low cost, portability, and ease of use.[55] Screen printed biosensors comprising conducting polymers are still scarce, but the emergence of commercial PEDOT:PSS based screen printing formulations may give rise to more applications.[56] A number of different formulations are for example provided by companies Agfa and Heraeus.
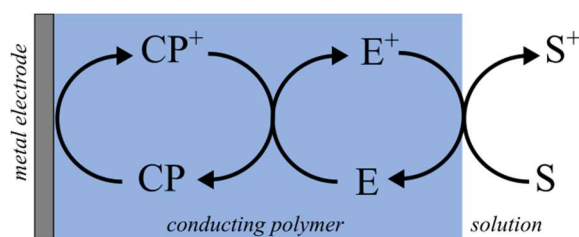
Fig. I-5: Suggested mechanism for charge transfer in conducting polymer based biosensors. An analyte substrate (S) gets oxidized, catalyzed by an enzyme (E). The enzyme is immobilized in a conducting polymer (CP), which mediates the charge transfer to the metal electrode.[53]

The first publication dealing with the effects of conducting polymers on mammalian cells studied the control of cellular properties by the oxidation state of polypyrrole.[57] The authors showed that cell growth was inhibited when the polymer was in its neutral state and unaltered in its oxidized state. Early publications then focused on polypyrrole modified electrodes as means to improve cell growth and interface impedance compared to bare metal electrodes.[58] It was, however, shown that polypyrrole exhibits poor electrochemical long-term stability. This is due to defect cross-couplings at the 3- and 4-position of the pyrrole ring, that eventually leads to irreversible oxidation of the polymer.[59] These positions are blocked by a dioxyethylene bridging group in PEDOT (cf. Fig. I-3), making it electrochemically much more stable. Electrodes modified with electrochemically polymerized PEDOT have since been used to analyze or control living cells.[52] The applications were mostly intended for functional contact with neuronal tissue to study and stimulate mammalian nervous systems.[60-62] Its softer nature was claimed to reduce the mechanical mismatch with neuronal tissue compared to bare metal electrodes.[63] Moreover, all-polymer biosensors for the impedimetric analysis of cell monolayers with a focus on cost efficiency, simplicity, and disposability have been developed. Kiilerich-Pedersen et al. presented a polymer-based microfluidic system with PEDOT:TsO as electrode material and measured the impedance response of human foreskin fibroblasts to a virus infection on interdigitated electrodes.[64] The tosylate anion (TsO, p-toluenesulfonate) is after PSS the most common dopant for highly conducting PEDOT coatings. An all-polymer device that comprised an ECIS layout with a small working and a large counter electrode was published by Karimullah et al.[65] The chip contained PEDOT:PSS electrodes and due to its supercapacitor properties exhibited a low interfacial impedance and thus improved sensitivity for cell analysis. The authors however reported problems concerning adhesion loss of the polymer after prolonged exposure to an aqueous environment caused by the water uptake of PEDOT:PSS.

Another interesting measurement principle that relies on the characteristics of conducting polymers is the organic electrochemical transistor (OECT). The OECT was originally developed in a transistor configuration by White et al. with polypyrrole as channel material between source and drain (Fig. I-6 A).[66] In OECTs the channel is in direct contact with the electrolyte and the gate is electrically connected to the channel via the electrolyte. Depending on the gate potential, the ions are directly injected into the polymer and cause doping or dedoping of the channel (cf. II.2.3 for a more detailed mechanism). The amount of doping controls the drain current that is generated upon application of a potential difference between source and drain. Thereby, small changes in the conductivity of the conducting polymer caused by ion injection can be amplified by several orders of magnitude. The highest signal amplification were reported for OECTs with PEDOT:PSS channels, again due to its hydrogel properties and strong interpenetration with the electrolyte.[67] While mostly Ag/AgCl wires immersed in the electrolyte are employed as gate electrode, Ramuz et al. took a more practical approach.[68] They used PEDOT:PSS as material for the channel and the planar gate electrode, both being in the same plane (Fig. I-6 B). That way, the combined optical and electrical sensing of epithelial cells was possible as the optical pathway was not blocked by a gate electrode wire. This planar transistor layout was also claimed to be compatible with low-cost production techniques like ink-jet printing or roll-to-roll processing, and would therefore be amenable to fabrication in industrial scales. The authors used the device to monitor the barrier function of different cell lines in a frequency dependent manner. This was achieved by defining a time constant τ to the speed of the transistor to reach steady state when the channel is saturated by ions. τ is thereby used to indirectly characterize the current flow through the cell layer.
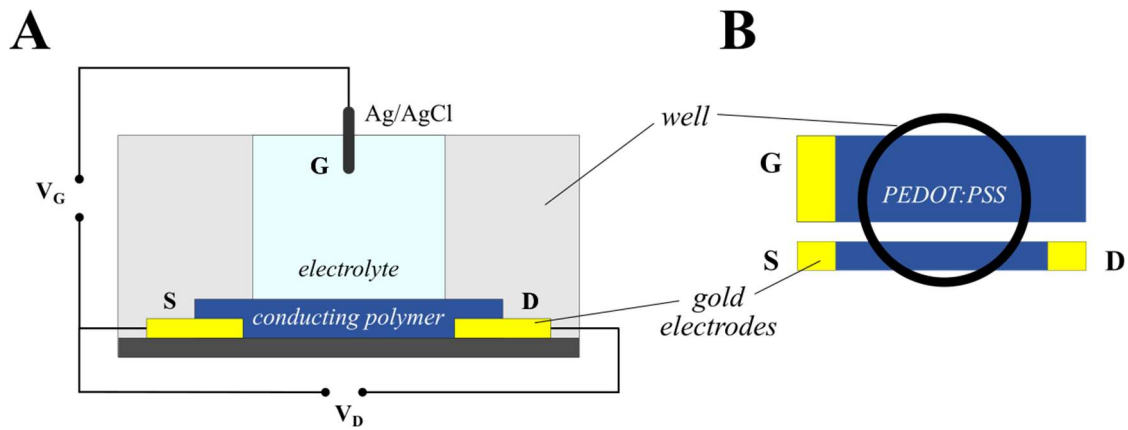
Fig. I-6: (A) Side view of the structure of a OECT with immersed Ag/AgCl gate electrode.[67] A drain current is generated upon application of a voltage V_D between source (S) and drain (D). The drain current depends on the conductivity of the conducting polymer and, therefore, on its doping level. The doping level, in turn, depends on the amount of ions injected into the polymer and is driven by the voltage V_G between source and gate (G). **(B)** Top view of a OECT with coplanar gate electrode.[68] The cell barrier function can be measured as the amount of ions injected into the polymer is restricted by the ion permeability of the cellular tight junctions.

3 Objective

The present PhD project is devoted to the advancement of impedance spectroscopy for whole-cell biosensors. The thesis tackles three different challenges of impedance spectroscopy, each addressing individual topics that are in different stages of their development process. The first project (cf. *III.2 PEDOT:PSS as Electrode Material*) aims to develop screen-printable polymer electrode arrays compatible with the well-established ECIS (electric cell-substrate impedance sensing) technique. PEDOT:PSS was chosen as electrode material instead of the common gold electrodes because of its enhanced interface capacitance and transmittance for visible light. These altered electrical and optical properties are evaluated and compared to gold electrodes by means of typical impedimetric cell-based assays like monitoring cell adhesion and spreading, cell proliferation, cytotoxicity, micromotion, and electroporation. Potential advantages and drawbacks are addressed. Furthermore, the electrodes' log-term and electrical stability, as well as the electrical and optical properties are examined. This project is intended to result in a commercially exploitable product in the near future. In a second project (cf. *III.3 Bipolar Electrodes*), a novel electrode design is introduced that uses the bipolar nature of a single high-resistance electrode for impedimetric cell sensing. These bipolar electrodes are compared with common two-electrode setups and differences in the respective impedance spectra and cell adhesion curves. Moreover, bipolar electrodes show a voltage gradient along their conduction path that is used to gradually wound cells growing on the electrode. Thereby, potential applications of bipolar electrodes are explored in a proof-of-principle approach. The third project (cf. *III.4 Derivative Impedance Spectroscopy (DIS)*) is entirely software-based and aims to evaluate data analysis methods that rely on the differentiation of impedance spectra. For this purpose, simulated raw data with known cell parameters are generated that are subsequently differentiated and subjected to a fitting algorithm. A method is presented to directly compare the fit results for spectra of different derivative orders, obtained with various fitting conditions like the weighting method, the number of increments in the fitting algorithm, and the type of spectrum to be analyzed.

II   THEORY

1   Impedance Spectroscopy in Aqueous Media

1.1   Electrical Current: Theory

The electrical resistance R is defined by the degree to which a conductor opposes an electric current flow through that conductor and is measured in Ohms (Ω). It depends on a material constant – the resistivity ρ (also specific electrical resistance) – and the physical dimensions of the device under test (DUT). The interdependence of the parameters is described by Eq. 1 with l being the length and A the cross section of the DUT.[69]

$$R = \rho \cdot \frac{l}{A}$$

Eq. 1

According to Ohm's Law R is the ratio between the voltage U in Volts (V) applied to the DUT and the current I in Amperes (A) flowing through it (Eq. 2).

$$R = \frac{U}{I}$$

Eq. 2

Ohm's Law is valid for direct current (DC) as well as alternating current (AC). In the latter case it is denoted as a complex quantity, the impedance Z. For sine wave signals as commonly used in impedance spectroscopy the impedance Z can be described in the time domain according to Eq. 3.[70-71]

$$Z = \frac{U(t)}{I(t)} = \frac{U_0 \cdot \sin(\omega t)}{I_0 \cdot \sin(\omega t - \varphi)} \qquad\qquad \text{Eq. 3}$$

with   U(t) as the applied voltage at time point t

I(t) as the resulting current at time point t

U_0 as the voltage amplitude

I_0 as the current amplitude

φ as the phase shift of the current

$\omega = 2 \cdot \pi \cdot f$ and f being the frequency

For ideally resistive circuit elements the phase shift φ between voltage and current is zero. Capacitive and inductive elements show a delayed ($\varphi = -\pi/2$) or a leading current ($\varphi = +\pi/2$), respectively. In order to facilitate the calculations with the trigonometric functions the impedance Z can be transformed into a complex quantity using Euler's formula. Hereby, the complex impedance Z is obtained, denoted in polar coordinates with a magnitude |Z| and a phase angle φ (Eq. 4). A Fourier transformation can be used to convert the time domain of the impedance into the frequency domain.[10,70-71]

$$Z = \frac{U(t)}{I(t)} = \frac{U_0 \cdot e^{j(\omega t)}}{I_0 \cdot e^{j(\omega t - \varphi)}} = \frac{U_0}{I_0} \cdot e^{j\varphi} = |Z| \cdot e^{j\varphi} \qquad\qquad \text{Eq. 4}$$

with: $j = (-1)^{0.5}$

magnitude of impedance |Z|

φ phase shift

The real and imaginary components of the impedance can be separated by transforming the impedance to its Cartesian coordinates (Eq. 5) using Eq. 6 – Eq. 9. A graphical representation of the complex impedance is shown in Fig. II-1 as a vector in a complex plane, where Im(Z) is the y-axis and Re(Z) the x-axis. The magnitude |Z| corresponds to the length of the vector, whereas the phase shift φ is represented by the angle between the x-axis and the vector.[10,70-71]

$$Z = |Z| \cdot e^{j\varphi} = \text{Re}(Z) + j \cdot \text{Im}(Z) = R + j \cdot X \qquad \text{Eq. 5}$$
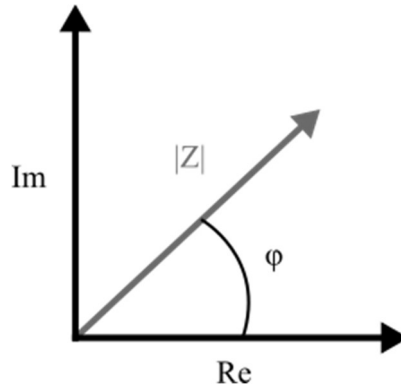
Fig. II-1: Graphical representation of the complex impedance in a vector plane with the real and the imaginary part of the impedance as the axes. Magnitude |Z| and phase shift φ correspond to the length of the vector and its angle with the x-axis respectively.

$$\text{Re}(Z) = |Z| \cdot \cos \varphi \qquad \text{Eq. 6}$$

$$\text{Im}(Z) = |Z| \cdot \sin \varphi \qquad \text{Eq. 7}$$

$$\varphi = \arctan \frac{\text{Im}(Z)}{\text{Re}(Z)} \qquad \text{Eq. 8}$$

$$|Z| = \sqrt{\text{Re}^2(Z) + \text{Im}^2(Z)} \qquad \text{Eq. 9}$$
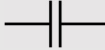
The real part of the impedance $\text{Re}(Z)$ is referred to as the resistance R, whereas the imaginary part $\text{Im}(Z)$ is called the reactance X. The reactance can be either capacitive (X_C) or inductive (X_L) and is represented by its respective circuit element as capacitor C (Eq. 10) or inductor L (Eq. 11).

$$X_C = - 1/(\omega \cdot C) \hspace{6cm} \text{Eq. 10}$$

$$X_L = \omega \cdot L \hspace{7cm} \text{Eq. 11}$$

Capacitor C, inductor L, and resistor R are passive circuit elements used to construct an equivalent circuit that represents the electrical properties of the DUT as close as possible. A transfer function can be derived from this *equivalent circuit* using Ohm's and Kirchhoff's laws. A very simple equivalent circuit model for a cell monolayer, for example, is a capacitor in parallel with a resistor. Capacitor, inductor and resistor, however, are merely idealized representations of reality and sometimes a more accurate approximation is necessary to account for the facts that ions are the charge carriers in electrochemical experiments and not electrons. Therefore, empirical and diffusion related circuit elements like the constant phase element (CPE) or the Warburg element (W) have been introduced. They are mostly used for the description of electrode-electrolyte interfaces and redox reactions in electrochemical applications and will be covered in chapter 1.3.

Tab. II-1: Electrical circuit elements used in this work to construct equivalent circuits for the different DUTs. Their equations for the complex impedance $Z(\omega)$ are listed along with the respective phase shifts φ and circuitry symbols. Refer to chapter 1.3 for more information on the Warburg element W and the constant phase element CPE. *equation for semi-infinite linear diffusion with A_W as Warburg coefficient (cf. 1.3)

	$Z(\omega)$	φ	symbol
R	R	0	
C	$(j \cdot \omega \cdot C)^{-1}$	$- \pi/2$	
L	$j \cdot \omega \cdot L$	$\pi/2$	
W	$A_W \cdot \omega^{-1/2} - j \cdot A_W \cdot \omega^{-1/2}$ *	$- \pi/4$	
CPE	$(j \cdot \omega)^{-n} \cdot A^{-1}$	$- n \cdot \pi/2$	

The impedance Z as an opposition to current flow may as well be expressed as its inverse, the admittance Y. Impedance and admittance are related by Y = 1/Z, therefore the admittance describes the ability to conduct current. The admittance is itself a complex quantity with a real and an imaginary part, measured in Siemens (S). Tab. II-2 summarizes the corresponding expressions and parameters in an overview. This work mostly refers to the dimensions related

to an opposition to current. The impedance is often expressed as *specific* impedance, meaning the area-normalized impedance.

Tab. II-2: Expressions and parameters for impedance, admittance, and their respective real and imaginary components. The related material constants are also included in the table.

	opposition to current		**ability to conduct current**	
Re + Im	impedance	Z / Ω	admittance	Y / S
Re	resistance	R / Ω	conductance	G / S
Im	reactance	X / Ω	susceptance	B / S
material constant	resistivity	ρ / $\Omega{\cdot}m$	conductivity	κ / $S{\cdot}m^{-1}$

For the characterization of thin, two-dimensional layers of a conducting material often the sheet resistance R_{sq} is used. R_{sq} is defined as the resistivity ρ divided by the thickness t of the conducting layer. It is only applicable when the current travels parallel to the surface and not in the bulk of the DUT. Since R_{sq} has the same dimension as R (Ω) it usually written as Ω/sq or Ω/$\square$ to avoid any confusion. Since the layer thickness t is included in R_{sq} the sheet resistance can be regarded as the resistive aspect ratio between width w and length l of a conductor (Eq. 12). Therefore, the resistance can be calculated if the dimensions and the sheet resistance are known.[72]

$$R = \rho \cdot \frac{1}{A} = \rho \cdot \frac{1}{w{\cdot}t} = R_{sq} \cdot \frac{1}{w} \qquad\qquad \text{Eq. 12}$$

1.2 Electrical Current: Practical Considerations

Several unwanted parasitic contributions have to be considered when performing impedimetric measurements. Every cable or electrical circuit element has a specific resistance R_{lead} and generates its own electromagnetic field. This causes interferences with adjacent cables and circuitry, which manifests itself as parasitic stray capacitance C_{prs} and inductance L_{prs}. If both are present they can also resonate at certain frequencies and cause major deflections from the ideal signal.[69,73] In addition, a contact resistance R_{cont} between the probe and the DUT may occur that depends on the contact area, the quality of the contact, and the conductor materials involved. The resistance is especially high at metal- or semiconductor-polymer interfaces.[74-75] All parasitic contributions that may arise during impedance measurements are summarized in a

simplified equivalent circuit in Fig. II-2. The circuit depicts the circuitry symbols schematically as elements localized in the connection cables. However, C_{prs}, L_{prs} and R_{lead} are actually distributed all over the network and cannot be reduced to one lumped component or location in the measurement setup. Nevertheless, R_{cont}, R_{lead}, and L_{prs} are always in series with the DUT, while C_{prs} is always in parallel.
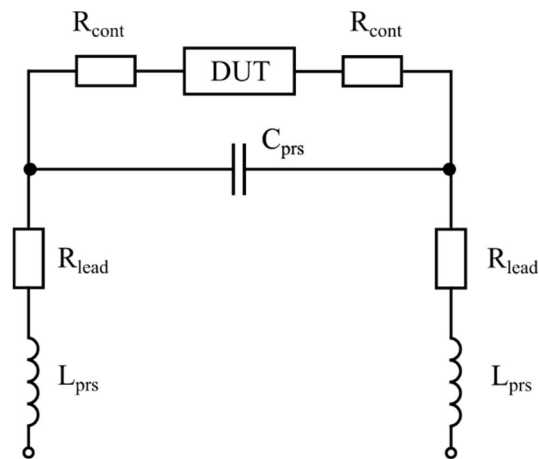
Fig. II-2: Simplified equivalent circuit for parasitic contributions during impedance spectroscopy. In reality the circuit elements (except R_{cont}) are not localized but distributed along the network.

When measuring the impedance, a sine wave shaped AC voltage is applied to the DUT and the resulting current is measured at various frequencies. The simplest setup consists of 2 terminals with just one working electrode (WE) and one counter electrode (CE). Here, the cables leading from the instrument to the DUT serve as both current source and sensing probe. This gives accurate results for high impedance DUTs where R_{lead} and R_{cont} do not carry any weight. However, if the impedance of the DUT is low or either R_{lead} or R_{cont} (or both) are high, the measurement is perturbed by these parasitic resistances. Therefore, all modern impedance analyzers are equipped with a 4-terminal connection, where a high current (Hi_{cur}) and a low current (Lo_{cur}) connection provide the measurement current, and a high potential (Hi_{pot}) and a low potential (Lo_{pot}) connection detect the potential drop across the DUT (Fig. II-3). In this setup the voltage drop in the connection cables and therefore R_{lead} can be neglected because almost no current flows through the sensing wires (Hi_{pot} and Lo_{pot}).[71,73] This is true when the Hi and Lo terminals are connected closely to the DUT as it can be achieved using a Kelvin probe. However, if the DUT is for example a microfluidic channel or an electrode array with leads showing significant resistivity between the contact pads and the measurement chamber, those leads still have to be taken into consideration as an additional series resistance R_{lead}. This is the case for example for very thin metal films or materials with low intrinsic conductivity.

Fig. II-3 shows the circuitry of a 4-terminal measurement as featured by a typical impedance analyzer. The Hi side of the current terminal is connected to the drive potential of the oscillator (OSC), whereas the Lo side interconnects the shields of all current and sensing wires. Therefore, the electromagnetic fields of the center conductors and the shield conductors cancel each other out so that the influence of parasitic capacitances and inductances C_{prs} and L_{prs} caused by the wires and overall circuitry are minimized.[73,76]
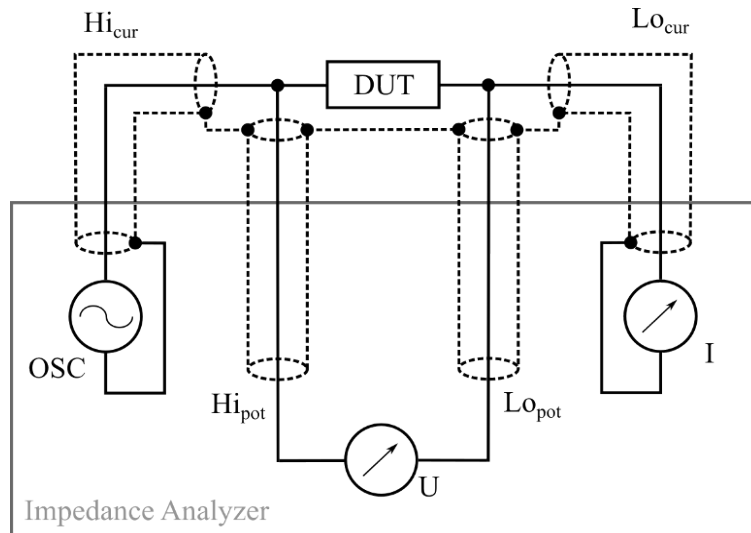
Fig. II-3: 4-terminal measurement setup.[73] Hi_{cur} and Lo_{cur} provide the measurement current via the oscillator (OSC), while Hi_{pot} and Lo_{pot} detect the voltage drop across the DUT. The impedance is given by division of the voltage drop U across the DUT by the current I through the DUT. The shields of the current and sensing wires are connected to the Lo side of the oscillator to minimize the influence of electromagnetic fields and avoid reflections of the measurement signal inside the wires.

1.3 The Electrode-Electrolyte Interface

When a DC potential is applied between two electrodes immersed in an electrolyte the ions begin to migrate to the cathode or the anode depending on their charge. According to a model by Helmholtz[77-78] the ions in the electrolyte and the charges in the electrode form an *electric double layer* with opposite charges on the electrode surface (Fig. II-4 A). This model is analogous to a plate capacitor where the two plate electrodes are separated by a dielectric. Since the Helmholtz model is only valid in highly concentrated electrolyte solutions and neglects ion diffusion and thermal motion, Gouy[79] and Chapman[80] developed a theory that takes ion mobility into account. Their model describes a *diffuse double layer* where the ions are distributed at a much larger distance from the electrode (Fig. II-4 B). This theory, however, fails for high ion concentrations or electrode potentials. Therefore, a third model was established by Stern[81] that combines both theories of the *Helmholtz layer* and the *Gouy-Chapman layer*. The Stern model

describes an inner layer, the *Stern layer*, that consists of ions adsorbed on the charged electrode surface, and is separated from a diffuse second layer, the *Gouy layer* (Fig. II-4 C). It also takes into account that dissolved ions are not point charges but have a finite size and are surrounded by a hydrate shell.[82-84]
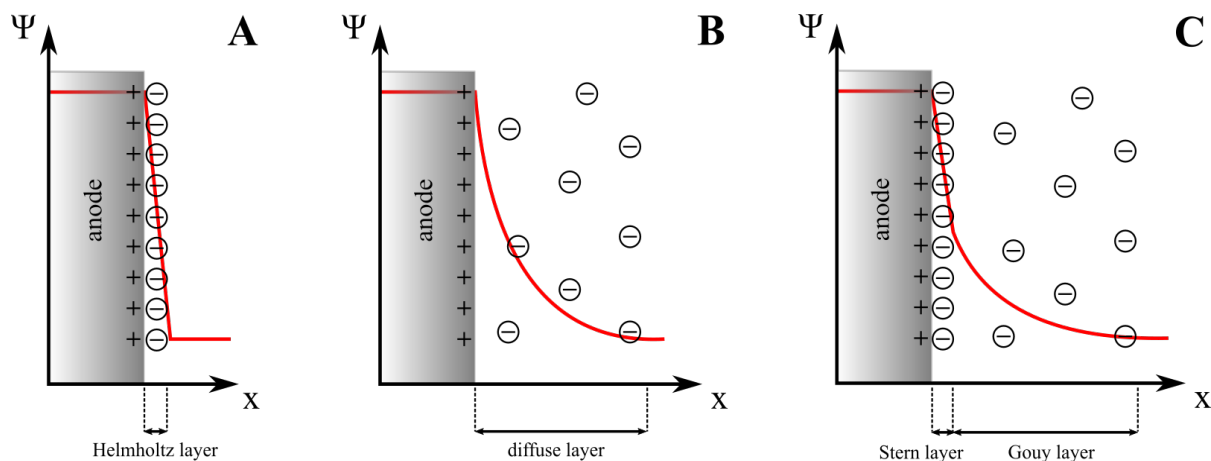
Fig. II-4: (A) Helmholtz model of the double layer at the anodic electrode-electrolyte interface. The change of the electric potential Ψ with distance x from the electrode surface is schematically shown in red. **(B)** Gouy-Chapman model with a diffuse layer. **(C)** Stern model consisting of the adsorbed Stern layer and the diffuse Gouy layer.[82]

All of these models describe the electrode-electrolyte interface for DC potentials that are below the redox potential of the electrolyte. At higher electrode potentials redox reactions occur and electrons are transferred from the cathode to an oxidant or from a reductant to the anode, causing a faradaic *charge-transfer current*. If there is no charge transfer between the electrode and the solution, the electrode is called *ideally polarizable*. Typical examples for electrodes that are ideally polarizable over a wide potential range are gold, platinum, or dropping mercury electrodes (up to 2 V).[70,83] However, polarizability of an electrode always depends on the applied potential and the electrolyte. Platinum for example is highly polarizable in NaCl solution, but becomes non-polarizable in the presence of the redox pair H_2/H^+. Gold is inert towards most chemicals, so that the reduction of the supporting electrolyte sets the limit for ideal polarizability.[70]

Application of a low AC potential periodically charges and discharges the electrode surface with positive and negative charges. This causes the ions in the solution to migrate back and forth between the electrodes, therefore generating a non-faradaic AC current that is only caused by ion movement. This ideal behavior can be described by a capacitor with the double layer capacitance C_{dl}. In reality frequency dispersion occurs at solid electrodes. Therefore, the so-called *constant phase element* (CPE) is commonly used to model the deviations from ideal

double layer capacitance behavior. A solution resistance R_s in series with the CPE gives the complete equivalent circuit for the electrode interface and the electrolyte (Fig. II-5 A). In the corresponding Bode plot the constant impedance at high frequencies corresponds to R_s (Fig. II-5 B). The slope of |Z| at low frequencies is equal to -n in double logarithmic plots and -1 for ideal capacitive behavior. For real gold film electrodes, n takes values from 0.9 to 0.98. φ lies between -n·90° at low frequencies and 0° at high frequencies. The impedance Z_{CPE} for the CPE is given by Eq. 13.
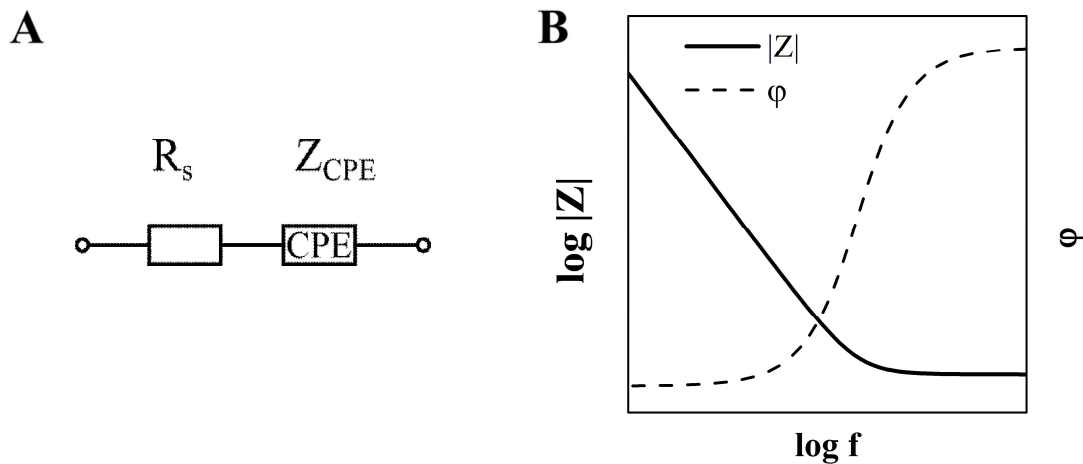
Fig. II-5: (A) Simple equivalent circuit to describe electrode and electrolyte. R_s is the solution resistance of the electrolyte and Z_{CPE} represents the non-ideal capacitive behavior of the double layer at the electrode-electrolyte interface. **(B)** Corresponding schematic Bode plot. The constant impedance at high frequencies corresponds to R_s. The slope of |Z| at low frequencies is equal to -n in double logarithmic plots and -1 for ideal capacitive behavior. φ ranges from -n·90° at low frequencies and 0° at high frequencies.

$$Z_{CPE} = \frac{1}{(j\omega)^n \cdot A} \qquad\qquad \text{Eq. 13}$$

Both parameters A and n ($-1 \leq n \leq 1$) are empirical and difficult to interpret physically. When modeling the electrode-electrolyte interface n is usually close to 1 and describes a predominantly capacitive behavior. If n = 1, the impedance is that of an ideal capacitor and A is equal to the capacitance C (Fig. II-6). Other special cases for values of n are shown in Tab. II-3.

Tab. II-3: Special cases of CPE behavior for different values of n. The parameter A corresponds to different parameters from other circuit elements depending on n.[85-86] The Warburg impedance will be addressed below.

	n	A
capacitance	1	C
resistance	0	R^{-1}
inductance	-1	L^{-1}
Warburg impedance	0.5	$(A_W \cdot \sqrt{2})^{-1}$
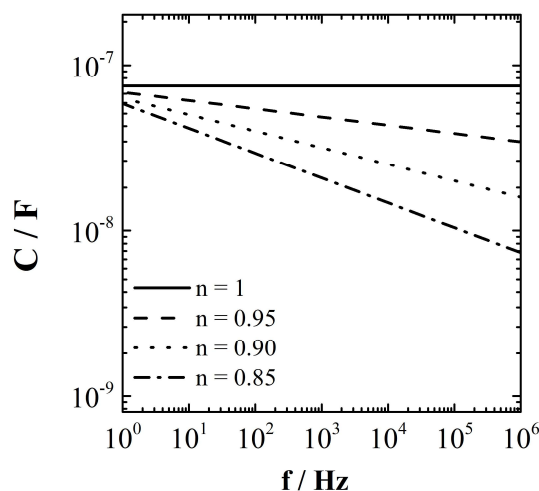
Fig. II-6: Capacitance dispersion effect of the CPE. In an ideal capacitor n is equal to 1 and the capacitance C is independent of the frequency. However, non-ideal capacitive behavior occurs at metal-liquid interfaces due to surfaces inhomogeneities and n usually ranges from 0.90 to 0.95. This causes a frequency dispersion of the capacitance.

The physical origin of CPE behavior at the electrode-electrolyte interface has been widely discussed in literature. Surface roughness, porosity, and varying thickness or composition of the electrode at a microscopic scale have been debated as being potential explanations for the so-called *capacitance dispersion* effect of a CPE.[87-91] In either case an inhomogeneous current density is present at the surface, so that the effects of solution resistance and interface capacitance are scrambled and cannot be regarded separately. Pajkossy[91] described these geometric inhomogeneities as being only indirectly related to the capacitance dispersion and instead attributed it to ion adsorption effects on the surface.

If charge transfer occurs, the CPE is no longer sufficient to accurately describe all processes at the electrode surface. Instead, the *Randles circuit*[92] is commonly employed (Fig. II-7 A). It consists of a solution resistance R_s, a double layer capacitance C_{dl}, a charge-transfer resistance R_{ct}, and a Warburg impedance Z_W. As mentioned above for non-faradaic current, C_{dl} is often replaced by a CPE.
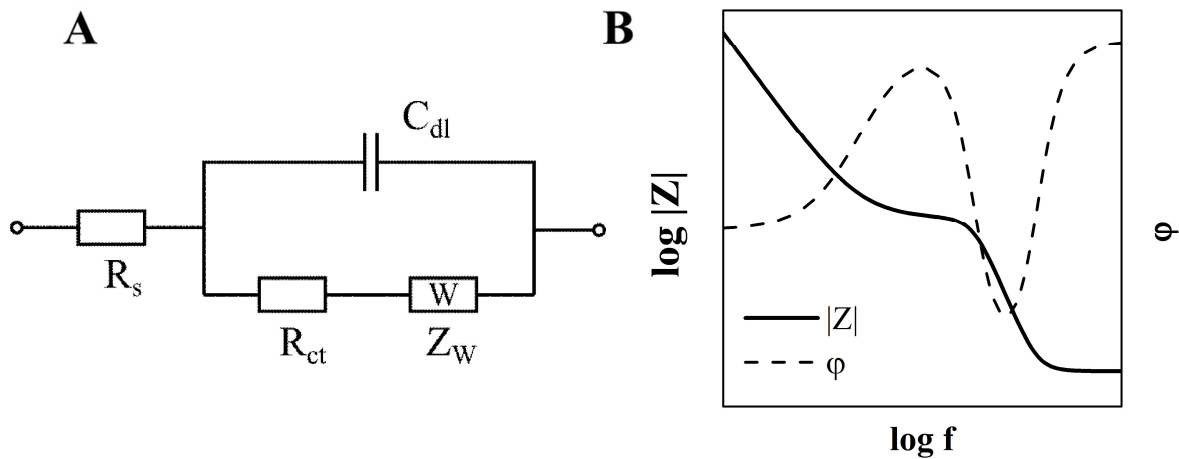
Fig. II-7: (A) Randles circuit with solution resistance R_s, double layer capacitance C_{dl}, charge-transfer resistance R_{ct}, and Warburg impedance Z_W. C_{dl} is often replaced by a CPE. **(B)** Corresponding schematic Bode plot. At very low frequencies the slope of |Z| is -1/2 and φ = -45°. The plateau in the medium frequency range corresponds to $R_s + R_{ct}$.

The Warburg element W is a diffusion related circuit element whose impedance Z_W is given by Eq. 14 for semi-infinite linear diffusion, i.e. unrestricted diffusion to a large planar electrode.[93]

$$Z_W = A_W \cdot \omega^{-1/2} - j \cdot A_W \cdot \omega^{-1/2} \qquad \text{Eq. 14}$$

In this equation A_W is the Warburg coefficient, which depends on the temperature, the surface area of the electrode, and the charge and concentration of the involved species in the electrolyte. The Warburg impedance Z_W can be recognized by a -45° phase angle at very low frequencies and a slope for |Z|(f) of -1/2 in the Bode plot (Fig. II-7 B).[70-71] The charge transfer resistance R_{ct} depends on the rate constant of the charge transfer and the concentration of the active species.[70]

1.4 Electric Cell-Substrate Impedance Sensing (ECIS)

The theory described in chapter 1.3 has been established particularly for electrochemical impedance spectroscopy (EIS). EIS is commonly used for the study of corrosion, semiconductors, batteries, and electro-plating. Its basic principles have also been successfully applied for the analysis of living cells *in vitro*. The first method of this kind was published by Giaever and Keese in 1984[20] and later termed Electric Cell-Substrate Impedance Sensing (ECIS). In 1991 the same authors presented an in-depth model for the analysis of a two-

dimensional cell monolayer.[19] This allowed the extraction of cell parameters from the impedance spectra and a detailed analysis of the morphological changes of cells grown on two coplanar gold electrodes became possible.

In ECIS measurements the impedance Z between one small working electrode (WE) and a significantly larger counter electrode (CE) is determined by application of a weak sine wave AC voltage (Fig. II-8 A). In nowadays' commercial electrode arrays the WE has an electrode area between $5 \cdot 10^{-4}$ cm² and $5 \cdot 10^{-3}$ cm² and the CE is about 100 - 1000 times larger. Therefore, the voltage drop and current density at the CE can be neglected and the impedance of the overall system is almost exclusively determined by the WE. There are two general pathways for the current to cross the cell layer. At low frequencies below 10 kHz the resistive pathway around the cell body is preferred, while at higher frequencies above 10 kHz capacitive coupling through the cell membranes dominates. The resistive and capacitive components of the impedance are, however, scrambled at intermediate frequencies.[10,94]

In order to model a cell layer Giaever and Keese[19] approximated the cells as circular disks with a radius r and a distance h from the electrode surface (Fig. II-8 B). The current was assumed to flow radially in the subcellular cleft underneath the cells and outward into the bulk electrolyte through the channels between adjacent cells. Along with the presence of capacitive coupling to the bulk electrolyte this creates a complicated electrical configuration in which the current pathway is frequency and position dependent. There is no lumped equivalent circuit element to describe the impedance arising from the subcellular cleft. Instead, the current flow between electrode and cell layer was modeled using the *finite element method* (FEM) (Fig. II-9).[19] The FEM is a numerical method where a complex problem is divided into small *finite elements* that are easier to handle. Later, the equations for these elements can be combined to a complex system to describe the entire problem.[95]
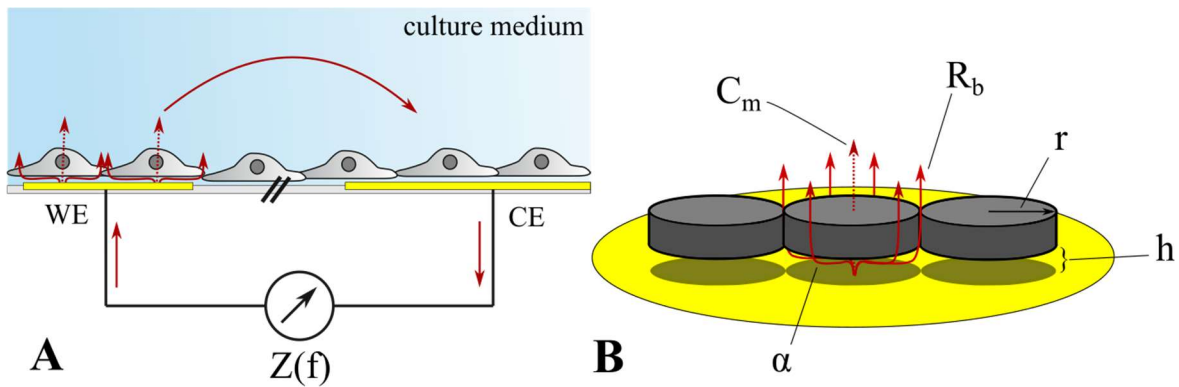
Fig. II-8: (A) Schematic representation of the ECIS measurement principle. In order to measure the impedance Z(f) a weak sinusoidal voltage is applied between a small working electrode (WE) and a larger counter electrode (CE). There are two principal pathways for the current to pass the cell layer: resistively underneath and in between the cells (solid lines), or capacitively through the cells (dashed lines). **(B)** ECIS model by Giaever and Keese. The cells are assumed to be insulating disks with a radius r at a distance h above the electrode. The parameters C_m, α, and R_b represent the capacitance of the cell membrane, the impedance contribution of the subcellular cleft and the specific resistance of the cell-cell junctions, respectivey.
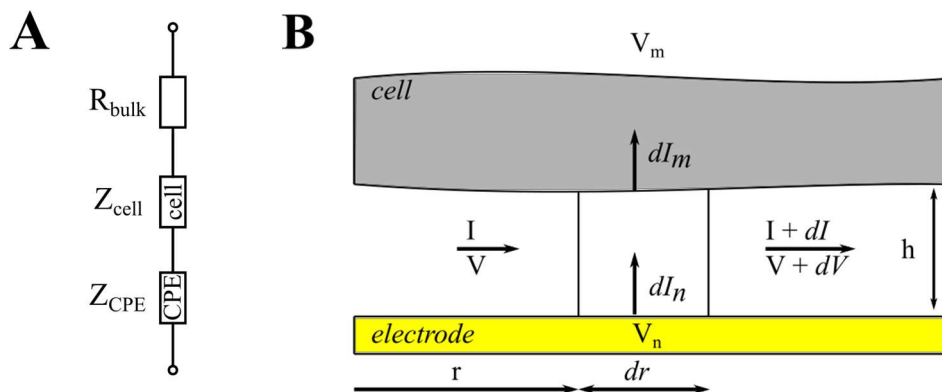
Fig. II-9: (A) Equivalent circuit of a cell-covered electrode. The impedance contribution of the cell layer Z_{cell} cannot be adequately described by a simple equivalent circuit element with lumped elements. Instead, a system of differential equations was used to describe the current flow around the cells and through the cell layer. **(B)** Sketch for setting up the differential equation for a 2D cell layer on a planar electrode as proposed by Giaever and Keese.[19] I and V are the current and potential in the subcellular cleft. V_n and V_m represent the potential of the electrode and the potential outside the cell in the bulk electrolyte respectively. Accordingly, dI_n and dI_m are the current coming from the electrode and the current leaving through the cell layer. dI and dV are current and potential change arising from the infinitesimal cell radius segment dr. The distance between cell and electrode is given by the parameter h.

Assuming a constant current density, an infinitesimal current change in the cleft dI in lateral direction was considered to be the difference between the current coming from the electrode dI_n and the current leaving through the cell membrane dI_m (Eq. 15).

$$dI = dI_n - dI_m \qquad\qquad \text{Eq. 15}$$

The corresponding potential change dV depends on the resistivity of the electrolyte in the subcellular cleft ρ and its physical dimensions: the distance between cell and substrate h and the cell radius r (Eq. 16). This equation is related to Eq. 1.

$$- dV = \frac{\rho dr}{h \cdot 2\pi r} \cdot I \qquad\qquad \text{Eq. 16}$$

Using Ohm's law (Eq. 2) the following equations were set up describing the potential differences between electrode and cleft V_n - V (Eq. 17), and cleft and electrolyte outside the cell layer V - V_m (Eq. 18), respectively.

$$V_n - V = \frac{Z_n}{2\pi r dr} dI_n \qquad\qquad \text{Eq. 17}$$

$$V - V_m = \frac{Z_m}{2\pi r dr} dI_m \qquad\qquad \text{Eq. 18}$$

Here Z_n is the specific impedance of the cell-free electrode and Z_m the specific impedance of the cell layer. Combining Eq. 15 – Eq. 18 resulted in a differential equation whose solutions were used to form the equation for Z_{total}, the specific impedance for a cell-covered electrode (Eq. 19).[19,96]

$$Z_{total} = R_{bulk} + \left[\frac{1}{Z_n} \left(\frac{Z_n}{Z_n + Z_m} + \frac{\frac{Z_m}{Z_n + Z_m}}{\frac{1}{2}\gamma r \frac{I_0(\gamma r)}{I_1(\gamma r)} + R_b \left(\frac{1}{Z_n} + \frac{1}{Z_m} \right)} \right) \right]^{-1} \qquad\qquad \text{Eq. 19}$$

with:

$$\gamma r = \sqrt{\frac{\rho}{h} \cdot \left(\frac{1}{Z_n} + \frac{1}{Z_m}\right)} \cdot r = \alpha \cdot \sqrt{\left(\frac{1}{Z_n} + \frac{1}{Z_m}\right)} \qquad \text{Eq. 20}$$

I_0 and I_1 are modified Bessel functions of the first kind of the order zero and one. The specific impedance Z_n of the cell-free electrode and is usually modeled by a constant phase element. Z_m is the sum of the impedances of the apical and basal membrane and is defined by Eq. 21:

$$Z_m = \frac{1}{j\omega C_{cl}} = \frac{2}{j\omega C_m} \qquad \text{Eq. 21}$$

where C_{cl} is the capacitance of the cell layer and C_m is the capacitance of one single membrane. Since the capacitances of the apical and basal membrane are in series they cannot be distinguished in this model. C_m is always the average membrane capacitance of both membranes, even though in reality their surface areas and therefore their capacitances may often differ in mammalian cells. The parameter α is associated with the current flow in the subcellular cleft and can thus be interpreted with regard to the cell-substrate interactions. It depends on the cell radius r, the resistivity of the electrolyte in the subcellular cleft ρ, and the distance between cell and substrate h (Eq. 22).

$$\alpha = r \cdot \sqrt{\frac{\rho}{h}} \qquad \text{Eq. 22}$$

R_b is the specific resistance between the cells and is therefore a measure for the tightness of the cell-cell junctions. R_b indirectly also depends on r as with larger cells the number of cells per unit area and hence the number of cell-cell contacts decreases. All cell parameters are summarized in Tab. II-4.

Tab. II-4: Description and units of the parameters used to model the electrical behavior of a 2D cell monolayer growing on a planar electrode.

parameter	unit	description
C_m	$\mu F \cdot cm^{-2}$	specific cell membrane capacitance
α	$\Omega^{1/2} \cdot cm$	impedance contribution of the cell-substrate contact
R_b	$\Omega \cdot cm^2$	specific resistance of cell-cell contacts

R_{bulk} is the resistance of the bulk electrolyte. This includes the solution resistance R_s as well as the constriction resistance R_{cs}. R_{cs} varies with $\rho_s/(2 \cdot d)$, with d being the electrode diameter and ρ_s the specific resistance of the electrolyte. Hence, R_{cs} dominates on small electrodes (Eq. 23) as long as the distance between WE and CE is small.

$$R_{bulk} = R_s + R_{cs} \approx R_{cs} \text{ for d} \ll 1 \text{ cm} \qquad \text{Eq. 23}$$

The origin of the constriction resistance is based on the fact that the WE is small compared to the CE and current flow is therefore restricted at the WE. In other words, a small electrode diameter makes the electrode the bottleneck for the current flow. A perturbation of the current caused by the cell layer on the electrode can therefore be measured with high sensitivity.[10,19-20,94,96] It should be noted that results obtained for R_{bulk} by fitting may also contain parasitic resistive elements like contact resistance R_{cont} and lead resistance R_{lead} (cf. 1.2). The size of the electrodes determines over how many cells the measurement signal is averaged. Hence, the movement of the cells on the electrode is increasingly revealed when the size of the WE is reduced. This cellular movement on a small times scale in the order of seconds is called *micromotion* and can be used as an analytical tool when the impedance is recorded with a correspondingly high time resolution. This will be discussed in more detail in chapter 3.2.1.4.

ECIS spectra are commonly displayed in double-logarithmic plots, where the decadic logarithms of the magnitude of the impedance |Z| and the frequency f are plotted against each other. Besides the contributions of the cell-free electrode, additionally the impedance of the cell layer shows up in the spectrum at intermediate frequencies (Fig. II-10 A). The low and high frequency ranges are dominated by the electrode-electrolyte interface (Z_{CPE}) and bulk resistance (R_{bulk}), respectively. At higher frequencies approaching 1 MHz parasitic capacitive elements C_{prs} often occur. They may arise from the electrical circuitry or conduction leads that are

separated from the electrolyte by a passivation layer (Fig. II-10 B). The passivation layer acts as a dielectric between the gold electrode and the electrolyte. It shows properties of a capacitor C_{psv}, where A_{psv} is the overlapping area between the electrode leads underneath the passivation layer and the electrolyte, ε_0 is the vacuum permittivity, ε_r is the permittivity of the dielectric (or *dielectric constant*), and d_{psv} is the thickness of the passivation layer (Eq. 24).

$$C_{psv} = \frac{\varepsilon_0 \varepsilon_r \cdot A_{psv}}{d_{psv}} \qquad\qquad \text{Eq. 24}$$
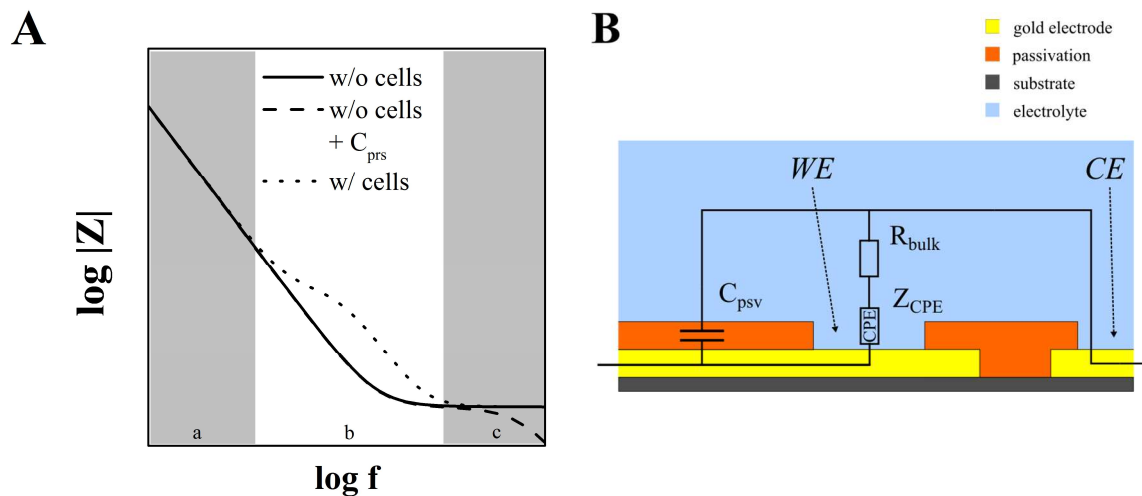
Fig. II-10: (A) Schematic impedance spectra for an (ideal) cell-free electrode (solid line), including a parasitic capacitance C_{prs} (dashed line), and a cell-covered electrode (dotted line). The low frequency region (a) is dominated by the interface impedance Z_{CPE}, the intermediate frequency (b) by the impedance of the cell layer. The high frequency region (c) is dominated by R_{bulk}, but may be overruled by a parasitic capacitance if present. **(B)** Graphical representation of the origin of the parasitic capacitance caused by the passivation layer. The passivated leads (yellow) run in parallel to the electrolyte and that way cause a parasitic capacitance C_{psv} that depends on the thickness, the surface area, and the dielectric constant of the passivation layer (orange).

2   Conducting Polymers as Electrode Material

As a part of this thesis we aimed to replace the – in ECIS and other electrical measurements – commonly used gold electrodes by electrodes made of conducting polymers and to investigate possible advantages and disadvantages. Among all conducting polymers PEDOT:PSS stands out as it is available as an aqueous dispersion. This is remarkable since nearly all other conducting polymers are barely soluble in any solvent due to the hydrophobicity of the polymer chains in combination with the high polarity at the charged doping sites. Manufacturing and handling is therefore considerably facilitated when using PEDOT:PSS. In order to shed light on the electrical behavior of PEDOT:PSS in an aqueous environment, this chapter will first cover the general conduction mechanism of conducting polymers. Then the specific electrode properties of PEDOT:PSS will be addressed.

2.1   Intrachain Charge Transport

Conductivity in an organic polymer chain can be explained according to the band theory. It states that for a large number of molecules, the bonding π- and the energetically elevated antibonding π_*-orbitals have condensed to electron bands. The electron band which is completely occupied by electrons in the ground state is called valence band, while the unoccupied band is termed conduction band. The highest energy level occupied by electrons is the Fermi level. The gap between valence and conduction band, the band gap, determines the intrinsic electrical properties of a material (Fig. II-11).[31]
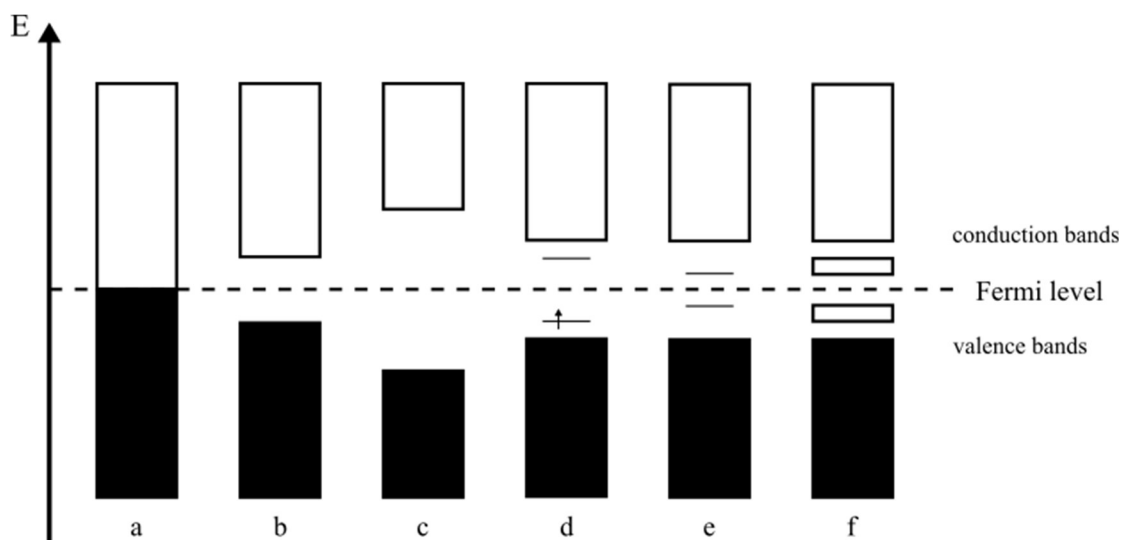
Fig. II-11: Energy diagram of the band structures of a conductor (a), a semiconductor (b), and an insulator (c). The band structures of conducting polymers are illustrated containing a positive polaron (d), a positive bipolaron (e), and bipolaron bands (f).[97]

In a conductor (or metal) valence and conduction band overlap and the electrons can easily move within the unoccupied orbitals of the conduction band. In semiconductors with a band gap smaller than ~ 3 eV the electrons cannot move in the ground state, but can be elevated into the conduction band upon thermal or radiation excitation. If the band gap is larger than ~ 3 eV and excitation is not possible or the required energy would destroy the material, the material is an insulator. According to this theory, any polymer with a conjugated π-system should be conducting. However, undoped polyacetylene and other conjugated polymers exhibit properties of poor semiconductors or even insulators. The reason for this is that by coupling of the wave functions of π-electrons and modes of lattice vibration (phonons), alternating double and single bonds become energetically more stable than a delocalized π-system (Fig. II-12). This lowers the Fermi level and increases the band gap. This phenomenon has been calculated theoretically but is also evident by the occurrence of alternating bond lengths along the polymer chain.[97]
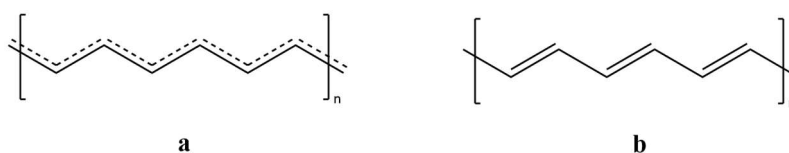
Fig. II-12: Instead of the expectable delocalized π-electron system (a) undoped polyacetylene exhibits alternating σ- and π-bonds (b) and is therefore only poorly electrically conductive.

The problem is circumvented by *doping* the polymer, using similar erms as established for inorganic semiconductors. Doping in this context means the oxidation (p-doping) or reduction

(n-doping) of the polymer chain. The former is more common. Generally, ionization creates an electron hole within the valence band in metals and semiconductors, which is completely delocalized. By contrast, in organic polymer chains it may be energetically favorable if the charge is localized and the lattice is locally distorted. This leads to the presence of localized electronic states in the band gap, meaning that the HOMO (highest occupied molecular orbital) experiences an upward shift and the LUMO (lowest unoccupied molecular orbital a downward shift. If – in the case of oxidation – the energy gained by removal of an electron from the HOMO exceeds the energy needed to distort the lattice, distortion occurs and a so called polaron is formed. A polaron is a charge associated with a lattice deformation. The corresponding electronic states are referred to as polaron states. When another electron is removed, it is energetically favorable that a so-called bipolaron is created instead of two single polarons (Fig. II-11). In a bipolaron two equal charges are associated with a strong lattice distortion. The energy gained by bipolaron formation must surpass the Coulomb repulsion of the charges, which is also alleviated by the screening effect of the counter ions. The hereby obtained bipolaron states are unoccupied for p-doping and completely occupied for n-doping. Electron transition can now more easily occur from the valence band into the lower bipolaron level in the former, and from the upper bipolaron level into the conduction band in the latter case. The formation of polaron and bipolaron bands strongly depends on the doping level. Low doping levels mainly lead to the formation of polarons, while at intermediate doping levels bipolarons are favored. High doping levels result in the creation of bipolaron bands (Fig. II-11). In fact, polarons, bipolarons, and bipolaron bands may all coexist in different proportions in a conducting polymer.[31,97] The structures of PEDOT in the undoped state, as polaron, and as bipolaron are shown in Fig. II-13. The positive charges of bipolarons are delocalized over several units. Their formation is accompanied by a conformational transition from a benzoid to a quinoid structure. The involved enhanced alignment of the individual PEDOT chains contributes to an increased conductivity.[98]
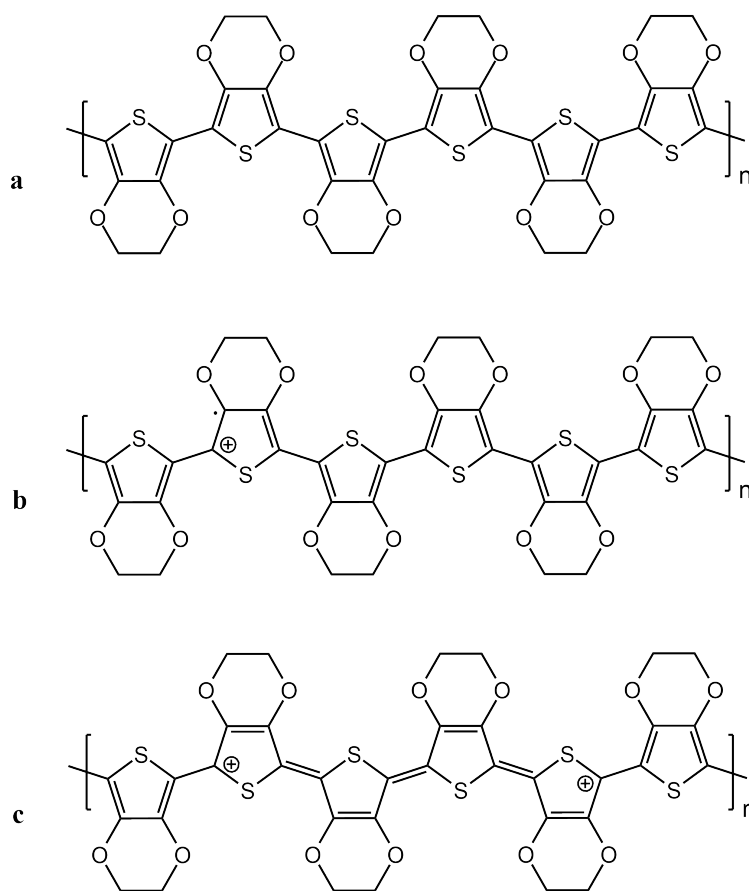
Fig. II-13: Structures of PEDOT in the undoped state (a), with a polaron after removal of one electron (b), and with a bipolaron after removal of two electrons (c).[41,99] The formation of bipolarons is accompanied by a transformation from a benzoid (a, b) to a quinoid structure (c).

2.2 Interchain Electron Hopping

In the previous chapter the charge transport along the polymer chains was described. However, the charges also have to move from chain to chain and this can be the conduction-limiting factor.[97] This interchain charge transport occurs by electron hopping mechanisms, i.e. thermally assisted tunneling between the chains.[100] Therefore, conducting polymers generally exhibit a semiconductor-like temperature dependence of the conductivity.[51] In PEDOT:PSS the electron hopping is especially impaired by the insulating PSS chains. In a PEDOT:PSS aqueous dispersion usually an excess of hydrophilic PSS surrounds and stabilizes the insoluble PEDOT polymer clusters in solution (Fig. II-14a). The clusters contain just the necessary amounts of 'dopant' PSS to compensate the positive charges on the PEDOT chain.[101] The micellar structure is conserved when the polymer dispersion is deposited on a substrate (Fig. II-14b). Typical values for PEDOT to PSS weight ratios range from 1:2.5 to 1:20, with a total PEDOT:PSS content between 1.1% and 2.8% (w/w).[41]
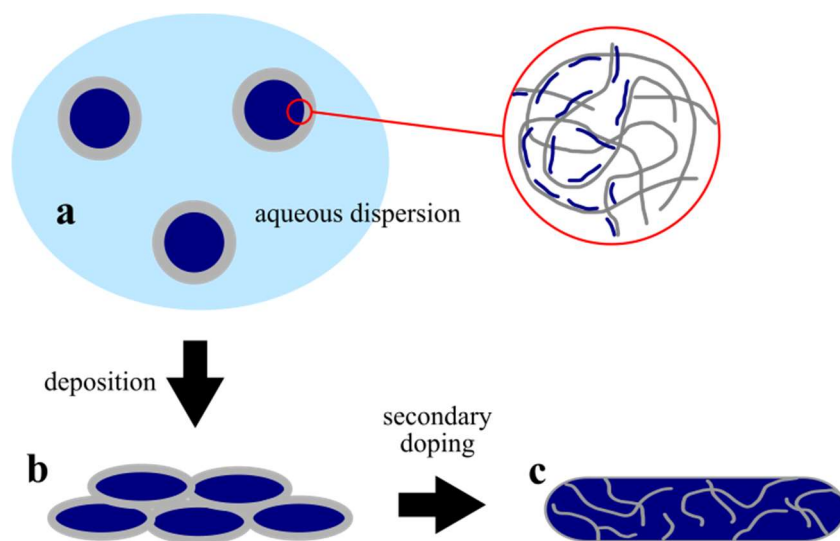
Fig. II-14: Illustration of PEDOT:PSS as aqueous dispersion (a), after deposition on a substrate (b), and after secondary doping (c). PEDOT rich areas are shown in dark blue, excess PSS in grey. A PEDOT:PSS dispersion is usually prepared by oxidative polymerization *in situ*. The dispersed particles are surrounded by a PSS shell which stabilizes them due to their hydrophilic character. After deposition on a substrate this micellar structure is maintained, so that the highly conducting PEDOT rich particles are separated by insulating PSS layers. After secondary doping the excess PSS is segregated or removed so that electron hopping between the PEDOT chains occurs more easily.[101]

In a thin film the highly conductive PEDOT grains are surrounded by insulating PSS chains, which impede electron hopping between the PEDOT domains.[99,102] Therefore, composition and morphology of the polymer have strong consequences on the conductivity. Reducing the amount of excess PSS is known to increase the conductivity. Electrochemically polymerized PEDOT:PSS displays a much lower PSS content and consequently a higher conductivity than PEDOT:PSS deposited from a chemically prepared dispersion. The conductivity is even higher when the small tosylate anions (TsO, p-toluenesulfonate) are used as dopant for PEDOT instead of the polymeric PSS.[103] The conductivity of chemically polymerized PEDOT:PSS is however drastically improved by so-called *secondary doping*, i.e. the addition of apparently inert chemical compounds that lead to morphological changes within the polymer. As first reported by Kim et al.[51] the addition of some high boiling polar (co-)solvents like dimethyl sulfoxide (DMSO) or ethylene glycol (EG) to the aqueous polymer dispersion increases the conductivity by up to several orders of magnitude (Tab. II-5).[51,99,104] The same effect has been observed for post-coating treatment of the dry polymer film with EG or solvent-water mixtures.[104-105] The addition of surfactants can improve conductivity and adhesion stability.[41] Even though the exact mechanisms may vary they are generally based on screening effects between the positive charges of the PEDOT chains and the negative charges of the PSS chains.[99] This induces a phase separation between the excess PSS stabilizing the PEDOT in the solution and the 'dopant'

PSS. It has been proposed that the insulating PSS layer becomes so thin that a three-dimensional network of interconnected highly conductive PEDOT:PSS in a matrix of PSS is formed (Fig. II-14c).[103] To my best knowledge, the highest conductivity for PEDOT:PSS so far reported in literature is 4600 S/cm, obtained by solution shearing and subsequent methanol treatment.[50] A detailed summary of the methods and mechanisms to enhance the conductivity of PEDOT:PSS has been published by Shi et al.[106] In this work, the PEDOT:PSS screen printing paste was used as received without further treatment.

Tab. II-5: Examples for the conductivity enhancement of PEDOT:PSS by secondary doping (cs = co-solvent doping, pt = post treatment, ACN = acetonitrile).

secondary dopant	method	κ / S/cm	source
-	-	0.1 - 10	51,104-105
DMSO	cs	80	51
EG	cs	735	104
EG	cs + pt	1418	104
ACN / H_2O	pt	78.9	105
MeOH	pt	4600	50

2.3   The Electrode-Electrolyte Interface of PEDOT:PSS

PEDOT:PSS – like PSS itself – is highly hygroscopic and may increase its layer thickness by up to 30% upon water uptake from ambient air, particularly in the case of a high PSS content.[41] Accordingly, if brought in contact with an aqueous solution, the electrolyte interpenetrates the polymer. This causes swelling and the formation of a polymer hydrogel.[107] Therefore, the effective contact area between the conducing polymer and the electrolyte – and consequently the specific interface capacitance – is drastically increased compared to metal or semiconductor electrodes.[65] PEDOT:PSS is a mixed conductor. This means conduction in the polymer has both an electronic and an ionic component. As described in the previous chapters (2.1 and 2.2) the electronic conduction path occurs by charge transfer within and in between the PEDOT chains. The ionic conductivity stems from a drift[b] of free ions present in the hydrated polymer, caused by the electric field of the applied voltage.[108-109] The charge transport in a PEDOT:PSS electrode contacted by a metal on one side and interconnected to the counter electrode via an electrolyte solution on the other side is schematically depicted in Fig. II-15. Upon application

---

[b] ion drift: ion movement caused by an electric field
ion diffusion: ion movement caused by a concentration gradient

of a small sinusoidal voltage, charge transfer occurs across the metal-polymer interface. PEDOT is successively oxidized and reduced, i.e. the polymer is reversibly doped and dedoped. In order to maintain electroneutrality, ions drift from and into the polymer at the polymer-electrolyte interface. Additionally, there is an excess of supporting electrolyte present in the polymer, which facilitates ion movement in the film. As a consequence, the effective migration length between the ions and the corresponding doping charges on the polymer is very short.[107-108,110]

Electron injection from the metal into the polymer leads to dedoping, accompanied by a cation drift into the polymer. Accordingly, cations injected at the polymer-electrolyte interface shield the negative charges of the (bi)polaron stabilizing anions located on the PSS chains and draw electrons out of the metal electrode. Cations present in the electrolyte are therefore detrimental to the conductivity to a certain degree by (reversibly) dedoping the polymer.[109,111]
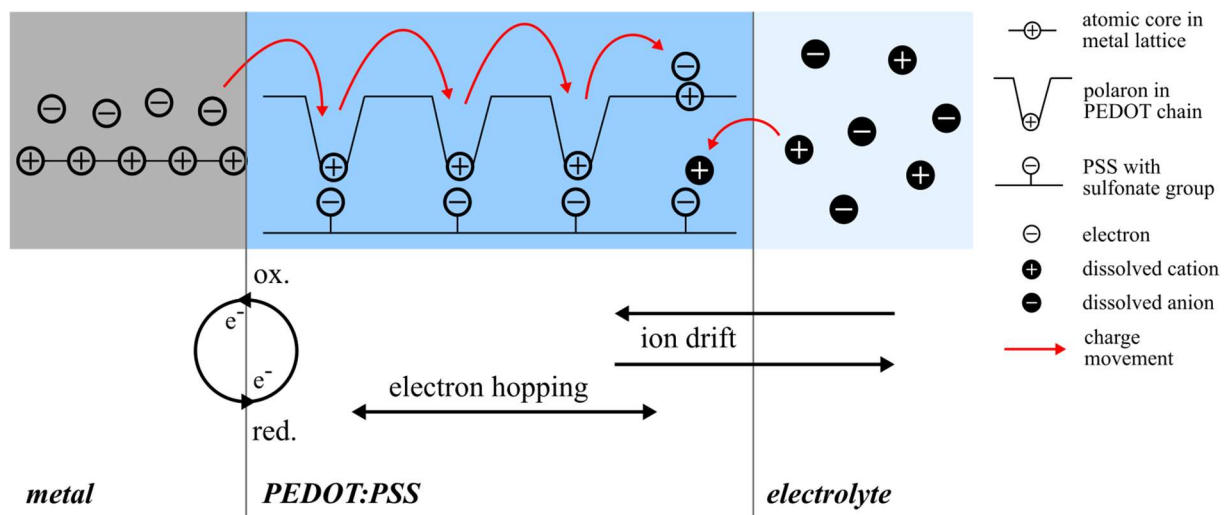
Fig. II-15: Schematic diagram of the charge transport in a PEDOT:PSS film that is in contact with a metal on one side and with the electrolyte on the other side. Charge movement is indicated by red arrows. A small sinusoidal voltage is applied and the respective reversible processes are sketched in the lower half of the diagram. For the sake of clarity, the upper half shows schematically only one direction of charge transport. Electrons are injected from the metal into the polymer and proceed by hopping along the (bi)polarons and among the PEDOT chains. In order to maintain electroneutrality cations from the electrolyte drift into the polymer film. The excess electrolyte also present in the polymer is not shown.[107-110,112]

3   Regression Analysis

3.1   General Approach

In order to analyze the impedance data acquired during an impedimetric measurement, the parameters of the equivalent circuit have to be fitted to the raw spectra. If the physicochemical analogies of the parameters are known, conclusions about the processes in the measurement chamber can be drawn. With respect to this work this means that changes in the cell parameters C_m, α, and R_b can be quantified and interpreted with respect to membrane properties, cell-substrate, and cell-cell contacts.

The method usually used to find the best fit parameters is the complex nonlinear least-squares (CNLS) method, first published in 1977 by Macdonald and Garber.[113] In this method the sum of squared errors (SSE) is calculated for the real (') and the imaginary part (") and multiplied by a weighting factor according to Eq. 25. The SSE is then minimized by varying the parameters of the transfer function until the minimum SSE is found.[70-71]

$$SSE \; = \; \sum_{i=1}^{N} \{\, w_i'[Y_i' - f(x_i)']^2 + w_i''[Y_i'' - f(x_i)'']^2 \,\} \qquad\qquad \text{Eq. 25}$$

with: x_i frequency

N number of frequencies

w_i weighting factor

$f(x_i)$ value of the transfer function at x_i

Y_i data point at x_i

Since this work only considers the magnitude of the impedance $|Z|$ for fitting, there is no necessity for imaginary components and the equation simplifies to Eq. 26. The differences between the calculated and the experimental values are called residuals (Fig. II-16). They correspond to the unweighted difference $Y_i - f(x_i)$ in Eq. 26. The relative residuals $[Y_i - f(x_i)]/f(x_i)$ should ideally be randomly distributed around the zero line. If that is not the case, the fit does not represent the impedance of the DUT equally well at all frequencies of the spectrum, which may indicate a systematic mismatch between DUT and model.[70]

$$SSE = \sum_{i=1}^{N} w_i [Y_i - f(x_i)]^2 \qquad\qquad \text{Eq. 26}$$

A

B
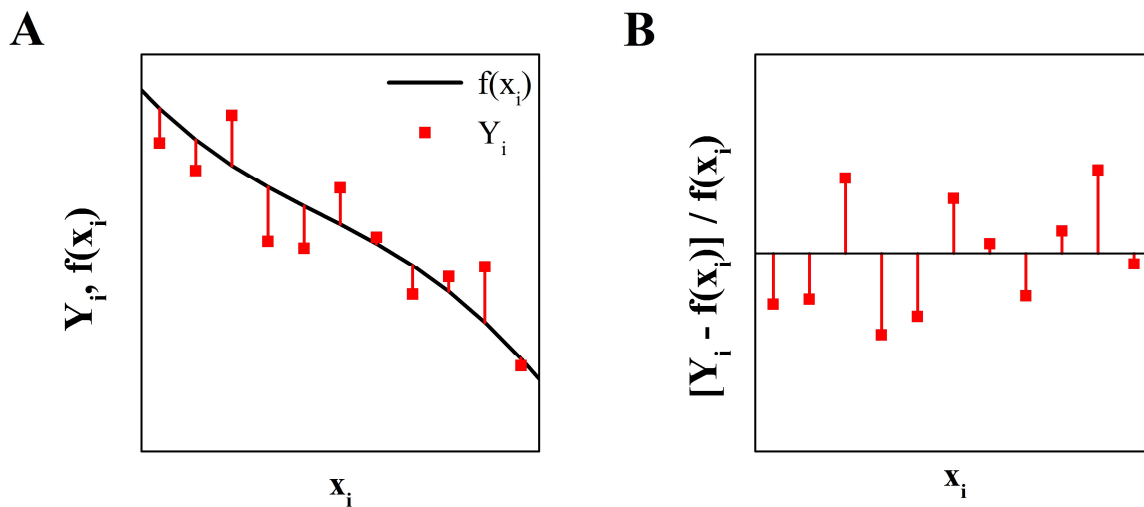
Fig. II-16: (A) Schematic example of a transfer function $f(x_i)$ and the corresponding raw data points Y_i. The differences between Y_i and $f(x_i)$ are termed residuals and are indicated as red lines between the data points and the transfer function. **(B)** Relative residuals $[Y_i-f(x_i)]/f(x_i)$ plotted against the frequency x_i. The relative residuals should ideally be randomly distributed around the zero line.

In the minimization algorithm n - 1 parameters define a hyperplane[c] in an n-dimensional space where the nth dimension is the SSE of the fit. In this n-dimensional space the minimum SSE has to be found by iteratively varying the parameters. The standard method for solving nonlinear least-squares problems is the *Levenberg-Marquardt method*. In short, the algorithm calculates the gradient from the partial derivatives in the hyperplane and moves downhill until the minimum is reached. Its disadvantage is independent of derivatives, more robust that it requires starting model parameters that are relatively close to those at the minimum. One method that is more robust, however relatively slow is the *downhill simplex method*. In each iteration step it reflects its highest point through the hyperplane given by the other points. The function therefore moves downwards and contracts around the minimum. One general problem of these methods is that the algorithm might end up at a local instead of the absolute minimum.[70,114] A more detailed description of these algorithms requires an in-depth mathematical engagement and is not within the scope of this thesis. An algorithm developed by J. Wegener successively confines the boundaries around the best fit in each iteration step until a final value is found with

[c] A hyperplane is a plane with n - 1 dimensions in an n-dimensional space. It is therefore the generalized analogy of a 2D plane in a 3D space. In nonlinear least-squares fitting n - 1 is the number of parameters and the nth dimension is the SSE of the fit.

sufficient accuracy. This method was used in the present work and will be described in detail in chapters 3.2 and 3.3.

In impedance spectroscopy the impedance values in a frequency spectrum usually vary over several orders of magnitude. This requires the introduction of an appropriate weighting factor w_i to avoid over-accentuation of the higher values (cf. Eq. 25). The most straightforward definition for w_i is related to the standard deviation σ of the mean of each measurement point and is termed *statistical weighting*. However, for practical reasons the relative errors are often considered to be constant. This method is called *proportional weighting*. It sometimes involves an additional proportionality constant p that has no influence on the outcome of the fit. The different approaches are summarized in Tab. II-6.[70-71] It should be mentioned that the definitions for the weighting methods were used in this work as described by Lasia et al.[70] and Barsoukov et al.[71] Different definitions for the same method names can, however, be found and are used for example by the data analysis software Origin (OriginLab Corporation, MA, USA).[115] Generally, empirical weighting factors like $1/x^{1/2}$, $1/x$, $1/x^2$, $1/y^{1/2}$, $1/y$, and $1/y^2$ are employed.[116]

Tab. II-6: Different weighting approaches, their respective definitions for the weighting factor w_i, and the SSE according to Eq. 26. The proportionality constant p has no influence on the outcome of the fit and is often equal to 1.[70-71]

weighting method	w_i	SSE
unity weighting	1	$\sum_{i=1}^{N} [Y_i - f(x_i)]^2$
statistical weighting	σ^{-2}	$\sum_{i=1}^{N} \dfrac{[Y_i - f(x_i)]^2}{(\sigma)^2}$
proportional weighting	$(p \cdot Y_i)^{-2}$	$\sum_{i=1}^{N} \dfrac{[Y_i - f(x_i)]^2}{(p \cdot Y_i)^2}$

3.2   Determination of the Boundary Conditions

Before iteratively fitting the cell parameters, the boundary conditions have to be fixed, i.e. the electrode parameters must be determined. As mentioned before, a CPE in series with a bulk resistance R_{bulk} serves as an equivalent circuit for the cell-free electrode (cf. II.1.4). The magnitude of the impedance $|Z|(\omega)$ of a CPE is expressed by Eq. 27 (cf. 1.1). In its logarithmic form, the equation can be rearranged to give a linear equation with a slope of -n and an intercept

of -log(A) (Eq. 28). Therefore, a linear fit of the low frequency part of the spectrum, which is entirely dominated by the CPE, yields the CPE parameters A and n. By default, the first 10 (#1 - #10) of the 61 logarithmically distributed data points between 1 Hz and 1 MHz are used for a linear least squares fit of the CPE (Fig. II-17). This gives reliable results for cell lines with low to medium Z_{cell} values ($|Z_{cell}| < \sim 100$ kΩ) like NRK and MDCK-II cells. Cell lines with high Z_{cell} values like MDCK-I cells may influence the impedance signal in that low frequency region, so the fewer data points are available for the linear fit of the CPE.

$$|Z|_{CPE} = \sqrt{Re_{CPE}^2 + Im_{CPE}^2} = \sqrt{\left(\frac{\cos\left(n\cdot\frac{\pi}{2}\right)}{\omega^n\cdot A}\right)^2 + \left(\frac{\sin\left(n\cdot\frac{\pi}{2}\right)}{\omega^n\cdot A}\right)^2} = \frac{1}{\omega^n\cdot A} \qquad \text{Eq. 27}$$

$$\log(|Z|_{CPE}) = \log\left(\frac{1}{\omega^n\cdot A}\right) = -n\cdot\log(\omega) - \log(A) \qquad \text{Eq. 28}$$

R_{bulk} is approximated by $|Z|$ of the last data point (#61) at 1 MHz (Fig. II-17). If a parasitic capacitance C_{prs} or constant phase element CPE_{prs} is present, the parasitic impedance has to be subtracted from the complex impedance of the whole system first.
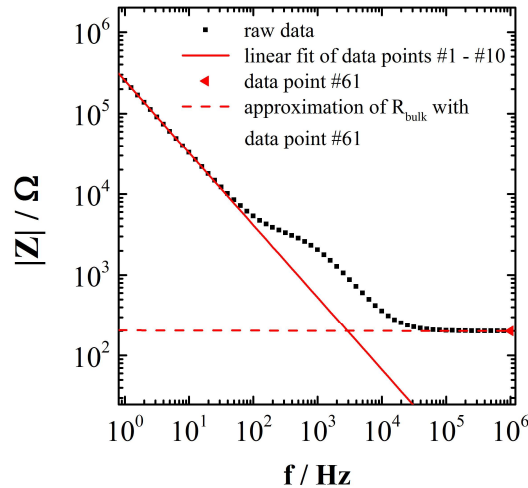
Fig. II-17: Determination of the parameters of the cell-free electrode. The CPE parameters are obtained by a linear fit of the first 10 data points (#1 - #10) in the low frequency region. R_{bulk} is approximated by $|Z|$ of the last data point (#61) at 1 MHz.

3.3 Fitting Method: The Hyperfunnel Algorithm

The fitting algorithm used in this thesis was adapted from J. Wegener. It is a relatively slow but robust method based on finding the minimum SSE by successively confining the boundaries around the best fit in each iteration step until a final value is found with sufficient accuracy. This results in a funnel shaped algorithm with a (n+1)-dimensional funnel for n parameters and will therefore be termed the *hyperfunnel algorithm* (Fig. II-18). The algorithm's sequence of operation is schematically shown in Fig. II-18 for one parameter x. Starting with a preassigned initial value x_0, the section between $0.33 \cdot x_0$ and $3 \cdot x_0$ is divided into a specified number of equidistant increments. It is a good compromise between accuracy and computing time to choose 5, 7, or 9 increments. Picking an odd number also includes the starting value x_0. For each increment the SSE between the respective transfer function and the raw data is determined and x_i with the minimum value SSE_{min} is used as starting value x_1 for the next iteration step. Here, the section to be considered is more confined and ranges from $0.5 \cdot x_1$ to $2 \cdot x_1$. Again, the data range is split into the same specified number of increments, of which the SSE are calculated and the respective SSE_{min} is used for further iteration. These steps are repeated with the ranges being narrowed down as depicted in Fig. II-18 and Tab. II-7. SSE_{min} of the section between $0.99 \cdot x_5$ and $1.01 \cdot x_5$ was considered to have sufficient accuracy (relative error equals 1%) to be taken as final fit result x_n.
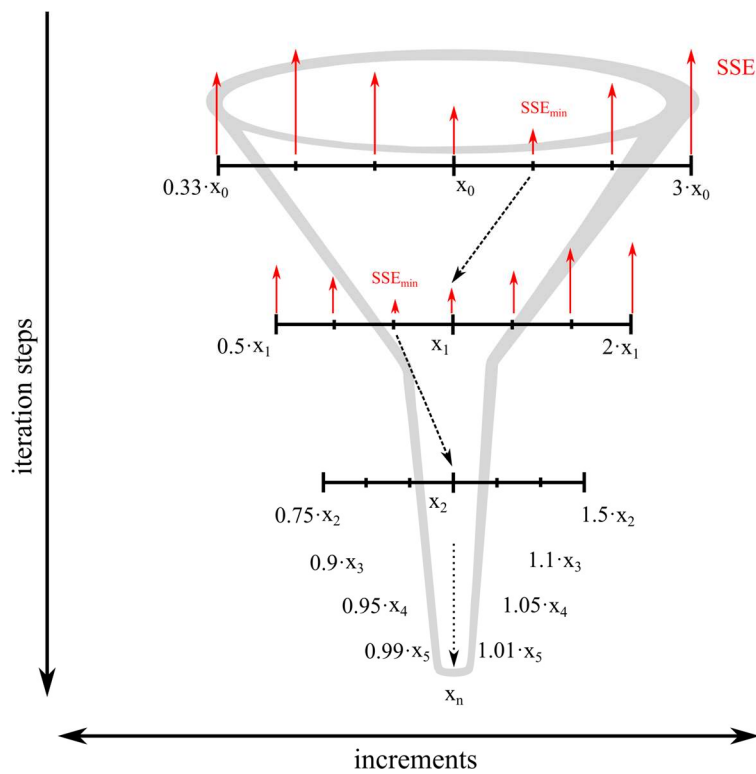
Fig. II-18: Fitting algorithm of the hyperfunnel algorithm for one parameter x. In each iteration step a defined range around a starting value x_i is divided into a specified number of increments and the SSE is calculated for each increment. The parameter with the minimum SSE (SSE_{min}) is used as starting value x_{i+1} for the next iteration step. The range is narrowed down in every step until a sufficiently accurate final value x_n is obtained.

Tab. II-7: Lower and upper limits used for each iteration step of the fitting algorithm. x_0 is a preset starting value and x_i ($i \in [0, 1, 2, 3, 4, 5]$) are the best fits of the respective previous iteration step i-1, used as starting value for iteration step i.

iteration step i	lower limit[d]	upper limit
0	$0.33 \cdot x_0$	$3 \cdot x_0$
1	$0.5 \cdot x_1$	$2 \cdot x_1$
2	$0.75 \cdot x_2$	$1.5 \cdot x_2$
3	$0.9 \cdot x_3$	$1.1 \cdot x_3$
4	$0.95 \cdot x_4$	$1.05 \cdot x_4$
5	$0.99 \cdot x_5$	$1.01 \cdot x_5$

---

[d] These empirical factors are based on statistical tables like for the χ^2 or the Student distribution.[117,118]

Since the transfer function of the ECIS model depends on the three parameters C_m, α, and R_b, SSE_{min} has to be found in a three-dimensional vector space where each axis corresponds to one of the parameters (Fig. II-19). In this hyperfunnel the ranges for every parameter are defined and confined during the iteration procedure as described for a single-parameter transfer function.
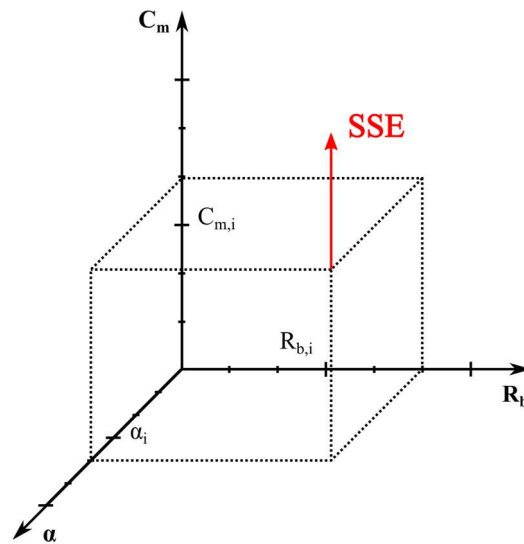
Fig. II-19: Graphical representation of the three-dimensional vector space in which SSE_{min} has to be found in each iteration step. An externally specified range around the starting values $C_{m,i}$, α_i, and $R_{b,i}$ is divided into a given number of increments and the SSE is calculated for every associated combination of C_m, α, and R_b. The SSE vectors of the 3D parameter space span the fourth dimension, schematically indicated by a different color (red) in the figure.

III EXPERIMENTAL AND THEORETICAL STUDIES

1 Materials and Methods

1.1 Cell Culture Techniques

1.1.1 Cell Culture Conditions

Cell culture work was performed under sterile conditions in a laminar flow hood (HERAsafe KS/KSP class II biological safety cabinet, Thermo Fisher Scientific, Waltham, MA, USA). Cell culture media were obtained in sterile form from Sigma-Aldrich (Taufkirchen, Germany) and supplemented with additives as listed in Tab. III-1. Sterile buffer solutions (Sigma-Aldrich) used in this work are shown in Tab. III-2. Other non-sterile solutions used for cell culture were passed through a sterile filter with a pore size of 0.2 µm. Cytochalasin D was acquired from Cayman Chemical (Ann Arbor, MI, USA). Saponin, trypsin, and fibronectin were purchased from Sigma-Aldrich. Pipette tips, glass pipettes, and reaction tubes were autoclaved at 120 °C for 20 min (DX-45, Systec, Wettenberg, Germany) prior to use. Cells were routinely grown in polystyrene culture flasks with a growth area of 25 cm² in 4 mL culture medium and kept in a cell culture incubator (Thermo Fisher Scientific) at 37 °C, 95% relative humidity, and 5 % CO_2.

Tab. III-1: Medium compositions for different cell lines used throughout this thesis. Minimum Essential Medium Eagle (MEM) and Dulbecco's Modified Eagle's Medium (DMEM) were obtained from Sigma-Aldrich and supplemented with fetal calf serum (FCS), penicillin, streptomycin, and L-glutamine.

	MDCK-I / MDCK-II	NRK
base medium	MEM	DMEM
$NaHCO_3$	2.2 g/L	3.7 g/L
D-Glucose	1 g/L	4.5 g/L
+ FCS	5% (v/v)	5% (v/v)
+ penicillin	100 µg/mL	100 µg/mL
+ streptomycin	100 µg/mL	100 µg/mL
+ L-Glutamine	4 mM	2 mM

Tab. III-2: Different compositions of Phosphate Buffered Saline (PBS) and Earle's Balanced Salt Solution (EBSS). All buffers were provided by Sigma-Aldrich.

	PBS^-	PBS^{++}	$EBSS^{++}$
NaCl	140 mM	140 mM	117.2 mM
KCl	2.7 mM	2.7 mM	5.3 mM
Na_2HPO_4	8.1 mM	8.1 mM	-
NaH_2PO_4	-	-	1.0 mM
KH_2PO_4	1.5 mM	1.5 mM	-
Ca^{2+}	-	0.9 mM	1.8 mM
Mg^{2+}	-	0.5 mM	0.8 mM
$NaHCO_3$	-	-	26.2 mM
D-Glucose	-	-	5.6 mM

1.1.2   Cell Lines

Strains of the two immortalized cell lines MDCK (Madin-Darby canine kidney) and NRK (normal rat kidney) were used throughout this thesis as model systems for epithelial cells with different dielectric structure.

The MDCK cell line is derived from the kidney of a cocker spaniel.[119] Two variants of clones with different morphologies and properties have been described. One high resistance strain

(MDCK-I) forms tight epithelial cell layers with strong tight junctions and with reported high transepithelial electrical resistance (TEER) values between 400 and 5000 $\Omega \cdot cm^2$. By contrast, the low resistance clone (MDCK-II) shows characteristics of a leaky epithelium with moderate TEER values from 40 to 150 $\Omega \cdot cm^2$.[120] MDCK-I and MDCK-II cells also exhibit microvilli on the apical side when grown as a confluent monolayer, and hence have an increased membrane surface.[121-122] The microvilli are more numerously expressed on MDCK-II cells.

The NRK cell line is derived from rat kidney and shows an even leakier diffusion barrier than MDCK-II monolayers. Consequently, relatively low TEER values of around 12 $\Omega \cdot cm^2$ have been reported in literature.[123-124]

1.1.3   Subcultivation

After 7 days in culture and upon reaching confluence cells were removed from the growth surface and seeded in new culture flasks following the protocol shown in Tab. III-3. All media and buffer solutions were pre-warmed to 37 °C before use. Incubation steps were also performed at 37 °C in an incubator. Every 3-4 days the supernatant was replaced by fresh culture medium to provide the cells with fresh nutrients and ensure constant culture conditions.

Tab. III-3: Subculturing protocol for the cell lines MDCK-I, MDCK-II, and NRK.

		MDCK-I	MDCK-II	NRK
1.	washing 2× with PBS^{--} to remove dead cells and medium residue			
2.	incubation with PBS^{--}	3× 5 min	-	-
3.	incubation with 1 mM EDTA in PBS^{--} to remove Ca^{2+} and Mg^{2+} cations	2× 10 min	10 min	10 min
4.	incubation with trypsin in PBS^{--}, supplemented with 1 mM EDTA to detach cells from surface	10 - 15 min 0.25% (w/v)	8 - 10 min 0.05% (w/v)	8 - 10 min 0.05% (w/v)
5.	tapping of the culture flask on solid surface to facilitate cell detachment			
6.	dilution with 10 mL cell culture medium to stop trypsin activity			
7.	centrifugation of cells and removal of supernatant	110 g for 10 min at RT	110 g for 10 min at RT	110 g for 10 min at RT
8.	resuspension in cell culture medium			
9.	cell seeding in a new culture flask with a dilution ratio of 1:20 with respect to the growth surface area			

1.1.4   Cryopreservation and Recultivation

In order to store cells for a longer period of time they were deep-frozen in a cryogenic tank. The cells were detached and collected starting with an almost confluently grown cell layer on a culture flask following the subculturing protocol steps 1-7 (Tab. III-3). After centrifugation, the cells were resuspended in freezing medium composed of 90% (v/v) FCS and 10% (v/v) of the cryoprotective agent DMSO, which prevents the formation of harmful ice crystals during freezing. The cell suspension was then filled in cryovials and slowly cooled down to -80 °C with a constant cooling rate of -1 °C/min using an isopropanol bath. After 24 h they were stored in liquid nitrogen at -196 °C.

For recultivation the the cryovial with the cell suspension was first put in a freezer at -20 °C for about 1 h and then the cells were quickly thawed in a water bath at 37 °C. Pre-warmed cell culture medium was added dropwise before centrifugation of the cell suspension at 110 g and aspiration of the DMSO containing solution. Subsequently, the cell pellet was resuspended in cell culture medium and seeded subconfluently in cell culture flasks. The cells were only used for experiments after performing at least one subcultivation cycle as described in chapter 1.1.3.

1.1.5   Live/Dead Staining

Living and dead cells were simultaneously stained using a Live/Dead Cell Viability Assay (Molecular Probes, Thermo Fisher Scientific) which includes the two dyes calcein acetoxymethylester (CaAM) and ethidium homodimer-1 (EthD-1). CaAM is a non-fluorescent, membrane permeable compound, whose ester groups get cleaved by intracellular esterases of living cells. Thereby, the dye becomes membrane impermeable and fluorescent, and gets trapped inside the cell. Living cells thus show the green fluorescence of the dye calcein (ex./em. 494/517 nm) in their cytoplasm. EthD-1, in contrast, is a DNA-intercalating dye (ex./em. 528/617 nm), of which the fluorescence intensity is enhanced around 40 times when it binds to DNA. It can only enter cells with disrupted membranes, as they occur in dead or necrotic cells. Therefore, dead cells show red fluorescence in their nuclei.

The dyes were applied according to the standard protocol. The stock solutions of CaAM (4 mM in DMSO) and EthD-1 (2mM in DMSO/H_2O) were diluted to final concentrations of 2 µM (CaAM) and 4 µM (EthD-1) in PBS^{++}. The cell culture medium was aspirated and the cells were washed once with PBS^{++} before adding the staining solution. After incubation at 37 °C in the dark for 45 min, the cells were analyzed using an upright confocal laser scanning microscope (CLSM). The CLSM was a Nikon Eclipse 90i equipped with three lasers (ex. 408,

488, and 543 nm) and three detectors (450/35, 515/30, 650 LP). For all images a PLAN objective with 10× magnification and a numerical aperture of 0.25 was used.

1.2 Impedance Spectroscopy

1.2.1 Experimental Setup

For a usual ECIS experiment with a self-made setup two 8-well arrays (cf. 1.2.3) were placed in a humidified incubator at 37 °C and 5% CO_2. The arrays were connected to a relay via an array holder manufactured by Applied BioPhysics (Troy, NY, USA). That way, the working electrodes could be individually addressed and successively measured against a common counter electrode. Relay and impedance analyzer (SI 1260, Solartron Instruments, Farnborough, UK) were connected to a personal computer and controlled with a LabVIEW software written by J. Wegener (Fig. III-1). Unless stated otherwise, a weak sinusoidal AC voltage of 50 mV was used to record the magnitude and phase shift of the impedance at 61 distinct frequencies between 10^0 and 10^6 Hz, equally distributed on a logarithmic scale. For each data point the impedance was averaged over five periods at that frequency or at least 10 ms in order to minimize the noise.
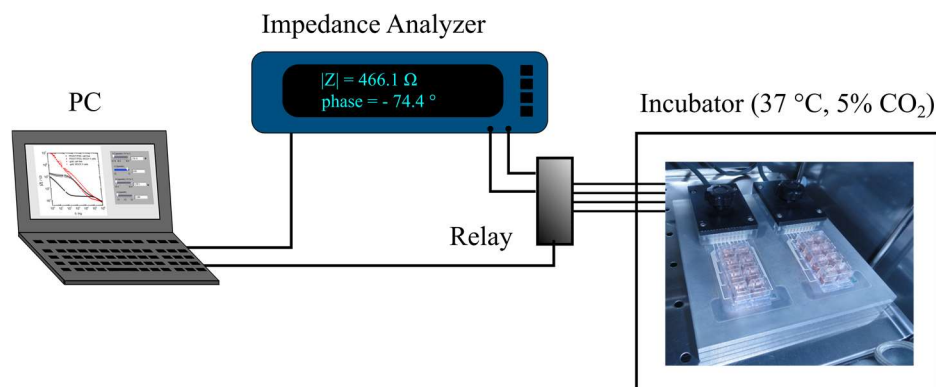
Fig. III-1: Self-made measurement setup used to perform ECIS recordings. Impedance analyzer and relay are controlled via LabVIEW software on a PC. The respective measurement chambers are located inside an incubator at 37 °C, 5% CO_2, and humidity saturated atmosphere.

For some experiments the commercial systems ECIS 1600R or ECIS Zθ (Applied BioPhysics) were used. Part of the electronics of the ECIS Zθ model are placed inside the incubator to minimize the parasitic capacitance that is caused by the leads between the impedance analyzer and the electrode contacts. In the case of the ECIS 1600R model the electronics are located

outside the incubator like in the self-made setup to avoid problems with the high humidity content of the surrounding atmosphere.

1.2.2   Basic Experimental Procedure

Unless stated otherwise the ECIS experiments were carried out with confluent cell monolayers that were seeded into the wells of the electrode arrays two days in advance at a seeding density of 450000 cells/cm². The cells in each well were provided with fresh cell culture medium one day before the experiment. On the day of the experiment, the cell culture medium was replaced by half of the volume using buffer or medium (200 µL), depending on the experimental conditions. The impedance was recorded for 1-2 h until a stable baseline was reached. The buffer or medium was complemented to the final volume with an analyte solution (200 µL) that contained twice the final concentration of the respective analyte. The solutions were mixed by aspirating and pipetting the solutions back into the wells. The measurement chambers were covered with a polystyrene lid at all times to reduce solvent evaporation and risk of contamination. All impedimetric experiments were carried out in an incubator at 37 °C with 5% CO_2 when cell culture medium or $EBSS^{++}$ were used as electrolyte. For PBS^{++} buffer the CO_2 level was set to 0%.

1.2.3   Electrode Layouts

This chapter describes only commercial electrode layouts. The individually designed and fabricated electrodes and electrode arrays used in this work will be addressed in the Materials and Methods sections of the respective chapters (cf. 2.2.2 and 3.3.2). Two different electrode layouts from Applied BioPhysics (Troy, NY, USA) were employed, 8W1E and 8W10E (Fig. III-2). Both contained wells with a small gold working electrode (WE) in each well that were successively measured against one common large gold counter electrode (CE). A 3.6 µm thick photoresist layer on top of the gold electrodes defined the electrode dimensions. The substrate was either a 0.51 mm thick polycarbonate or a 0.25 mm thick polyethylene terephthalate (PET) sheet. The polystyrene 8-well chambers glued on top of the substrates defined 8 compartments or wells with a growth area of 0.8 cm² and a volume of 150 – 400 µL. The WE of the 8W1E arrays are single electrodes with a diameter of 250 µm and an electrode area $A_{el} = 5 \cdot 10^{-4}$ cm². The CE is about 500-fold larger (~ 0.25 cm²). The 8W10E arrays have a similar layout, but contain 10 equally sized parallel WEs, each 250 µm in diameter. This results in an overall WE area of $A_{el} = 5 \cdot 10^{-3}$ cm² in each well.

Fig. III-2: Layouts of 8W1E (left) and 8W10E (right) electrode arrays. The photographs were taken from http://www.biophysics.com/cultureware.php.

Commonly, the 8W1E electrode arrays are used for micromotion measurements (cf. 1.4). Due to the smaller electrode area, the measurement signal is averaged over a smaller number of cells and the difference between cell-covered and cell-free electrode is more pronounced. If a smoother signal is required like in adhesion or proliferation assays, the 8W10E electrode arrays are preferred, where more cells contribute to the measurement signal. That way, the impedace signal is averaged over more cells and the signal appears less noisy.

1.2.4   Equivalent Circuits

Three different equivalent circuits were employed within the main chapters *2 PEDOT:PSS as Electrode Material*, *3 Bipolar Electrodes*, and *4 Derivative Impedance Spectroscopy (DIS)*.

The simplest setup comprises the interface impedance Z_{CPE}, represented by a CPE, the impedance of the cell layer Z_{cell}, and the bulk resistance of the electrolyte R_{bulk} (cf. II.1.4) in series (Fig. III-3 A). This equivalent circuit was used for the simulation of the impedance spectra in chapter *4 Derivative Impedance Spectroscopy (DIS)*. It is valid, for example, for ideally polarizable gold electrodes with low R_{bulk} like the 8W10E electrode arrays and was employed accordingly to model the data recorded with the commercial ECIS electrodes.

For the polymer electrodes used in chapter *2 PEDOT:PSS as Electrode Material* the equivalent circuit had to be slightly altered. The interface impedance of PEDOT:PSS electrodes has been a matter of debate for some time and numerous models have been proposed.[65,107-108,110,125] They usually contain a Warburg impedance Z_W and other diffusion related elements to account for the ion diffusion between the electrolyte and the polymer hydrogel, as well as inside the polymer. Additionally, resistive elements like the charge transfer resistance R_{ct} have been suggested to describe the redox processes on the polymer chains. This combination of ion diffusion in the bulk electrolyte, restricted ion diffusion inside the polymer[108], and the concurrent presence of charge transfer processes is highly complex and not in all detail relevant

for this work. Therefore, the interface impedance was instead described by two parallel CPEs (Fig. III-3 B). One of them (Z_{CPE-C}) was defined to have a capacitive character with n_{cpe-c} close to 1, while the other one (Z_{CPE-R}) had a more resistive nature with n_{cpe-r} near 0 (cf.II.1.3). Both circuit elements in parallel proved to be suitable to represent all capacitive and resistive components of the electrode-electrolyte interface empirically in the relevant frequency range between 1 Hz and 1 MHz.

The bipolar electrodes category 2 (cf. 3.3.2) used in chapter *3 Bipolar Electrodes* were modeled using the equivalent circuit depicted in Fig. III-3 C. It represents the ideal ECIS equivalent circuit (Fig. III-3 A), complemented with an additional parallel resistance $R_\parallel$. $R_\parallel$ corresponds to the DC resistance of the bipolar electrode in between the contact pads as will be discussed later in the corresponding chapter.
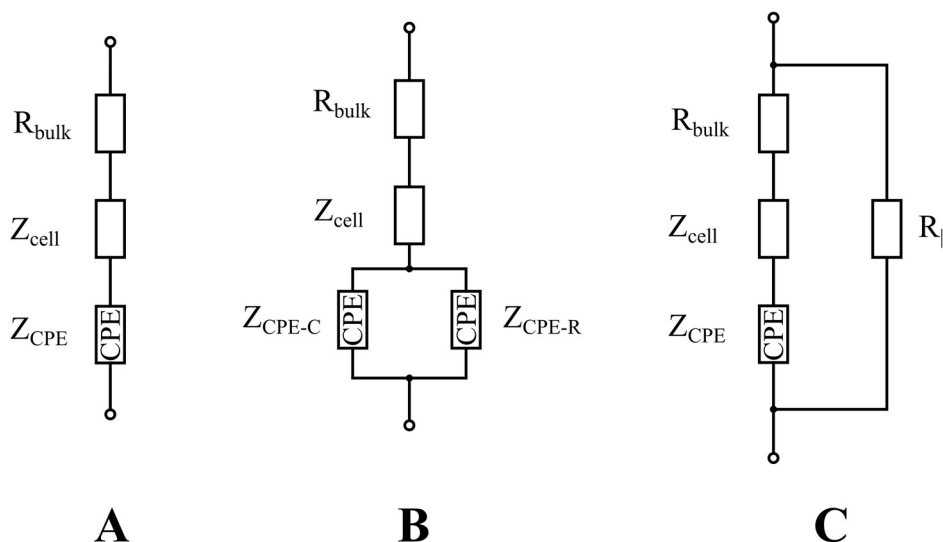
Fig. III-3: Equivalent circuits relevant for this work. **(A)** Ideal ECIS equivalent circuit, valid e.g. for 8W10E electrodes. **(B)** Equivalent circuit model applied for PEDOT:PSS electrodes (PDT). **(C)** Equivalent circuit used for the bipolar electrodes category 2.

If present, the parasitic impedance Z_{prs} was represented by a CPE in parallel to the respective equivalent circuit. The parasitic impedance was largely capacitive and n_{prs} ranged therefore between 0.9 and 1. It was included as a correction factor in the equivalent circuit and experimentally quantified from individual experiments (cf. 2.3.1.3).

1.2.5   Data Presentation

1.2.5.1   Impedance Spectra and Time Course

The impedance was usually recorded at frequencies equally spaced on a logarithmic scale and plotted against the frequency in a double logarithmic presentation. $|Z|$, R, and C were followed over time at each of these frequencies. $|Z|$ and R at 4 kHz or lower frequencies are commonly used for the analysis of morphological changes of the cell layer, while C at 32 kHz or 40 kHz is applied as a measure for the cell coverage of the electrode. The frequency spectra of $|Z|$ of a cell-free ($|Z|_{\text{w/o cells}}$) and a cell-covered electrode ($|Z|_{\text{w/ cells}}$) are exemplarily plotted in Fig. III-4 A. Dividing $|Z|_{\text{w/ cells}}$ by $|Z|_{\text{w/o cells}}$ yields the normalized presentation, where the maximum indicates the most sensitive frequency in the spectrum (Fig. III-4 B). This presentation will be used as indication for the sensitivity of an electrode throughout this work. The change of $|Z|$ at the sensitive frequency is commonly followed over time and used for further analysis (Fig. III-4 C). Depending on the application, any other frequency of the spectrum can be selected as well. For better comparability between the individual wells or experiments, $|Z|$ was normalized to the last data point before cell seeding, the addition of a compound, or electroporation, and plotted as $|Z|$ norm. versus time (Fig. III-4 D).

A

B

C

D
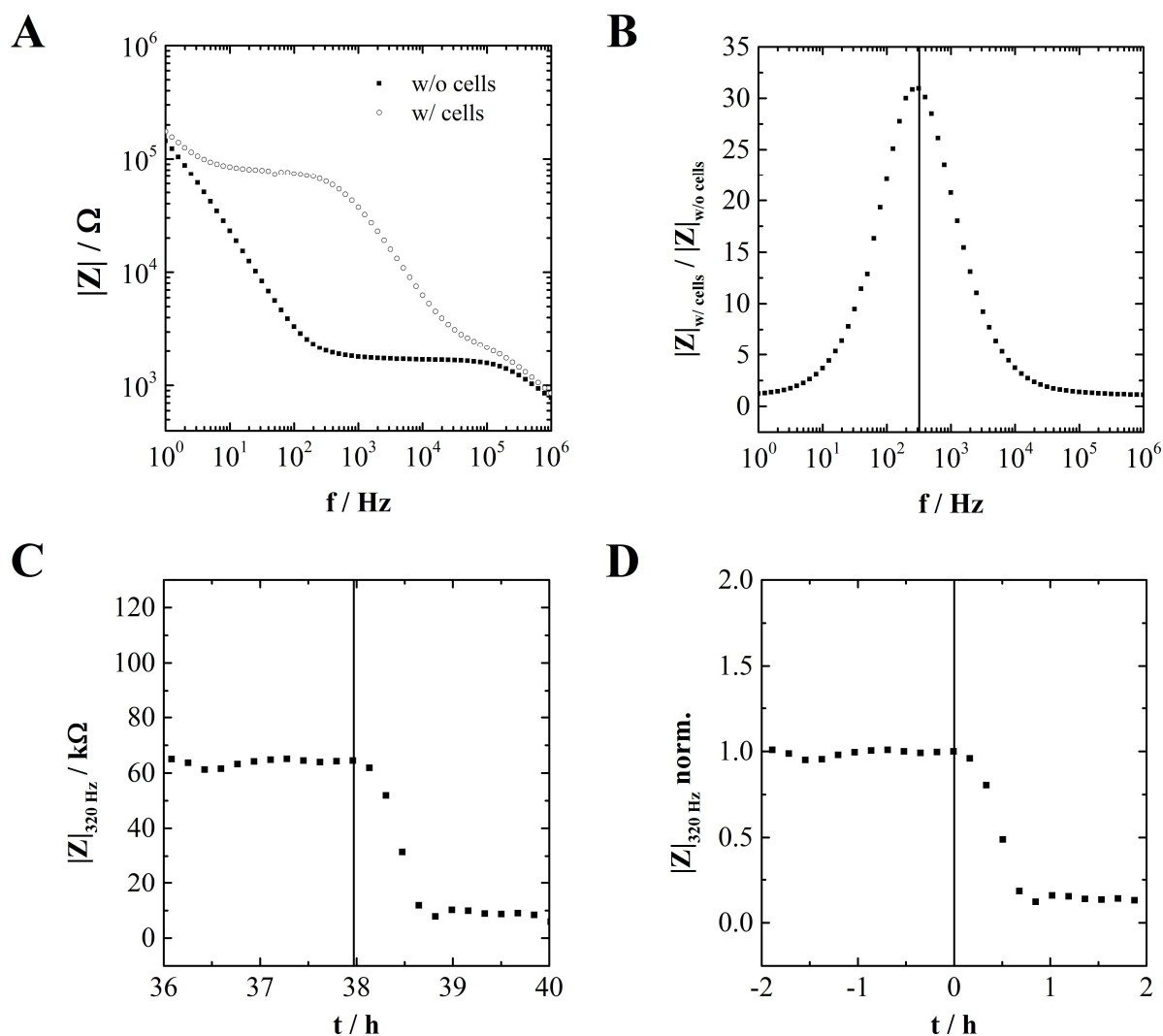
Fig. III-4: (A) Impedance spectra of a cell-free and a cell-covered electrode. **(B)** Dividing $|Z|_{w/\ cells}$ by $|Z|_{w/o}$ cells yields the normalized presentation. The maximum, marked by the vertical line at 320 Hz, indicates the most sensitive frequency in the spectrum. **(C)** Time course of $|Z|$ at a frequency of 320 Hz. The addition of a compound is marked by a vertical line. **(D)** Time course of $|Z|$, normalized to the last time point before addition of a compound.

Unless stated otherwise, the decimal logarithm was used for all logarithmic presentations throughout this work. The customary representation of the decimal logarithm of X, $\log_{10} X$, was simply expressed as log X.

1.2.5.2   Errors

The errors were expressed by the standard deviation (SD) or the standard error of the mean (SEM). The SEM is defined as the SD (Eq. 29) divided by the square root of the number of measurements (Eq. 30).

$$SD = \sqrt{\frac{1}{N-1} \sum_{i=1}^{N} (x_i - \mu)^2} \qquad \text{Eq. 29}$$

$$SEM = \frac{SD}{\sqrt{N}} \qquad \text{Eq. 30}$$

Here, N is the number of measurements, x_i defines the inividual data points, and μ is the mean of the sample. The SEM can be seen as describing the deviations of a sample from the true mean. It approaches zero for an infinite number of measurements. This accounts for the theorem that the probability of the measured mean approaching its expected value increases with the number of repetitions (*law of large numbers*).[117] The SEM was employed for cell analysis, where the well-to-well variations of an experiment are likely to originate from random errors like experimental variations or the inhomogeneity of the biological material. On the other hand, the SD is the degree to which individual results within a sample differ from the sample mean.[126] It contains information on the sample distribution. Therefore, the SD was used for the characterization of the electrodes to retain the information to which degree the individual electrodes or electrode arrays differ from one another in terms of e.g. electrode size or passivation thickness. These dimensions depend on the quality and repeatability of the fabrication process, which should be considered in the evaluation.

1.3 Electrical Cell Manipulation

The application of low voltages of only a few millivolts for the impedance analysis of living cell is the precondition for a non-invasive operation of the measurement technique. On the other hand, with the directed use of short pulsed higher voltages, the cells on the electrode can be manipulated in a controlled manner. Two commonly used techniques are *electroporation* and *wounding* (see below). In terms of the technical implementation, the methods differ mainly in the duration of the high voltage pulse. When electroporation or wounding are combined with ECIS, the impact of the cell manipulation can directly be followed over time. This makes ECIS a highly versatile measurement tool and increases the scope of possible applications.

1.3.1   Electroporation

Under normal conditions the cell membrane forms a selective, semi-permeable barrier and prevents the diffusion of large or hydrophilic molecules and ions across the lipid bilayer. Only small lipophilic molecules can diffuse freely across the cell membrane without the assistance of transport proteins. However, applications in many fields of cell biology and biomedical research require the introduction of such non-membrane-permeable molecules like peptides, antibodies, oligonucleotides, pharmaceuticals, or fluorescent probes into the cells. An efficient method to introduce a broad range of molecules and probes into the cell by experimental means is electroporation. The application of short, well-defined pulses of micro- to millisecond time duration and amplitudes of a few volts leads to the formation of transient pores in the membranes of adherent cells. Macromolecules can diffuse through these openings and become trapped inside the cell after resealing of the membrane.[127-128] Traditionally, electroporation has been conducted on suspended cells using high DC voltages.[129] That, however, requires the cells to be removed from the substrate beforehand, causing severe stress and delaying further investigation until after the cells are re-plated. Moreover, the applied voltage drops predominantly across the whole bulk electrolyte in the electroporation cuvette. Extremely high voltages ($\sim 10^2$ V – 10^3 V) are thus necessary to exceed the threshold of the electrical field at which the membrane disruption occurs.[130-131] In the ECIS setup, the impedance of the whole system is dominated by the working electrode. During electroporation, the electric field thus only extends over the thickness of the cell layer of a few micrometers and the required AC voltage amplitudes are drastically reduced (~ 4 V).[127]

1.3.2   Wounding

If, by contrast to electroporation, the duration of the high-field application is in the range of several seconds to tens of seconds, the resulting AC current is fatal for the cells. This allows the use of ECIS as wound healing assay.[132] Wound healing assays are used to quantify cell migration, which is important in several aspects of biology such as inflammation, tumor metastasis, and wound healing.[133] When a high voltage pulse of 60 s is applied to cells grown onto ECIS electrodes, this creates a wound that is restricted to the area of the electrode. The dead cells on the electrode surface are subsequently replaced by cells migrating from the periphery, repopulating the electrode and recovering a confluent cell layer. Wounding causes the impedance signal to drop to the level of the cell-free electrode immediately after pulse application. The signal slowly recovers over the course of several hours until the confluence of the monolayer is reestablished. This time span represents the migration rate of cells.

1.4 Micromotion

Adherent cell monolayers show cell shape fluctuations with amplitudes in the nanometer range. These dynamic changes in cell shape were first discovered by Giaever and Keese using the ECIS technique.[19] The cellular movements are referred to as micromotion and are caused by metabolically driven fluctuations of the plasma membrane, mediated by the cytoskeleton.[134] Micromotion has been linked for example to the cellular metabolic activity and the metastatic potential of cancer cells.[135-137] Several numerical methods have been used to quantify and interpret the associated changes in the measured impedance time series, including variance analysis, increment analysis, power spectral density (PSD) analysis, and detrended fluctuation analysis (DFA).[135-138] Each of these methods provides information on either the intensity or the nature of time correlations in the signal. Commonly, only the resistance R, the real part of the impedance, is used for the evaluation of the time series.[19,136,139] In this work, only the last 512 of a total of 612 data points were used for the analysis in order to exclude the strong drift at the onset of some of the measurements. PSD, DFA, and the detrended variance analysis (DVA), were employed for the noise evaluation and the results were compared. The methods were implemented as follows. The scaling exponents of the PSD and the DFA, k and D, serve to quantify the periodicity of a data set, or indicate to what degree the data points are correlated. By comparison, the variance of the detrended times series V_{32}, provided by the DVA, is a straightforward measure for the amplitude or the intensity of the fluctuations.[140]

1.4.1   Power Spectral Density (PSD) Analysis

The time series was subjected to a fast Fourier transformation (FFT) and the power spectral density (PSD) was calculated and plotted in a double logarithmic representation. A linear least squares fit was applied to the PSD spectrum excluding the 5 lowest frequencies to suspend long-range drifts. Periods longer than 150 s were suspended as long-range drifts tend to show strong peaks in the PSD spectrum at low frequencies. Taking them into account would over-accentuate the low-frequency range, which is represented by only very few data points. The elimination of the data points in the PSD spectrum caused by such long-range drifts is a more straightforward method than detrending the time series before the Fourier transformation as will be discussed in chapter 2.3.7.

The negative slope k of the linear fit was used for the characterization of the noise. There are special cases for noise with the PSD showing power-law behavior f^{-k} but individual scaling

exponents k that are summarized in Tab. III-4. Noise colors are a rough analogy to the corresponding frequency relationships of the visible light spectrum. Pink and red noise are more prominent in the low frequency region, while blue and violet noise have higher amplitudes at high frequencies. White noise is statistically uncorrelated and reflects frequency independent 'flat' noise (Fig. III-5 A and B). It may arise from thermal fluctuations, however only in a certain frequency range.[141] An ideal white noise over all frequencies does not occur in practice. Pink noise occurs in a variety of biological time patterns such as heartbeat, neuronal activity, and cellular micromotion (Fig. III-5 C and D).[136,138,142] Pink noise indicates correlations in time and shows fractal properties, i.e. repeating patterns with a certain degree of self-similarity. Red noise is generated by processes that show even stronger correlations than pink noise and can be described by the random walk model. The Brownian motion of a particle in a liquid, or cell migration are two examples linked to random walk (Fig. III-5 E and F).[29,143] Blue and violet noise are listed for the sake of completeness, but will not be relevant for this work.

Tab. III-4: 'Colors' of noise, possible occurrences, and the respective power law scaling exponent k.[144] The scaling exponent D of the detrended fluctuation analysis (DFA) can be correlated to k (cf. 1.4.2).

noise color	designation	occurrence	k	D
white		thermal noise[141]	0	0.5
pink	1/f, fractal or flicker noise	heartbeat, neuronal activity, micromotion[136,138,142]	1	1
red	Brown or Brownian noise	random walk (particle diffusion, cell migration)[29,143]	2	1.5
blue		Cherenkov radiation[145]	-1	
violet		acoustic thermal noise of water[146]	-2	
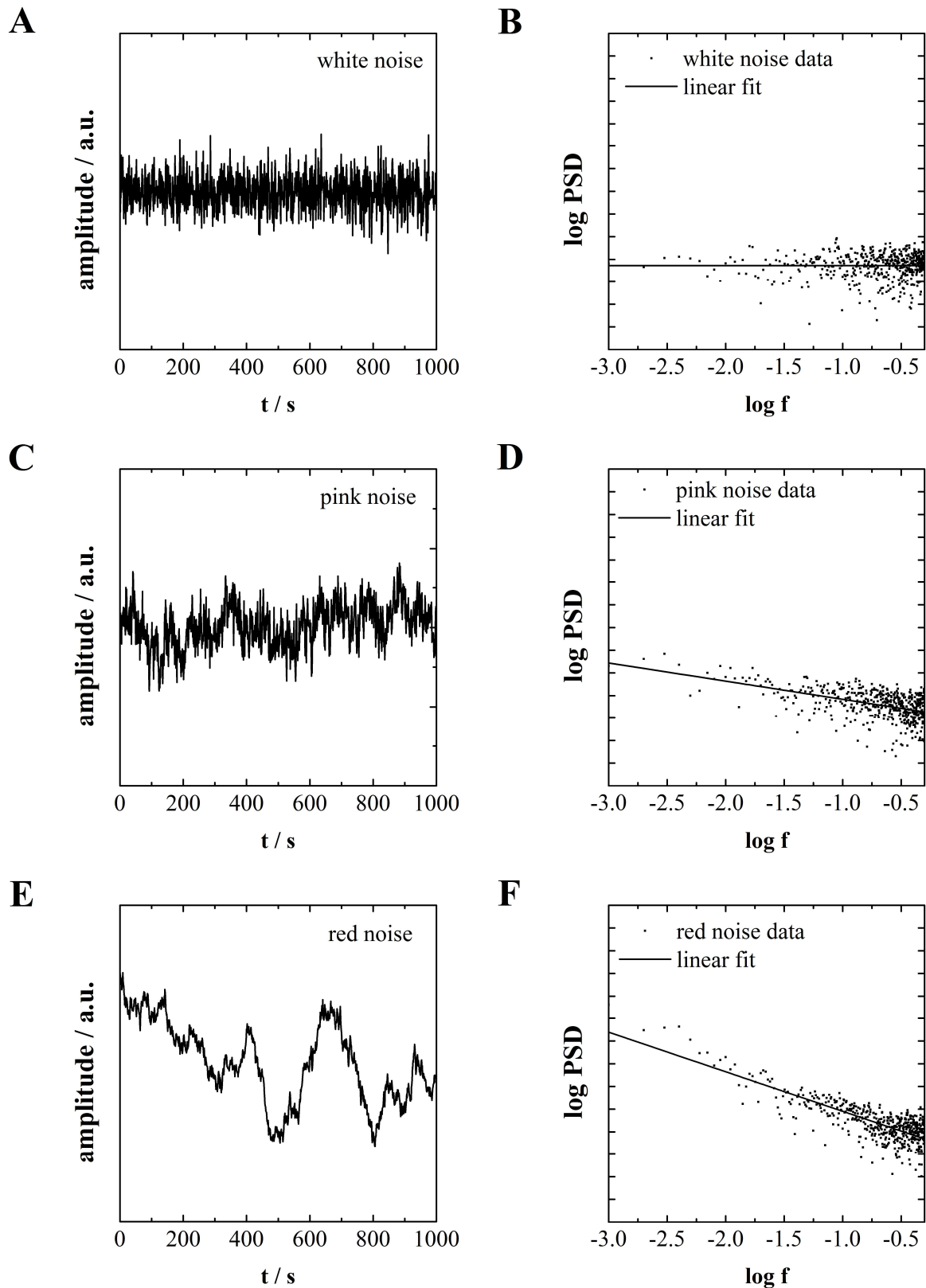
Fig. III-5: Simulated random time series with different noise color. **(A)**, **(C)**, and **(E)** show a white, pink, and red noise signal, respectively. Their power spectral densities (PSD) are plotted in **(B)**, **(D)**, and **(F)** together with a linear fit. The negative slope k is a measure for the type of signal noise (white noise: k = 0, pink noise: k = 1, red noise: k = 2). The data were simulated using a LabVIEW software.

1.4.2   Detrended Fluctuation Analysis

The detrended fluctuation analysis (DFA) was introduced in 1994 by Peng et al.[147] and adopted for the micromotion analysis in this work. The data analysis was performed according to the following steps:[148]

(1) Integration

Integration of the time series R(t) according to Eq. 31 gives the cumulative sum r(t) with r_i as the individual amplitude values of R(t) and $\bar{r}$ as the mean amplitude of the entire record (Fig. III-6 A and B).

$$r(t) = \sum_{i=1}^{t} (r_i - \bar{r})$$

Eq. 31

(2) Sectioning

The cumulative sum r(t) with record length N is divided into N/s non-overlapping segments with length s (Fig. III-6 B).

(3) Detrending

Subtraction of the local trend $p_v(t)$ in each segment v from r(t) results in the detrended cumulative sum $r_s(t)$ (Eq. 32). The local trends are calculated using a second order polynomial least squares fit (Fig. III-6 B and C).

$$r_s(t) = r(t) - p_v(t)$$

Eq. 32

(4) Calculation of the Segment Variances

For each segment v the variance $\sigma_s^2(v)$ of the detrended cumulative sum is calculated (Eq. 33). This is repeated for different segment lengths s that are powers of 2 between 2 and 8, thus covering values between 4 und 256.

$$\sigma_s^2(v) = \frac{1}{s} \sum_{t=1}^{s} r_s^2(t)$$

Eq. 33

(5) Calculation of the Fluctuation

The fluctuation F(s) of the detrended cumulative sum is determined by calculating the square root of the mean of all variances $\sigma_s^2(v)$ with same segment length s (Eq. 34).

$$F(s) = \sqrt{\frac{1}{N} \sum_{v=1}^{N} \sigma_s^2(v)} \qquad \qquad \text{Eq. 34}$$

(6) Determination of the Scaling Exponent D

F(s) is plotted in a log-log graph and the slope D is determined using a linear least squares fit (Fig. III-6 D). The local trends fit the cumulative sum time series less well if the segment size gets larger. Therefore, the variances and the fluctuations increase with the segment length. D is the scaling exponent utilized for the quantification of the noise signal and can be correlated to the PSD scaling exponent k (cf. Tab. III-4). A relationship according to k = 2·D - 1 has been found by Buldyrev et al.[149]

A

B

C

D
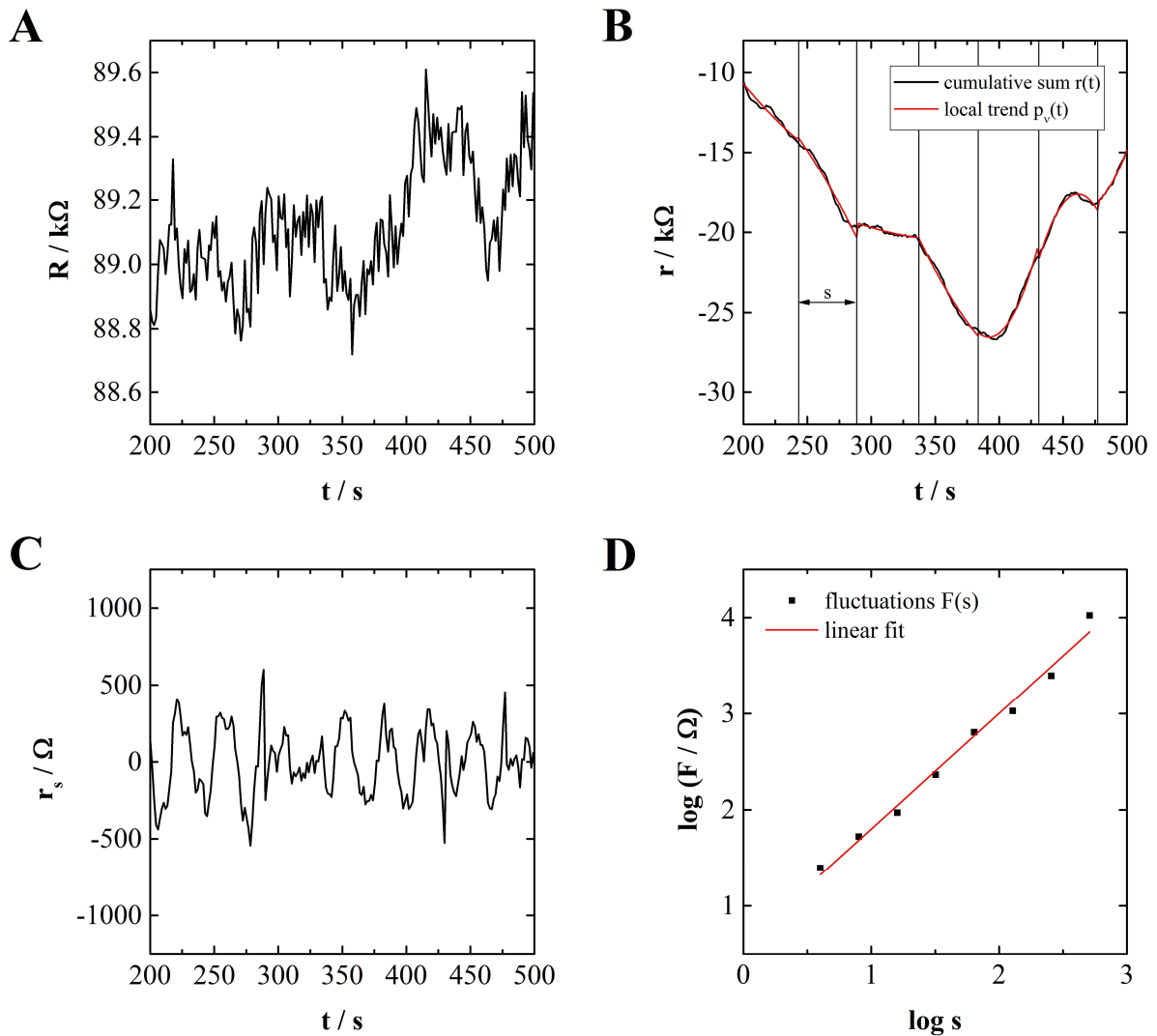
Fig. III-6: The different steps of the DFA, exemplarily shown for a fraction of an MDCK-II micromotion record. The time course is show between 200 and 500 s. **(A)** Resistance raw data R(t) of the time series. **(B)** Cumulative sum r(t), divided in segments of s = 32 data points. The local trends are determined using a second order polynomial fit. **(C)** Detrended cumulative sum $r_s(t)$. **(D)** Double logarithmic plot of the fluctuations F(s). The slope of the linear fit D is used as parameter for the quantification of the noise signal.

1.4.3   Detrended Variance Analysis (DVA)

The detrended variance analysis (DVA) is a relatively straightforward method to estimate the fluctuation intensity of a time series by means of its variance after detrending. For the data analysis the data were first differentially normalized by subtracting the mean of the whole series of the 512 data points from each value. Then, this normalized time series $\Delta R(t)$ was sectioned and detrended with a segment length of $s = 32$ as described in steps (2) and (3) in chapter 1.4.2 (Fig. III-7), using a second order polynomial. This resulted in the detrended time series $R_D(t)$ (Eq. 35). The variance V_{32} of the detrended time series $R_D(t)$ was employed as a measure for the micromotion intensity.

$$R_D(t) = \Delta R(t) - p_v(t) \hspace{4cm} \text{Eq. 35}$$
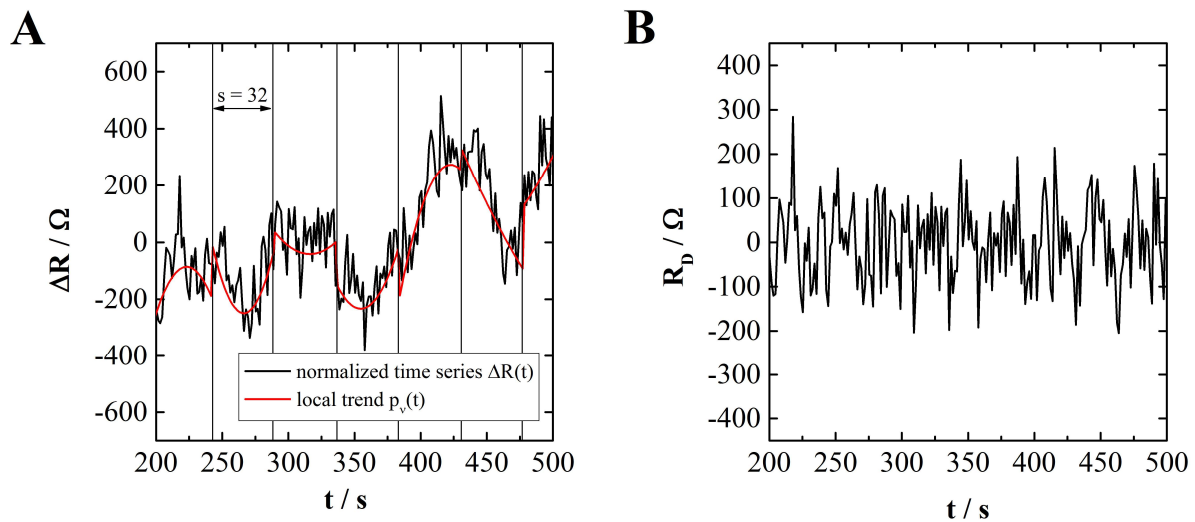
Fig. III-7: Numerical data processing during the DVA. (A) The differentially normalized time series $\Delta R(t)$ is divided in segments with a length of $s = 32$ data points. The local trend in each segment is subtracted from $\Delta R(t)$, which gives **(B)** the detrended time series $R_D(t)$. The variance of the whole detrended time series V_{32} is used for the quantification of micromotion.

1.5 LabVIEW Programs

Several LabVIEW programs were written for the simulation, fitting and evaluation of impedance data throughout this thesis. While some were just simple tools for data handling and analysis, others were less straightforward and will be described briefly in this chapter.

1.5.1   Simulation

The core of the program (cf.V.3.1) used for the simulation of impedance spectra consisted of an equivalent circuit that contained all elements occurring in this work, including the 'basic' ECIS model ($Z_{total} = Z_n + Z_{cell} + R_{bulk}$), a parallel resistance ($R_{\parallel}$) to model the bipolar electrodes, a parasitic CPE in parallel (Z_{prs}), and a term for the lead resistance (R_{lead}). The interface impedance Z_n was modeled by a capacitive CPE (Z_{CPE-C}) and an optional parallel resistive CPE (Z_{CPE-R}) for the description of the interface impedance of the PEDOT:PSS electrodes. The lead resistance can only be distinguished from R_{bulk} in the impedance spectrum if $R_{\parallel}$ is finite and known. The respective impedance values were set to infinity (if parallel) or zero (if in series) in case they were not needed for a certain application. The complete equivalent circuit is shown in Fig. III-8.
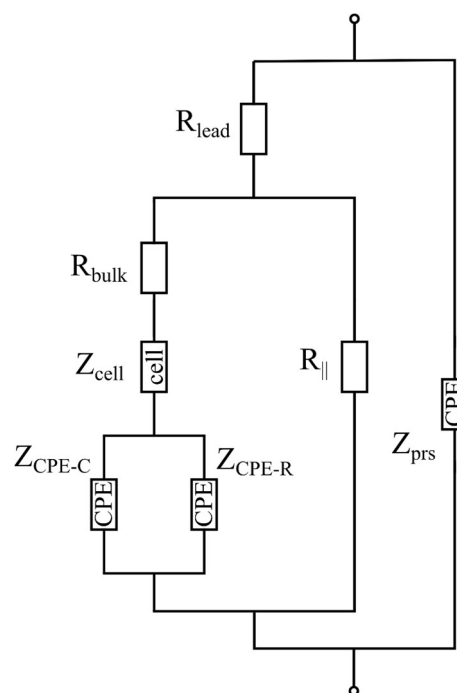
Fig. III-8: Equivalent circuit used in the LabVIEW simulation program.

Since the employed LabVIEW version (8.0) cannot handle modified Bessel functions with complex arguments that occur in the term for Z_{total} (cf. Eq. 19), a semi-empirical workaround was required. $I_\nu(z)$ is the *modified Bessel function* of order ν and is defined by Eq. 36.[150] It was found to be applicable in LabVIEW for small arguments z, where both the value of the imaginary and the real part of z were below 20. In case of the ECIS model, z was substituted by γr (Eq. 20). The sum term in Eq. 36 was calculated for values of k between 0 and 70. This provided high accuracy for the given argument range. When k was higher, the computing time for an impedance spectrum became excessively high. For absolute values of z higher than 20, an approximation from Abramowitz and Stegun[151] was used with i = 1..10 (Eq. 37). In certain high frequency cases, LabVIEW returned 'NaN' (not a number), so that an additional approximation for z→∞ was required (Eq. 38).[152]

$$I_v(z) = \left(\frac{z}{2}\right)^v \sum_{k=0}^{\infty} \frac{\left(\frac{z^2}{4}\right)^k}{k!\Gamma(v+k+1)}, \text{ where } \Gamma(a) \text{ is the gamma function} \qquad \text{Eq. 36}$$

$$I_v(z) \sim \frac{e^z}{\sqrt{2\pi z}} \cdot \left[1 + \sum_{i=1}^{10} \left(\frac{\prod_{k=1}^{i}\left[4v^2 - (2\cdot k - 1)^2\right]}{i!(8z)^i} \cdot (-1)^i\right)\right] \qquad \text{Eq. 37}$$

$$I_v(z) \sim \frac{e^z}{\sqrt{2\pi z}} \qquad \text{Eq. 38}$$

Each of the parameters in the equivalent circuit could be adjusted individually and the impedance spectra were simulated accordingly in a predetermined frequency range. The program returned the frequency spectra for cell-free and cell-covered electrodes of the impedance magnitude $|Z|$, the phase angle φ, the resistance R, the reactance X, and the capacitance C, as well as the normalized impedance $|Z|_{w/\text{ cells}} / |Z|_{w/o\text{ cells}}$. Furthermore, the program comprised the option to superimpose the impedance magnitude spectra with artificial noise (cf. 4.3.1.2).

1.5.2   Manual Fitting

If a least-squares fitting algorithm does not work on certain spectra because either the number of parameters is too high or the exact algorithm has not yet been established for that problem, manual fitting is still applicable. The impedance spectra measured with bipolar and PEDOT:PSS electrodes fell into that category and were thus fitted manually. For that purpose, the simulation program (cf.V.3.1) was complemented with an option to load raw impedance data into the interface. The parameters of the simulated data could be visually adjusted to match the raw data. The relative residuals are also displayed in a separate plot to facilitate the fitting procedure.

1.5.3   Regression Analysis

The regression analysis as performed in this thesis is described in detail in chapter *II.3 Regression Analysis*. It is implemented in a LabVIEW program accordingly. Furthermore, the impedance spectra could be differentiated for the derivative impedance spectroscopy (DIS) as elaborated in chapter 4.3.1.1. The program (cf. V.3.5.1 and V.3.5.2) allowed for batch

processing of multiple data files with varying fitting conditions. The fitting conditions comprised the number of iterations, the number of increments, the weighting method, the derivative order, the data type (logarithmic or linear), and the spectrum type ($|Z|_{w/\,cells}$ or $|Z|_{w/\,cells}$ / $|Z|_{w/o\,cells}$). For each file, the fit results were saved in a log file together with the respective conditions applied during the fit. This log file was used for further evaluation of the results (see next chapter).

1.5.4   Regression Analysis Evaluation

The log file mentioned in the previous chapter contained a list of all fit results and the corresponding fitting conditions. The conditions were varied in a combinatorial-like approach on 100 different simulated impedance files (cf. 4.3.1.3). This resulted in an overall number of 7200 fits, of which the results needed to be sorted according to their fitting conditions and the results with identical conditions were averaged. This was achieved with a LabVIEW evaluation program (cf. V.3.5.3) that worked according to the following routine. First, the log file was sorted and split into three files according to the number of increments (5, 7, and 9) to reduce the data load. These log files with 2400 fit results each were analyzed separately. In every split log file, a parameter that quantitatively compared the fit results of α, C_m, and R_b to the corresponding cell parameters used for the simulations, Q_{rel} (cf. 4.3.1.3), was calculated. The 1D-array containing the Q_{rel} values was sorted and split according to the data file name and stacked in different columns (Fig. III-9). This created a 2D-array, where each column contained the results of a different file, each containing randomly generated added noise to the original spectrum (cf. 4.3.1.2). These columns are in turn split and stored in a third dimension, sorted by derivative order. Now the Q_{rel} values were arranged in a way that each plane belonged to one file and equal fitting conditions were stacked on top of each other. Averaging the Q_{rel} values of equal fitting conditions resulted in a 4×6 array listing the results of the derivative orders in one dimension and those of the remaining conditions (weighting, spectrum type) in the other dimension. The large amount of data was thereby reduced to a much more manageable scale.
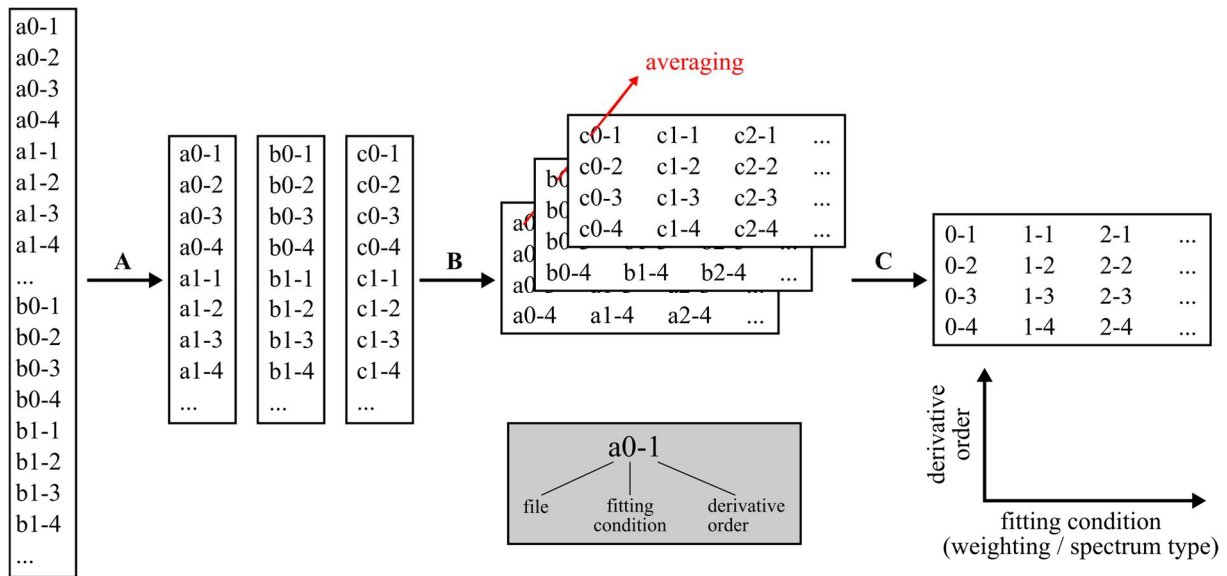
Fig. III-9: Sorting of fit results to reduce the data load to a more manageable scale. (A) Sorting and splitting by data file. (B) Sorting and splitting by derivative order. (C) Averaging of the fit results with identical fitting conditions (but different noise) to yield a clearly laid out 4×6 array (only partly shown here). This procedure has to be repeated for every number of increments.

2 PEDOT:PSS as Electrode Material for Impedance-based Cellular Assays

2.1 Objective

The goal of this project was to develop polymer based electrode arrays with PEDOT:PSS as electrode material that could be used for the impedimetric analysis of adherent cells *in vitro*. The design should be based on the layout of commercial ECIS arrays electrode so that the respective measurement setups could be used. The electrodes were to be characterized with respect to their physical dimensions, optical and impedimetric properties, and their long-term stability under ambient conditions. Several commonly used impedance-based cellular assays should be tested with the newly developed polymer electrodes and their performance was to be compared to commercial gold electrodes. These applications were in particular monitoring of cell adhesion, proliferation, and cytotoxicity assays, as well as micromotion and electroporation. The dielectric parameters of cells growing on the polymer electrodes should be determined and related to those adhered on gold electrodes. For each experiment, the commercial layout of electrode arrays, which would normally be employed in order to obtain the best results, was used for comparison (cf. 1.2.3). The PEDOT:PSS electrode arrays were designed to show high transparency in the visible light region so that they were compatible with inverse microscopes. During the development of the electrode arrays a focus was put on scalability to industrial volumes with emphasis on low-cost fabrication in order to minimize the cost of production and therefore the price per unit.

2.2 Materials and Methods

2.2.1 Screen Printing

Screen printing is a technology commonly used for the fabrication of printed electronics like for example OLEDs (organic light emitting diodes), FETs or solar cells.[153-155] The volume fabrication costs are much lower compared to silicon-based electronics. However, the performance of printed electronics cannot match the highly developed semiconductor technologies in terms of sophistication and integration density.[156] This does not pose a problem for the manufacturing of electrode arrays whose purpose is to be utilized for the impedance

analysis of living cells. The measurement chambers require a certain minimum volume for the cells not to run out of nutrients over longer measurement periods and to minimize the effect of medium or buffer evaporation. The space requirement of these chambers is therefore often the bottleneck for miniaturization. Depending on the ink and the substrate, the resolution for screen printing can be as low as $50 - 100 \, \mu m$.[157] In order to achieve good resolutions, a rather high viscosity of around $10 - 300 \, Pa \cdot s$ is required for the screen printing paste (or ink) not to interfuse under the mesh of the screen mask. A low surface energy of the substrate also enhances the line resolution due to reduced wettability. The setup of a screen printer is shown in Fig. III-10. It consists of a screen printer stage with a press bed, and a squeegee. The screen printing paste is placed on the screen mask, squeezed through the mesh of the screen mask by the squeegee, and thereby gets deposited on the substrate. Ultimately, the ink gets cured at elevated temperatures (cf. Tab. III-5).
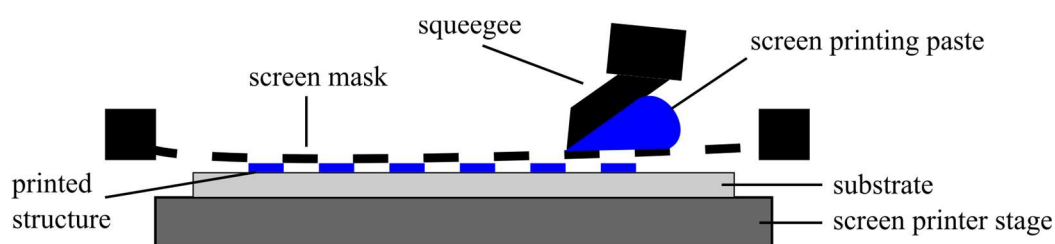
Fig. III-10: Setup of a screen printer.[157]

2.2.2   *Electrode Design*

The conducting polymer electrode arrays were fabricated with the screen printing technique. Their design was leaned on the commercially available 8W1E electrode arrays by Applied BioPhysics (Troy, NY, USA) with one small working electrode (WE) and a larger counter electrode (CE) in each well (cf. 1.2.3). The PEDOT:PSS electrode arrays will be referred to as PDT. All screen printed electrode arrays used in this thesis were printed on a PEN (Poly(ethylene 2,6-naphthalate) substrate. The electrodes consisted of three layers: a silver screen printing paste (*ESL 1901-SD*, ESL ElectroScience, King of Prussia, PA, USA), a special high viscosity PEDOT:PSS formulation for screen printing (*Clevios S V3*, Heraeus, Hanau, Germany), and a silicone passivation layer (*7165 EL Overcoat/Moisture Barrier*, DuPont Microcircuit Materials, Wilmington, DE, USA). Clevios S V3 is PEDOT:PSS dispersed in glycols to achieve the high viscosity required for screen printing. This is to some extent

detrimental for the conductivity and the sheet resistance is specified in the data sheet with a relatively high value of 700 Ω/sq. The specifications and curing conditions of all coating layers are shown in Tab. III-5. After the application of each layer, the screen printing paste is cured under the specified conditions before the next formulation is cast on top.

Tab. III-5: Coating layers, their respective sheet resistance R_{sq} after curing, and viscosity η of the screen printing formulation as specified by the manufacturer. The curing time t_{cur} and curing temperature T_{cur} were employed as shown.

layer number	layer material	relevant component	R_{sq} / Ω/sq	η / Pa·s	t_{cur} / min	T_{cur} / °C
1	ESL 1901-SD	silver	< 0.020	60 ± 10	10	125
2	Clevios S V3	PEDOT:PSS	700	15 – 60	10	120
3	7165 EL	silicone	n/a	20 – 40	5	120

Initial experiments showed that the intrinsic resistivity of screen printed PEDOT:PSS was too high for impedance spectroscopy because the lead resistance masked the signal of the cells. Even relatively broad leads did not sufficiently reduce the resistance of the polymer, besides being highly impractical with respect to the design of whole electrode arrays. Furthermore, the contact resistance between the metal pins commonly used to contact the ECIS electrode arrays and PEDOT:PSS was extremely high and barely reproducible. Therefore, a silver screen printing paste with much higher conductivity was used instead for the contact pads and leads (Fig. III-11a). The silver was led until right in front of the well so that the highly toxic silver particles were kept out of the measurement chamber and could not get in contact with the cells. The contact area between the silver layer and the PEDOT:PSS layer leading into the wells was maximized to minimize the contact resistance between the two conducting materials (Fig. III-11b). A silicone passivation layer on top was used to protect the silver leads and define the sizes and shapes of the working and counter electrodes (Fig. III-11c). The smallest possible diameter of 500 µm (in the template) was chosen for the working electrode. Using smaller diameters runs the risk of the silicone flowing inwards, closing the hole, and thereby insulating the electrode. The actual dimensions as determined by phase contrast microscopy are summarized and compared to commercial ECIS electrodes in Tab. III-6. The same polystyrene 8-well chambers as used for the 8W1E and 8W10E electrode arrays were glued on top of the printed electrodes (cf. 1.2.3) with common aquarium silicone glue (Fig. III-12).
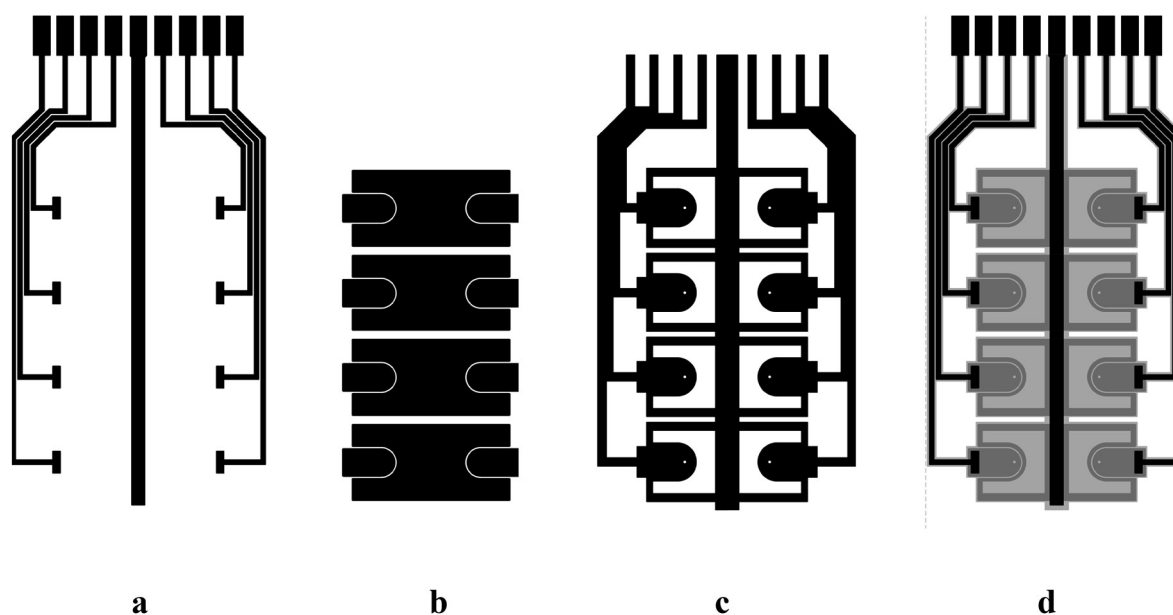
Fig. III-11: Electrode design of the PDT electrode arrays comprising three different screen printed layers on a PEN substrate: a silver conducting paste for the contact pads and leads (a), PEDOT:PSS as active electrode material (b), and a silicone passivation layer to define the electrode sizes and shapes. The overlay of all layers is also shown (d).
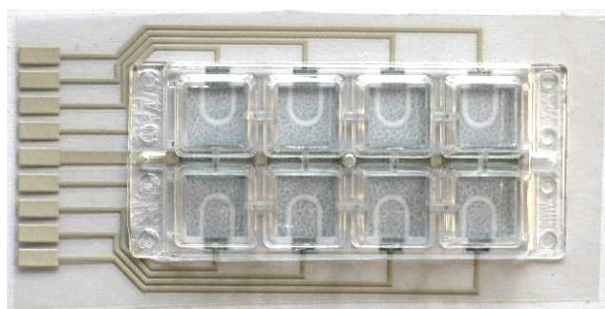
Fig. III-12: Photograph of a PDT electrode array with a polystyrene 8-well chamber glued on top.

2.2.3 Electrode Preparation for Impedance-based Assays

2.2.3.1 PEDOT:PSS Electrodes

After fabrication, all PDT electrodes were stored in the dark under ambient conditions until being used for experiments. The PDT electrodes were prepared for cell culture according to the following procedure. The arrays were subjected to argon plasma treatment for 30 s before immediate incubation in 200 µL poly-L-lysine solution (0.01% in dest. H_2O, mol. wt. 150000 – 300000 g/mol, Sigma-Aldrich) per well at room temperature. After 10 min the wells were rinsed twice with bidest. H_2O and left to dry for at least 2 h under the laminar flow hood. About

1 – 2 h before cell seeding, 400 µL pre-warmed cell culture medium was placed in each well and the impedance baseline was recorded in case of an adhesion or proliferation experiment. The medium was replaced by 400 µL cell suspension and the cells were allowed to settle for 20 min before placing the array into the incubator at 37 °C. This allows for a homogeneous distribution of the cells on the bottom of the wells without temperature-driven convection.

2.2.3.2   Gold Electrodes

The commercial gold electrodes (8W1E and 8W10E) were treated in a similar fashion as the PDT electrodes. After plasma treatment for 30 s the electrodes were coated with cysteine by placing 200 µL cysteine solution (10 mM in H_2O) in each well. The thiol groups of the amino acid form a quasi-covalent bond with the gold surface and thereby stabilize the electrode capacitance. The solution was aspirated after 10 min of incubation. The electrodes were washed twice with bidest. H_2O and subsequently coated with poly-L-lysine before cell seeding as described before.

If the cell adhesion was not followed over time and only the confluent cell layer was investigated 2 days after seeding, the electrodes were not pre-coated with cysteine or poly-L-lysine. Instead, cell culture medium was pipetted into each well directly after plasma treatment. The cysteine and cystine contained in the cell culture medium adsorbs to the gold surface providing a highly hydrophilic substrate suitable for cell adhesion.

2.2.4   Electrode Characterization

2.2.4.1   Determination of the Physical Dimensions

The profile of the PDT working electrodes (WEs) was determined with a mechanical contact profilometer at OTH Regensburg. This type of profilometer moves a stylus laterally across a sample surface and records the vertical stylus displacement. Thereby, the profile of the sample is obtained. The steepest slope was calculated from the average of the minimum absolute value and the maximum value of the first derivative of the profile. Three WEs on three different PDT arrays were probed each and averaged for the analysis. The lateral dimensions of the WEs were also optically determined with a phase contrast microscope. The images were analyzed with the software ImageJ.

2.2.4.2   Optical Characterization

The transmission of the PDT arrays was measured using a standard UV/VIS spectrometer. Small parts of an array with PEDOT/PSS printed on the PEN substrate were cut out and placed inside the spectrometer. A second sample with only the PEN substrate was also measured as reference. The transmission spectra were smoothed using a Savitzky-Golay filter with a 15-point window and a polynomial order of 5. The transmission spectrum of the PEDOT:PSS layer was calculated by Eq. 39 and smoothed again by adjacent averaging and a 23-point window.

$$T(\lambda)_{PEDOT} = \frac{T(\lambda)_{tot}}{T(\lambda)_{PEN}} \cdot 100\% \qquad \text{Eq. 39}$$

with: $T(\lambda)_{PEDOT}$ as the transmission of PEDOT:PSS

$T(\lambda)_{tot}$ as the total transmission of PEDOT:PSS printed on PEN

$T(\lambda)_{PEN}$ as the transmission of the PEN substrate

2.2.4.3   Impedimetric Characterization and Parameter Fitting

The impedimetric characterization of the PDT arrays was performed using two different hardware setups. The ECIS Zθ unit showed problems in the frequency range below 10 Hz where the recorded capacitance was cropped to a maximum of 1 μF. This limitation prevented the low-frequency analysis of the PDT electrodes, where the 'resistive' circuit element of the polymer-electrolyte interface Z_{CPE-R} (cf. 1.2.4) becomes relevant. Therefore, the CPE parameters of Z_{CPE-R} were determined using a Solartron Gain/Phase Analyzer (SI 1260) and the results were used for further modeling. Cell adhesion and cytochalasin D treatment experiments were conducted on the ECIS Zθ device to minimize the influence of the parasitic stray capacitance. The remaining parasitic impedance was modeled by a CPE with experimentally determined parameters (cf. 2.3.1.3).

ECIS spectra are usually fitted by regression analysis algorithms to obtain the cell parameters (cf. *II.3 Regression Analysis*). Because of the large number of parameters required for modeling PEDOT:PSS electrodes, the spectra were fitted manually using a self-written LabVIEW software (cf. 1.5.2) instead. For better comparison, the corresponding spectra measured with 8W10E gold electrodes were fitted in the same manner. First, the electrode parameters were obtained from a cell-free electrode, where the cells had been permeabilized and killed with 0.5 mg/mL saponin. These spectra were assumed to represent the electrode parameters of the cell-free electrode more closely than a freshly prepared electrode, because

a) the extracellular matrix (ECM) stays on the electrode after saponin treatment and is likely to have an influence on the electrode capacitance, and

b) the cells were treated with saponin more than 50 h after seeding. By then, the electrode drift has drastically diminished and the impedance is largely constant at all frequencies. This will be discussed in detail in chapter 2.3.1.5.

The electrode parameters then served as a basis for the determination of the cell parameters from the spectrum of a cell-covered electrode, recorded 40 h after confluent seeding.

2.2.4.4   Determination of the Parasitic Impedance

Because of the high resistivity of PEDOT:PSS compared to gold, the PDT electrodes exhibited a high bulk resistance. Therefore, parasitic elements had a relatively strong impact on the impedance at high frequencies. Before fitting the impedance spectra, it was necessary to correct for this parasitic impedance. The parasitic impedance Z_{prs} was determined by insulating the working electrode with a small droplet of aquarium silicone glue (Fig. III-13). Thus, the only way for the current to the counter electrode was by coupling capacitively through the passivation layer. This part of the parasitic impedance was termed Z_{psv}. There is, however, a second term, arising from the electronic circuitry of the measurement setup, the stray impedance Z_{str}. While both components are largely capacitive, they deviate from ideal behavior and are better represented by two parallel CPEs. The overall parasitic impedance Z_{prs} is given by Eq. 40. Z_{str} and Z_{psv} are not clearly distinguishable. However, an attempt was made to qualitatively estimate their relative contributions using differently shielded impedance analyzers (cf. 1.2.1). Comparing the results of the well shielded ECIS Zθ setup to measurements conducted on a customized setup based on a SI 1260 should alter the stray impedance Z_{str} and keep the passivation impedance Z_{psv} constant.

$$Z_{prs} = \left(\frac{1}{Z_{str}} + \frac{1}{Z_{psv}} \right)^{-1} = \frac{1}{(j \cdot \omega)^{n_{prs}} \cdot A_{prs}} \qquad \text{Eq. 40}$$
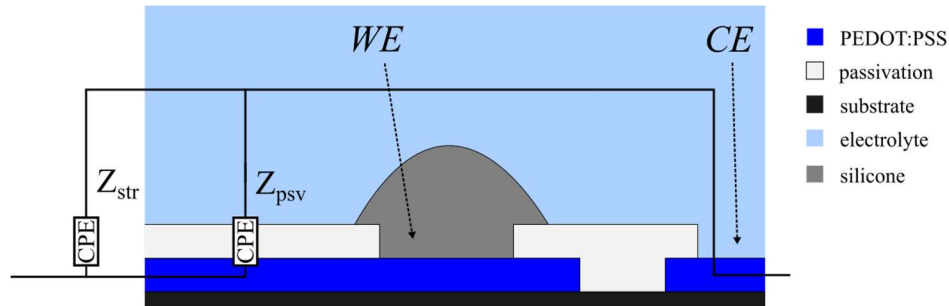
Fig. III-13: Schematic of the measurement setup used to determine the parasitic impedance Z_{prs} and illustration of its components Z_{str} and Z_{psv}.

The working electrodes of PDT and 8W1E electrodes were insulated with a small amount of silicone glue using the tip of a 10 µL pipette and allowed to cure over night at room temperature. The measurements were performed in MDCK cell culture medium after plasma treatment of the electrode array for 30 s. Before starting the measurement, the electrodes were placed inside the incubator for 2 h. The impedance data were recorded with the customized setup (SI 1260) and the ECIS Zθ device, respectively (cf. 1.2.1). A linear fit of the double logarithmic impedance magnitude spectrum $|Z|(\omega)$ between 1 kHz and 100 kHz was used for the determination of the CPE parameters A_{prs} and n_{prs} of the parasitic impedance (cf. II.3.2). At frequencies below 1 kHz, the impedance values became so high that the impedance analyzer reached its low-current limit and showed non-linear behavior. Those frequencies were therefore not included in the fit.

2.2.4.5   Influence of the Cell Culture Medium on the Electrode Impedance

The influence of the cell culture medium on the electrode impedance was investigated to determine the electrode drift of the PDT electrodes during the measurements. The arrays were treated with argon plasma for 30 s and subsequently incubated with pre-warmed MDCK cell culture medium. The incubation was followed over time at 37 °C on the customized setup for 90 h.

2.2.4.6   Long-Term Stability Upon Storage in Ambient Air

PEDOT:PSS is known to show degradation in air at elevated temperatures and upon irradiation with UV light.[103] In order to minimize the risk of light-induced degradation, the printed PDT sheets were kept in the dark at all times. They were only exposed to ambient light when the polystyrene chambers were glued on top of the arrays, during the preparation steps of the electrodes, and during cell seeding. The additional effort of keeping the electrode arrays under oxygen-free conditions was not made. This would not be practical for potential future practice when the electrodes are commercialized. Degradation of PEDOT:PSS reduces the conductivity of the conducting polymer and thus increases the lead resistance. Since R_{bulk} contains the terms for the constriction resistance as well as the lead resistance, polymer degradation was assumed to affect R_{bulk}. The long-term stability of the PDT arrays was studied by comparing R_{bulk} of all impedance spectra recorded after roughly 1 h of incubation with cell culture medium at 37 °C, but before cell seeding. Only the measurements in cell culture medium of before unused PDT arrays were included. This covered a time period of 362 – 832 days after the fabrication process of the screen printed electrode sheets. R_{bulk} was approximated by $|Z|$ at 10 kHz.

2.2.4.7   Voltage Dependence

The electrical stability of the PDT electrodes was analyzed and compared to 8W1E electrodes by recording the impedance between 1 Hz and 1 MHz with voltage amplitudes of 10 mV, 50 mV, 100 mV, 150 mV, 200 mV, 300 mV, and 500 mV (rms). The measurement was repeated 5 times in a row before switching to the next higher amplitude. Subsequently, the recording was repeated at 50 mV with the same electrodes to be able to draw conclusions about the reversibility of the alterations. Like in the previous chapter, R_{bulk} was used as a measure for the integrity of the electrode. R_{bulk} was approximated by $|Z|$ at 10 kHz for PDT electrodes and at 100 kHz for 8W1E electrodes. All measurements were carried out using cell culture medium as electrolyte.

2.2.5   Cell Adhesion, Cytochalasin D, and Saponin Treatment

Cell adhesion, cytochalasin D, and saponin treatment of confluent cell layers were conducted in a combined experiment. The effect of cytochalasin D on a confluent MDCK-II cell monolayer was monitored to quantify the influence of disintegrated cell-cell contacts on the cell parameters. Afterwards, the cells were permeabilized and killed to get the impedance of the cell-free electrodes required for parameter fitting (cf. 2.2.4.3). The experiments were performed using PDT and 8W10E electrodes, that had been prepared as described in chapter

2.2.3. The cell adhesion was followed over time for 48 h after confluent seeding, before the cells were treated with cytochalasin D. A 5 mg/mL cytochalasin D stock solution (in DMSO) was diluted with cell culture medium to a concentration of 10 µM/L and pre-warmed to 37 °C. 200 µL of the cell culture medium was removed in each well and replaced with an equal amount of the prepared cytochalasin D solution, yielding a final concentration of 5 µM. The impedance was recorded for 2 h before replacing 200 µL of the supernatant with 200 µL of a 0.1 mg/mL saponin solution in cell culture medium. This lead to a final saponin concentration of 0.05 mg/mL in the wells. Finally, the impedance signal was followed for another 1.5 h. Phase contrast images were taken in an independent experiment, where the electrode arrays were briefly taken out of the incubator for microscopic inspection at the specified time points.

2.2.6   Proliferation

In proliferation assays, the cells are seeded in low densities to provide space for the dividing cells, and the cell growth is followed over time. When the cells divide, they increasingly occupy a larger proportion of the electrode surface. This causes the impedance signal to rise, while the capacitance drops. Wegener demonstrated in 2000 that increasing the cell coverage of the electrode is linearly correlated to the decrease in capacitance at 40 kHz.[158] This relationship can be used to monitor cell proliferation with the ECIS technique in a quantitative manner. The capacitance is commonly measured at either 32 kHz or 40 kHz. 8W10E electrode arrays are preferred for proliferation assays as their larger electrode size compared to 8W1E arrays covers a larger portion of the few cells growing on the bottom of the well, thus providing more reliable results.

Before the experiments, the PDT arrays were treated with argon plasma for 30 s and subsequently kept in MDCK medium for 3 days under the laminar flow hood. Thereupon, they were washed with bidest. H_2O and coated with fibronectin to facilitate cell adhesion. The 8W10E electrodes were incubated for 10 min with 10 mM cysteine solution after 30 s plasma treatment, washed with bidest. H_2O, and then also coated with fibronectin. The fibronectin coating was performed by adding 150 µL of a 50 µg/mL fibronectin solution to all wells (PDT and 8W10E), and subsequent incubation at room temperature. After 1 h the solution was aspirated and replaced with cell culture medium and the impedance baseline was recorded for about 1 h. During this time, the cells were passaged and then seeded at a cell density of 20000 cells/cm² in the measurement chamber. The cells were allowed to settle under the laminar flow hood for 30 min before transferring the array to the incubator and starting the measurement. Cell proliferation was quantified by the time-point of half-maximal decline of C

at 32 kHz, $t_{1/2}$ (Fig. III-14). The final capacitance values were approximated by a linear fit with a fixed slope of 0 of the normalized capacitance, $C_{32 \text{ kHz}}$ norm., between 100 h and 150 h for each well separately. The difference between the starting point and this baseline was used for the calculation of $t_{1/2}$.
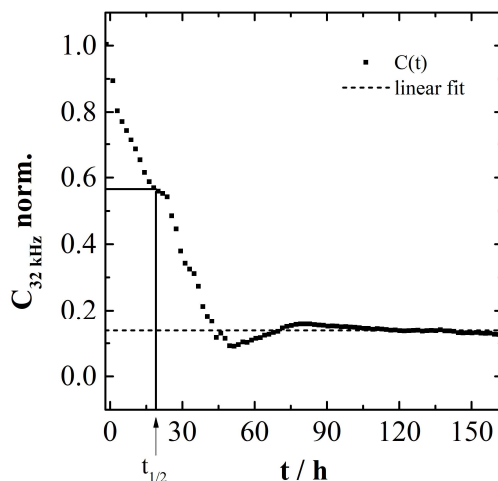
Fig. III-14: Proliferation analysis shown for a typical measurement. The baseline was approximated by a linear fit with a fixed slope of 0 of the time points between 100 h and 50 h (dashed line). The time of half-maximal change of C at 32 kHz between the starting point and the base line, $t_{1/2}$, was used for the quantification. 37 °C.

2.2.7   Cytotoxicity Assay for Saponin

The cytotoxicity of saponins, a group of herbal glycosides with detergent properties, was tested on NRK cells growing on PDT and 8W1E electrodes. The cells were seeded to confluency and used two days after. On the day of the experiment, the cell culture medium was replaced by PBS^{++} buffer. After two hours of equilibration, different concentrations of saponin (Sigma-Aldrich, St. Louis, MO, USA) dissolved in PBS^{++} were pipetted into the wells to give final concentrations of 0, 10, 15, 20, 25, 30, 50, and 75 µg/mL. For data evaluation, the time course of the impedance magnitude at 32 kHz was normalized to the last imepdance value before the saponin addition. A monitoring frequency of 32 kHz was chosen because saponin was expected to primarily affect the cell membrane integrity, whose capacitance determines the impedance at higher frequencies. The difference between the normalized impedance of the untreated control cells and the treated samples 3 h after the addition ($\Delta|Z|_{32 \text{ kHz}}$ norm.) was used for the calculation of the EC_{50} value. The EC_{50} describes the half maximal effective concentration of a drug or toxicant. The data were fitted in Origin using a sigmoidal Boltzmann fit of the following form (Eq. 41):

$$y = \frac{A_1 - A_2}{1 + e^{(x - x_0)/dx}}$$

Eq. 41

with x_0 as the EC_{50} concentration.

2.2.8   Micromotion

Micromotion measurements were performed on confluently seeded MDCK-II cells. The cells were seeded two days in advance on 8W1E and PDT electrode arrays. One hour before the start of the measurement the cell culture medium was replaced by $EBSS^{++}$ buffer and the arrays were placed inside the incubator about. The impedance signal of each electrode was recorded for 15 min at 400 Hz with a temporal resolution of 1.5 s. Subsequently, the cells were fixed with a 0.5% (w/v) solution of glutardialdehyde (GDA) (Sigma-Aldrich St. Louis, MO, USA) in $EBSS^{++}$. GDA covalently crosslinks and immobilizes the cellular proteins and thus prevents micromotion, while still maintaining most of the cell morphology. After 20 min of incubation the GDA solution was replaced by $EBSS^{++}$ and impedance time series of the fixed cells were recorded as described above. Measurements with GDA fixed cells and on cell-free electrodes served as control to distinguish electronic noise from the signal of viable cells.

2.2.9   Electroporation

NRK cells were seeded to confluency on PDT and 8W1E electrodes two days before the experiment. On the day of the experiment, the cell culture medium was replaced by a 2 mg/mL FITC-dextran solution in $EBSS^{++}$ The cells were allowed to equilibrate for at least 1 h. Electroporation was performed with a 200 ms pulse at varying frequencies and amplitudes with an ECIS 1600R (Applied BioPhysics, Troy, NY, USA). A FITC (fluorescein isothiocyanate) labeled dextran with a molecular mass of 4 kDa (Sigma-Aldrich, St. Louis, MO, USA) was used as model compound to be transferred into the cell. The degree of FITC-dextran loading, and therefore the electroporation efficiency, was estimated by the intensity and distribution of the fluorescence in the cells. Before the microscopic examination by confocal microscopy the cells were washed twice with $EBSS^{++}$. The impedance was followed over time before and after the electroporation.

2.2.10   Comparison of MDCK-I, MDCK-II, and NRK Cells

The three cell lines MDCK-I, MDCK-II, and NRK were grown to confluency on PDT electrodes and monitored by impedance spectroscopy using the SI 1260 setup and an amplitude of 10 mV (rms). All cells were seeded at a density of 450.000 cells/cm² on electrodes that had been pre-coated with poly-L-lysine as described before. For normalization, the frequency spectra recorded 40 h after seeding were compared to cell-free electrode spectra recorded during the equilibration phase before seeding. The electrode and cell parameters were fitted manually using the impedance magnitude spectra from before and 40 h after seeding, respectively.

2.3   Results and Discussion

2.3.1   Electrode Characterization

2.3.1.1   Determination of the Physical Dimensions

The electrode area A_{el} of the PDT WEs (working electrodes) as determined by phase contrast microscopy was $(1.30 \pm 0.07) \cdot 10^{-3}$ cm² (Fig. III-15). Accordingly, the average diameter of the circular shaped WEs was calculated to be (407 ± 11) µm. The size of the PDT WEs is thus in between that of the 8W1E electrodes $(0.5 \cdot 10^{-3}$ cm²$)$ and that of the 8W10E electrodes $(5 \cdot 10^{-3}$ cm²$)$. The phase contrast image shows a clear-cut contrast difference between the WE and the surrounding passivation layer, which however recedes with increasing distance from the WE. The edge of the electrode is, however, poorly visible as soon as cells cover the electrode.
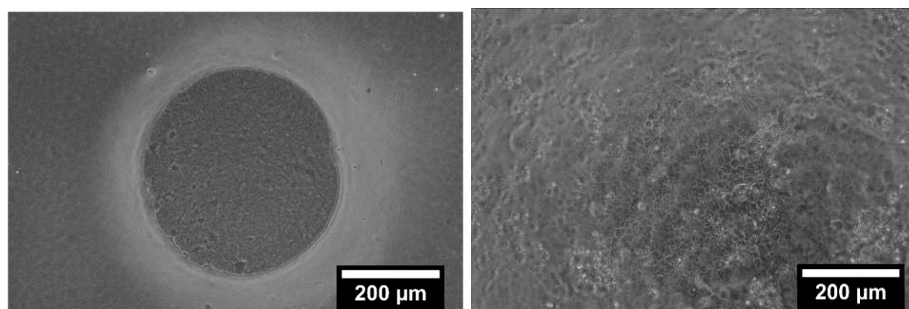
Fig. III-15: Phase contrast image of a PDT working electrode. The average electrode size was $(1.30 \pm 0.07) \cdot 10^{-3}$ cm² (N = 16). (*left*) cell-free electrode. (*right*) electrode covered with confluent MDCK-II cells.

The averaged depth profile of 9 different PDT working electrodes is shown in Fig. III-16 A. It shows a cone-like shape, supporting the results from the phase contrast images with an electrode diameter of roughly 400 µm at the bottom of the cone. The depth of electrode, i.e. the thickness of the passivation layer at the edge of the WE, is (12 ± 2) µm. The slope profile of the WEs was obtained by calculating the first derivative of the depth profile (Fig. III-16 B). Its extrema show the positions of the steepest slope at the onset of the passivation layer. The maximum slope is (0.085 ± 0.007) µm/µm, declining with increasing distance from the WE.
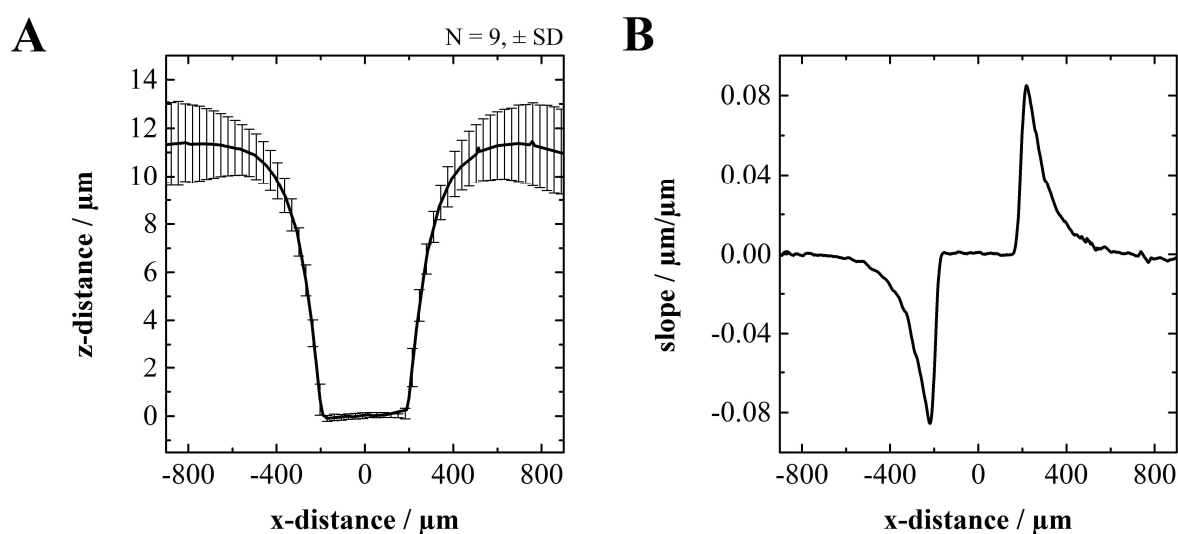
Fig. III-16: (A) Averaged depth profile of the working electrodes of PDT arrays. **(B)** First derivative of the averaged depth profile. The maximum slope is (0.085 ± 0.007) µm/µm.

The dimensions of the PDT electrodes are summarized and compared to the commercial 8W1E and 8W10E gold electrodes in Tab. III-6. The depth of the WE profile is not necessarily equal to the average thickness of the passivation layer, because the phase contrast is different close to the edge of the WE as compared to a distance of about 200 µm from the edge of the WE (Fig. III-15). This may indicate varying passivation thickness with increasing distance from the WE.

Profilometer measurements over larger distances that could determine the passivation layer thickness proved unreliable due to a strong drift in the profile. A differential determination may solve this problem.

Tab. III-6: Dimensions of the working electrodes of the PEDOT:PSS electrode arrays (PDT) compared to commercial gold electrodes from Applied BioPhysics (cf. 1.2.3). The passivation contact angle describes the angle of the passivation layer with the working electrode. [*] J. Wegener, personal communication.

	PDT ($\pm$ SD)	8W1E	8W10E
diameter / μm	407 ± 11	250	10×250
A_{el} / 10^{-3} cm²	1.30 ± 0.07	0.5	5
passivation contact angle	4.9 ± 0.4	n/a	n/a
depth / μm	12 ± 2	3.6 [*]	3.6 [*]

In all experiments throughout this chapter, the experimental mean value for $A_{el} = 1.30 \cdot 10^{-3}$ cm² for PDT electrodes was employed for the calculations if required. The SD of the PDT electrode area accounts for 5% relative error. This error must be considered when fitting the electrode and cell parameters to an impedance spectrum, since the interface impedance as well as the cell parameters are normalized to the electrode surface area. If a more accurate determination of the parameters is required, the electrode size should be measured for each electrode individually and the respective value should be used for fitting. However, biological materials tend to have much higher variances, so that a 5% error does not carry much weight. The reason for the comparatively high SD is the minimal resolution of screen printing being around $50 - 100$ μm.[157] By contrast, laboratory-level photolithography processes can have resolutions of $2 - 3$ μm.[159]

The thickness of the passivation layer of (12 ± 2) μm layer seems relatively high. It is higher than the cell layer thickness, which was reported to be (7.1 ± 0.7) μm by Zehnder et al. and (4.0 ± 0.5) μm by Janshoff et al.[160-161] However, there is no abrupt step between the WE surface and the passivation layer. Instead, there is a steady increase over a distance of roughly 200 μm. The slope of (0.085 ± 0.007) μm/μm at the steepest section means that for every 10 μm in lateral direction, the ascent is only about 1 μm in vertical direction. This corresponds to an angle of (4.9 ± 0.4) ° (deg). This was assumed not to have a significant impact on cell growth.

2.3.1.2   Optical Characterization

The PEN substrate shows high transmission T in the visible range of the electromagnetic spectrum between a wavelength of 400 and 700 nm (Fig. III-17 A). At 700 nm, the transmission

is about 77% and declines with decreasing wavelength to a value of 46% at 400 nm. The transmission of UV light below 400 nm is almost completely blocked and drops to zero at 370 nm. When PEDOT:PSS was printed on the PEN substrate, the transmission was reduced to 50% between 600 and 700 nm, and to 34% at 400 nm. Complete blockage of UV light occurs at lower wavelengths. From these spectra, the transmission spectrum of PEDOT:PSS was calculated (Fig. III-17 B). It shows a maximum transmission of 74% at 450 nm but is almost flat. At higher wavelengths, the transmission is slightly lower and decreases to a value of 67% at 700 nm. The transmission in the UV region could not be calculated because of the opacity of PEN in that range.
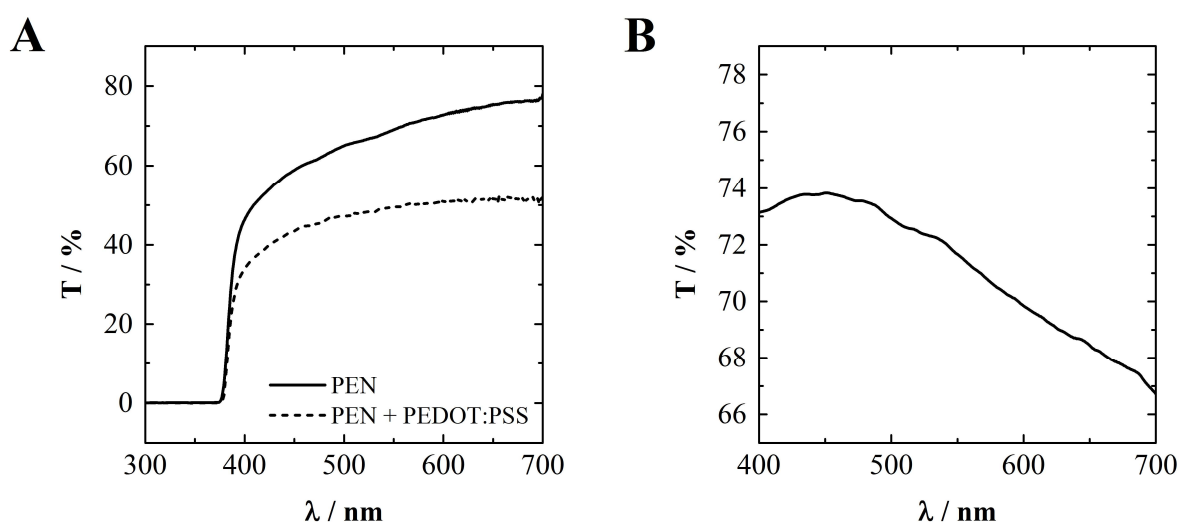
Fig. III-17: (A) Smoothed transmission spectra of PEN and of PEDOT:PSS printed on a PEN substrate. **(B)** Calculated transmission spectrum of PEDOT:PSS. Smoothing was performed using adjacent-averaging and a 23-point window.

PEN contains two condensed aromatic rings per monomer unit, which are responsible for the strong UV absorption of the polymer. This causes a cut-off wavelength of around 400 nm, below which no light is transmitted through the substrate. Since most fluorescent dyes have an excitation wavelength in the visible spectrum, the PDT arrays are compatible with inverse microscopes and fluorescence staining as long as the excitation wavelength is beyond 400 nm. (Tab. III-7). It is noteworthy that, for instance, the excitation wavelengths of the nucleus staining dye DAPI and one of the many available Alexa Fluor dyes (λ_{ex} = 346 nm) lie within the opaque range of the transmission spectrum.

Tab. III-7: List of common fluorescent dyes used in cell based assays and their excitation wavelength λ_{ex}. EthD-1: ethidium homodimer-1, FITC: fluorescein isothiocyanate, TRITC: tetramethyl rhodamine-isothiocyanate, DAPI: 4',6-diamidino-2-phenylindole, DiI: 1,1'-dioctadecyl-3,3,3',3'-tetramethylindo-carbocyanine

dye	purpose	λ_{ex} / nm
EthD-1	Live/Dead staining	528
Calcein	Live/Dead staining	494
FITC	label	495
TRITC	label	550
Alexa Fluor	label	346 – 784
DAPI	nucleus staining	358
DiI	membrane staining	549

The calculated spectrum of PEDOT:PSS is in good accordance with the results published by other authors.[41,162] PEDOT:PSS shows slightly higher absorption in the red region, causing the blue appearance of the polymer. The transmission spectrum is also influenced by the thickness of the layer, which is not known in this case. Judging from transmission spectra published by Elscher in 2010 for a standard low-viscosity dispersion, the PEDOT:PSS layer thickness in this work was assessed to be between 200 and 500 nm.[41] This is only a very crude estimation because the compositions of the PEDOT:PSS formulations differ.

2.3.1.3   Impedimetric Characterization

Fig. III-18 shows the averaged |Z| and φ spectra of cell-free PDT electrodes covered with MDCK cell culture medium, recorded with the customized impedance setup (cf. 1.2.1). The spectra are divided in different sections, depending on which equivalent circuit element they are dominated by (Tab. III-8). The boundaries are not as clear-cut as depicted in the figure. Instead, they are meant to roughly indicate at what frequencies the respective equivalent circuit elements were adjusted to the spectrum during the manual fitting process.

The very low frequencies between 1 and 50 Hz are exclusively dominated by the interface impedance. The presence of the capacitive part of the interface impedance Z_{CPE-C} is more obvious as |Z| increases linearly with decreasing frequency. At the same time φ amounts to around -70°, but is not purely capacitive (-90°). While the subtle bend in section (a) is barely visible in |Z| (partly due to the averaging), the presence of a second, more resistive element is clearly visible in φ. Going down from 4 Hz to 1 Hz, φ increases from -70° to -60° and thus

indicates the contributions of the resistive Z_{CPE-R}. In section (b) Z_{CPE-C} dominates the spectrum, so that this part is similar to gold electrodes, where no Z_{CPE-R} exists. Section (c) is a transition segment between (b) and (d) with φ covering a wide range from -60° to -10°. (d) is mostly determined by the resistive element R_{bulk}. This is indicated by $|Z|$ being largely constant at around 2400 Ω and φ being close to zero, i.e. between -10° and 0°. Section (e) shows another capacitive component with $|Z|$ linearly decreasing and φ becoming more negative. The section is due to the parasitic impedance Z_{prs}.
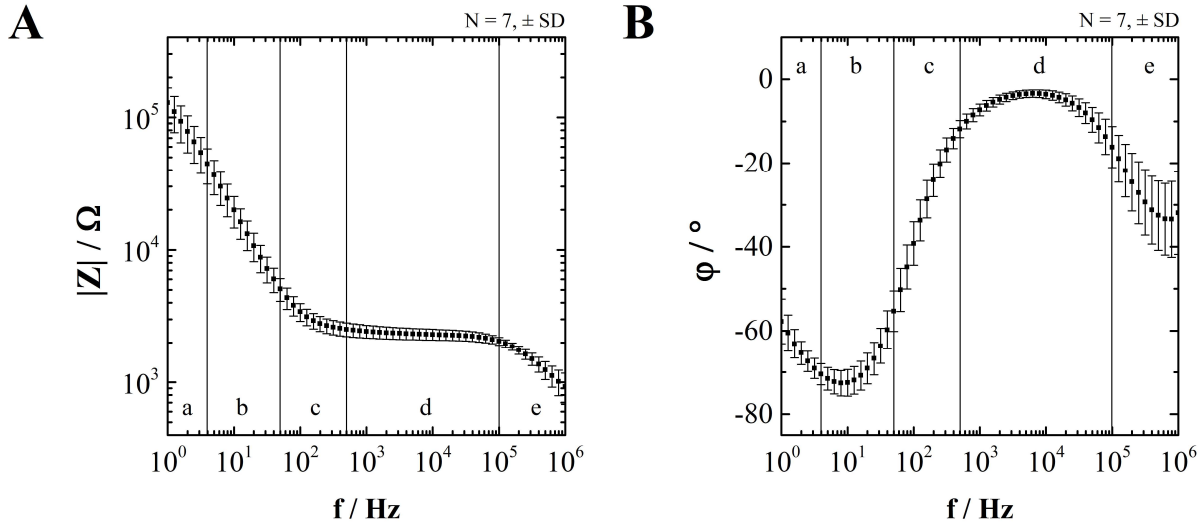
Fig. III-18: (A) Spectrum of the impedance magnitude of cell-free PDT electrodes. **(B)** Phase spectrum of cell-free PDT electrodes. The spectra were recorded with the customized setup (cf. 1.2.1) in cell culture medium. The sections a – e are dominated by different elements of the equivalent circuit (see text and Tab. III-8). T = 37 °C

Tab. III-8: List of the different frequency sections from Fig. III-18 and the dominating equivalent circuit (EQC) elements and electrode parameters.

	frequency range	EQC element	parameters
a	1 – 4 Hz	Z_{CPE-R}	A_{cpe-r}, n_{cpe-r}
b	4 – 50 Hz	Z_{CPE-C}	A_{cpe-c}, n_{cpe-c}
c	50 – 500 Hz	(transition segment)	
d	500 Hz – 100 kHz	R_{bulk}	R_{bulk}
e	100 kHz – 1 MHz	Z_{prs}	A_{prs}, n_{prs}

The electrode parameters were fitted according to the previously described equivalent circuit (cf. 1.2.4) with a fixed electrode area of $1.3 \cdot 10^{-3}$ cm². Since n_{cpe-r} was close to zero ($n_{cpe-r} = 0.2 \pm 0.1$), Z_{CPE-R} was considered largely resistive, however showing significant deviation from an ideal resistor. A value of 0.94 ± 0.01 was determined for n_{cpe-c}. This is in the range of a

typical CPE describing the non-ideal double layer capacitance of metal-electrolyte interfaces (cf. II.1.3). The fit results for A_{cpe-r} and A_{cpe-c} were $(2.1 \pm 0.3) \cdot 10^{-3}$ and $(9 \pm 3) \cdot 10^{-4}$ $F \cdot s^{(n-1)}/cm^2$, respectively ($\pm$ SD). The electrode parameters will be discussed in detail in chapter 2.3.2 and compared to the parameters of gold electrodes.

In general, three different processes have to be considered as possible contributors to the interface impedance of PEDOT:PSS:

- Electron **charge-transfer**, including the charge injection from the silver leads into the conducting polymer, as well as the charge transport in between the polymer chains. This process is often described by a charge-transfer resistance R_{ct}.[65]

- **Ion conduction**, caused by the voltage-dependent drift of ions inside the polymer. The ion conduction has been reported to show Warburg behavior.[108]

- Voltage-driven **ion drift** between the electrolyte and the polymer. This leads to the 'classical' double layer behavior.

The equivalent circuit assumes that the more resistive Z_{CPE-R} accounts for charge-transfer and ion conduction. The deviation from ideal resistive behavior was attributed to the diffusion controlled ion conduction. The voltage-driven ion drift between electrode and electrolyte that leads to the formation of an electrical double layer is expressed by Z_{CPE-C}. A clear discrimination between all individual processes that are involved at the electrode-electrolyte interface of PEDOT:PSS is, however, neither possible nor necessary for the scope of this work.

2.3.1.4 Determination of the Parasitic Impedance

The results of the fits determining the parasitic impedance Z_{prs} are displayed in Fig. III-19. The CPE parameters of Z_{prs} were analyzed for PDT and 8W1E electrode arrays with insulated working electrodes. The measurements were performed using the customized setup with the SI 1260 impedance analyzer and the commercial ECIS Zθ. The results show that A_{prs} takes on similar values for electrodes measured on the same device, independent of the electrode type (Fig. III-19 A). The values for 8W1E electrodes (0.24 ± 0.04 nF·s$^{(n-1)}$/cm²) and PDT electrodes (0.28 ± 0.05 nF·s$^{(n-1)}$/cm²), both determined on the ECIS Zθ, do not differ within the error margin. At the same time, they are significantly lower than those obtained from the SI 1260 for 8W1E (0.49 ± 0.06 nF·s$^{(n-1)}$/cm²) and PDT electrodes (0.43 ± 0.05 nF·s$^{(n-1)}$/cm²). A similar phenomenon is observed for n_{prs} (Fig. III-19 B). However, the results are similar for the same electrode type and different measurement devices, but differ for different electrode types. The parameter values of the PDT electrodes are not distinguishable within the error margin (ECIS

Zθ: 0.945 ± 0.003, and SI 1260: 0.940 ± 0.008), while the values of the 8W1E electrodes are considerably higher (ECIS Zθ: 0.981 ± 0.003, and SI 1260: 0.971 ± 0.002).

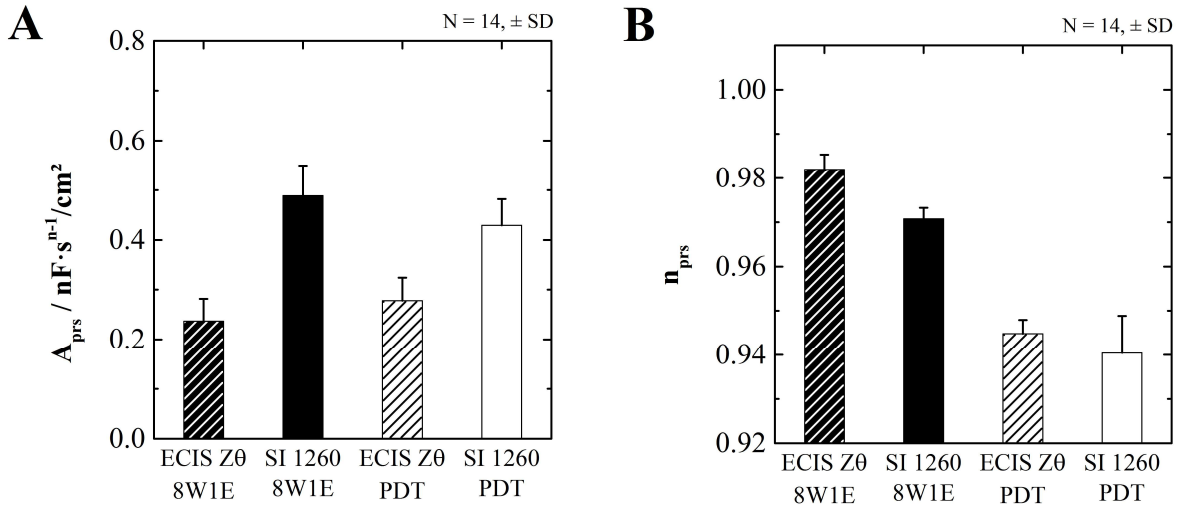**Fig. III-19:** CPE parameters of the parasitic impedance Z_{prs} for different electrodes and measurement devices. From left to right: **(A)** A_{prs} = 0.24 ± 0.04, 0.49 ± 0.06, 0.28 ± 0.05, and 0.43 ± 0.05 nF·s$^{(n-1)}$/cm². **(B)** n_{prs} = 0.981 ± 0.003, 0.971 ± 0.002, 0.945 ± 0.003, and 0.940 ± 0.008. T = 37 °C

As mentioned before, Z_{prs} is made up of the two components Z_{str} and Z_{psv}. The individual components of Z_{prs} cannot be distinguished in the impedance spectrum, but are influenced by different structural conditions. Z_{str} is mainly affected by the cables between measurement electronics and electrode array, and by how well the measurement setup is shielded from external electromagnetic fields. In contrast, Z_{psv} represents the parasitic contributions of the electrode array. Considering its capacitive nature, Z_{psv} depends mainly on the thickness of the passivation layer, its dielectric constant, and the contact area between passivation covered leads and electrolyte.

For the interpretation of the empirical parameters A_{prs} and n_{prs}, two assumptions have to be made. The first assumption is that A_{prs} corresponds to the overall non-ideal parasitic capacitance and can be interpreted as such. This seems reasonable since all occurring n_{prs} values are higher than 0.94 and thus very close to 1. On the other hand, A_{prs} and n_{prs} both affect the capacitance of the system C(f) to different degrees, depending on the frequency. Therefore, interpretations of the parameters should be treated with care. Nevertheless, it is clear from Fig. III-19 A that the influence of the electrode type on A_{prs} is negligible compared to the effect of the measurement setup. This means that Z_{prs} is mainly caused by stray capacitance and is determined by Z_{str}. It thus makes sense that the results of A_{prs} for the electrodes measured on the well-shielded ECIS Zθ show a much lower value than the results on the customized SI 1260

setup. Shielding the electric circuitry from parasitic electromagnetic fields reduces the stray capacitance and, therefore, A_{prs}. When the stray capacitance is low (on the ECIS Zθ setup), no significant difference can be observed between both electrode types (p < 0.01). The dielectric constants for the passivation materials for both electrode types have not been determined. However, it seems as if different parameters of the passivation layer cancel each other out, so that both passivation layers show the same parasitic passivation impedance Z_{psv} within the error margin. This is, however, not to be seen as a general statement for all electrode types, as the lead width and passivation thickness reportedly affect the parasitic impedance.[163] The second assumption concerns the interpretation of n_{prs}. Fig. III-19 B shows that the differences in n_{prs} between the measurement devices is far less pronounced than between the electrode types. Hence, we can assume that most of the impact on the parameter is caused by Z_{psv}, i.e. the properties of the passivation layer. In 1985, Nyikos et al. correlated n to the fractal dimension of the electrode surface.[164] This statement was later generalized and deviation of n from the ideal value 1 for capacitive behavior was attributed to current density inhomogeneities caused by microscopic surface roughnesses.[91] While research on the origin of the CPE has mostly been conducted on bare electrode surfaces, dielectric barrier coatings have also been described by a CPE with 0.86 < n < 0.97.[89] The different values for n_{prs} are therefore suggested to be caused by a higher degree of surface roughness or inhomogeneity of the PDT passivation layer compared to the 8W1E photopolymer passivation layer. This remains to be confirmed by additional investigations of the passivation topography.

In conclusion, the parasitic impedance was found to depend on the type of electrode as well as the measurement device. Interpretations for the parameters A_{prs} and n_{prs} were suggested, but could ultimately not be proved. The results obtained from these measurements were used during the fitting of the electrode parameters in the following chapters.

2.3.1.5   Influence of Cell Culture Medium on the Electrode Impedance

Fig. III-20 A displays the impedance spectrum recorded 96 h after incubation with MDCK medium, normalized to the spectrum at the beginning of the measurement after 1 h of equilibration at 37 °C. It indicates the relative impedance changes after 96 h (measured at 37 °C in the dark) at the respective frequencies of the spectrum. The change of |Z| in the electrode-electrolyte interface region below 50 Hz shows a slight decrease between -10% and 0%. The standard deviations in that range are relatively high with values up to 8% of the mean at frequencies close to 1 Hz. By contrast, for the remaining frequency spectrum above 50 Hz, the relative SD is only between 2% and 3%. Around 100 Hz, there are barely any changes in |Z|

and the normalized spectrum shows values close to 1. A maximum increase of about 20% occurs between 500 Hz and 100 kHz, where R_{bulk} determines the spectrum. Fig. III-20 B resolves the normalized impedance for the frequencies 10 Hz, 100 Hz, 1 kHz, 10 kHz, and 100 kHz as a function of time. At 10 Hz, there is almost no change in the first 7 h after medium addition. Thereupon, |Z| increases by a maximum of 10% at approximately 20 h, and then slowly declines to its initial value over the next 70 h. As observed for the low frequency region in Fig. III-20 A, the standard deviation becomes relatively high around the time point of the maximum increase. The time courses at 100 Hz, 1 kHz, 10 kHz, and 100 kHz show a biphasic form with a relatively steep increase in the first 12 h. The curve at 100 Hz then remains constant at the 5% level. By contrast, the curves at 1 kHz, 10 kHz, and 100 kHz show a subtle bend after 12 h and then asymptotically approach values between 20% and 25% higher than the initial impedance value.

The spectrum of the normalized capacitance (Fig. III-20 C) shows an increase in the frequency region below 10 Hz by about 20% after 96 h. Between 10 Hz and 2 kHz, the capacitance is stable. At higher frequencies, however, the capacitance drops by up to 30% at 63 kHz, the minimum of the spectrum. The capacitance time courses confirm the biphasic nature of the equilibration in the first 12 h, as observed for the impedance magnitude in a similar way (Fig. III-20 D). The 10 Hz, 100 Hz, and 1 kHz curves experience a subtle decline after 12 h, before asymptotically going back to their starting values. The capacitance at 100 Hz and 1 kHz never deviates more than 5%. As discussed for the normalized spectrum, the higher frequencies are more susceptible to electrode drift. The capacitance at 100 kHz eventually reaches a constant level at around 70% of the starting value after about 48 h.

The normalized resistance (Fig. III-20 E) shows an increase between 10 – 20% over almost the whole frequency spectrum. This is also reflected in the time course (Fig. III-20 F) where all frequencies display a steady, approximating a maximum of about 20% more than the initial value. An exception is the time course at 10 Hz – and to a lesser degree at 100 Hz – where the biphasic nature of the time course is well pronounced in the first 12 to 20 h of the experiment.
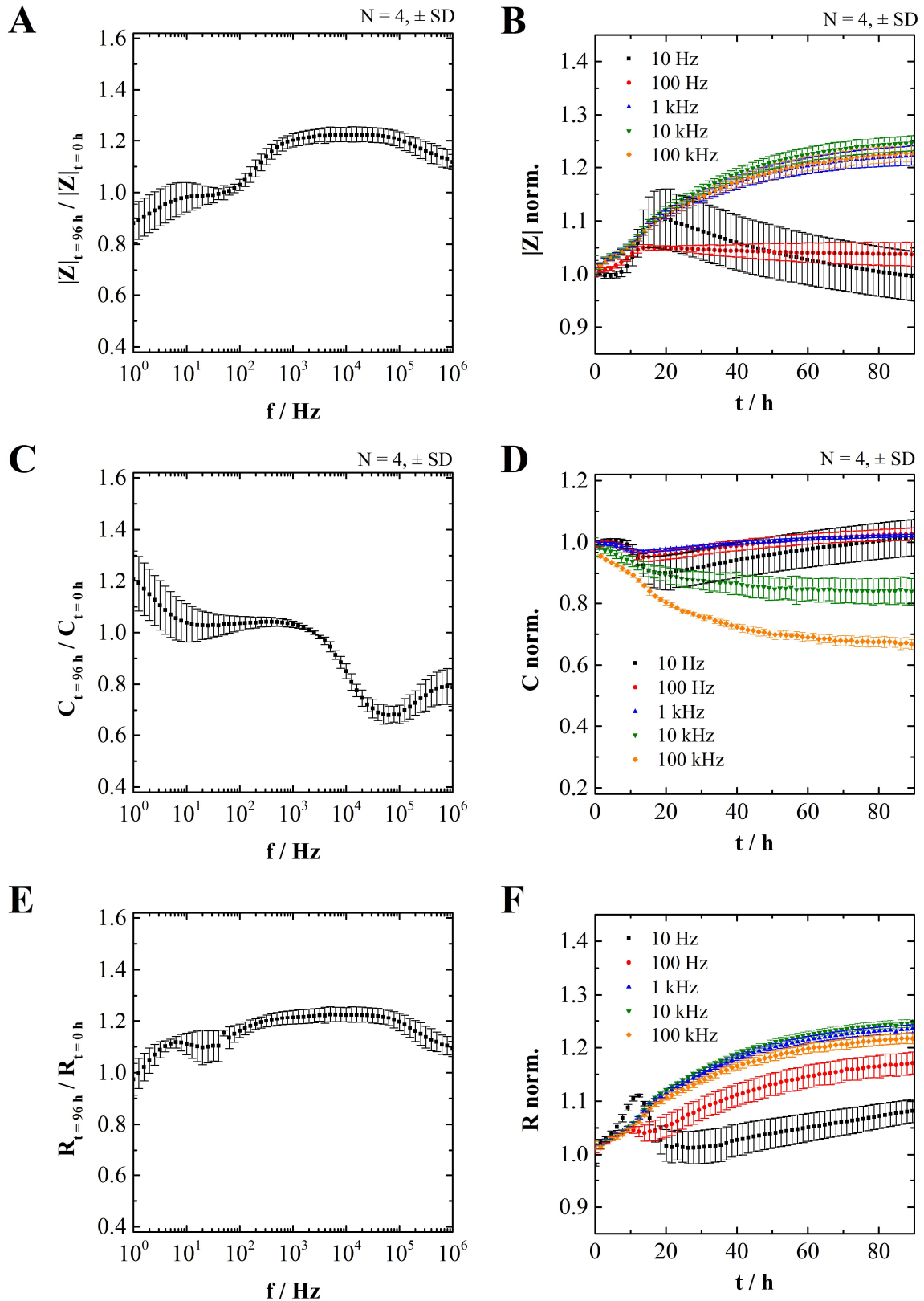
Fig. III-20: Influence of cell culture medium on the electrode impedance. **(A)** Normalized impedance magnitude spectrum that shows the relative change after 96 h of incubation. **(B)** Time course of the normalized impedance magnitude at different frequencies. **(C)** Normalized capacitance spectrum. **(D)** Time course of the normalized capacitance at different frequencies. **(E)** Normalized resistance spectrum that shows the relative change after 96 h of incubation. **(F)** Time course of the normalized resistance magnitude at different frequencies. T = 37 °C

The different frequency regions of the normalized impedance magnitude spectrum in Fig. III-20 A can be correlated to the frequency ranges described in chapter 2.3.1.3. The low frequency part of the spectrum (a and b in Tab. III-8) is determined by the interface impedance, where |Z| decreases. While a more mechanistic explanation cannot be provided, it is reasonable that the uptake of medium and the involved swelling of the polymer affects the interface capacitance. Moreover, the adsorption of proteins and other biomolecules from the cell culture medium on the electrode needs to be considered to affect the interface capacitance. The R_{bulk} dominated region (d in Tab. III-8) shows an increase that is most likely caused by cations from the medium dedoping the polymer (cf. II.2.3). The dedoping process reduces the conductivity of PEDOT:PSS and thus increases the lead resistance. The lead resistance, in turn, is connected in series with R_{bulk} in the equivalent circuit and, therefore, affects the spectrum in the same way as R_{bulk}. The time courses of |Z| and C reveal that the electrode drift occurs over a long time period of several days. This is somewhat surprising as the PEDOT:PSS layer is only a few hundred nm thick and should be soaked with the electrolyte rather quickly. Water uptake in PEDOT:PSS occurs within minutes, even when only subjected to humid air.[41] One conceivable explanation is that – while water uptake occurs fast – the ion exchange with the polymer takes much longer to reach equilibrium. It is also possible that the electrolyte diffuses along the polymer hydrogel underneath the passivation layer and thus impacts the electrode parameters on a prolonged time scale.

In terms of the practical implementation, these results lead to the conclusion that the PDT electrodes should be allowed to reach equilibrium over at least 48 h before an experiment. After that time, the electrode drift has largely diminished and the signal is sufficiently stable. Especially for cell adhesion and proliferation experiments, the electrodes should be incubated with the respective cell culture medium in order to get a stable base line. It noteworthy that this signal drift is small compared to the signal change caused by cells. A confluently grown MDCK-II cell layer for example causes |Z| to increase by up to 1200% compared to the cell-free electrode (cf. Fig. III-23 B). This depends of course on the monitoring frequency and the cell line.

2.3.1.6   Long-Term Stability Upon Storage in Ambient Air

The long-term stability of unused PDT electrodes when stored in ambient air was investigated by analysis of R_{bulk} of all used electrodes over a long time period. In Fig. III-21 all relevant measurements of cell-free electrodes in cell culture medium in a time interval of about 16 months, starting 10 months after fabrication, are plotted. Excluding the outliers, the statistically

weighted mean of R_{bulk} is $(1800 \pm 100)\ \Omega$ ($\pm$ SD). According to the Neumann trend test, no trend is found in the given time range.

The deviations of the individual PDT electrodes either occur during the manufacturing process or are caused by different pretreatment procedures like electrode coating or plasma treatment. However, no correlation between the pretreatment of the electrode and the measured R_{bulk} values was found, so that the fabrication related error presumably dominates. The observed deviations are not detrimental for the measurement, as each spectrum or time course can be individually normalized to the cell-free electrode. A potential oxygen induced degradation is entirely negligible as R_{bulk} does not change over time. Storing the electrodes in the dark thus provides sufficient stability for this application. The electrodes were, however, only stored in the dark due to cautionary measures and degradation in ambient light over time was not studied.
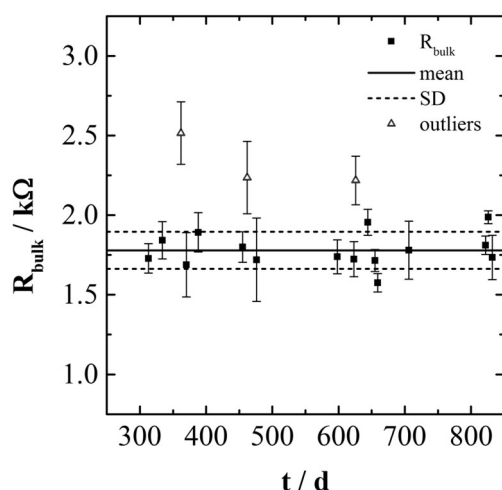
Fig. III-21: R_{bulk} (approximated by |Z| at 10 kHz) determined from cell-free electrodes after increasing storage time t at ambient temperature in the dark, measured in cell culture medium. The mean is calculated by statistical weighting. N varies between 4 and 16 for each displayed data point. T = 37 °C

2.3.1.7   Voltage Dependence

In accordance with the chapter on the long-term stability, the electrical stability was also evaluated by analyzing the change of R_{bulk} upon increasing the AC amplitude during the measurement. Fig. III-22 A shows R_{bulk} of PDT and 8W1E electrodes as a function of the excitation voltage. R_{bulk} of the 8W1E electrodes exhibits a linear dependence up to 500 mV with a slightly negative slope of $(-0.09 \pm 0.01)\ \Omega/mV$. By contrast, R_{bulk} of the PDT electrodes is linearly correlated only up to 300 mV with a positive slope of $0.38 \pm 0.01\ \Omega/mV$. In that range R_{bulk} increases from $(1840 \pm 30)\ \Omega$ at 10 mV to $(1950 \pm 40)\ \Omega$ at 300 mV. The application of a 500 mV amplitude, however, leads to a strong increase of R_{bulk} to a value of $(5000 \pm 2000)\ \Omega$. The respective spectra of |Z| are exemplarily depicted in Fig. III-22 B for 50 mV,

500 mV, and again 50 mV after the intermittent application of 500 mV. The two 50 mV impedance spectra from before and after the application of 500 mV are basically identical for 8W1E electrodes. While the 500 mV spectrum shows a significant shift towards lower frequencies in the capacitive region below 20 kHz, it remains unchanged at higher frequencies. This is in good agreement with the small slope of R_{bulk} in Fig. III-22 A, which was determined at 100 kHz. The situation is different for PDT electrodes. The frequency region of the interface impedance is only slightly displaced towards lower frequencies when 500 mV are applied. In this region, the alteration is reversible when going back to 50 mV. The impact is more severe above 20 Hz, where a significant and entirely irreversible increase of |Z| occurs.
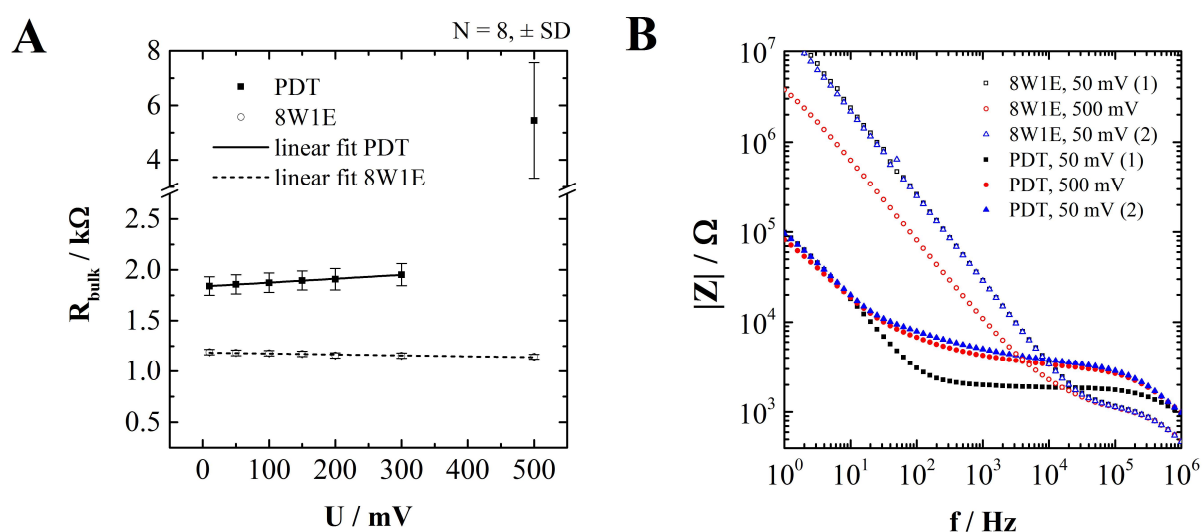
Fig. III-22: Voltage dependence of PDT electrodes, measured in cell culture medium. **(A)** Change in R_{bulk} of PDT and 8W1E electrodes with increasing excitation amplitudes. The linear fits have slopes of (0.38 ± 0.01) Ω/mV (PDT) and (-0.09 ± 0.01) Ω/mV (8W1E). R_{bulk} was approximated by |Z| at 10 kHz for PDT electrodes and at 100 kHz for 8W1E electrodes. **(B)** Typical impedance magnitude spectra for 50 mV and 500 mV amplitudes. The spectrum was recorded twice with 50 mV, once before (1) and once after the application of 500 mV (2). T = 37 °C

The results demonstrate that the 8W1E electrodes are stable in the observed amplitude range and do not show any signs of voltage induced degradation. Given the minor negative slope in Fig. III-22 A, R_{bulk} can be seen as constant. The reversible impedance shift in the capacitive region of the spectrum was explained by an enhanced interface capacitance. The enhanced potential difference between electrode and electrolyte increases the electrical attractive forces between the electrode and the counter ions in the electrolyte.[165] Thus, more charges accumulate on the electrode surface during the charging and discharging process of the double layer capacitor, which causes the increased capacitance. By contrast, the PDT electrodes show clear signs of PEDOT:PSS degradation at 500 mV. The nonlinear behavior of R_{bulk} at that amplitude

is irreversible, which leads to the conclusion that parts of the conducting polymer were destroyed by overoxidation, thereby obstructing the charge transport along the polymer. Irreversible oxidation has been reported in the literature to start above 0.8 V vs. SCE.[166] A proposed mechanism is the oxidation of the sulfur atom in the thiophene ring with subsequent SO_2 elimination and chain cleavage.[167] The positive slope in the range up to 300 mV in Fig. III-22 A is not substantial, but noteworthy. It is possible that, due to a higher excitation potential, more charges are transferred from the silver leads to the conducting polymer. Consequently, the charge density is increased, leading to an enhanced cation drift into the polymer hydrogel and causing a reduced conductivity by dedoping the polymer.

It should be stressed that polymer degradation strongly depends on the time scale and the frequency of the excitation signal. While a voltage amplitude of 500 mV is highly detrimental when recording whole frequency spectra, short (200 ms) high frequency voltage pulses of up to several volts did not do any harm to the polymer during electroporation (cf. 2.3.8).

2.3.2   *Comparison of Impedance Spectra of MDCK-II cells recorded with PDT and 8W10E Electrodes*

In this chapter, PDT and 8W10E electrodes are compared with respect to their sensitivities to monitor cellular monolayers. MDCK-II cells were used as model cells to evaluate the performance of both electrode types. The frequency spectra of the cell-free and cell-covered electrodes of the impedance magnitude |Z|, the resistance R, and the capacitance C are shown in Fig. III-23 together with their respective normalized presentation.

Impedance magnitude |Z|. The |Z| spectra of the cell-free PDT and 8W10E electrodes differ in two main aspects (Fig. III-23 A). First, the frequency-independent constant region, to which R_{bulk} is fitted, is considerably lower for 8W10E electrodes (range: ~ 30 kHz – 100 kHz), than for PDT electrodes (range: ~ 500 Hz – 100 kHz). Accordingly, R_{bulk} has a value of (2610 ± 80) Ω on PDT and (288 ± 6) Ω on 8W10E electrodes (Tab. III-9). Secondly, despite the smaller electrode area, the capacitive region of the PDT electrode spectrum is shifted towards significantly lower frequencies (~ 10 Hz – 50 Hz) compared to the 8W10E electrodes (~ 10 Hz – 10 kHz). This is well reflected in the parameter A_{cpe-c} representing the interface capacitance of the electrode. A_{cpe-c} reaches an about 25-fold higher value of (440 ± 20)·$\mu F \cdot s^{(n-1)}$/cm² for PDT electrodes than 8W10E electrodes with only (17.3 ± 0.3)·$\mu F \cdot s^{(n-1)}$/cm². The presence of a confluent MDCK-II monolayer increases |Z|. The two spectra of cell-free and cell-covered electrode delineate the frequency region where sensitive ECIS measurements are possible. The spectrum of the cell-covered electrode exhibits a more resistive, approximately constant region

that is dominated by α and R_b, and a capacitive region with a negative slope that is due to C_m. The negative slope at low frequencies is equal to the CPE parameter $n_{cpe\text{-}c}$ (PDT: 0.976 ± 0.003, 8W10E: 0.9452 ± 0.0002, Tab. III-9). While the resistive region of the PDT electrodes covers a wide frequency range from 10 Hz up to 1 kHz, the same region on 8W10E electrode reaches only from 200 Hz to 1 kHz. The lower frequency range of the latter is still dominated by the electrode impedance. Moreover, at frequencies higher than 100 Hz, |Z| generally attains higher values on PDT electrodes. The resistive region, for example, is at a level of around 40 kΩ – 60 kΩ, while being significantly lower on 8W10E electrodes at roughly 10 kΩ – 25 kΩ. These findings are also expressed in the normalized spectrum of |Z|(f) (Fig. III-23 B). Despite its high bulk resistance, the PDT electrodes show a tremendously higher sensitivity over a large part of the spectrum. Their maximum sensitivity is at 400 Hz with a value of 12.5 ± 0.5 for the normalized impedance. By contrast, the maximum sensitivity of 8W10E electrodes was found with an average normalized impedance of 5.09 ± 0.06 at 5 kHz. Particularly in the frequency range below 200 Hz, the impedance of the 8W10E electrodes is determined by the interface capacitance and does not show any sensitivity for the cells. On the other hand, the PDT electrodes show high sensitivity in that region and even frequencies as low as 10 Hz can in principle be used for cell analysis with a sensitivity of 2.2 ± 0.1. However, the normalized spectra of both electrodes share a crossover point close to the maximum of the 8W10E electrodes. Thus, at frequencies higher than 5 kHz, the PDT electrodes display a lower sensitivity due to the relatively high bulk resistance.

Resistance R. The resistance spectra mainly deviate from the impedance magnitude spectra by being shifted to slightly lower frequencies (Fig. III-23 C). This is particularly pronounced on the cell-free 8W10E electrodes. Thereby, the area enclosed by the two spectra gets bigger, which leads to a strongly increased sensitivity and a shift of the sensitivity peak towards lower frequencies compared to the impedance magnitude (Fig. III-23 D). The maximum sensitivity of the 8W10E electrodes in the resistance spectrum is at 630 Hz with a value of 13.1 ± 0.2. The maximum value of the normalized resistance for PDT electrodes (13.2 ± 0.5) does not differ much from the normalized impedance. However, the peak is shifted to lower frequencies and exhibits a relatively broad maximum at 160 Hz.

Capacitance C. The capacitance of the cell-free 8W10E electrodes is almost constant between about 50 and 70 nF over the whole frequency range with a small bend at the high frequency end of the spectrum (Fig. III-23 E). It shows a slightly negative slope, which is in accordance with $n_{cpe\text{-}c}$ deviating from 1 (Tab. III-9). The presence of the cells leads to a decrease of the capacitance at frequencies higher than 200 Hz to a level of around 8 nF. This is roughly

the frequency range where the impedance magnitude of the cell-free and the cell-covered electrode start to deviate as well. The PDT electrode capacitance can be divided into three sections. It is considerably higher and exhibits values between 500 and 600 nF in the constant frequency range from 10 Hz to 250 Hz. In the second section between 250 Hz and 10 kHz, the initially minor negative slope becomes steeper. The third section ranges from 10 kHz to 100 kHz and exhibits an even more negative slope. Below 20 Hz, the capacitance of the cell-covered PDT electrode shows values that are slightly higher than those of the cell-free electrode. At higher frequencies, the capacitance drops down to $2 - 3$ nF, and shows a subtle bend at the high frequency end of the spectrum. Since the capacitance of the cell-free electrode is higher than the capacitance of the cell-covered one, the normalized capacitance shows a minimum at the most sensitive frequency. The minima of both electrode types are relatively broad and cover a wide frequency range from approximately 5 kHz to 100 kHz (8W10E) and from 800 Hz to 16 kHz (PDT), respectively (Fig. III-23 F). The minimum is considerably lower on PDT electrodes (0.019 ± 0.002) in comparison to 8W10E electrodes (0.169 ± 0.002). PDT electrodes thus show a higher sensitivity over almost the entire frequency range.

Tab. III-9: Electrode parameters of PDT and 8W10E electrodes obtained by manual fitting (N = 8, ± SEM). The following parameters were predetermined before the fitting process (PDT | 8W10E): $A_{el} = 1.30 \cdot 10^{-3}$ cm² $| 5 \cdot 10^{-3}$ cm², $A_{prs} = 0.28 | 0.24$ nF·s$^{(n-1)}$/cm², $n_{prs} = 0.945 | 0.981$, $A_{cpe-r} = 2.1 |$ n/a mF·s$^{(n-1)}$/cm², $n_{cpe-r} = 0.2 |$ n/a.

parameter	PDT	8W10E
A_{cpe-c} / μF·s$^{(n-1)}$/cm²	440 ± 20	17.3 ± 0.3
n_{cpe-c}	0.976 ± 0.003	0.9452 ± 0.0002
R_{bulk} / Ω	2610 ± 80	288 ± 6
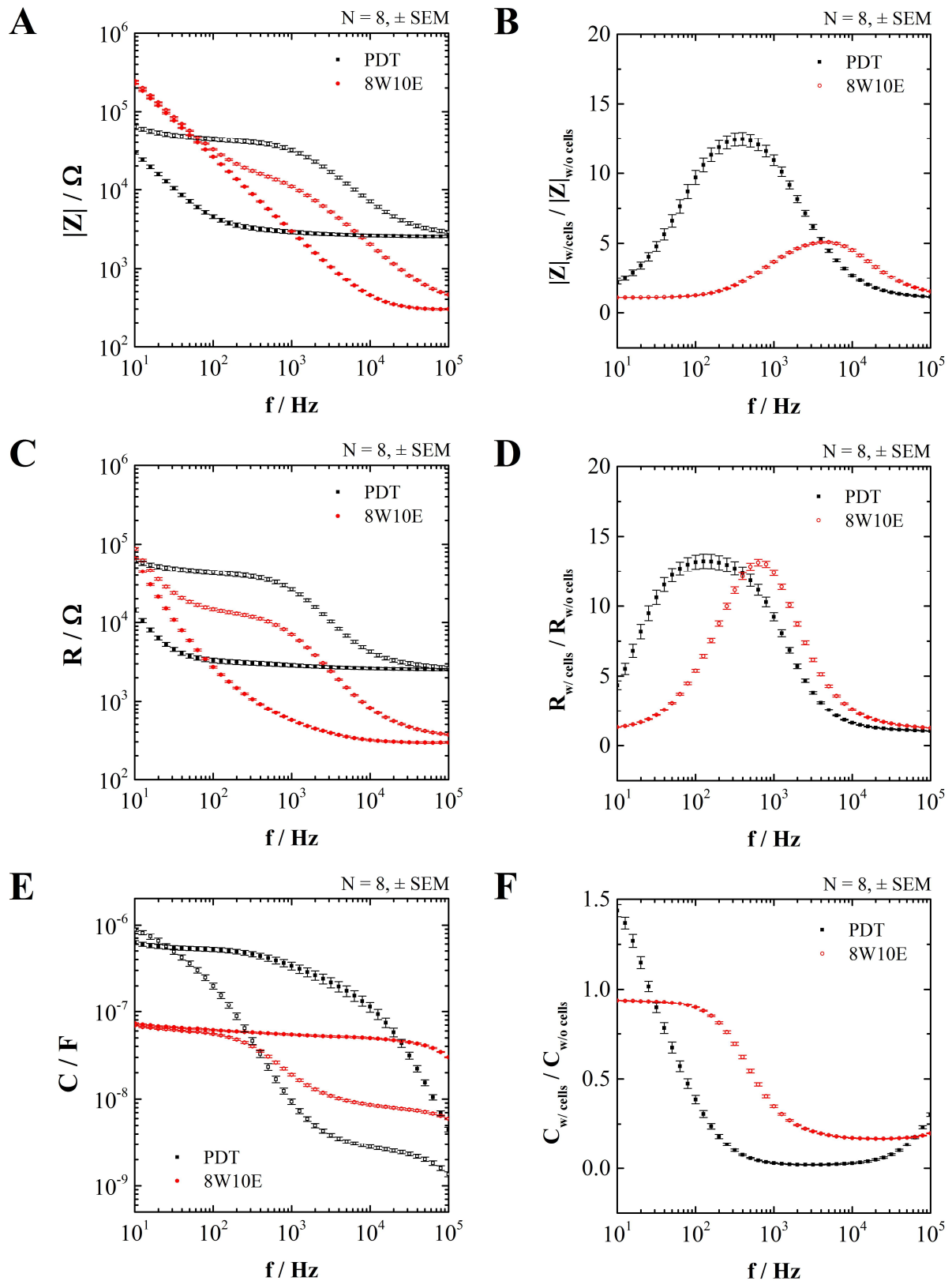
Fig. III-23: Frequency spectra of |Z|, R, and C comparing PDT to 8W10E electrodes, measured in cell culture medium. **(A)** Impedance magnitude |Z|, **(B)** normalized impedance magnitude, **(C)** resistance R, **(D)** normalized resistance, **(E)** capacitance C, **(F)** normalized capacitance. In (A), (C), and (E), full symbols (■, ●) correspond to cell-free electrodes and empty symbols (□, ○) to cell-covered electrodes. The cell-covered electrodes were recorded 40 h after confluently seeding MDCK-II cells. T = 37 °C

The results described above show that the PDT electrodes exhibit two opposing trends compared to the 8W10E electrodes that both influence their sensitivity in cell-based assays: The high interface capacitance works in favor of the sensitivity, while the high bulk resistance is detrimental. Due to the hydrogel properties of the electrode material PEDOT:PSS, the electrolyte interpenetrates the conducting polymer. Thus, an extremely high effective surface area is created, which enhances the measured interface capacitance.[46,107] Therefore, the sensitivity is increased by reducing the impedance of the electrode in the capacitive low frequency region of the spectrum. Karimullah et al. reported a value of A_{cpe-c} = 320.8 µF·s$^{(n-1)}$/cm² for spin coated PEDOT:PSS, which is in good agreement with the results of this work (A_{cpe-c} = 440 ± 20 µF·s$^{(n-1)}$/cm²).[65] The disadvantage of using PEDOT:PSS as electrode material instead of gold is its high resistivity. The screen printing ink used for the fabrication of the PDT arrays is specified having a surface resistivity of 700 Ω/sq. A crude estimate using this value and the electrode geometries of the PEDOT:PSS-based WE and CE together with the respective silver leads yield a lead resistance of around 1200 Ω (cf. Fig. V-1 and Eq. 55, supplementary information). The resistance of the silver leads is negligible. Considering R_{bulk} for the average freshly prepared PDT electrodes of (1800 ± 100) Ω (cf. 2.3.1.6), the constriction resistance then accounts to about 600 Ω. Due to manufacturing related variations and long-term electrode drift, the actual lead resistance of individual electrodes can be much higher. Taking into account this chapter's fit results for R_{bulk} of (2610 ± 80) Ω and assuming a constant constriction resistance of 600 Ω, the calculated lead resistance is in the order of 2 kΩ. This high lead resistance affects the level of the constant region in the |Z| and R spectrum and is thus unfavorable for the sensitivity by causing a high electrode impedance at high frequencies.

When using commercial ECIS electrode arrays, the barrier function and cell-substrate interactions of cells are usually analyzed at frequencies below 5 kHz, using either the magnitude |Z| or the real part R of the impedance. Due to the high sensitivity in the |Z| spectrum, the PDT electrodes allow access also to the low frequency region between 10 Hz and 200 Hz, where the impedance of the 8W10E electrodes is entirely dominated by the electrode and cannot be used for cell analysis. Like the impedance magnitude, the resistance is also much more sensitive in the low frequency region. This should allow for a highly sensitive analysis of cell barrier function as well as the cell-substrate interactions. On the other hand, both quantities |Z| and R show a slightly lesser sensitivity above a certain threshold frequency. In the high frequency region, the capacitance is often the quantity of interest. Cell adhesion and cell proliferation are commonly quantified by following the capacitance at 32 kHz or 40 kHz due to its linear

correlation with the fractional cell coverage of the electrode at that frequency.[158] At 32 kHz (40 kHz), the capacitance of the cell-covered 8W10E electrodes is 17.0% ± 0.2% (17.2% ± 0.2%) of the value of the cell-free electrode, while the PDT electrodes drop down to 1.5% ± 0.5% (1.6% ± 0.6%). Even in the high-frequency region, the PDT electrodes show a much higher sensitivity than the 8W10E electrodes, when the capacitance is considered instead of the impedance magnitude or the resistance.

What remains to be discussed is the strong disparity between the nearly ideal capacitance spectrum of the cell-free 8W10E electrodes and the complicated nature of the PDT capacitance spectrum. A close inspection of the fit in comparison with the raw data revealed that the nearly constant region between 10 Hz and 250 Hz corresponds to the interface capacitance of the electrode (cf. Fig. V-2, supplementary information). The intermediate region (250 Hz – 10 kHz) does not fit to the model and its origin is currently unknown. The steep region between 10 kHz and 100 kHz fits well to the experimentally determined parasitic impedance. Simulations disclosed that the parasitic impedance is emphasized by high R_{bulk} (cf. Fig. V-3, supplementary information). We therefore concluded that the high R_{bulk} value of the PDT electrodes leads to the strong presence of the parasitic impedance. Nevertheless, due to the high base capacitance of the electrode, the sensitivity still surpasses that of the 8W10E electrodes.

It might be important to verify that the described results are not just caused by a change of the cell behavior, i.e. by altered cell parameters. Therefore, simulations were performed, using the parameters of the cell-free PDT and 8W10E electrodes, while keeping the cell parameters constant. The results confirmed that even for identical dielectric structures of the cells on the electrode surface, the electrodes themselves induced the observations discussed in this chapter (cf. Fig. V-4, supplementary information).

The results of this chapter can be summarized as follows. In comparison to the 8W10E electrodes,

- the PDT electrodes show a higher interface capacitance due to the hydrogel properties of PEDOT:PSS, which is favorable for the sensitivity.
- the PDT electrodes show a higher bulk resistance R_{bulk} due to the high resistivity of PEDOT:PSS, which is detrimental for the sensitivity.
- the impedance magnitude and the resistance of the PDT electrodes exhibit a substantially higher sensitivity in cell-based assays at low frequencies, where the cell-cell and the cell-surface interactions are analyzed.
- the capacitance of the PDT electrodes is significantly more sensitive at high frequencies, which are relevant for adhesion and proliferation studies.

2.3.3   Cell Adhesion and Spreading

2.3.3.1   Time Course of Impedance Magnitude, Resistance and Capacitance

This chapter discusses the adhesion and spreading characteristics of MDCK-II cells on PDT and 8W10E electrodes in a comparative manner. Fig. III-24 shows the time courses at different commonly used frequencies, normalized to the last time point before confluent cell seeding (t = 0). The curves of $|Z|$ and R at 400 Hz exhibit similar shapes (Fig. III-24 A and B). The 8W10E electrodes show a transient maximum of $|Z|_{400\ Hz}$ norm. = 2.8 ± 0.6 ($R_{400\ Hz}$ norm. = 12.1 ± 0.3) ~ 12 h after cell seeding, before going back to a constant level of $|Z|_{400\ Hz}$ norm. = 2.16 ± 0.04 ($R_{400\ Hz}$ norm. = 8.7 ± 0.3). The maximum of the PDT electrodes is shifted to ~ 16 h and shows a highly enhanced signal change to $|Z|_{400\ Hz}$ norm. = 37 ± 3 ($R_{400\ Hz}$ norm. = 33 ± 2). The decline to a constant value of $|Z|_{400\ Hz}$ norm. = 13.5 ± 0.6 ($R_{400\ Hz}$ norm. = 14.1 ± 0.7) occurs on an apparently longer time scale. The time courses of $|Z|$ and R at 4 kHz are again similar to the previously described ones, but with the transient maxima occurring at earlier time points (8W10E: t ~ 10 h, PDT: t ~ 13 h for $|Z|$) (Fig. III-24 C and D). At the maximum, $|Z|_{4\ kHz}$ norm. reaches values of 5.4 ± 0.2 (8W10E) and 9.6 ± 0.3 (PDT), whereas $R_{4\ kHz}$ norm. is 5.6 ± 0.3 (8W10E) and 6.0 ± 0.2 (PDT). The electrodes show almost overlapping resistance time courses at that frequency with final constant levels around 3.4 ± 0.2 (8W10E) and 3.8 ± 0.1 (PDT). Towards the end of the observation time the final $|Z|_{4\ kHz}$ norm. value for 8W10E electrodes (4.2 ± 0.1) is in the same order as the corresponding $R_{4\ kHz}$ norm. value, whereas it is significantly higher for PDT electrodes (6.3 ± 0.2). At 32 kHz, the $|Z|$ maximum for 8W10E electrodes is again shifted towards an earlier time point (~ 8 h, $|Z|_{32\ kHz}$ norm. = 3.2 ± 0.1) (Fig. III-24 E). By contrast, the curve shape of the PDT electrodes is slightly altered and exhibits a broad maximum with a central point at ~ 12 h ($|Z|_{32\ kHz}$ norm. = 2.58 ± 0.06). Rather constant values (8W10E: 2.23 ± 0.08, PDT: 1.83 ± 0.04) are reached after roughly 25 h in both cases. The capacitance at 32 kHz shows an immediate linear decrease for both electrode types before reaching a constant level at 0.045 ± 0.003 (PDT) and 0.237 ± 0.008 (8W10E), respectively (Fig. III-24 F). It drops much faster on PDT electrodes, whereas the final value, indicating that the surface is completely covered with spread cells, is reached after about 6 h on both electrodes. This leads to the conclusion that the seemingly different kinetics are due to the unequal sensitivities at that frequency.
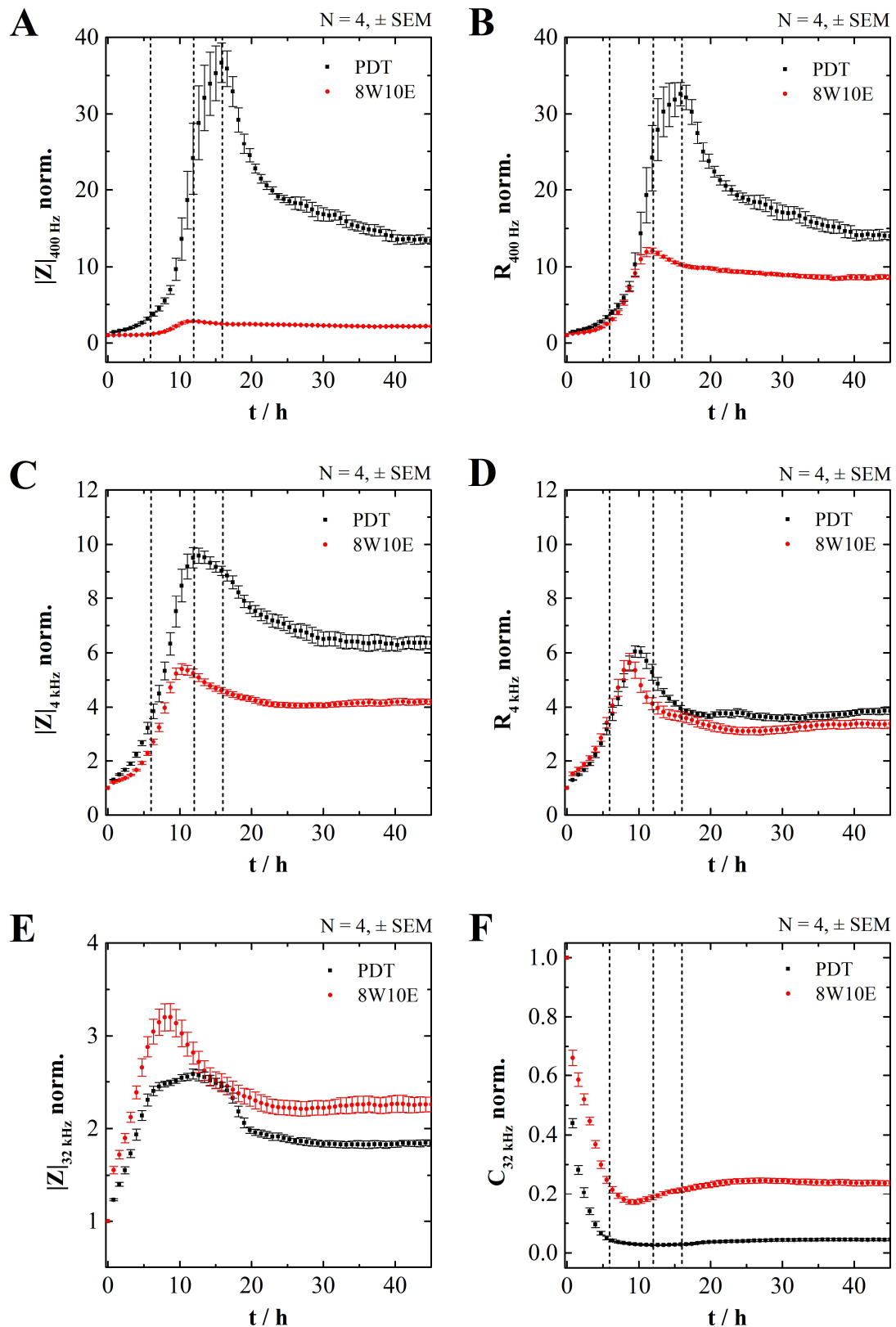
Fig. III-24: Cell adhesion and spreading of MDCK-II cells followed at different frequencies. The time courses were normalized to the time point before cell seeding (t = 0). The vertical lines indicate the time of the fully adhered and spread cells (6 h), the maximum R at 400 Hz on 8W10 electrodes (12 h), and on PDT electrodes (16 h). **(A)** |Z| norm. at 400 Hz. **(B)** R norm. at 400 Hz. **(C)** |Z| norm. at 4 kHz. **(D)** R norm. at 4 kHz. **(E)** |Z| norm. at 32 kHz. **(F)** C norm. at 32 kHz. Only results from one cell preparation are directly compared. T = 37 °C

Wegener[168] correlated the resistance at 400 Hz to the formation of tight junctions between adjacent MDCK-II cells by staining for the tight junction-associated protein ZO-1. The protein was shown to be present at the cell-cell junctions after 10 h when R had reached its maximum value, whereas only scarce ZO-1 staining was found after 4 h. At that time, the capacitance at 40 kHz had dropped to its final level, which is indicative for completely attached and spread cells. Judging by the time course of C at 32 kHz, we found both electrode types entirely covered with spread cells after 6 h. This is also the time point when R at 400 Hz shows a steep increase, revealing the beginning establishment of cell-cell contacts. The formation of the tight junctions on 8W10E electrodes is complete after 12 h, while on PDT electrodes they are not fully established until 16 h after seeding. The subsequent decrease is caused by cell proliferation, i.e. an increased number of cells per cm² and thus more parallel current pathways through the cell layer along the cell-cell contacts. The subtle increase during the first 6 h is attributed to the restricted current flow underneath the spreading cells.[168] Taken together, the attachment and spreading kinetics seem to be independent of the electrode type, while the complete establishment of the cell layer takes more time on PDT electrodes.

2.3.3.2   Analysis of the Cell Parameters C_m, α, and R_b during the Adhesion and Spreading of MDCK-II Cells

In accordance with the frequency spectra discussed in chapter2.3.2, the time courses of |Z| and R clearly show a highly enhanced signal change on PDT electrodes at low frequencies (here at 400 Hz), which is less pronounced at intermediate frequencies (here at 4 kHz). At 32 kHz, the signal change of the impedance magnitude is slightly higher on 8W10E electrodes, while being significantly more pronounced when considering the capacitance. This is also supported by the sensitivity spectra in Fig. III-23. To elucidate the degree to which either the sensitivities of the electrodes or morphological differences of the cells contribute to the signal change, the cell parameters according to the ECIS model were determined at several time points (Fig. III-25). The first time point was fitted 6 h after seeding the cells, when the cell layer was fully established. The membrane capacitance C_m shows similar time courses for both electrode types (Fig. III-25 A). 6 h after cell seeding it starts at values well below 3 µF/cm² and then slowly increases to a maximum of over 4 µF/cm² after 40 h. The α curves start at a minimum value and cover a transient maximum, of which the time point coincides with the respective maximum of the impedance magnitude at 400 Hz (Fig. III-25 B). It is noteworthy that the α values of the PDT electrodes before 10 h and after 20 h are significantly lower than those of the 8W10E electrodes, while the maximum is higher. R_b shows the most significant difference between

both electrode types (Fig. III-25 C). After 6 h, the cells on both electrode types take on low values of well below 10 $\Omega \cdot cm^2$. However, while R_b remains largely constant after 12 h at approximately 40 $\Omega \cdot cm^2$ on 8W10E electrodes, the cells show an immense increase to over 130 $\Omega \cdot cm^2$ when growing on PDT electrodes. Eventually, they also reach a final value of around 40 $\Omega \cdot cm^2$ after 40 h. The dielectric cell parameters of the fully established cell layer after 40 h are summarized in Tab. III-10 and Fig. III-26.
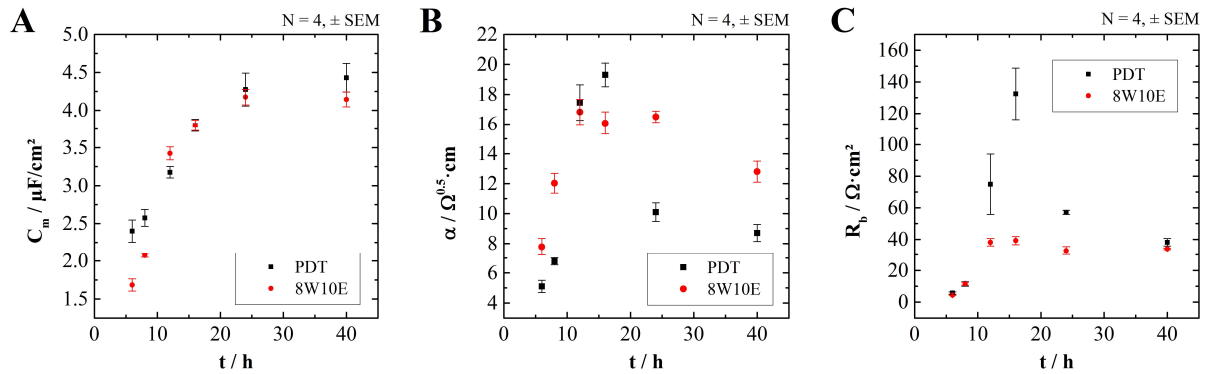
Fig. III-25: Fitted cell parameters C_m, α, and R_b of 8W10E and PDT electrodes (6, 8, 12, 16, 24, 40 h after seeding). **(A)** Membrane capacitance C_m, **(B)** subcellular cleft resistance α, **(C)** paracellular resistance R_b. Only results from one cell preparation are directly compared. T = 37 °C

Tab. III-10: Fit results of impedance recordings of a confluent MDCK-II cell layer 40 h after seeding on PDT electrodes in comparison with 8W10E electrodes (N = 4, ± SEM). Raw data was analyzed by the ECIS-model. T = 37 °C

parameter	PDT	8W10E
C_m / $\mu F/cm^2$	4.4 ± 0.2	4.2 ± 0.1
α / $\Omega^{0.5} \cdot cm$	8.7 ± 0.6	12.8 ± 0.7
R_b / $\Omega \cdot cm^2$	38 ± 2	33.9 ± 0.4
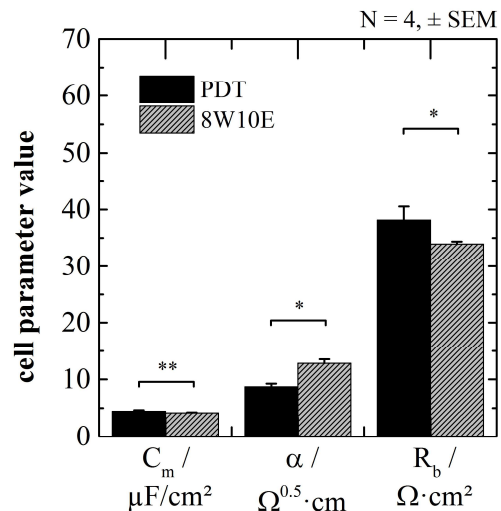
Fig. III-26: Graphical depiction of the fit results from Tab. III-10. * significantly different, ** not significantly different (p < 0.05), T = 37 °C

MDCK-II cells are known to develop microvilli on their apical surface.[121-122] The presence of microvilli increases the surface area of the cell membrane and thus the membrane capacitance. We can therefore assume that the rise in C_m shown in Fig. III-25 A is correlated to the formation of microvilli on the confluent cell layer, which is complete after about 24 h. Generally, if the

electrode material did not have any influence on cell physiology, the cell parameters would be independent of the electrode type. Accordingly, C_m does not show any major deviations between cells growing on PDT or 8W10E electrodes. The situation is somewhat different for R_b and α. The time course of R_b fits very well to the time course of the resistance at 400 Hz, which supports the common understanding that R represents the barrier properties of a cell layer at low frequencies.[168] The initial and final R_b values are not significantly different for both electrode types. There are, however, large differences especially between 12 h and 16 h. Moreover, α takes on higher values during the same time span, while being significantly lower before and after that. Since both parameters depend on the cell radius, we presume that on PDT electrodes, less cells take part in the initial attachment, so that the remaining adhered cells have more room for spreading (cf. 2.3.3.3). As a consequence, the cells become larger and thereby restrict the current flow through the cell layer as discussed before. By cell growth the number of cells eventually increases over time until a final R_b value is reached that is not significantly different from the one of the cells on 8W10E electrodes. According to Eq. 22 the lower final α value of cells growing on PEDOT:PSS can principally be caused by alterations of the height of the subcellular cleft h, the resistivity of the electrolyte in the subcellular cleft ρ, and the cell radius r. In a study from 2011, Eisenberg et al. reported a correlation between substrate stiffness and cell adhesion and spreading.[169] They found that alveolar epithelial cells (AEC) seeded on soft substrates take more time to spread compared to those on stiffer substrates. The cells were also shown to exhibit an altered expression of the ECM and smaller focal adhesions. PEDOT:PSS is much softer than metals, particularly when hydrated.[170] It is therefore convenient to assume that a similar mechanism applies for MDCK-II cells growing on PEDOT:PSS. Smaller focal adhesions increase the average distance between cell and electrode and thereby reduce the associated resistance and its quantitative parameter α. However, the surface topography of PEDOT:PSS cannot be entirely excluded to affect the lateral conductivity in the subcellular cleft as well. While the surface of the gold electrodes is smooth, spin coated and electropolymerized PEDOT:PSS layers have been shown to exhibit a highly porous nanostructure with pore dimensions in the order of 15 – 30 nm.[60,103,171-172] We can assume that the general morphology of screen printed PEDOT:PSS is very similar. Thus, the distance between the cells and the electrode is an averaged value that includes the pore depth as well as the superficial distance. If this average distance is higher than the uniform distance of cells to the gold electrode surface, α is lower. Furthermore, the role of the ion conduction that occurs inside the polymer is not clear (cf. II.2.3). This additional conduction path could affect α by increasing the overall conductance beneath the cell layer.

2.3.3.3   Optical Study of Adhesion and Spreading

In order to gain further insight into the cellular adhesion and spreading mechanisms, the first 7 h after cell seeding were followed by phase contrast microscopy 20 min, 70 min, 160 min, 270 min, 350 min, and 440 min after seeding (8W10E: Fig. III-27, PDT: Fig. III-28). When the cells have settled after 20 min and start to adhere to the surface, they are initially spherically shaped like in suspension. After 70 min, the images show that some cells already start to spread, while others are still rounded or even lying on top of the adhered cells. At that time point, the cell coverage of the 8W10E electrodes seems more homogeneous (Fig. III-27), while the PDT electrodes exhibit gaps within the cell layer (see white arrows, Fig. III-28). Those gaps, however, are covered after 160 min and the cells seem fully spread on both electrode materials. During the next 5 h, the cell-cell contacts show up more distinct, possibly indicating the beginning formation of tight junctions, which is in good agreement with the time course of R at 400 Hz, as discussed above.
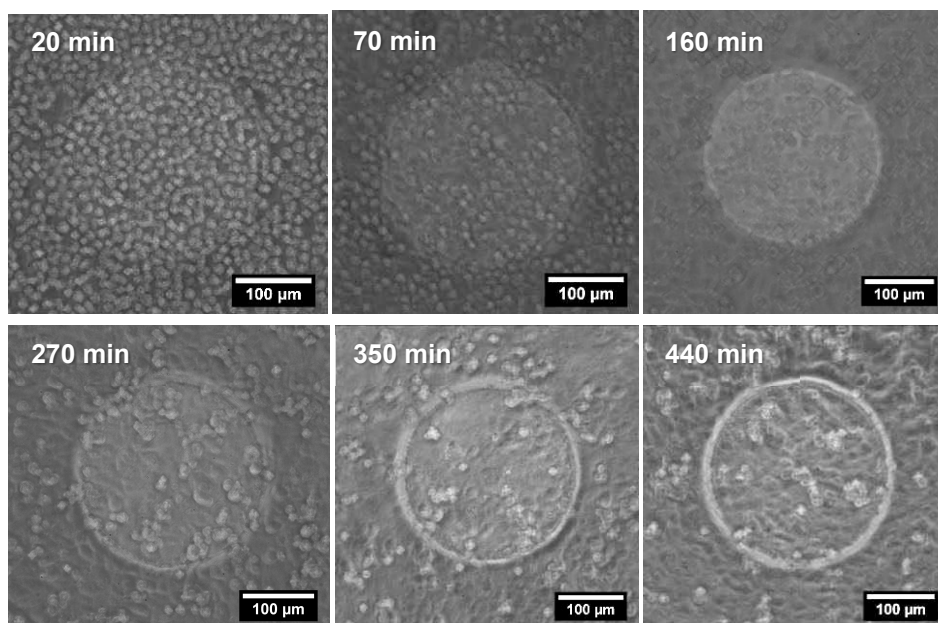

Fig. III-27: Phase contrast images of MDCK-II cells during adhesion and spreading on one of the 10 parallel gold electrodes of an 8W10E electrode array. *Upper row:* 20 min, 70 min, 160 min after seeding. *Lower row*: 270 min, 350 min, 440 min after seeding. The images were corrected for improved display (contrast: +20%, brightness: +10%). T = 37 °C
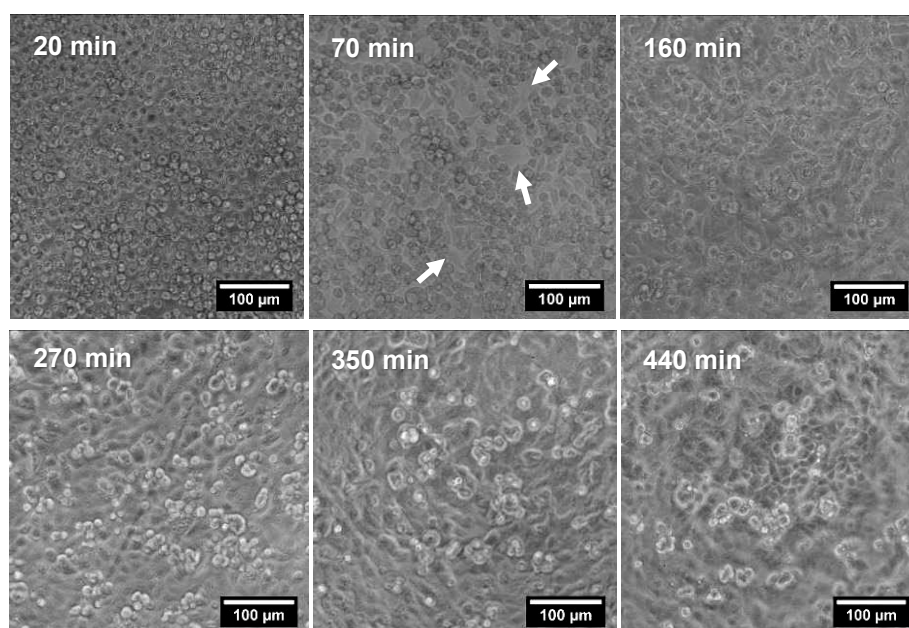
Fig. III-28: Phase contrast images of MDCK-II cells during adhesion and spreading on a PDT electrode. *Upper row:* 20 min, 70 min, 160 min after seeding. *Lower row*: 270 min, 350 min, 440 min after seeding. The white arrows indicate gaps in the cell layer. The images were corrected for improved display (contrast: +20%). T = 37 °C

The gaps showing up in the cell layer on PDT electrodes after 70 min support the assumption that less cells take part in in the initial attachment of the cells despite using the same seeding density, leading to a lower overall number of cells and, thus, transiently a higher R_b value. Not yet or loosely attached cells were supposedly detached from the surface while carrying the electrode arrays from the incubator to the microscope. The size of the cells is, however, hard to determine on the phase contrast images. To verify the theory of less adhered but larger cells, the cells have to be stained in further studies and investigated with higher resolution microscopy techniques like CLSM on both electrode types. The previously mentioned study by Eisenberg et al. on the dependence of cell spreading on the substrate stiffness, however, fits well to this explanation.[169] Brown et al. published analogous results for cell adhesion, stating that less cells adhere to a surface if the stiffness is decreased.[173] The elastic modulus[e] of a hydrated PEDOT:PSS layer is relatively inhomogeneous and varies between 0.3 and more than 50 MPa in relation to the surface topography.[170] This inhomogeneity of the substrate stiffness across the electrode area could lead to irregular cell adhesion and spreading and thus cause the observed time course. We propose that, on PDT electrodes, cell adhesion and spreading on the relatively soft PEDOT:PSS is delayed for a certain proportion of cells, while others start to spread earlier

---

[e] elastic modulus = stress / strain

and thereby block the electrode surface. This leads to an initially smaller number of large cells covering the electrode. The cell layer eventually reaches a steady state by cell proliferation. The low substrate stiffness of PEDOT:PSS can explain both the lower α values after 40 h and the transient peaks of α and R_b between 12 and 16 h after cell seeding.

2.3.3.4   Conclusion

In practice, the main difference between PEDOT:PSS and gold electrodes during adhesion is that the cells take more time to reach a steady state with constant cell parameters. In this study, we found the MDCK-II cell signal on the PDT electrodes to be stable after about 40 h, while on 8W10E gold electrodes it was on a steady level more than 10 h earlier. This should be kept in mind when using previously seeded cells for further testing. It is advisable to seed the cells at least 48 to 72 h before starting an experiment to ensure the cell layer is already in its steady state. In order to get results that are more comparable to those obtained with gold electrodes or cells on other substrates with high stiffness, an appropriate coating for the electrodes has to be found. In preliminary experiments, we found that gelatin coating reduces the peak height during cell spreading and shortens the time until the cell layer is in its steady state. On the other hand, soft substrates can be biologically more relevant than metals if they provide an elasticity that resembles their natural environment in an organism more closely. As an example, Engler et al. found that in contractile muscle cells, myosin and actin filaments emerge only on polymer gels with stiffness typical of normal muscle, not on much softer or stiffer gels.[174] This substrate dependence may become particularly important for the impedimetric investigation of normal cells. They tend to show much stricter limitations than cancer cells regarding their capability to proliferate on substrates with suitable rigidity.[175-176] The elastic modulus of tissue varies from several hundred Pa for brain and liver to more than 12 kPa for muscle.[177] On the other hand, the elastic moduli of tissue culture plastic or glass are in the GPa range, so that cells *in vitro* often grow in a highly nonphysiological mechanical environment. Independent of the electrical and optical properties, PEDOT:PSS electrodes may thus become a valuable tool to tune the substrate rigidity for impedimetric cell assays.

2.3.4   Cytochalasin D Treatment

In order to investigate the way cells growing on PDT electrodes react to biochemical manipulation in comparison with cells seeded on gold electrodes, MDCK-II cells were treated with cytochalasin D as model compound. The fit results of MDCK-II cells treated with 5 µM cytochalasin D (CytD) are summarized in Tab. III-11 and graphically compared to the untreated

cell layer from the previous chapter in Fig. III-29. The cell parameters of the untreated and the CytD treated cells were determined 40 h after seeding and 1 h after the addition of CytD, respectively. CytD does not have any effect on the membrane capacitance C_m. However, α and R_b are perceptibly reduced and also show statistically significant changes. While the α value of untreated cells is lower on PDT electrodes, it exhibits a slightly lower value on 8W10E electrodes after CytD treatment. The difference of the R_b values is more severe. The R_b value of cells grown on PDT electrodes is more than double the value of cells on 8W10E electrodes after CytD exposure.

Tab. III-11: Fit results of impedance recordings of MDCK-II cells after treatment with 5 µM cytochalasin D for 1 hour at 37 °C on PDT electrodes in comparison with 8W10E electrodes (N = 4, ± SEM).

parameter	PDT	8W10E
C_m / µF/cm²	4.1 ± 0.1	3.8 ± 0.1
α / $\Omega^{0.5} \cdot cm$	4.7 ± 0.5	3.7 ± 0.2
R_b / $\Omega \cdot cm^2$	6.4 ± 0.4	2.9 ± 0.1

Fig. III-29: Fit results of impedance recordings of MDCK-II cells after treatment with 5 µM cytochalasin D for 1 hour at 37 °C on PDT electrodes in comparison with 8W10E electrodes (N = 4, ± SEM). * significantly different, ** not significantly different (p < 0.05). The data of the untreated cell layer (cf. Fig. III-26) were added for comparison.

Cytochalasins are a class of mycotoxins that permeate the cell membrane and disrupt the cytoskeleton by inhibition of the actin polymerization.[178-179] Cytochalasin D is a particularly potent member of this group and is known to also manipulate the barrier function integrity of cell layers.[179-181] Several microscopic studies have shown that CytD leads to the aggregation of ZO-1 and both apical and basal populations of actin.[179,182-183] This fits well to the results presented in this thesis. The disruption of the actin belt and aggregation of the tight junction-associated protein ZO-1 causes a strong decrease of R_b by opening up the intercellular junctions. Similarly, CytD has been shown to interfere with focal adhesions that mediate the contact between the actin cytoskeleton and the ECM and thereby reduce the adhesion area and decrease α.[184] Even though CytD also disrupts the actin filaments in the microvilli and inhibits their growth, we did not observe any effect on C_m.[183,185] The membrane surface area seems not to have changed within
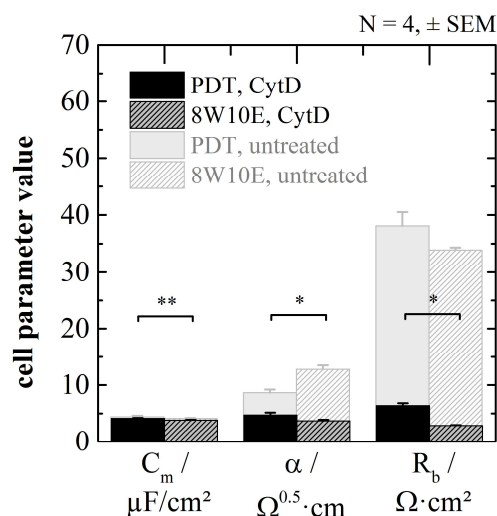
the time scale of the experiment despite of the supposed aggregation of the underlying cytoskeleton. CytD shows a similar impact on cells growing on PDT and 8W10E electrodes. The origin of the differences between the cell parameter values of cells growing on either electrode type is unknown. However, the significant differences in R_b and the fact that α is higher on PDT electrodes after CytD treatment, whereas being lower for untreated cells, indicate some alterations in the physiological properties of the cells. As elaborated earlier, the stiffness of the substrate affects the size of the focal adhesions, which are connected to the actin cytoskeleton (2.3.3).[169] There is a bidirectional push-pull relationship between the substrate and the cytoskeleton that is mediated by the focal adhesions.[177] This means the cells mechanically sense the stiffness of the substrate and regulate downstream signaling in response to that. The effects can be manifold and include altered proliferation, differentiation, apoptosis, or changes in ECM composition, depending on the cell type and the corresponding living tissue *in vivo*. It is, therefore, not surprising that certain deviations between PDT and 8W10E electrodes have been observed in our experiments.

2.3.5   *Proliferation*

Cell proliferation is often studied to examine tumor progression and the potency of cytostatic drugs. In this chapter, the effect of using PEDOT:PSS as substrate instead of gold in an impedimetric proliferation assay was investigated. The capacitance at 32 kHz was followed as a measure for the proliferation of MDCK-II cells on PDT and 8W10E electrodes over time (Fig. III-30). Both curves show an almost linear decline before remaining at a constant level after about 55 h (PDT) or 40 h (8W10E), respectively. The corresponding values of the half-maximum electrode coverage $t_{1/2}$ are (21 ± 3) h for PDT ($\pm$ SEM, N = 7) and (17 ± 2) h for 8W10E electrodes ($\pm$ SEM, N = 8). That means, proliferation occurs slightly faster on gold electrodes, but the results do not differ significantly within the error margin ($p < 0.05$). However, the time course of cell growth is distinctly more inhomogeneous on PDT electrodes with a standard deviation of $t_{1/2}$ of 9.1 h. One curve was excluded from the calculation of the average as outlier (cf. Fig. V-5, supplementary information). By contrast, the 8W10E electrodes exhibit only minor deviations between the individual curves and show only about half the $t_{1/2}$ standard deviation (4.6 h).
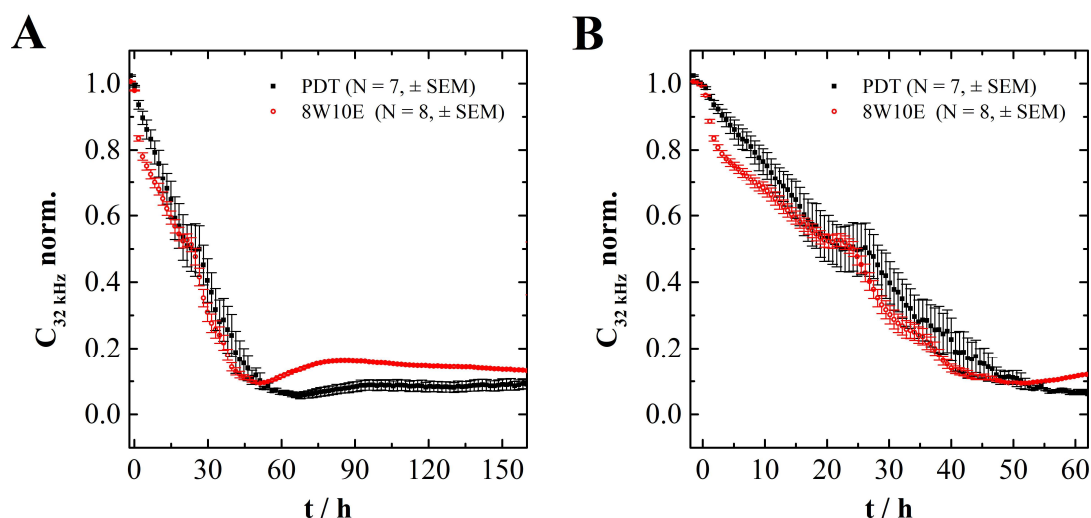
Fig. III-30: Proliferation of MDCK-II cells as recorded by impedance measurements using PDT and 8W10E electrodes. The time course is presented as the normalized capacitance at 32 kHz. The cells were seeded at a density of 20000 cells/cm² at time point t = 0 h. T = 37 °C. **(A)** Time course of the entire time period between t = 0 and t = 162 h. **(B)** Time course of the first 60 h of the experiment.

For proliferation experiments, usually electrodes with a large electrode area are used to enhance the reproducibility. The large electrode area leads to a measurement signal that is averaged over more cells and is less prone to statistical variations in the lateral cell distribution. This is especially important for proliferation measurements as only very few cells are seeded per well and the surface coverage is accordingly low. In this experiment, the cells were seeded at a seeding density of 20000 cells/cm². As a result, on 8W10E electrodes with an electrode area of $5 \cdot 10^{-3}$ cm², there are on average initially 100 cells covering the electrode area. These cells then start to proliferate and cover the electrode over time. By contrast, on PDT electrodes with an electrode area of $1.3 \cdot 10^{-3}$ cm², the initial average cell number on an electrode is only 26. Thus, deviations from this average cell number carry much more weight than on 8W10E electrodes or generally electrodes with larger surface area. This problem could, however, easily be solved by increasing the electrode area of the PDT electrodes. Furthermore, when the standard deviation is reduced by this correction of experimental conditions, a possible difference between the proliferation times on both electrode types could be quantitatively assessed more reliably. In chapter 2.3.3, the dependence of cell adhesion and spreading on the substrate stiffness was discussed. We suggested that cell adhesion and spreading does not occur uniformly across the PDT electrode due to an inhomogeneous surface distribution of PEDOT:PSS stiffness.[170] The same mechanisms may apply here and contribute to the relatively large standard deviation of $t_{1/2}$. In order to exclude or confirm a potential role of the substrate stiffness, electrodes with equal electrode area need to be compared.

2.3.6   Cytotoxicity Assay: Saponin

A cytotoxicity assay was performed on NRK cells using the toxic detergent saponin. Fig. III-31 A and B show the time courses of the normalized impedance magnitude at 32 kHz ($|Z|_{32\ kHz}$ norm.) after saponin addition to a confluent NRK cell layer grown on a PDT and an 8W1E electrode array, respectively. In both plots, $|Z|$ drops down to the value of the cell-free electrode after a certain amount of time, which depends on the saponin concentration. The higher the concentration, the faster is the signal decline. The signals drop down to lower values on 8W1E electrodes as the difference between cell-covered and cell-free electrode at 32 kHz is larger (Fig. III-31 C). Moreover, the time course is slightly different for both electrode types. While on PDT electrodes, the signal changes almost linearly with time except for a 20 µg/mL saponin solution, there is a biphasic decline on 8W1E electrodes with the highest concentration of 75 µg/ml as the only exception. The results are similar in the other experiments that are not shown here. Despite of these differences, the sigmoidal fits yield similar EC_{50} values on both electrode types (Fig. III-31 D). All measurements included, the EC_{50} values is found to be (18 ± 2) µg/mL for PDT and (21 ± 4) µg/mL for 8W1E electrodes (N = 2, $\pm$ SD), which is not significantly different ($p < 0.05$).
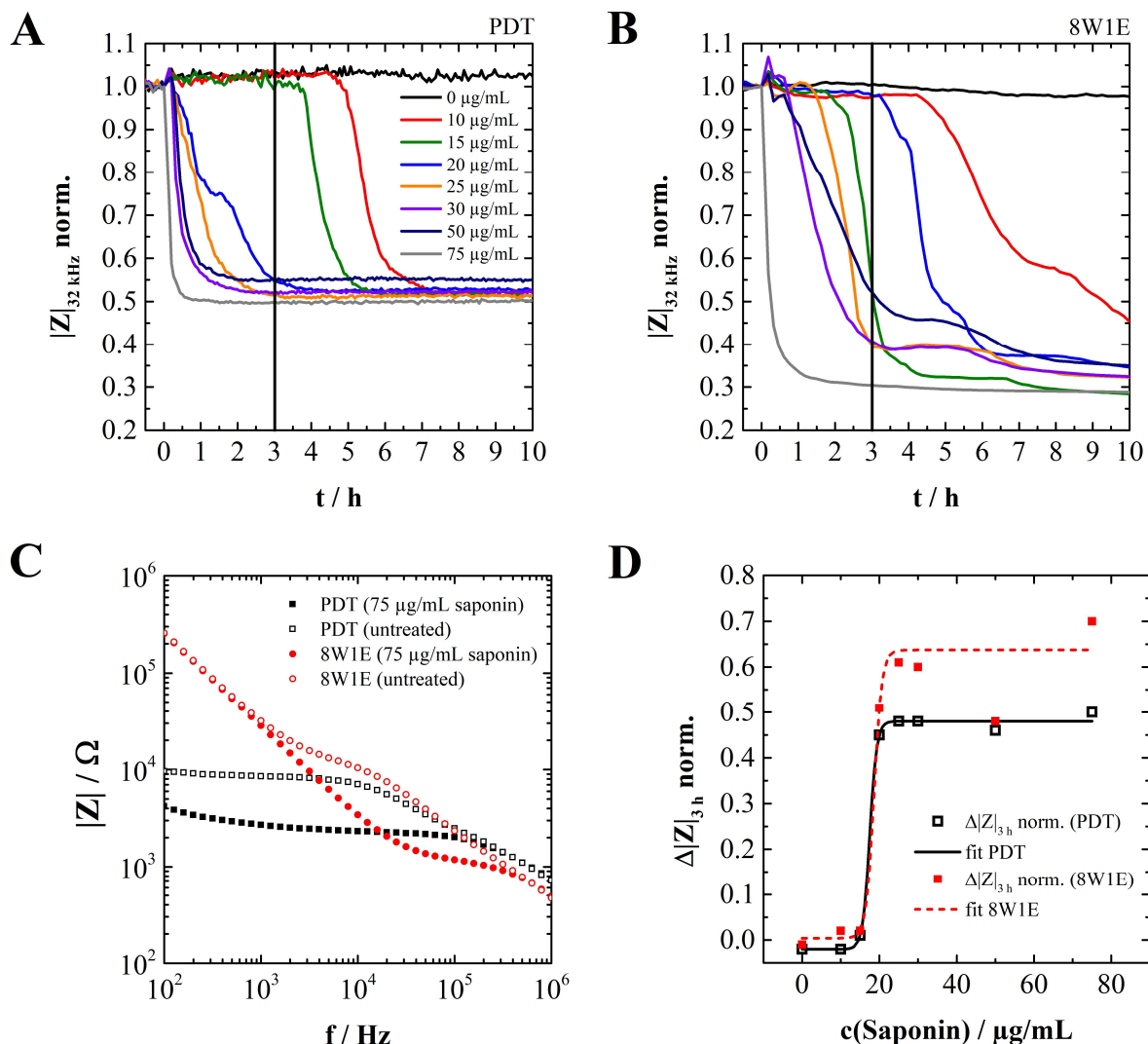
Fig. III-31: Cytotoxicity assay for saponin using confluent NRK cells as model organisms. **(A)** Time course of $|Z|$ at 32 kHz, normalized to the last time point before the saponin addition (PDT). The vertical line shows the 3 h mark, which was used for the determination of the EC_{50} value. **(B)** $|Z|_{32\,kHz}$ norm. for 8W1E electrodes. **(C)** Impedance spectra of a PDT and an 8W1E electrode with confluently grown NRK cells, before ($\square$, $\circ$) and after ($\blacksquare$, $\bullet$) treatment with 75 µg/mL saponin for 3 h. **(D)** Difference between $|Z|_{32\,kHz}$ norm. at $t = 0$ h and at $t = 3$ h, plotted against the saponin concentration. The graph shows a dose-response curve of a typical PDT and an 8W1E electrode array, respectively. The data were fitted in Origin using a Boltzmann fit. The EC50 values for two independent measurements per electrode type are (18 ± 2) µg/mL (PDT) and (21 ± 4) µg/mL (8W1E) ($N = 2$, $\pm$ SD). $T = 37\,°C$

Saponins are known to cause cell lysis and induce cell death, which has been primarily investigated on erythrocytes (red blood cells) and cancer cells.[186] The exact mechanisms are still under dispute and strongly depend on the saponin type and its glycoside side chain. Several pathways have been discussed including membrane disruption by interacting with membrane cholesterol and induction of apoptosis via the mitochondrial apoptosis pathway.[187-188] Both pathways may occur independently of each other and be triggered by different saponins.[189] There are two potential reasons for the discrepancies in the time course data of $|Z|$ after saponin treatment of cells grown on PDT and 8W1E electrodes: a biological and a technical one. The

first one is related to the possible physiological alterations in the cell caused by the lower substrate stiffness of PEDOT:PSS that has been discussed in previous chapters (cf. 2.3.3, 2.3.4, and 2.3.5). Substrate stiffness can affect apoptosis of adherently grown cells.[190] Accordingly, the mechanism of cell death could be altered subject to the softer substrate. As discussed before, this would not necessarily be a disadvantage of the PDT electrodes, rather the mechanical environment is closer to the *in vivo* situation. It should be noted though, that the mechanism of cell death that saponin induces in NRK cells has to my best knowledge not yet been studied. On the other hand, the reason could also be of technical nature and caused by the higher bulk resistance of the PDT electrodes. This is supported by the fact that the EC_{50} values on both electrode types do not differ significantly. The biphasic nature of the time courses of the 8W1E electrodes becomes apparent mainly at $|Z|_{32\ kHz}$ norm. < 0.5, where the high bulk resistance of the PDT electrodes is the bottleneck for the sensitivity and limits the signal drop to a minimum of about 0.5. In that case, it would be crucial to further reduce the bulk resistance of the PDT electrodes to avoid missing certain curve features that might be helpful for more mechanistical studies.

2.3.7 Micromotion

The fluctuations of adherently grown MDCK-II cells before and after fixation with GDA were recorded at 400 Hz using PDT and 8W1E electrodes and compared to the noise of the respective cell-free electrodes. Even without quantitative analysis, differences between both electrode types become apparent (Fig. III-32). Under all conditions (living, fixed, and cell-free), the normalized data $\Delta R(t)$ of the 8W1E electrodes are noisier (Fig. III-32 A) than the PDT electrodes (Fig. III-32 B). Furthermore, a strong drift at the onset of the measurements appears in the recordings of the fixed cells for both electrode types. This drift was largely excluded in the data analysis by taking into account only the last 512 of the overall 612 data points. The PDT electrodes show an initial drift for cell-free electrodes, which is, however, only in the range of a few tens of Ohms. Such a drift of the cell-free 8W1E electrodes is not visible, but would probably be masked by the much more intense electrode noise if it was present. Fig. III-32 C and D depict the detrended time series $R_D(t)$ of 8W1E and PDT electrodes. The respective fluctuations of the living cells are clearly stronger on 8W1E electrodes, ranging from about -250 to 250 Ω, compared to only -50 to 50 Ω on PDT electrodes. However, on PDT electrodes the noise of the fixed cells and the cell-free electrodes is much less prominent in comparison. Remarkably, the noise of the cell-free PDT electrodes even varies only between about -0.1 and 0.1 Ω.
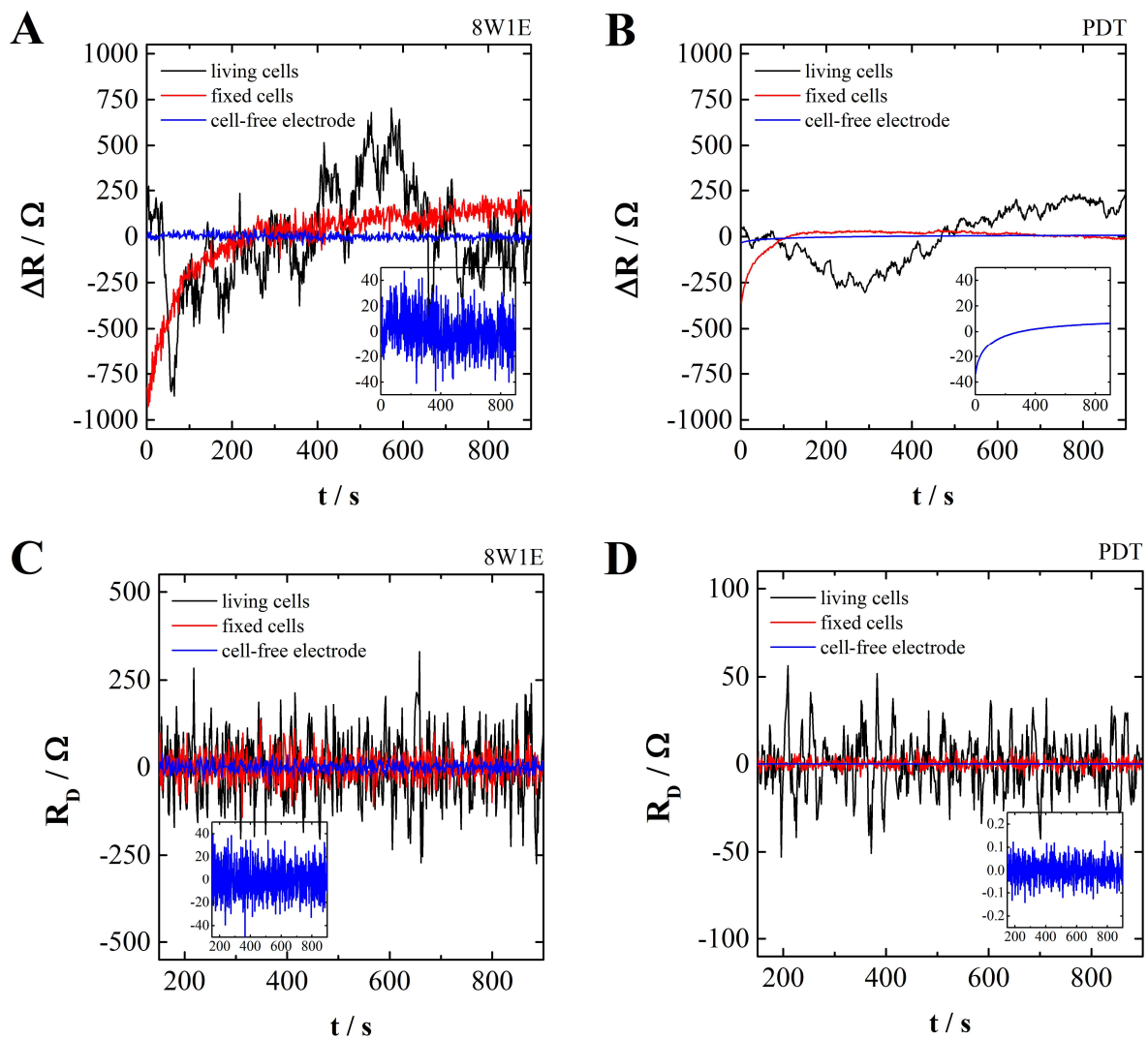
Fig. III-32: Typical time series of MDCK-II cells before fixation, after fixation, and of a cell-free electrode, recorded at 400 Hz. **(A)** Normalized data $\Delta R(t)$ measured with an 8W1E gold electrode and **(B)** with a PDT electrode. The data were normalized by subtracting the mean of the time series from the original time series as described in chapter 1.4.3 **(C)** Detrended time series $R_D(t)$ measured with an 8W1E gold electrode and **(D)** with a PDT electrode. The data were detrended as described for the detrended variance analysis (DVA) in chapter 1.4.3 using a second order polynomial. The insets show the noise of the cell-free electrode in a rescaled plot. (A) and (B) display the full data set, whereas only the last 512 of the overall 612 data points were used for analysis as shown in (C) and (D). T = 37 °C

For a more quantitative evaluation the times series were subjected to power spectrum density (PSD) analysis, detrended fluctuation analysis (DFA) and detrended variance analysis (DVA). All results of the cell-free and cell-covered electrodes before and after treatment with GDA are listed in Tab. III-12 for 8W1E and PDT electrodes. The cell-free electrodes were also treated with GDA but, as expected, did not show any significant alteration and will thus not be discussed any further. For the correlation between the scaling exponents k and D to the noise colors refer to Tab. III-4.

Tab. III-12: Parameters extracted by time series analysis from micromotion data of MDCK-II cells grown onto 8W1E and PDT electrodes, recorded at 400 Hz. A cell coverage of 1 and 0 correspond to a cell-covered and a cell-free electrode, respectively. The parameter k is the scaling exponent of the power spectral density (PSD) of the time series, D is the scaling exponent of the detrended fluctuation analysis (DFA) plot, and V_{32} is the variance of the detrended normalized time series (DVA) (cf. 1.4). N represents the number of measurements. T = 37 °C

cell coverage	electrode type	k (PSD)	D (DFA)	V_{32} / Ω^2 (DVA)	N
before treatment with GDA (± SEM)					
1	8W1E	0.72 ± 0.09	1.07 ± 0.03	$(9 \pm 2)\cdot10^3$	7
0	8W1E	-0.19 ± 0.03	0.49 ± 0.01	$(2.5 \pm 0.2)\cdot10^2$	8
1	PDT	1.7 ± 0.1	1.48 ± 0.04	$(3.7 \pm 0.4)\cdot10^2$	8
0	PDT	0.17 ± 0.04	1.35 ± 0.06	$(2.0 \pm 0.2)\cdot10^{-3}$	8
after treatment with GDA (± SEM)					
1	8W1E	0.16 ± 0.07	0.81 ± 0.05	$(1.22 \pm 0.07)\cdot10^3$	14
0	8W1E	-0.15 ± 0.03	0.49 ± 0.01	$(3.3 \pm 0.2)\cdot10^2$	16
1	PDT	0.62 ± 0.07	1.14 ± 0.02	$(9.5 \pm 0.6)\cdot10^0$	16
0	PDT	0.13 ± 0.03	1.29 ± 0.03	$(2.2 \pm 0.2)\cdot10^{-3}$	15

For living MDCK-II cells recorded with 8W1E electrodes, the PSD function shows a scaling exponent k of 0.72 ± 0.09, which indicates fluctuations resembling pink noise. By comparison, the measurements performed with PDT electrodes yield a significantly higher k of 1.7 ± 0.1, which is much closer to red (or Brownian) noise. After fixation, k drops to 0.16 ± 0.07 and thus almost white noise for 8W1E electrodes and to 0.62 ± 0.07 for PDT electrodes. As would be expected for fluctuations that are ideally only caused by thermal fluctuations, all cell-free electrodes show k values that are close to zero and thus deviate only slightly from white noise. It should be mentioned that the noise of the 8W1E electrodes are slightly 'bluish' (k = -0.19 ± 0.03), while the PDT electrodes noise are more 'pinkish' (k = 0.17 ± 0.04). The statistical significance of this observation is however disputable.

To some extent, the DFA results are similar to those obtained from the PSD. Due to the previously mentioned correlation between k and D (cf. 1.4), the scaling exponent D can be related to the noise colors accordingly. As discussed for the PSD, the DFA indicates pink noise (D = 1.07 ± 0.03) and red noise (1.48 ± 0.04) for 8W1E and PDT electrodes, respectively. After fixation, D is also reduced, but to a lesser extent than k. The value of D = 0.81 ± 0.05 (8W1E) is far off from white noise and D = 1.14 ± 0.02 (PDT) even suggests pink noise. Moreover, while the cell-free 8W1E electrodes show basically ideal white noise (D = 0.49 ± 0.01), the

cell-free PDT electrodes exhibit values that would point to something between pink and red noise (D = 1.35 ± 0.06). This, however, does not match the flat noise pattern that is evident in the detrended time series of the cell-free PDT electrodes (Fig. III-32 D, inset).

The overall fluctuation amplitude, expressed by V_{32}, of living MDCK-II cells grown onto 8W1E electrodes ($V_{32} = (9 \pm 2) \cdot 10^3 \ \Omega^2$) exceeds that of cells on PDT electrodes ($V_{32} = (3.7 \pm 0.4) \cdot 10^2 \ \Omega^2$) by more than an order of magnitude. At first glance, this suggests a remarkably more intense micromotion on the gold electrodes. However, when treating the cells with GDA, V_{32} is only reduced to $(1.22 \pm 0.07) \cdot 10^3 \ \Omega^2$ on 8W1E, but to $(9.5 \pm 0.6) \cdot 10^0 \ \Omega^2$ on PDT electrodes. This means that the base levels of the fluctuations are entirely different. Furthermore, comparing the cell-free electrodes reveals that the noise intensity of the 8W1E electrodes ($V_{32} = (2.5 \pm 0.2) \cdot 10^2 \ \Omega^2$) is more than 5 orders of magnitude higher than the PDT noise ($V_{32} = (2.0 \pm 0.2) \cdot 10^{-3} \ \Omega^2$). It is therefore crucial to refer to the *signal*-to-*noise* ratio (SNR) when trying to evaluate the performance of both electrodes types in a comparative manner. For the calculation of the SNR, the *signal* was defined as the unimpaired micromotion of viable MDCK-II cells and the *noise* is the fluctuation signal of a specified reference. In terms of analytical relevance, the completely fixed cell layer was considered a convenient *noise* reference as it can be expected to give the minimum achievable fluctuation signal intensity as long as the cell layer is still structurally intact.

The SNR was calculated by dividing the respective parameter values obtained for living cells by those yielded after fixation (Tab. III-13). The PSD exhibits a better SNR for 8W1E electrodes, however with considerable error. Taking this error into account, the SNR of both electrode types is roughly in the same order. By contrast, the SNR of the DFA is barely higher than 1 for both electrode types, which would indicate an insignificant difference in the signal between the living and the fixed cells. The best SNRs are obtained using the DVA with 8 ± 2 for 8W1E and even 39 ± 7 for PDT electrodes. The PDT electrodes thus promise to significantly enhance the quality of the micromotion analysis when employing the DVA.

Tab. III-13: Signal-to-noise ratios (SNR) of the PSD scaling exponent k (SNR_k), the DFA scaling exponent D (SNR_D), and the variance V_{32} of the detrended time series used in the DVA (SNR_V) for 8W1E and PDT electrodes.

electrode type	SNR_k (PSD)	SNR_D (DFA)	SNR_V (DVA)
8W1E	5 ± 2	1.3 ± 0.1	8 ± 2
PDT	2.7 ± 0.1	1.29 ± 0.05	39 ± 7

Computing SNR_k and SNR_D may create problems since the parameters of both methods are slopes, which can be both positive and negative. The SNR could thus become negative as it would be the case, for example, if the cell-free 8W1E electrodes were used for the calculation of the SNR_k (Tab. III-12). It may be a convenient alternative to simply use the absolute difference ΔSN between the *signal* and the *noise* value of the respective parameter for the comparison between the electrode types. The results of this consideration are listed in Tab. III-14. By contrast to SNR_k, ΔSN_k is significantly higher using PDT electrodes (1.1 ± 0.2) than when using 8W1E electrodes (0.6 ± 0.2). In case of the DFA, both electrode types exhibit about the same value of $\Delta SD_D = 0.3 \pm 0.08$ and $\Delta SD_D = 0.3 \pm 0.06$ for 8W1E and PDT electrodes, respectively. Comparing the relative errors σ_{rel} of both electrode types and analysis methods and using it as a measure for the sensitivity results in the following order: PSD (PDT) > DFA (PDT) > DFA (8W1E) > PSD (8W1E).

Tab. III-14: Differences between the signal and the noise values (ΔSN) of the PSD scaling exponent k and the DFA scaling exponent D. The relative errors σ_{rel} are denoted in brackets.

electrode type	ΔSN_k (PSD)	ΔSN_D (DFA)
8W1E	0.6 ± 0.2 (0.33)	0.3 ± 0.08 (0.27)
PDT	1.1 ± 0.2 (0.18)	0.3 ± 0.06 (0.20)

The results discussed in this chapter lead to the conclusion that, at a recording frequency of 400 Hz, the PDT electrodes surpass the performance of the 8W1E electrodes due to their lower overall noise level and the thereby improved SNR and ΔSN values. This is particularly true for the DVA, where the SNR of the PDT electrodes is almost 5 times higher. Moreover, the difference ΔSN between living and fixed MDCK-II cells in the PSD scaling exponent k is about twice as high on PDT electrodes compared to the 8W1E electrodes. This provides a broader bandwidth for the discrimination of subtler changes as has been tried to achieve before. Lovelady et al. used PSD analysis, DFA, and the Hurst coefficient, a measure for the fractal

character of time series data, to distinguish cancerous from noncancerous human ovarian surface epithelial (HOSE) cells, however with poor significance.[136] In a publication by Tarantola et al., the fluctuations of three cell lines with varying metastatic potential were analyzed using DFA, PSD, and variance analysis, recorded with both ECIS and QCM in a comparative manner.[137] The correct order of invasiveness as determined with a classical migration assay could, however, only be confirmed with the QCM technique. Both techniques showed merely subtle changes in the analysis parameters, the variance analysis of the ECIS recordings still being the most sensitive method. Opp et al. also found that cytochalasin B acting on confluent HUVECs displays the strongest effect on the variance of the ECIS time series compared to the PSD and the Hurst coefficient.[139] This is in good agreement with our findings, where the variance based analysis (DVA) shows the best sensitivity.

DFA and PSD analysis both describe the frequency behavior of a time series and the temporal correlations of the data points and thus contain congruent information.[191] Accordingly, the question emerges if the application of both methods is meaningful. Depending on whether the SNR or ΔSN is considered, the DFA shows either very poor sensitivity or one that does not differ substantially from that of the PSD analysis. In this work, the DFA was found to be more prone to false results, like in the case of the cell-free PDT electrodes. The electrodes show extremely low noise in combination with a subtle but distinct bend in the curve (cf. Fig. III-32 B, inset). Thus, the polynomial fit matches the time series data well for small segment sizes s ($\leq$ 32), but increasingly less for larger s ($\geq$ 32). This leads to a biphasic curve in the log-log plot of the fluctuations F(s) (cf. Fig. V-6, supplementary information). Here, a linear fit through s $\leq$ 32 exhibits a slope indicative of white noise (0.64 $\pm$ 0.02) and the slope of the linear fit for s $\geq$ 32 is 2.55 $\pm$ 0.07. The slope of the whole data set (1.35 $\pm$ 0.06) in this case has no analytical relevance as the data cannot be adequately represented by just one linear fit. The usefulness of the DFA as in comparison to PSD analysis has already been questioned by Heneghan et al., stating that *"there is no particular reason to recommend the use of detrended fluctuation analysis over spectral analysis for stochastic processes with longterm correlation"*.[191] Moreover, Lovelady et al. found the PSD analysis to be more distinct than the DFA.[192] We therefore consider the use of the PSD slope to be sufficient to quantify the temporal correlations of a time series. In combination with the DVA, this provides comprehensive information about the nature and the intensity of the signal.

It should be mentioned, though, that the scaling exponents k are only interpretable in terms of the temporal correlations in a comparative manner for systems with the same ground noise level. This is not the case when comparing 8W1E and PDT electrodes. As a result, the fact that

8W1E electrodes show different values of k than PDT electrodes for living cells does not necessarily imply altered micromotion dynamics. Rather are the short-term correlations less pronounced on PDT electrodes due to their low noise, leading to lower PSD values at the high frequency end of the spectrum (Fig. III-33 A). At the same time, the long-term correlations show similar intensity in the low frequency range, which results in a more negative slope (and higher k) for PDT electrodes. Accordingly, the PSD of the fixed cells on 8W1E electrodes is dominated by the electrode noise and thus appears more 'white' than on PDT electrodes (Fig. III-33 B). The latter reveal a slope different from white noise, even though the cells are fixed and cannot perform active micromotion. Instead, these fluctuations can be attributed to thermal shape fluctuations that have also been observed in liposomes.[140,193] The difference in the noise levels between the cell-free 8W1E and PDT electrodes is most evident in the relative positions of the linear PSD fits in Fig. III-33 C.
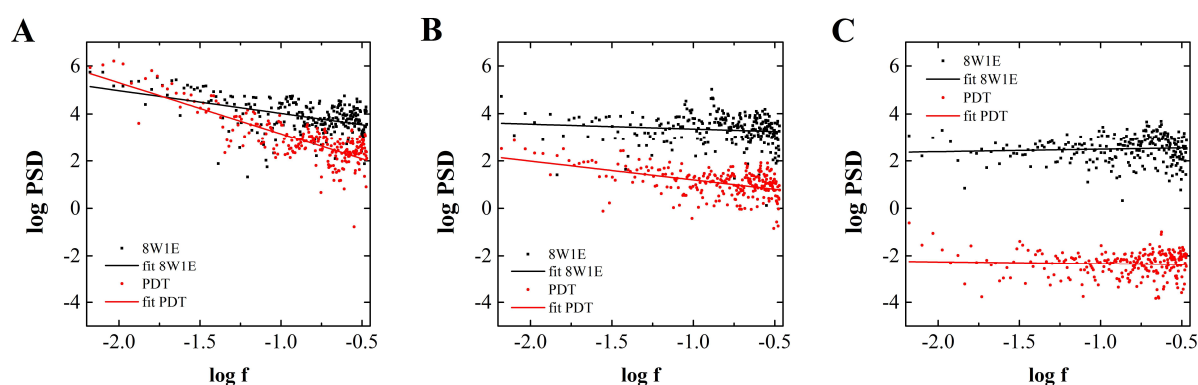

Fig. III-33: Typical data of the PSD analysis of MDCK-II cells grown onto 8W1E or PDT electrodes including the raw data and the corresponding linear fits. **(A)** Living cells. **(B)** Fixed cells. **(C)** Cell-free electrode. For the analysis, only the last 512 of the overall 612 data points of the time series were used. Moreover, the lowest 5 frequencies in the PSD spectrum (not shown in this figure) were discarded to get rid of long-term drifts. The measurements were recorded at 400 Hz. T = 37 °C

What remains to be discussed is the origin of the extremely low noise of the cell-free PDT electrodes compared to the 8W1E electrodes. The thermal noise at the electrode-electrolyte interface is inversely proportional to the electrode capacitance.[194] Approximating the electrode capacitance by the results for A_{cpe-c} from chapter 2.3.2 multiplied by the electrode area yields a value of (0.57 ± 0.05) µF for PDT and (0.0087 ± 0.0002) µF for 8W1E electrodes, which would certainly explain the differences in the noise level. However, regarding the resistance spectra in Fig. III-34 reveals that for 8W1E electrodes, the recording frequency falls into the region determined by the electrode-electrolyte interface, whereas it is dominated by the bulk resistance for PDT electrodes. As a result, the noise in both electrode types is caused by different equivalent circuit elements. Indeed, measurements recorded at 4 kHz with cell-free 8W1E

electrodes have been published showing a noise level in the power spectrum that is more similar to the results presented for PDT electrodes.[140,193] For a more detailed understanding of the dependencies of the electrode noise and the signal-to-noise-ratios, the time series should be repeated at different frequencies analyzing the capacitive and resistive regions in the spectrum of both electrode types. The high electrode capacitance of the PDT electrodes is expected to allow for highly sensitive micromotion recordings at even lower frequencies. The resistive cellular fluctuations are decoupled from capacitive cell membrane fluctuations[195-197] and moved towards the frequency region most sensitive to changes in α and R_b. The PDT electrodes are expected to show increasingly better performance compared to 8W1E electrodes the lower the recording frequency, but similar sensitivity for readings at 4 kHz, where both electrode types are determined by the bulk resistance. This is yet to be verified experimentally.
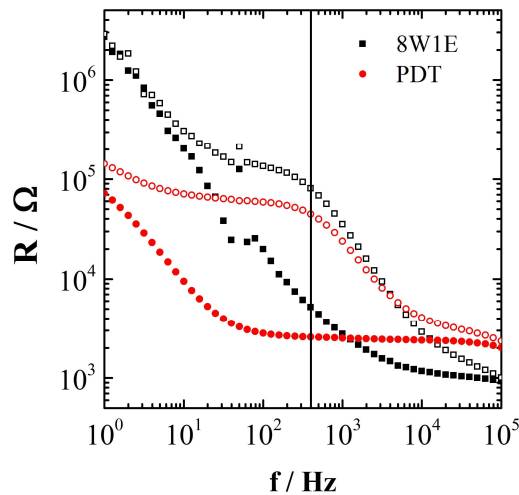

Fig. III-34: Typical resistance spectra of an electrode used for the micromotion experiments. The vertical line marks the recording frequency at 400 Hz. Spectra of cell-free electrodes are shown as full symbols (■, ●) and of cell-covered electrodes as empty symbols (□, ○). T = 37 °C

In summary, the PDT electrodes were successfully used to record the micromotion of adherent MDCK-II cells. A comparison of the biological impact of the different electrode materials gold and PEDOT:PSS on the cells was not established due to the different noise levels of the electrodes. However, the low electrode noise of the PDT electrodes leads to an enhanced SNR compared to the 8W1E electrodes at 400 Hz and, therefore, to an improved sensitivity. Independent of the electrode type, the PSD analysis and the DVA were estimated to sufficiently describe the micromotion periodicities and amplitudes. The DFA provides no additional information and was found to be more error prone.

2.3.8 *Electroporation*

In this chapter, a membrane impermeable FITC-labeled dextran (4 kDa) was transferred into adherently grown NRK cells by electroporation using PDT and 8W1E electrodes. An electroporation pulse with a frequency of 40 kHz, 200 ms pulse duration, and 4 V amplitude reportedly gives the best results for NRK cells with respect to dye uptake and non-invasiveness.[127] We additionally used a frequency of 1.5 kHz for the electroporation pulse to elucidate whether lower frequencies could be employed for PDT electrodes due to their better access to the low frequency range. In order to be able to compare the fluorescence intensities of both electrode types, the same excitation settings for pinhole size and intensity of the excitation laser had to be employed during CLSM. Therefore, some of the displayed images appear overexposed, which was accepted in favor of the comparability (cf. Fig. V-8, supplementary information, for images with reduced gain).

Fig. III-35 shows fluorescence images of cells electroporated at 40 kHz about 1.5 – 2 h after the electroporation. The images clearly illustrate that only cells growing directly on the electrode are permeabilized for the dye. Accordingly, the PDT electrodes (upper row) exhibit a larger fluorescent area because of the larger electrode surface area ($1.3 \cdot 10^{-3}$ cm²) compared to the 8W1E electrodes ($5 \cdot 10^{-4}$ cm², lower row). Neither electrode shows any dye uptake in the control (0 V), while the fluorescence intensity increases from 2 V to 4 V (rms). The fluorescence is more distinct at the edges of the electrodes. Compared to the 8W1E electrodes, the dextran uptake on the PDT electrodes appears less efficient as indicated by the overall weaker fluorescence. The corresponding time courses of the impedance magnitude are depicted in Fig. III-36. |Z| is plotted at 8 kHz as both electrode types exhibit similar sensitivities at this frequency (Fig. III-39 B). By application of a 2 V voltage pulse, |Z| drops down by roughly 10% and subsequently recovers within 20 – 30 min. A pulse with higher amplitude of 4 V has a stronger impact on the cells, so that |Z| declines by about 30 – 40% and takes more time to recover (about 60 min). No significant differences between the electrode types are observable in the time courses at the applied electroporation pulses 40 kHz.
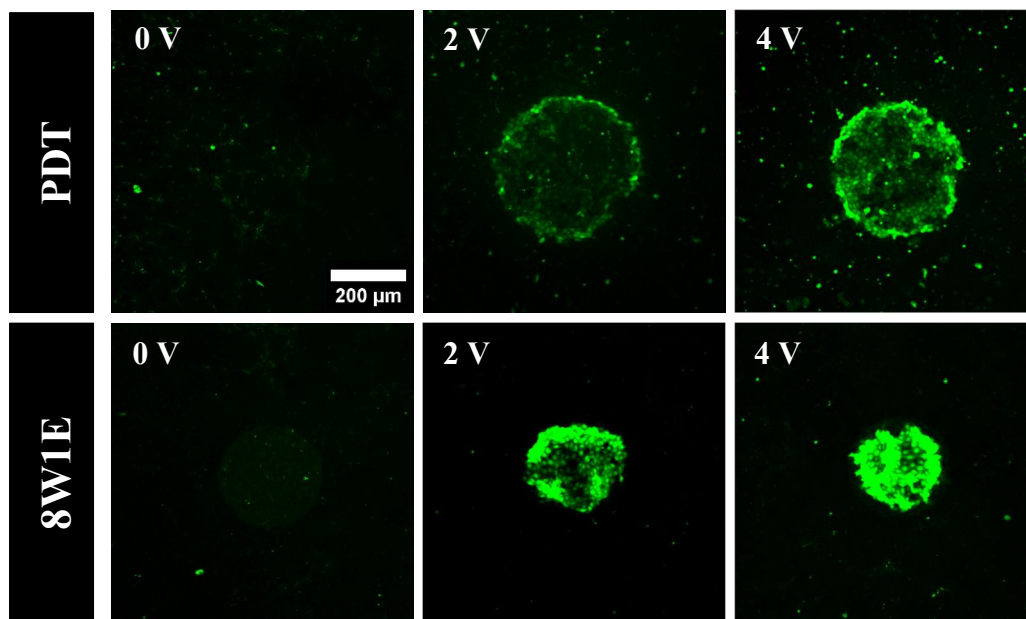
Fig. III-35: Typical micrograph of electroporated NRK cells using a 4 kDa FITC dextran as model compound at different electric pulse voltages (pulse duration: 200 ms, pulse frequency: 40 kHz; CLSM properties: pinhole size s, gain 105, laser excitation: 488 nm). The electroporation was performed two days after confluent seeding. *Upper row:* PDT electrode. *Lower row:* 8W1E electrode. T = 37 °C
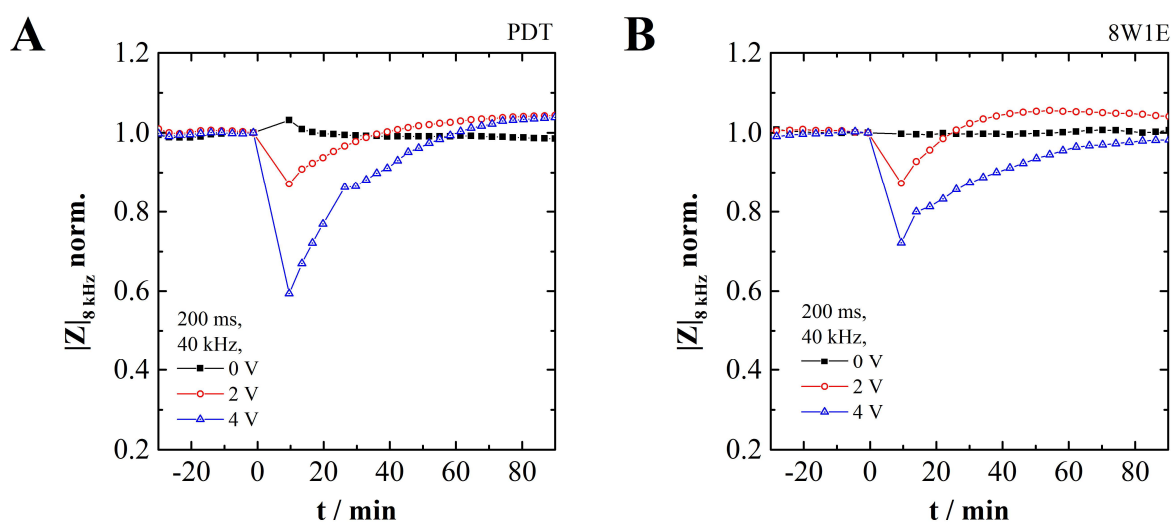

Fig. III-36: Typical time course of the normalized impedance magnitude at 8 kHz before and after the electric pulse application at t = 0 min. The electroporation was performed two days after confluent seeding **(A)** PDT electrodes, 200 ms pulse duration, 40 kHz pulse frequency, NRK cells. **(B)** 8W1E electrodes, 200 ms pulse duration, 40 kHz pulse frequency, NRK cells. T = 37 °C

With a 2 V pulse at 1.5 kHz, the NRK cells growing on PDT electrodes show slightly stronger fluorescence than with 40 kHz at the same voltage (Fig. III-37). At 4 V, the intensity is even higher, but the cell layer looks disrupted as indicated by the black spot in the lower right corner of the electrode. Furthermore, the corresponding impedance magnitude drops by about 50 –

60% and stays at that level during the time course of the experiment (Fig. III-38 A). By contrast, the 2 V curve shows the typical sudden decline with subsequent recovery over the next 60 min as described for 40 kHz. The 8W1E electrodes exhibit a drastically enhanced fluorescence intensity for both 2 and 4 V excitation amplitude. The outlines of the electrodes are clearly delineated compared to the somewhat frayed appearances entailed by the other electroporation conditions. However, the time courses indicate an irreversibly permeabilized cell layer as the signal does not recover after the application of the electroporation pulse (Fig. III-38 B).

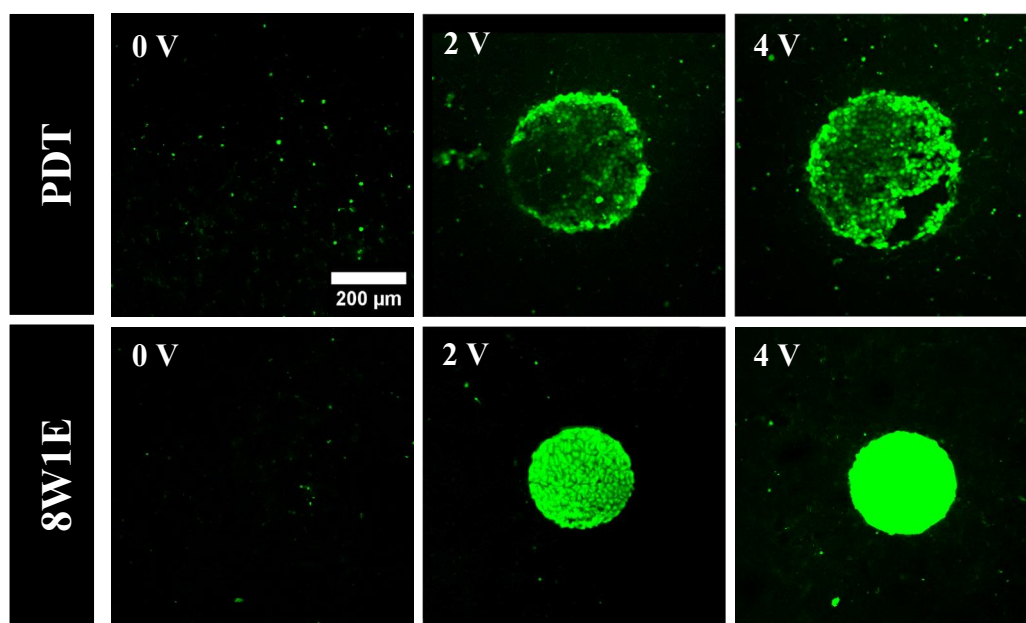**Fig. III-37:** Typical micrograph of electroporated NRK cells using a 4 kDa FITC dextran as model compound at different electric pulse voltages (pulse duration: 200 ms, pulse frequency: 1.5 kHz; CLSM properties: pinhole size s, gain 105, laser excitation: 488 nm). The electroporation was performed two days after confluent seeding *Upper row:* PDT electrode. *Lower row:* 8W1E electrode. T = 37 °C
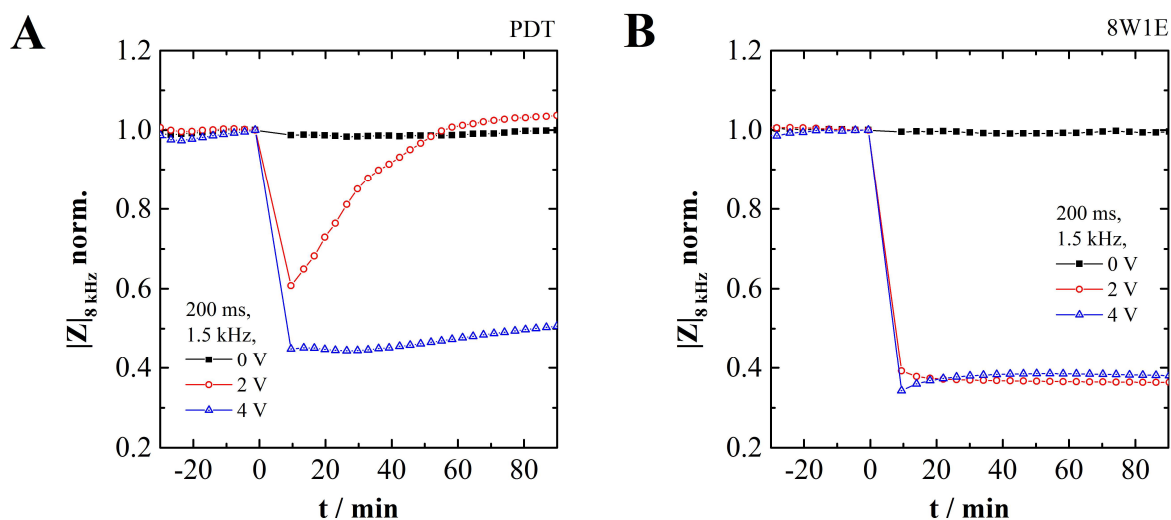
A

B

Fig. III-38: Time course of the normalized impedance magnitude at 8 kHz before and after the electric pulse application at t = 0 min. **(A)** PDT, 200 ms, 1.5 kHz, NRK cells. **(B)** 8W1E, 200 ms, 1.5 kHz, NRK cells. T = 37 °C

Wegener et al. performed a detailed study about the loading efficiency and invasiveness of electroporation by varying pulse frequency, pulse duration, and pulse amplitude.[127] NRK cells adherently grown onto 8W1E electrodes were electroporated using the fluorescent dye Lucifer yellow as model compound. In their research, it was shown that electroporation is most efficient at frequencies where the impedance signal is mainly determined by the cell layer. At low frequencies (below ~ 1 kHz on 8W1E electrodes, Fig. III-39), the impedance is dominated by the electrode interface, so that electrochemical reactions can lead to electrode disruption. Furthermore, an enhanced loading efficiency with increasing amplitudes was reported up to a certain threshold voltage when the electrical field becomes fatal for the cells.

Our results demonstrate that electroporation can be performed at 40 kHz with PDT electrodes, yielding similar results in terms of the impedance time course as with 8W1E electrodes. The brighter fluorescence observed on 8W1E electrodes is probably due to the high lead resistance of the PDT electrodes in series with the constriction resistance. At 40 kHz, a large part of the applied voltage drops across the resistive PEDOT:PSS leads (estimated to more than 1.2 kΩ, cf. 2.3.2), so that the voltage drop across the cell layer is a lot smaller (Fig. III-39 A). The combined resistance that primarily determines the electrode impedance at 40 kHz consisting of contact resistance, lead resistance, solution resistance, and constriction resistance in series accounts to about 2 – 3 kΩ on PDT electrodes. By comparison, it is only in the range of ~ 1 kΩ on 8W1E electrodes. Accordingly, the higher effective electrical field across the cell layer on 8W1E electrodes leads to more dye uptake. Furthermore, the gold surface of the 8W1E electrodes reflects the excitation light as well as the fluorescence light. As a result, the

fluorescence intensity is increased as more fluorescence dye in the cells growing on the 8W1E electrodes is excited and additionally the fluorescence light reflected by the gold surface reaches the detector.

Electroporation at 1.5 kHz is visibly more disruptive for both electrode types as indicated by the stronger impact on the impedance signal (cf. Fig. III-38). An irreversible damage to the cells like by the generation of cytotoxic chlorine species explains the strong fluorescence intensity and the stationary low signal after the electroporation on 8W1E electrodes. When the cells are unable to reseal the membrane after the electric pulse, dye keeps diffusing into the cells and the resistance across the cell layer breaks down (cf. Fig. III-38). During the continuous measurement after electroporation, the FITC-dextran probably adsorbs to cell organelles and other cell structures and is thus prevented from being washed out during the washing steps. The electric field appears to be less invasive on PDT electrodes as the electroporation was successfully performed with an amplitude of 2 V. At 4 V, a large part of the cells shows homogeneously distributed dye inside the cells, whereas some cells did not survive the voltage pulse, were permeabilized, and detached from the surface. Most likely, the cells that were killed by the electric field were washed off during the washing steps preceding the microscopic examination. The electroporation at 1.5 kHz is more harmful to the cells on 8W1E electrodes than on PDT electrodes. 1.5 kHz is a frequency corresponding to the electrode-electrolyte interface dominated frequency region for 8W1E electrodes, whereas it is determined by the bulk resistance for PDT electrodes. On 8W1E electrodes, the voltage drops predominantly across the electrode-electrolyte interface and not the cell layer. As a result, 8W1E electrodes produce more cytotoxic electroactive species at the electrode surface and the pulse is more invasive than PDT electrodes at 1.5 kHz.[127] Even though the values of the impedance magnitude of PDT electrodes are the same at 1.5 kHz and 40 kHz and both frequencies are determined by the bulk resistance, they show invasiveness to different degrees. At lower frequencies, the ions have more time to accumulate on the electrode surface. This increases the chance of a charge-transfer and thus the electrochemical reaction rate at the electrode surface that leads to reactive cytotoxic species is enhanced. Therefore, the invasiveness also depends directly on the frequency of the applied voltage pulse.
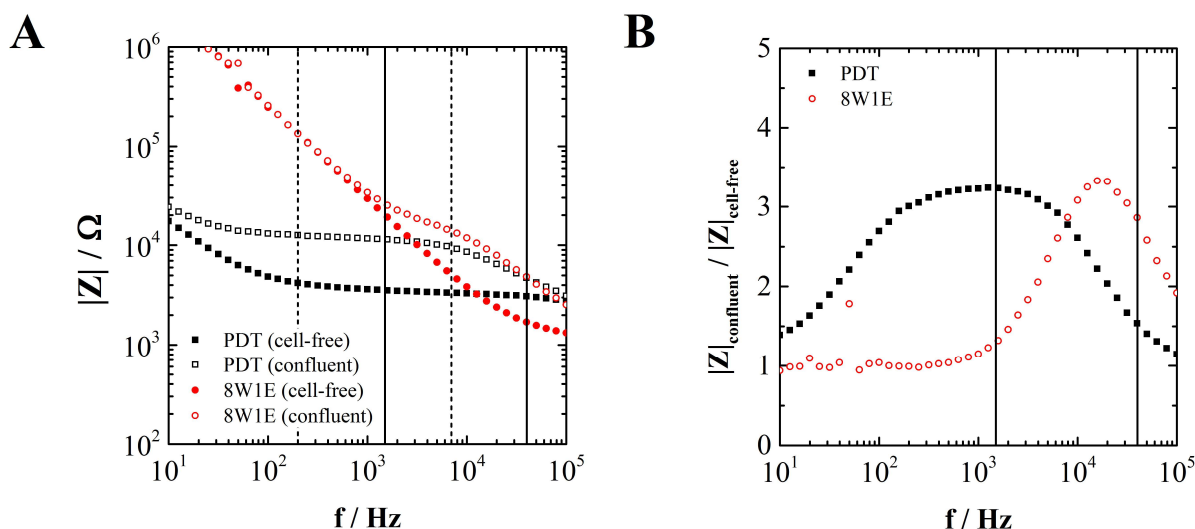
Fig. III-39: (A) Typical impedance magnitude spectra of cell-free electrodes (■, ●) and with adherently grown NRK cells (□, ○) 40 h after seeding onto PDT and 8W1E electrodes. **(B)** Corresponding normalized impedance magnitude spectra for PDT (■) and 8W1E electrodes (○). The vertical lines indicate the pulse frequencies applied in this chapter (1.5 kHz, 40 kHz). The spectra were recorded in an experiment independent from the electroporation experiments discussed in this chapter. T = 37 °C

In conclusion, the PDT electrodes were shown to be suitable for electroporation with slightly reduced loading efficiency compared to 8W1E electrodes. We suggest that this is due to the high resistance of the PEDOT:PSS leads, where a fraction of the excitation voltage is lost. An adequate adjustment of the electroporation conditions is thus required. The electric field at 1.5 kHz was found to be less invasive for PDT electrodes as the voltage drops mainly across the bulk resistance and not the electrode-electrolyte interface like for 8W1E electrodes. Therefore, the generation of cytotoxic species is reduced.

2.3.9   Comparison of MDCK-I, MDCK-II, and NRK Cells

In order to evaluate the ability of the PDT electrodes to analyze and discriminate between different cell lines, the impedance spectra of confluently grown MDCK-I, MDCK-II, and NRK cells were compared. The cell parameters C_m, α, and R_b were determined for each cell line. The three cell lines were selected to represent high-impedance (MDCK-I), medium- impedance (MDCK-II), and low- impedance (NRK) monolayers. These properties are well represented in the impedance magnitude and the resistance spectra (Fig. III-40 A and C). The horizontal regions in the impedance and resistance spectrum, approximating the sum of the impedance contributions from cell-cell and cell-substrate contacts, account to about 500 kΩ, 60 kΩ, and 10 kΩ, respectively. Accordingly, the sensitivities of |Z| (R) are about 80 (110) for MDCK-I cells, 20 (25) for MDCK-II cells, and 6 (6) for NRK cells, each with broad maxima (Fig. III-40 B and D). Even the peaks of the leaky NRK cells reach down to the low frequency range. In the

impedance magnitude spectra, the capacitive part of the MDCK-II cell layer is shifted towards lower frequencies compared to the MDCK-I and NRK cells (Fig. III-40 A). This is due the microvilli expressed by MDCK-II cells, which increase the surface of the cell membrane and thus the membrane capacitance. Correspondingly, the capacitance spectrum of the MDCK-II cells shows a higher capacitance in the high frequency range, than the other cell lines (Fig. III-40 E). This region is determined by the membrane capacitance and exhibits noticeable frequency dispersion. The transition region within the capacitance spectrum between electrode interface ($\sim \mu F$) and region dominated by the membrane capacitance ($\sim nF$) is shifted towards lower frequencies with increasing R_b and/or α. This is also well reflected in the normalized capacitance, which shows good sensitivities over a broad frequency range due to the high base capacitance of the PDT electrode (Fig. III-40 F).
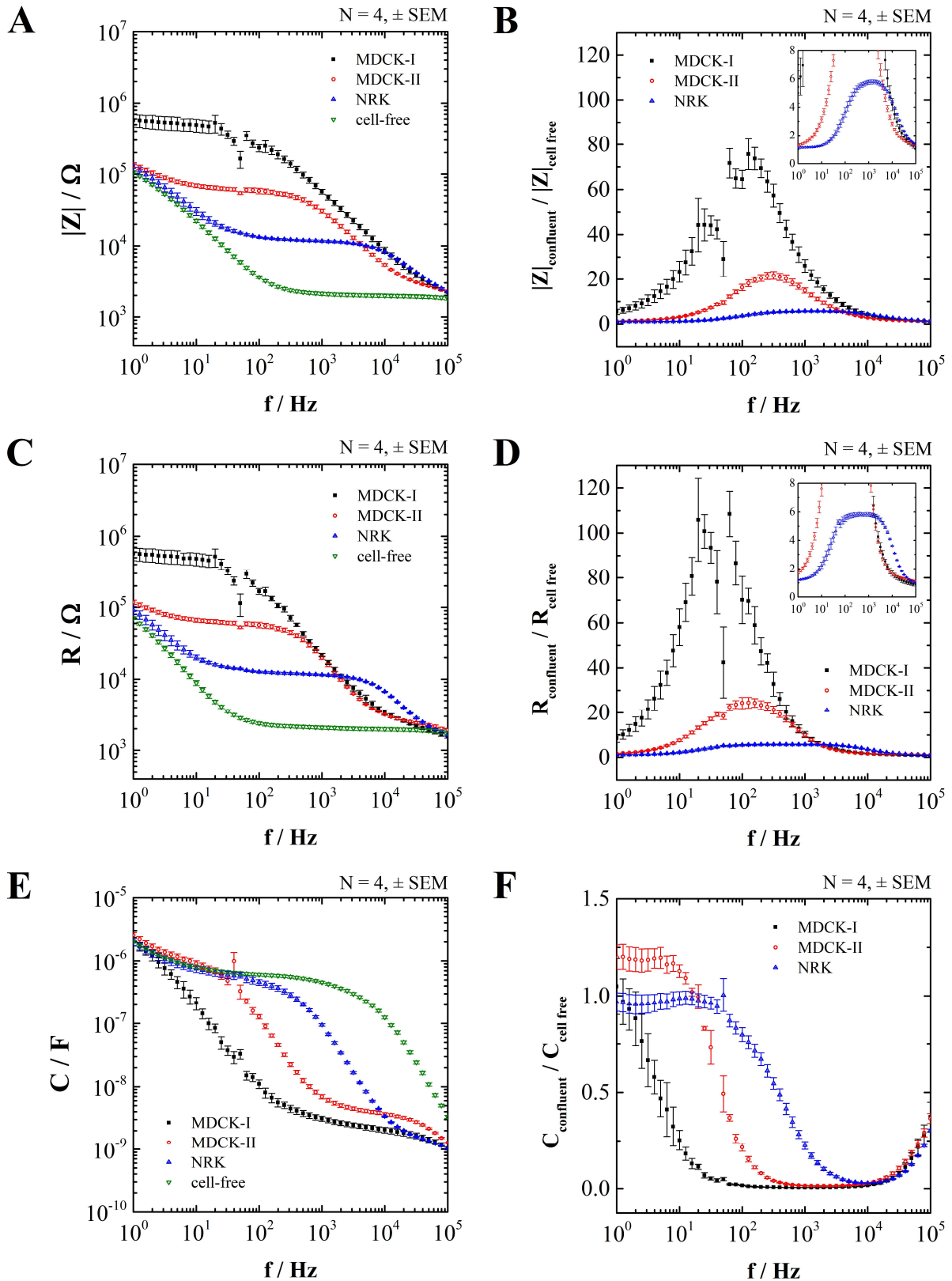
Fig. III-40: Frequency spectra recorded for MDCK-I (■), MDCK-II (○), and NRK cell layers grown to confluence on PDT electrodes (▲) as well as cell-free electrodes (▽). **(A)** Impedance magnitude |Z|, **(B)** normalized impedance magnitude, **(C)** resistance R, **(D)** normalized resistance, **(E)** capacitance C, **(F)** normalized capacitance. The insets in (B) and (D) show the spectra scaled to the NRK cells. The MDCK-I cells exhibit interference noise around the line frequency of 50 Hz due to their high impedance and because the measurement was recorded at an amplitude of only 10 mV. T = 37 °C

Ideally smooth cells exhibit a membrane capacitance of ~ 1 µF/cm², whereas ruffles, folds and microvilli increase the surface area and, thus, the capacitance considerably.[198-199] In our study, NRK cells are the cells closest to this unfolded value with $C_m = (1.85 \pm 0.05)$ µF/cm² (Fig. III-41). MDCK-II cells are known to express microvilli on their apical surface.[121-122] As a consequence, they exhibit the highest C_m value of (5.6 ± 0.4) µF/cm². By comparison, MDCK-I cells have less microvilli on the apical side, but exhibit a more folded lateral membrane.[200-201] This results in an intermediate C_m value of (3.4 ± 0.2) µF/cm². α and R_b show both the same tendency in a sense that the tightness of the epithelium is correlated with both parameters. The MDCK-I cells, forming tight epithelia, exhibit the highest α and R_b values [$\alpha = (34 \pm 6)$ $\Omega^{0.5} \cdot$cm, $R_b = (600 \pm 100)$ $\Omega \cdot$cm²], followed by the MDCK-II cells with intermediate tightness [$\alpha = (8 \pm 1)$ $\Omega^{0.5} \cdot$cm, $R_b = (67 \pm 6)$ $\Omega \cdot$cm²]. The leaky NRK cells display the lowest values for both parameters [$\alpha = (4.8 \pm 0.1)$ $\Omega^{0.5} \cdot$cm, $R_b = (11.0 \pm 0.3)$ $\Omega \cdot$cm²]. The parameter R_b directly represents the barrier function of the cell layer, while α is determined by the specific resistance of the electrolyte in the subcellular cleft ρ, the distance between cell and substrate h, and the cell radius r (Eq. 22). Reiß suggested a functional correlation between α and R_b based on a detailed study of ρ, h, and r involving several cell lines.[202] It was reasoned that only tight paracellular barriers allow for the establishment of a high ion gradient between the apical and the basolateral side of the cell layer and thus a substantially lower conductivity in the subcellular cleft. As soon as there is free ion exchange between culture medium and subcellular cleft, the ions diffuse across the cell layer and the respective specific resistances are in balance, which is reflected in the parameter α.
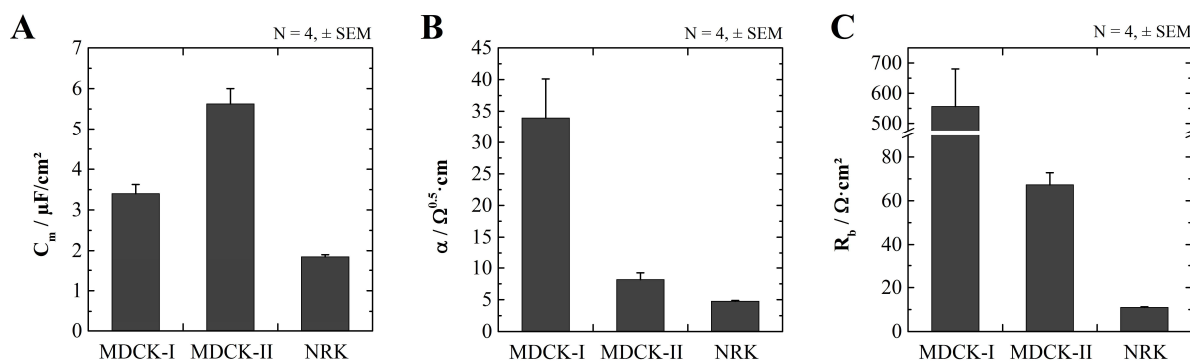
Fig. III-41: ECIS parameters of different cell monolayers 40 h after confluent seeding upon PDT electrodes (N = 4, ± SEM). **(A)** C_m / µF/cm²: 3.4 ± 0.2 (MDCK-I), 5.6 ± 0.4 (MDCK-II), 1.85 ± 0.05 (NRK). **(B)** α / $\Omega^{0.5}$·cm: 34 ± 6 (MDCK-I), 8 ± 1 (MDCK-II), 4.8 ± 0.1 (NRK). **(C)** R_b / Ω·cm²: 600 ± 100 (MDCK-I), 67 ± 6 (MDCK-II), 11.0 ± 0.3 (NRK). T = 37 °C

ECIS parameters from this work and other publications are summarized in Tab. III-15. The R_b is also compared to the TEER (*italic* numbers). The TEER is usually determined by measuring the electrical DC resistance between the upper and the lower liquid compartment for cells grown on permeable filters. This measurement includes the resistance of the filters, for which the results must be corrected in order to be comparable.[120] Our results concerning the barrier function of the cell layers (R_b) obtained for PDT electrodes fit well to the range covered by the literature values. The parameter α, on the other hand, seems to be consistently lower than the reported values for all three cell lines. This has been discussed in previous chapters for MDCK-II cells and was attributed to reduced focal adhesions caused by the softer substrate PEDOT:PSS. The C_m results cover a similar range on PDT and 8W10E electrodes as the reported literature values. The differences could lie within the naturally occurring batch-to-batch variations of biological material, since a direct comparison within same passages of MDCK-II cells did not show any differences between gold and PEDOT:PSS (cf. 2.3.3). The main morphological characteristics are, however, assumed to be retained on the conducting polymer as the general trends of these cell lines are similar to the literature for all parameters.

Tab. III-15: ECIS parameters for confluent MDCK-I, MDCK-II, and NRK cell layers (± SD or in terms of intervals). All values denoted in *italic* numbers are TEER values obtained from transwell filter measurements. * For MDCK-II cells, the results from chapter 2.3.3.2 are considered as well.

cell line	C_m / µF/cm²	α / $\Omega^{0.5}$·cm	R_b *or TEER* / Ω·cm²	source
MDCK-I	3.4 ± 0.4	30 ± 10	600 ± 200	this work (PDT)
	1.91 ± 0.07	117 ± 3	2900 ± 200	Reiß[202]
	1.8 – 5.0		400 – 3500	Wegener[120]
			2500 – 5000	Stevenson[203]
MDCK-II	4 – 6	8 – 9	40 – 70	this work (PDT) *
	4.2 ± 0.2	13 ± 1	33.9 ± 0.8	this work (8W10E)
	3.03 ± 0.03	16.0 ± 0.6	88 ± 4	Reiß[202]
		18 ± 2	60 ± 4	Lo[204]
	1.8 – 5.0		40 – 100	Wegener[120]
			50 – 70	Stevenson[203]
NRK	1.9 ± 0.1	4.8 ± 0.2	11.0 ± 0.6	this work (PDT)
	1.20 ± 0.08	7.9 ± 0.3	9.3 ± 0.8	Reiß[202]
			13 ± 1	Prozialeck[124]
			12	Limonciel[123]

2.4 Summary and Outlook

Screen printed electrode arrays with the conducting polymer PEDOT:PSS as electrode material and a silicone passivation layer were successfully fabricated and characterized. In contrast to published results for spin coated PEDOT:PSS, no problems with adhesion loss in aqueous environment were observed. The PDT electrodes showed high transparency in the visible light spectrum and can thus be used in combination with transmitted light microscopes. No long-term degradation of the electrode material was detected over a time interval of 16 months when the electrodes were stored in the dark. An immediate disruption of the polymer was only found to occur when impedance measurements were performed at voltage amplitudes higher than 300 mV, whereas it remained stable at a common voltage for label-free cell sensing of 50 mV. The impedance magnitude drift during exposure with cell culture medium was only small compared to the signal change caused by cells (max. ~ 2% of the impedance change caused by confluently

grown MDCK-II cells). However, the capacitance drift at higher frequencies remains a challenge and requires the electrodes to be adequately equilibrated before performing cell proliferation or adhesion assays. In comparison with commercial gold electrodes, PEDOT:PSS exhibits a significantly enhanced interface capacitance due to its hydrogel properties. This improves the electrode sensitivity at lower frequencies for the parameters |Z| and R, which indicate the barrier function and the cell-substrate interaction of adherent monolayers. Moreover, the PDT electrodes outperform the gold electrodes in terms of the sensitivity of C along the whole frequency spectrum, which is important for cell proliferation or adhesion assays. A disadvantage of PEDOT:PSS is its high inherent resistivity and, thus, high lead resistance, reducing the sensitivities for |Z| and R at higher frequencies. This could lead to a loss of information in mechanistic studies concerning the cell membrane topography. Alterations in the cell-substrate contact and the adhesion and spreading kinetics compared to commercial 8W10E gold electrodes were attributed to the lower substrate stiffness of PEDOT:PSS compared to gold. The softer mechanical environment is much closer to the *in vivo* situation than common cell culture substrates and sensor surfaces, which can have a substantial impact on the cell metabolism. Several common analytical assays investigating the micromotion, proliferation, cytotoxicity, and electroporation performance of PDT electrodes were successfully conducted, yielding results that were overall at least similar to those obtained with gold electrodes. Nevertheless, several differences were established. Due to the high interface capacitance, the PDT electrodes showed an extremely low noise level during micromotion experiments compared to gold electrodes. This resulted in a high signal-to-noise ratio and sensitivity. The proliferation assay provided more scattered results on PDT electrodes, which could be either attributed to the smaller electrode size or an inhomogeneous substrate stiffness across the electrode surface. Because of a reduced generation of cytotoxic species at the electrode surface, the electroporation at lower frequencies (1.5 kHz) was found to be less invasive on PDT electrodes. Eventually, different cell lines with varying dielectric parameters were analyzed using the PDT electrodes and were shown to qualitatively retain their specific morphological characteristics like barrier function, substrate contact, and membrane capacitance.

The two main challenges remaining to be tackled are the electrode drift during cell culture medium exposure and the high lead resistance. The drift needs to be addressed by appropriate equilibration of the electrode, while several measures can be taken in terms of the electrode design to reduce the lead resistance. A first suggestion is to replace the PEDOT:PSS formulation Clevios S V3 with a sheet resistance of 700 Ω/sq by a more conductive dispersion,

called Clevios S V4. Its sheet resistance is specified to be only 400 Ω/sq, so that changing the screen printing ink could considerably improve the sensitivity of the electrodes. Another option is to place the silver leads further inside the well, until right in front of the working electrode. This would probably have the most dramatic effect since the resistance of the silver leads is in the one-digit ohm range and therefore entirely negligible. As long as the silver is entirely covered by the passivation layer, no problems concerning the cytotoxic effect of silver should arise. Another improvement to the electrode arrays would be to dye the transparent passivation layer in order to enhance the visibility of the working electrode. At the moment, the edges of the electrodes are rather hard to identify by phase contrast microscopy if cells are growing on top. Using a sensor dye for this purpose could even combine the electrical detection method with optical sensors to detect for example the pH value or the oxygen concentration in the subcellular cleft.[205]

In summary, the screen printed polymer electrode arrays prepared and described in this thesis are a low-cost alternative to the established gold electrodes that exhibit many advantages like high sensitivity, low noise level, optical transparency, and closer mechanical resemblance to the biological environment due to a softer substrate stiffness. Screen printed PEDOT:PSS electrodes provide great potential for other bioanalytical applications where they can replace established electrode materials like gold, ITO, or silicon. The low fabrication cost gives rise to a comprehensive use in high throughput screening, where they can help to identify potential drug candidates in an early phase of the drug discovery process or help to exclude failing ones.

3   Bipolar Electrodes

3.1   Introduction

For the impedimetric examination of living cells, commonly two coplanar gold film electrodes are used and a constant AC current is applied.[19,158,206] A low amplitude guarantees that the measurement is non-invasive and does not affect the cells. The interface capacitance between electrode and electrolyte produces a typical frequency spectrum with an increasing impedance towards lower frequencies (cf. Fig. II-10 A). Below a certain frequency, which depends on the electrode capacitance and the cell type, the spectra of cell-free and cell-covered electrode converge and the impedance is exclusively determined by the interface capacitance. There is no relevant information describing the cells under test in the frequency region that is dominated by the interface impedance at the low frequency end of the spectrum.

One important area of application expanding the scope of impedance-based assays of adherent cells on gold film electrodes is their manipulation with pulses of elevated electric fields (cf. 1.3) like, for instance, in situ electroporation or cell wounding. Both methods, electroporation and wounding, require extensive optimization with respect to pulse duration, number of pulses, pulse amplitude, and – only for electroporation – the concentration of the analyte to be transferred from the extracellular fluid into the cell.[127,132,207] Because of the larger number of parameters, the optimization can be very complex and time-consuming. For this reason, efforts have been made to reduce the necessary number of measurements using voltage gradients to cover a range of amplitudes within a single experiment. These approaches involve imaging and mathematical modeling of the electric field around the electrodes[208], parallel microfluidic channels with different lengths to generate variable electric field strengths[209], and special electrode structures that produce a voltage gradient between two coplanar electrodes.[210-211] All methods have the disadvantage of requiring very high DC voltages of several hundred volts, where electrochemically reactive and cytotoxic molecular species are generated at the electrode surface.[127] In particular, they are restricted to the execution of the electroporation or wounding and cannot be combined with electrical detection methods.

3.2 Objective

In this work, a novel bipolar electrode layout with a continuous potential gradient is described. Instead of two coplanar electrodes, only one electrode is employed that requires a sufficiently high resistance between its contact pads to ensure coupling of the electrical current with the electrolyte (Fig. III-42). This design should be used for the impedimetric analysis of adherent cells using low driving voltages in the range of 10 to 50 mV, similar to the ECIS method. At elevated amplitudes, the position dependent voltage gradient between two point of the bipolar electrode should allow for the gradual electroporation or wounding of adherent cells. The proof-of-principle was to be demonstrated by wounding experiments with subsequent staining of the dead cells. In order to be able to compare the bipolar electrodes to the established impedance analysis of adherent cells employing two electrodes, the bipolar electrodes were to be covered with a passivation layer, providing two openings delineating working and counter electrode in an ECIS-like fashion. That way, a modified version of the ECIS model was to be applied to determine the cell parameters. Eventually, simulations with the modified ECIS model describing the bipolar electrodes were to be carried out to investigate the effect of varying the electrode resistance on the impedance spectrum.
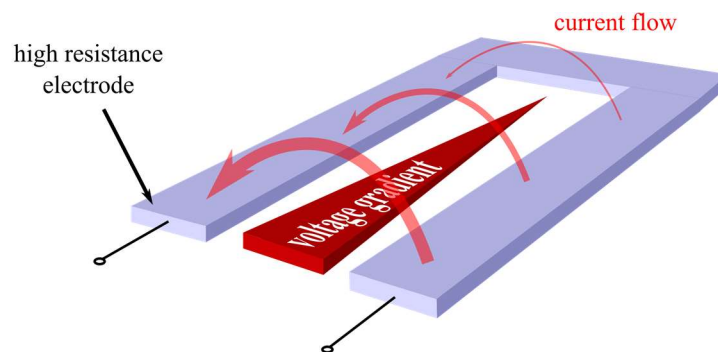

Fig. III-42: Simplified schematic of a bipolar electrode. Using an electrode with high resistance allows the AC current to couple through the electrolyte and sense adherent cells growing on top. The high-resistance conduction path creates a voltage gradient along the electrode that can be used to gradually electroporate or wound cells when applying elevated electric fields. A low resistance bipolar electrode would short-circuit the electrode poles and prevent coupling through the electrolyte.

3.3 Materials and Methods

3.3.1 Photolithography

The bipolar electrodes were structured by a photolithography process. In a first process step, the ITO electrode structure was fabricated. Thereupon, a passivation photoresist layer was deposited on the ITO structure to delineate size and shape of the active electrode area that gets in contact with the electrolyte.

The photoresist (AZ ECI 3027, MicroChemicals GmbH, Ulm, DE) was deposited on ITO coated PET substrates with a surface resistivity of 60 Ω/sq (Sigma-Aldrich, St. Louis, MO, USA) by spin coating. A WS-400B2-6NPP-Lite spin coater (Laurell Technologies Corporation, North Wales, PA, USA) was used for this purpose applying a two-step spinning program (Tab. III-16). The first step allowed for an even distribution of the photoresist on the substrate. In the second step an elevated rotation speed ensured that excess photoresist solution heaped up at the edges of the substrate was removed.

Tab. III-16: Spinning program used for the deposition of the photoresist on the ITO-PET substrate.

step	duration / s	rotation speed / rpm
1	40 s	2000
2	5	5000

The substrates were dried on a hot plate at 100 °C for 5 minutes to evaporate the solvent residues (soft bake). The dry photoresist needs to be rehydrated in order to provide homogeneous development rates across the layer. This was achieved by keeping it at ambient conditions for another 5 minutes before UV illumination. The substrate was exposed to UV light for 2 min (UV-Belichter 1, Reichelt Elektronik GmbH & Co. KG, Sande, DE) through a photolithographic mask. The mask layout was printed on a PET printer foil using a customary laser printer. Three identical masks were pinned on top of each other to increase the optical density and prevent UV light transmission through the mask. Subsequently, the substrate was etched and developed by successively slewing it in the solutions listed in Tab. III-17. The AZ Developer (MicroChemicals) was used to develop the photoresist. After each washing step with H_2O the substrate was blow-dried in an airstream. The etched electrode was then subjected to UV light for a second time without the mask and the steps 1 and 2 in Tab. III-17 were repeated. Thereby, the ITO structure was uncovered from the previously unexposed photoresist.

Tab. III-17: Photolithographic process steps following UV illumination. After each washing step the substrate was blow-dried in an airstream.

step	solution	duration / s	purpose
1	developer	20	dissolution of illuminated photoresist
2	bidest. H_2O		washing
3	$H_2O/HCl/HNO_3$ (47:47:6)	60	ITO etching
4	bidest. H_2O		washing

The passivation layer consisted of the same photoresist, which was deposited on top of the ITO structure in the same manner as described before. However, after the soft bake and illumination through the respective mask, only the steps 1 and 2 in Tab. III-17 were performed. This was followed by a hard bake, where the photoresist gets crosslinked and stabilized by heat treatment in an oven at 118 °C for 2 h.

3.3.2   Electrode Design

The electrode designs of the bipolar electrodes used in this work can be divided in two categories, both of which are described below.

3.3.2.1   Bipolar Electrodes Category 1

Category 1 is basically a U-shaped ITO conduction layer with contact pads on each side (Fig. III-43a). The passivation layer deposited on top of the ITO structure either left the whole structure open (Fig. III-43b), or smaller equally sized openings in the photoresist with an area of $5.8 \pm 0.2 \cdot 10^{-3}$ cm² (N = 5, ± SD) at positions on the conduction path with different distances (1 mm, 5.5 mm, and 10.5 mm) from the contact pads (Fig. III-43c – e). The different structures were designated as shown in Tab. III-18. The corresponding photographs are shown in Fig. III-44. The bulk resistance of the electrolyte was minimized by placing the two poles of the bipolar electrode close to one another. For the conduction path to exhibit a sufficiently high resistance, the following considerations for the electrode design were implemented. That way, current coupling with the electrolyte was ensured.

(1) Minimization of the Electrode Width

The width of the conduction path was set to 500 µm as a compromise between maximum resistivity and sufficient geometric reproducibility. Further reducing the width lead to strong variations in the electrode dimensions due to limitations in the precision of the

photomask and lithography wet etching process and, therefore, in the resistance between the contact pads.

(2) Maximization of the Electrode Length

The entire conduction path between the contact pads was 2.5 cm. A U-shape was chosen because of its simplicity. A meander structure with several turns would certainly increase the resistance and at the same time require less space, but also complicate the equivalent circuit and the interpretation thereof.

(3) Use of ITO as Electrode Material

ITO has a conductivity that is several magnitudes lower than that of gold and thus shows a much higher resistance given the same thickness, length, and width of the conduction path. Preliminary experiments showed that gold, sputtered with a layer thickness of only 20 nm, is applicable for bipolar electrode measurements and is even thin enough to be used in combination with an inverse microscope. However, the resistance of ITO was still about 3 to 4 times as high with the same layout.

Tab. III-18: Designations of the different electrode designs of category 1 bipolar electrodes as used in this work.

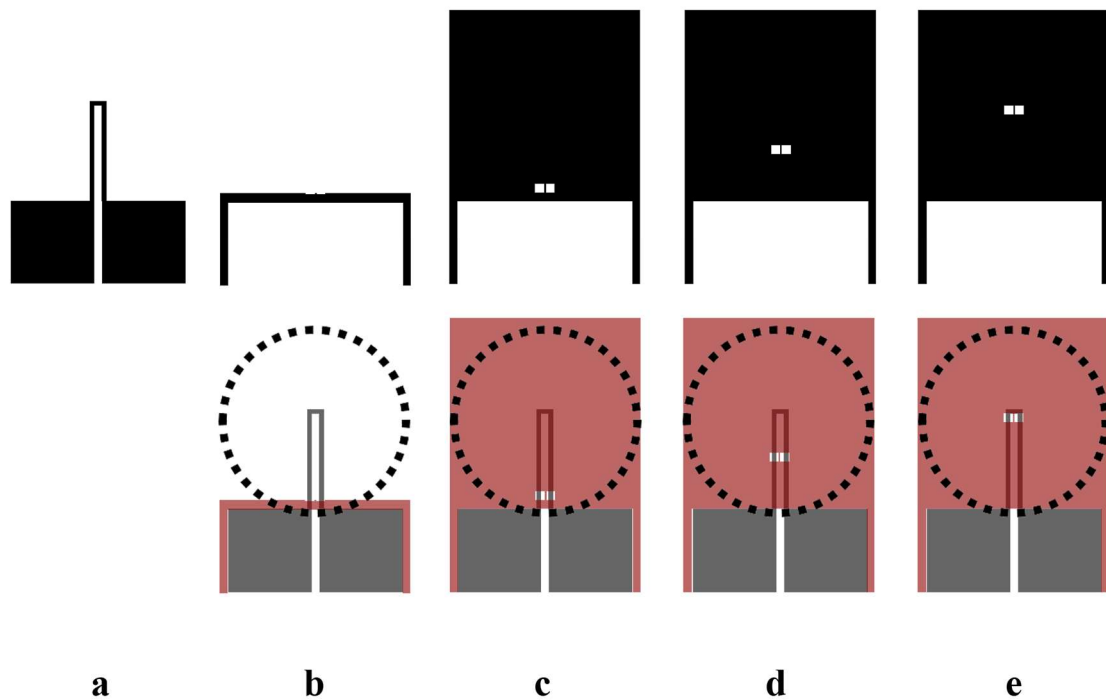| designation	abbreviation	structure
voltage gradient / open structure	VG	Fig. III-43b
high voltage	HV	Fig. III-43c
medium voltage	MV	Fig. III-43d
low voltage	LV	Fig. III-43e

Fig. III-43: Electrode designs of category 1 bipolar electrodes. The ITO structure (a) and the passivation layer structures (b – e) are shown for an open structure (b), and for electrode openings at different distances from the contact pads (c – e). The photolithography masks are depicted in the upper row and the corresponding overlays of ITO and passivation layer in the lower row. The position of the well (a glass ring with 2.3 cm in diameter) is indicated by a dashed line on each overlay (grey: electrode structure, red: photoresist structure, white: holes in the structures).
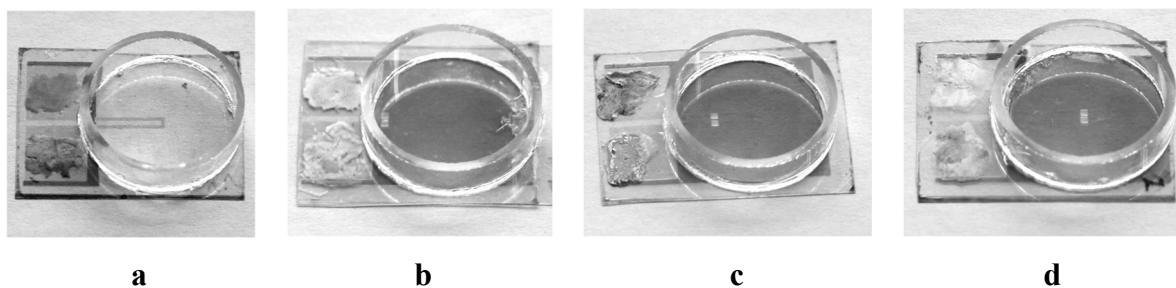

Fig. III-44: Photographs of category 1 bipolar electrodes with an open structure (a), and with electrode openings at different distances (1 mm, 5.5 mm, and 10.5 mm) from the contact pads (b – d). A glass ring with a diameter of 2.3 cm was used as measurement chamber. The contact pads were covered with silver conducting paste to avoid scratches caused by the clamps.

3.3.2.2   Bipolar Electrodes Category 2

The category 2 bipolar electrodes were designed to be able to interpret the impedance spectra with regard to the electrode and cell parameters using a modified ECIS model. The ITO structure comprised two larger areas that were connected via a meander structure (Fig. III-45). The passivation layer had an opening on each of these larger areas, accounting for a small WE ($5.2 \cdot 10^{-3}$ cm², N = 3, ± SD) and a roughly 500 times larger CE like in the ECIS layout. For

comparison, electrode layouts were fabricated, where the meander structure was discontinued with a scalpel. This corresponds to an ECIS layout with the WE and CE being only coupled via the electrolyte. Thereby, the bipolar electrode was turned into a regular two-electrode ECIS electrode arrangement with otherwise similar dimensions.
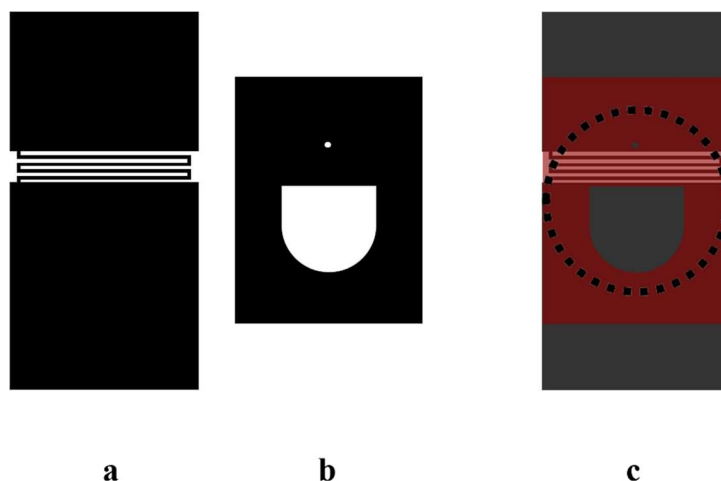

Fig. III-45: Electrode design of category 2 bipolar electrodes: (a) ITO structure, (b) passivation layer, and (c) overlay. The position of the well (a glass ring with 2.3 cm in diameter) is indicated by a dashed line on the overlay (grey: electrode structure, red: photoresist structure).
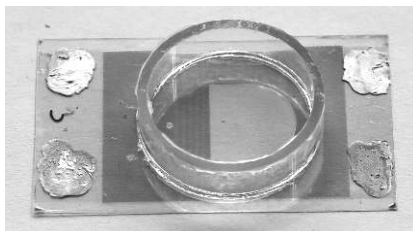

Fig. III-46: Photograph of a category 2 bipolar electrode. A glass ring with a diameter of 2.3 cm was used as measurement chamber. The contact pads were covered with silver conducting paste.

A glass ring glued on top of the electrodes was used as measurement chamber for both electrode categories. It created a well area of 4.15 cm² with a volume of 1.5 mL. This required a relatively high number of cells for confluent seeding (2000000 cells) and a correspondingly large amount of all experimental solutions. Consequently, for Live/Dead staining experiments, a PDMS (polydimethylsiloxane) inset was placed inside the glass ring to reduce the well area to 0.52 cm² and volume to 200 µL, and thereby minimize unnecessary wastage of the expensive and toxic dyes (cf. 3.4.1.3).

3.3.3   Electrode Preparation and Cell Manipulation

All ITO electrodes prepared for cell inoculation according to the following procedure. The arrays were subjected to argon plasma treatment for 30 s before subsequent addition of 1.5 mL pre-warmed cell culture medium and recording of the baseline impedance. After about 1 h, the medium was replaced by 1.5 mL cell suspension and the cells were allowed to settle for 20 min before placing the array into the incubator. This allows for a homogeneous distribution of the cells on the bottom of the wells. All measurements were performed on confluent MDCK II cell layers.

In case of cytochalasin D treatment, 750 µL of the supernatant were aspirated and replaced by an equal amount of a 10 µM cytochalasin D solution in cell culture medium, yielding a final concentration of 5 µM. The impedance was recorded for 1 h before substituting 750 µL of the cytochalasin D containing cell culture medium with 750 µL of a 0.1 mg/mL saponin solution in cell culture medium to give a final concentration of 0.05 mg/mL in each well.

The electrode and cell parameters were obtained by manual fitting. The electrode area A_{el} was optically determined using a phase contrast microscope. The resulting average value was employed as preset value to fit each electrode.

3.3.4   Wounding

MDCK-II cells were seeded to confluency on category 1 bipolar electrodes two days before the wounding experiment. For wounding, the cells were kept in medium, subjected to a 5 V pulse over 60 s at an AC frequency of 40 kHz and were subsequently stained by Live/Dead assay (cf. 1.1.5). Since only the shape of the wound and the cell viability after application of the electric field was of interest in this work, the repopulation of the electrode – as performed in regular ECIS-based wound healing assays – was not followed over time.

3.4 Results and Discussion

3.4.1   Bipolar Electrodes Category 1

3.4.1.1   Characterization of Open Bipolar Electrodes

Fig. III-47 A shows the impedance magnitude spectra of cell-free and cell-covered open bipolar electrodes (category 1) with adherent MDCK-II cells as model system. Up to 10 Hz, the impedance magnitude of the cell-free electrode is constant at around 2700 Ω. In this frequency region, |Z| of each individual electrode corresponds to the inherent resistance of the conduction

path $R_{\parallel}$, i.e. the DC resistance between the two contact pads. The frequency segment between 100 Hz and 10 kHz shows capacitive behavior with decreasing impedance until a second impedance level at $\sim 900\ \Omega$ is reached for frequencies >10 kHz. The phase spectrum reveals the constant regions in the |Z| spectrum to be resistive as the phase is approximately 0° in the respective frequency regions (< 10 Hz) (Fig. III-47 B). In between, the phase shows a minimum whose position (1.3 kHz) coincides roughly with the half-maximum drop between the two constant regions in the impedance magnitude spectrum (Fig. III-47 A). The phase minimum is about -25° and therefore not purely capacitive. The impedance magnitude of cell-covered electrode differs from the spectrum of the cell-free electrode between 250 Hz and 100 kHz, very similar to ECIS recordings (a more detailed comparison between bipolar and ECIS electrodes is provided in chapter 3.4.1.3). The phase spectrum of the cell-covered electrode retains its shape, but is shifted towards higher frequencies with a minimum at 8 kHz.
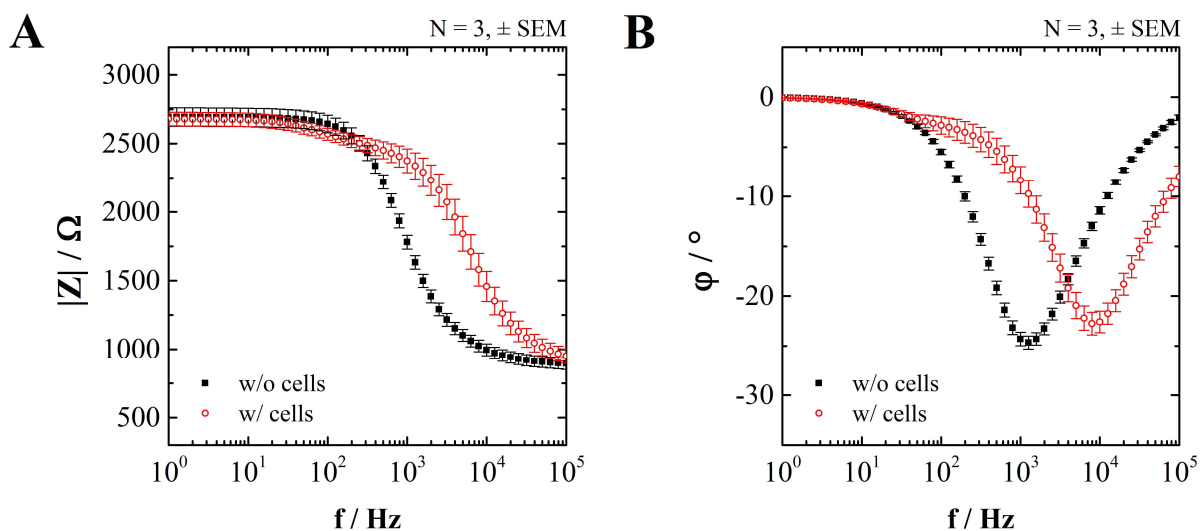

Fig. III-47: Cell-free open bipolar electrode (■) and covered with a confluent MDCK-II cell monolayer 40 h after seeding to confluence (○). **(A)** Frequency spectrum of the impedance magnitude |Z|. **(B)** Frequency spectrum of the phase angle φ. T = 37 °C, V = 10 mV

3.4.1.2   Comparison of Electrodes with Different Potentials

In order to gain access to defined voltages between two areas along the bipolar electrode, a passivation layer was deposited on top of the open bipolar electrodes with openings at different positions along the conduction path (cf. 3.3.2). The corresponding impedance magnitude spectra are depicted in Fig. III-48 A in comparison with the open structure. All electrodes exhibit a constant impedance magnitude up to at least 10 Hz, that corresponds to the electrode resistance $R_{\parallel}$. Compared to the open structure (VG = voltage gradient), the HV (high voltage) and MV (medium voltage) spectra are shifted towards higher frequencies. It is notable that there

is a frequency shift towards higher frequencies from the HV to the MV spectrum, even though both electrodes have the same active electrode area. The LV (low voltage) spectra are merely determined by $R_\parallel$ and a parasitic element, indicated by a subtle bend at the high frequency end of the spectra. Furthermore, the frequency region between 10 kHz and 100 kHz, which is commonly attributed to R_{bulk} in series with R_{lead}, shows an increasing impedance magnitude in the order VG < HV < MV < LV, whereas the difference between VG and HV is rather small. Accordingly, the corresponding normalized impedance magnitude spectra indicate a decreasing sensitivity in the same order (Fig. III-48 B). The maximum sensitivity of the HV and MV electrodes is at 16 kHz, whereas it is shifted to lower frequencies for the VG electrodes. Due to a lack of significant difference between the cell-covered and the cell-free electrode, the LV electrodes do not show any notable sensitivity.
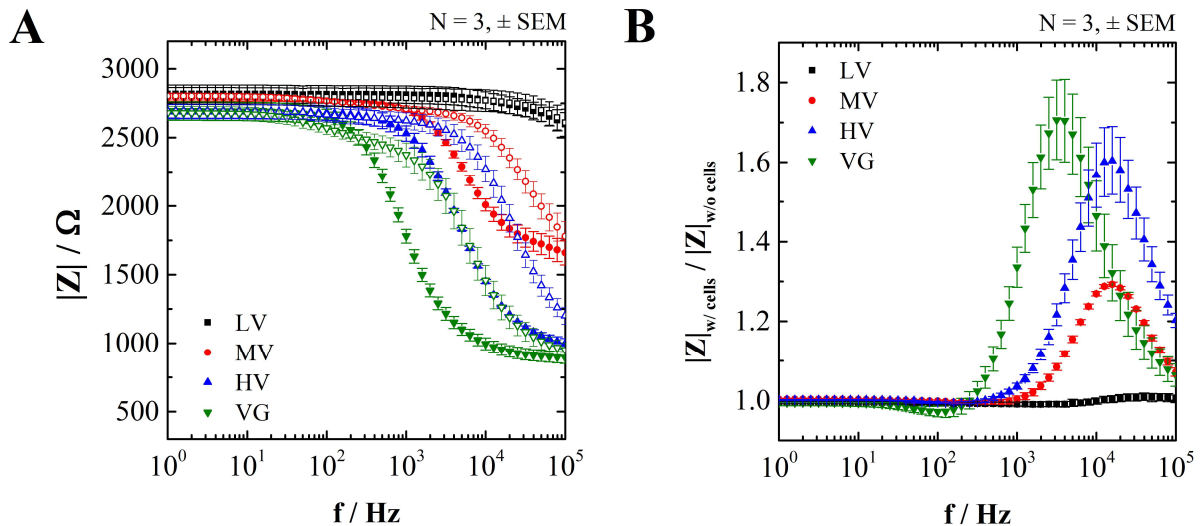

Fig. III-48: (A) Impedance magnitude spectra of different bipolar electrode structures (category 1). The open structure is designated VG (voltage gradient), whereas the other structures have distinct voltages defined by openings in a passivation layer at different positions along the conduction path of the electrode (HV = high voltage, MV = medium voltage, LV = low voltage). Full symbols stand for cell-free electrodes and empty symbols for cell-covered electrodes. The spectra of the cell-covered electrodes were recorded 40 h after seeding MDCK-II cells. **(B)** Corresponding normalized impedance magnitude spectra. T = 31 °C, V = 10 mV

3.4.1.3   Wounding

Wounding experiments were conducted on MV, HV, and VG bipolar electrodes using MDCK-II cells to investigate the invasiveness of the voltage pulse depending on the position on the conduction path of the electrode. Since the LV electrodes do not show any significant cell signal they were not included in this study. The Live/Dead images of the cells on the electrodes at the end of the wounding experiments (cf. 3.3.4) are shown in Fig. III-49. The images of the MV and HV electrodes (Fig. III-49, *left* and *central column*) are recorded to show

the conduction path covered by the passivation layer on the left half and the active electrode area on the right half of the image for comparison. This is not possible for the open VG electrodes (Fig. III-49, *right column*). Here, the conduction path close to the contact pads is depicted, where the potential gradient and its impact on the cells are most apparent. In all images, the contact pads are on the right-hand side. The MV electrodes appear completely unaffected by the wounding current (Fig. III-49, *left column*). The cells are throughout viable, independent of the position on the electrode or the passivation layer. By contrast, the HV electrodes clearly show EthD-1 staining delimited to the active electrode area (Fig. III-49, *central column*). The upper left corner of the electrode is devoid of cells as is evident by the absence of both CaAM and EthD-1 dye. The electrode area in the VG electrode image can be divided into three 'zones' in which the cells reacted differently to the wounding pulse (Fig. III-49, *right column*). In the zone farthest away from the contact pads (on the left), the cell layer is viable with only scarcely distributed red stained cells (> 600 µm from the edge of the passivation layer). The central zone shows both live and dead cells, however mostly still adhered to the electrode surface (~ 200 – 400 µm from the edge of the passivation layer). By contrast, in the zone closest to the contact pads (on the right), the cells are for the most part detached or dead and only few viable cells remain (< 200 µm from the edge of the passivation layer). Both poles of the electrode are equally affected (not shown).
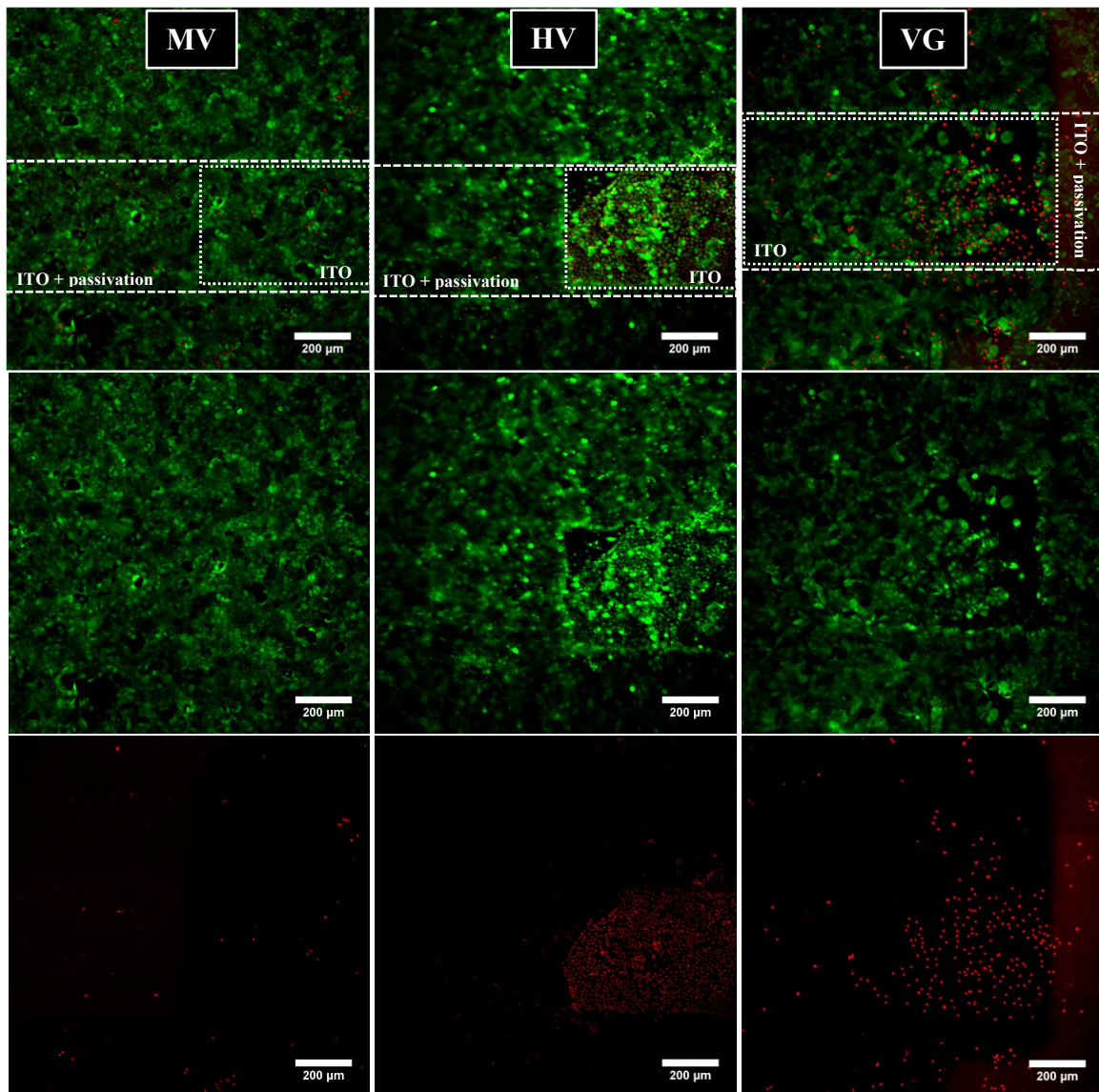
Fig. III-49: MDCK-II cells after wounding (60 s, 5 V) and subsequenz Live/Dead staining using different bipolar electrode category 1 layouts (*left column*: MV, *central column*: HV, *right column*: VG). *Upper row*: Overlay of CaAM (green) and EthD-1 (red) staining) with marked electrodes. *Central row*: CaAM staining of living cells. *Lower row*: EthD-1 staing of dead cell. In each image, the conduction path of the electrode runs horizontally across the visual field (dashed lines). The dotted lines delineate the active electrode areas not covered by a passivation layer. The contact pads are located on the right-hand side of the images.

3.4.1.4   Discussion

a) Open structure / voltage gradient (VG)

Based on these results, we suggest that the constant low frequency region (< 10 Hz) of the spectra is entirely determined by the electrode resistance. At higher frequencies, the interface impedance Z_{CPE} and the bulk resistance R_{bulk}, or the dielectric properties of the cell layer dominate the spectrum like in the ECIS model. However, the ECIS model cannot be applied to analyze data for the VG layout. It requires a small working electrode dominating the overall interface impedance to hold true, whereas in this case, there is only one large bipolar electrode over which the applied voltage is distributed.

Fig. III-50: Schematic equivalent circuit for a cell-free open bipolar electrode structure (category 1). The saw-toothed line was used to describe distributed elements.

The proposed equivalent circuit is shown in Fig. III-50. The electrode resistance $R_{||}$ is the sum over all infinitesimal resistance segments dR_i and runs parallel to the interface impedance Z_{CPE} and the bulk resistance R_{bulk}, which are delocalized along the conduction path of the electrode. The resistance between a certain position on the electrode and the contact pads has to be regarded as lead resistance R_{lead}. Accordingly, the voltage drop across R_{lead} reduces the effective voltage potential V_{eff} at that point. Therefore, V_{eff} declines with the distance L from the contact pads and there is a potential gradient along the electrode. For an application of bipolar electrodes for the electroporation or wounding optimization as proposed in the introductory chapter 3.1, it is necessary to calculate $U_{eff}(L)$. However, implementing the delocalized circuit elements Z_{CPE} and R_{bulk} requires a more sophisticated mathematical effort as the current along the conduction path is not constant. This was not established within the scope of this thesis, where the focus was set on a proof of principle approach.
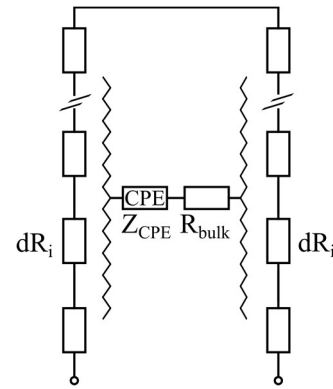
b) High voltage (HV), medium voltage (MV) and low voltage (LV) structure

Considering the electrodes with defined voltages (HV, MV, and LV), their increasing impedance magnitude in the high-frequency region supports these interpretations. The further away any given point on the conduction path is from the contact pads, the higher is the lead resistance. It is in series with the electrolyte resistance and thus affects the high-frequency region between 10 kHz and 100 kHz as displayed in Fig. III-48 A. The corresponding proposed equivalent circuits are shown in Fig. III-51.

Fig. III-51: Schematic equivalent circuit for cell-free category 1 bipolar electrode structures HV, MV, and LV.

The electrode openings of the LV electrodes are separated by only a small distance of the conduction path. Accordingly, the resistance between these positions along the conduction path is so small that the corresponding voltage drop does not allow sufficient coupling through the electrolyte and the cells cannot be sensed. Working and counter electrode are basically short-circuited by the conduction path. The impedance shift towards higher frequency when comparing the open (VG) with the partially passivated structures (HV, MV, LV) can be explained by the smaller electrode area of the latter. For the same reason, the high-frequency region (> 20 kHz) of the HV electrodes shows a slightly higher impedance magnitude than the VG electrodes, even though the lead the resistance is the same. This can be explained by the smaller electrode area. It entails a higher constriction resistance, which is included in R_{bulk}. The reason for the frequency shift from the HV to the MV electrodes with identical electrode areas has not yet been clarified.

c) Wounding

The Live/Dead staining reveals a clear difference in the potential difference between different positions along the conduction path of the electrode. Close to the contact pads, where the lead resistance is at its minimum, the applied voltage is sufficient to wound the cell layer (HV electrode). However, at a distance of 5.5 mm too much voltage is lost over the leads to reach the required electric field threshold across the cell layer and the cells remain unharmed (MV electrode). On the open VG electrode, the cells show a 'death gradient', ranging from viable cells (at maximum distance from the contact pads) over an increasing number of dead cells to mostly detached cells (close to the contact pads). We can, therefore, assume that a voltage
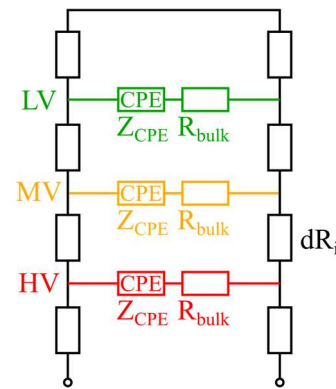
gradient along the electrodes leads to an electric field across the cell layer, which depends on the respective position on the conduction pathway. In the current setup, the relevant gradient only extends over about 800 µm. Before using the bipolar electrodes for the optimization of the wounding parameters, it is advisable to extend this distance in order to enhance the accuracy of the determination of the optimal voltage. This is achieved by appropriate electrode design. Wu et al. achieved a similar gradient using two coplanar electrodes with hyperbolic shape, however applying large DC electric fields.[211] Originally designed for electroporation optimization, the cells were also wounded in the areas with the highest electric fields. Our setup is presumed to be applicable for both wounding and electroporation in a similar fashion.

3.4.2   Bipolar Electrodes Category 2

The category 2 bipolar electrodes are covered with a passivation layer, delineating a small working electrode and a large counter electrode like the ECIS electrodes. The conduction path of the electrode runs beneath the passivation layer and thus retains its bipolar nature. That way, it is possible apply a modified ECIS model to determine the electrode and cell parameters. The results from these bipolar electrodes were compared to ECIS-like ITO electrodes, where the conduction path was discontinued underneath the passivation layer as described in chapter 3.3.2.2.

3.4.2.1   Analysis of Impedance Spectra

Between 250 Hz and 100 kHz, the impedance magnitude spectra of the cell-free bipolar and ECIS electrodes do not differ significantly (Fig. III-52 A). Both electrode types show capacitive behavior between 250 Hz and 10 kHz, determined by the electrode-electrolyte interface, and show a resistive region from 10 kHz to 100 kHz, caused by R_{bulk}. The minor differences are probably due to an inaccurate fabrication process of the ECIS electrodes. Below 250 Hz, the ECIS electrodes portray the typical interface impedance with a negative slope around -1, whereas the bipolar electrodes show strong depression towards a value that corresponds to the resistance of the bipolar bridge $R_{\parallel}$ (~ 11 kΩ). Accordingly, the cell signal of the MDCK-II cells is capped by the electrode resistance at frequencies below 1 kHz. This is also reflected in the normalized impedance magnitude, where the bipolar and ECIS electrodes show similar values at frequencies above 1 kHz, but are perceptibly reduced for the bipolar electrodes below this frequency (Fig. III-52 B). The peak maxima are in the same order (~ 3), but the peaks have a much broader shape for ECIS electrodes. The differences between the spectra are more severe when regarding the real part of the impedance (Fig. III-52 C). The frequency dependent

behavior of the resistance is only caused by the interface impedance not being purely capacitive ($n_{cpe} < 1$). Therefore, the cell-free ECIS electrodes appear at relatively low frequencies in the resistance spectrum compared to the impedance magnitude spectrum. By contrast, the bipolar electrodes exhibit largely the same impedance magnitude and resistance spectra with the latter being slightly shifted towards lower frequencies. As a consequence, the normalized resistance of the ECIS electrodes is significantly higher below 1 kHz, when compared to the bipolar electrodes (Fig. III-52 D). The capacitance spectra of the bipolar electrodes display a very distinct feature that sets themselves apart from the ECIS electrodes (Fig. III-52 E). The capacitance of the cell-free ECIS electrodes exhibits a slightly negative slope caused by the CPE behavior of the interface capacitance (cf. II.1.3), but is otherwise mostly linear. The cell-covered spectrum is determined by the electrode capacitance up to about 250 Hz and drops to the level of the capacitance of the cell layer beyond that. The spectra of both electrode types look very much alike between 5 kHz and 100 kHz. However, the capacitance of the cell-free bipolar electrodes shows strong frequency dependent behavior below 1 kHz. A linear fit through the data points of the double logarithmic plot between 1 Hz and 200 Hz yields a slope of -1.84 ± 0.06 (N = 3, ± SEM). Remarkably, the spectra of the cell-free and the cell-covered bipolar electrodes share a crossing point at 1 kHz, so that their capacitance values are inverted below that frequency. As a result, the normalized capacitance is > 1 between 10 Hz and 1 kHz and < 1 at higher frequencies as observed for ECIS electrodes along the entire frequency spectrum (Fig. III-52 F). The maximum of the normalized capacitance is at 250 Hz with a value of about 2.4.
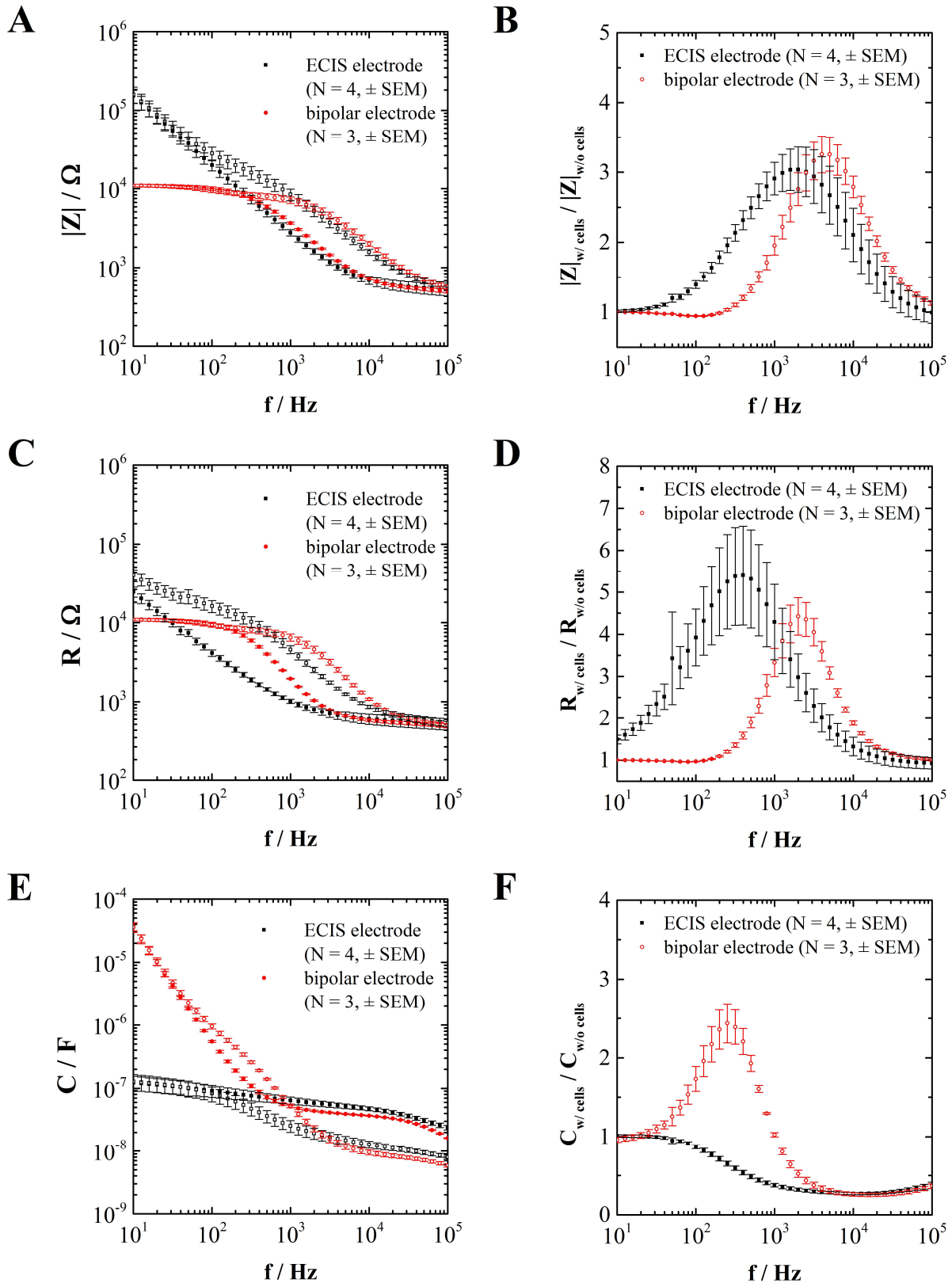
Fig. III-52: Frequency spectra of different impedance components comparing ITO ECIS electrodes to bipolar electrodes category 2. **(A)** Impedance magnitude |Z|, **(B)** normalized impedance magnitude, **(C)** resistance R, **(D)** normalized resistance, **(E)** capacitance C, **(F)** normalized capacitance. In (A), (C), and (E), full symbols (■, ●) correspond to cell-free electrodes and empty symbols (□, ○) to cell-covered electrodes. The cell-covered electrodes were recorded 40 h after confluently seeding MDCK-II cells on the electrodes. T = 37 °C, V = 10 mV

3.4.2.2   Cell Attachment and Spreading

In this chapter, the kinetics of MDCK-II cell attachment and spreading on ECIS and bipolar electrodes are described using frequencies and dimensions that are either common for classical ECIS recordings or portray notable differences between ECIS and bipolar electrodes. Recording the impedance magnitude at 4 kHz is a widespread way to monitor changes in cell shape and morphology. At this frequency, the normalized impedance exhibits almost the same value for both electrode types (cf. Fig. III-52 B). It is apparent from Fig. III-53 A that the time courses for cell attachment and spreading are very similar as well. Directly after cell seeding ($t = 0$), $|Z|$ stays almost constant for about 5 h and then increases considerably for the next 6 to 7 h, after which the impedance level of the fully spread cell layer is reached. The time course of the resistance at 400 Hz has been shown to represent the barrier function formation of a cell layer.[168] The time course of resistance upon cell attachment and spreading is similar to the impedance magnitude, however with different magnitudes of the signal change (Fig. III-53 B). At 400 Hz, the ECIS electrodes show higher sensitivity (cf. Fig. III-52 D) and thus a much stronger signal change in the time course. The capacitance at 32 kHz or 40 kHz is commonly used to follow changes in the the electrode coverage with cells.[158]. At 32 kHz, no major differences between ECIS and bipolar electrodes are found (Fig. III-53 D). Both electrode types exhibit a sudden drop in the capacitance directly after cell seeding and reach their minimum level after about 11 h. However, the time courses differ considerably when regarding the capacitance at 250 Hz, which is the frequency of the normalized capacitance maximum of the bipolar electrodes. Here, the capacitance of the ECIS electrodes remains constant during the first 10 h after seeding and then declines by about 30% during the next 5 h. By contrast, the bipolar electrodes display an increasing capacitance, whose curve shape resembles that of the impedance magnitude or resistance during adhesion more closely.
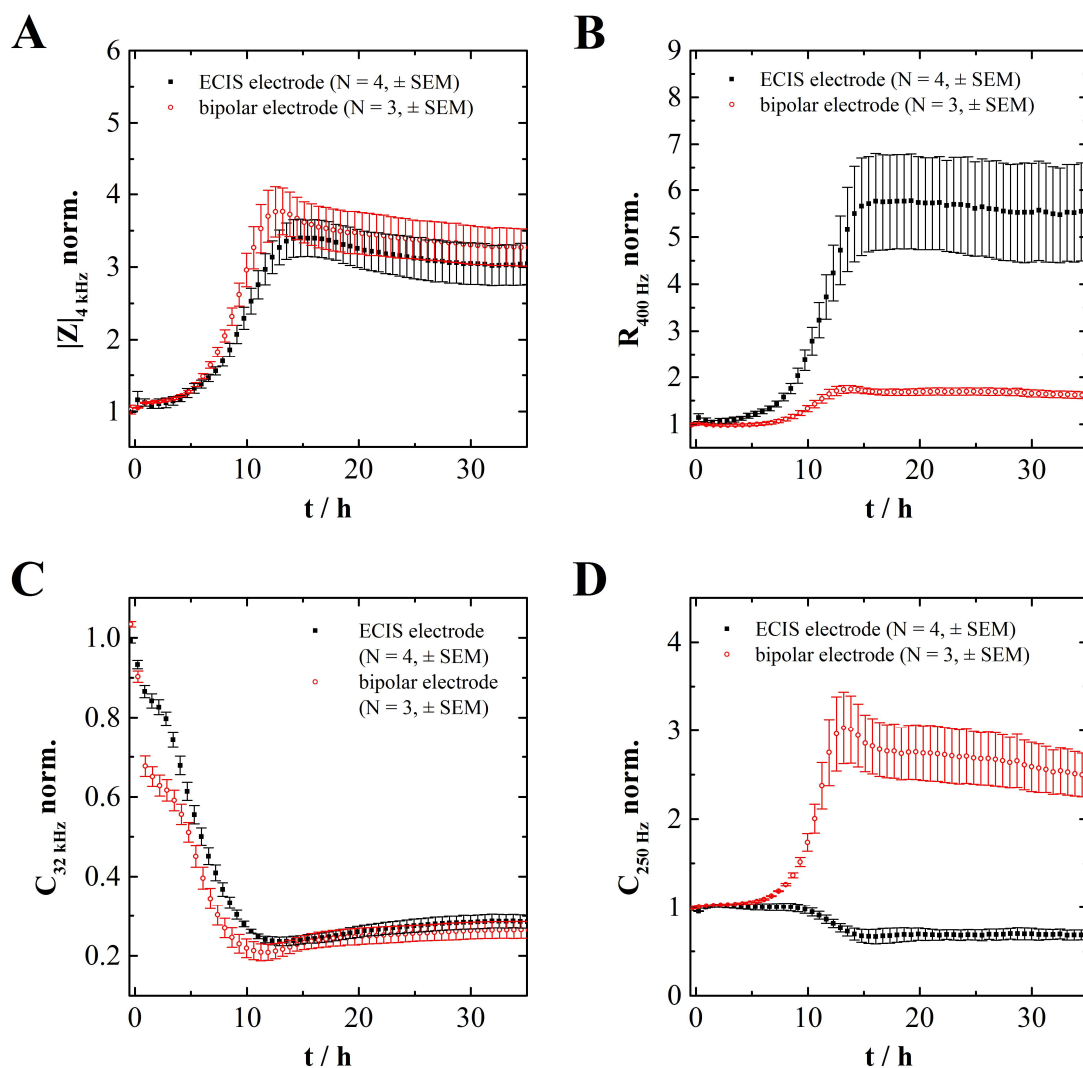
A

B

C

D

Fig. III-53: Cell attachment and spreading of MDCK-II cells followed at different frequencies using ITO ECIS and bipolar electrodes with equal electrode dimensions. The time courses were normalized to the time point before cell seeding (t = 0). **(A)** |Z| norm. at 4 kHz. **(B)** R norm. at 400 Hz. **(C)** C norm. at 32 kHz. **(D)** C norm. at 250 Hz. T = 37 °C

3.4.2.3   Determination of the Electrode and Cell Parameters

The electrode parameters of the bipolar electrodes category 2 as obtained by manual fitting are listed in Tab. III-19. The ECIS electrodes with ITO as electrode material that were described in chapters 3.4.2.1 and 3.4.2.2 could not be used for comparison due to certain parasitic influences with unknown origin, which impeded the fitting (cf. Fig. III-52 A and E, between ~ 1 kHz and 10 kHz). The parasitic element did not affect the qualitative interpretations from the previous chapters, while fitting the spectra yielded unrealistic electrode parameters. Instead, the results for the 8W10E gold electrodes from chapter *2 PEDOT:PSS as Electrode Material* were adopted and compared to the results obtained from the bipolar electrodes category 2 in this chapter. The interface parameters of the bipolar electrodes $A_{cpe} = 15 \pm 5 \ \mu F \cdot s^{(n-1)}/cm^2$ and $n_{cpe} = 0.92 \pm 0.03$

are in the typical range of ECIS gold electrodes. A value of $R_{\parallel} = 11.0 \pm 0.4$ kΩ is found for the resistance of the conduction path, which corresponds to the DC resistance between the contact pads. Despite having about the same electrode area, the bipolar electrodes show almost twice the value for the bulk resistance as the 8W10E electrodes. This indicates different lead resistances caused by the relatively low conductivity of ITO. The parasitic impedance was fitted directly to the spectrum of the cell-free bipolar electrodes. For the bipolar electrodes, A_{prs} is roughly an order of magnitude higher than for 8W10E electrodes, which is probably due to the different measurement setups used to record the impedance spectra. Some parameters of the cell-free bipolar electrodes show relatively large errors. Those are in particular A_{cpe} and R_{bulk} with relative standard deviations σ_{rel} of 60% and 20%, respectively.[f]

Tab. III-19: Electrode parameters of the bipolar electrodes category 2 (N = 3, ± SEM). The electrode area was determined with a phase contrast microscope. All other parameters were obtained by manual fitting. The electrode parameters of 8W10E electrodes from chapter *2 PEDOT:PSS as Electrode Material* were added for comparison (N = 4, ± SEM). T = 37 °C

parameter	bipolar	8W10E
A_{el} / cm²	$(5.2 \pm 0.1) \cdot 10^{-3}$	$5 \cdot 10^{-3}$
A_{cpe} / μF·s$^{(n-1)}$/cm²	15 ± 5	17.3 ± 0.3
n_{cpe}	0.92 ± 0.03	0.9452 ± 0.0002
$R_{\parallel}$ / kΩ	11.0 ± 0.4	inf
R_{bulk} / Ω	560 ± 60	288 ± 6
A_{prs} / nF·s$^{(n-1)}$/cm²	3.5 ± 0.6	0.24 ± 0.04
n_{prs}	0.86 ± 0.00	0.981 ± 0.003

Tab. III-20 and Fig. III-54 summarize the fit results of confluent MDCK-II cell monolayers seeded on bipolar and 8W10E electrodes. The differences between both electrode types are quite noticeable, with R_b and α showing almost twice the value on the bipolar electrodes. The C_m values are in the same range, but still significantly lower on the bipolar electrodes. There are, however, some different experimental conditions that have to be kept in mind when comparing the cell parameters. First of all, the experiments were several months apart and were conducted with cells of different passage numbers. Moreover, unlike the bipolar electrodes, the 8W10E electrodes were pre-coated with poly-L-lysine before seeding. This, as well as the

---

[f] $\sigma_{rel} = \dfrac{\text{SEM} \cdot \sqrt{N}}{\mu}$, where σ_{rel} is the relative standard deviation, SEM is the standard error of the mean, N is the number of measurements, and μ is the mean.

different electrode materials, could affect the cell parameters. There are, however, also technical considerations to be accounted for. The large SEM of R_b that corresponds to $\sigma_{rel} = 60\%$ is most likely due to the electrode parameters being hard to determine in this case, as can be seen from the errors of A_{cpe} and R_{bulk} in Tab. III-19.

Tab. III-20: Fit results of impedance recordings of MDCK-II cells 40 h after seeding on bipolar ITO electrodes (N = 3, ± SEM) in comparison with 8W10E gold electrodes (N = 4, ± SEM). T = 37 °C

parameter	bipolar	8W10E
C_m / $\mu F/cm^2$	3.5 ± 0.2	4.2 ± 0.1
α / $\Omega^{0.5} \cdot cm$	21 ± 1	12.8 ± 0.7
R_b / $\Omega \cdot cm^2$	70 ± 20	33.9 ± 0.4

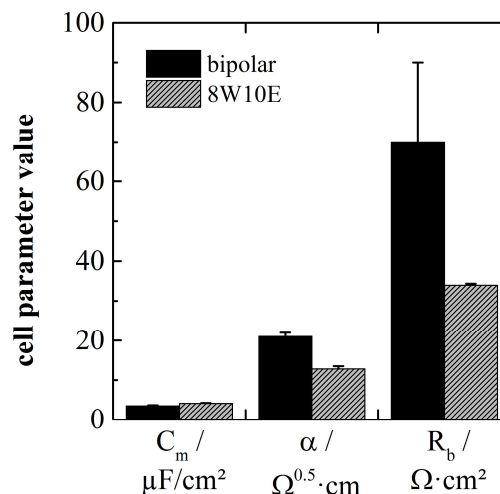**Fig. III-54:** Fit results of impedance recordings of MDCK-II cells 40 h after seeding on bipolar ITO electrodes (N = 3, ± SEM) in comparison with 8W10E gold electrodes (N = 4, ± SEM). T = 37 °C

Tab. III-20 and Fig. III-55 summarize the fit results of MDCK-II cells treated with 5 μM cytochalasin D (CytD) and compare them to the untreated cell layer. The cell parameters were determined 40 h after seeding and 1 h after the addition of CytD, respectively. On bipolar electrodes, all cell parameters are significantly reduced relative to control conditions, while CytD does not have a significant impact on C_m when using 8W10E electrodes. Only α and R_b are affected in a similar fashion. The magnitudes of all cell parameters after CytD treatment are roughly in the same order for both electrode types, given the afore mentioned experimental and technical differences. A more detailed quantitative analysis and comparison is not reasonable in this case.

Tab. III-21: Fit results of impedance recordings of MDCK-II cells after treatment with 5 μM cytochalasin D for one hour on bipolar ITO electrodes in comparison with 8W10E gold electrodes (N = 4, ± SEM). T = 37 °C

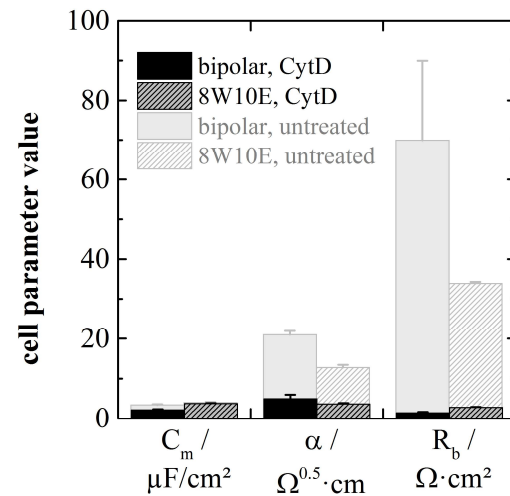| parameter	bipolar	8W10E
C_m / μF/cm²	2.2 ± 0.2	3.8 ± 0.1
α / $\Omega^{0.5}\cdot$cm	5 ± 1	3.7 ± 0.2
R_b / $\Omega\cdot$cm²	1.5 ± 0.2	2.9 ± 0.1

Fig. III-55: Fit results of impedance recordings of MDCK-II cells after treatment with 5 μM cytochalasin D for one hour on bipolar electrodes (N = 3, ± SEM) in comparison with 8W10E electrodes (N = 4, ± SEM). The data of the untreated cell layer (cf. Fig. III-54) were added for comparison. T = 37 °C

3.4.2.4 Simulation of Impedance Spectra with Discrete Bipolar Electrode Resistances

In order to investigate the influence of the electrode resistance $R_\parallel$ on the impedance spectra, simulations were performed using the equivalent circuit described in chapter 1.2.4 with $R_\parallel$ = 100 Ω, 1 kΩ, 10 kΩ, and inf (infinity) (Fig. III-56). Setting $R_\parallel$ to infinity corresponds to a common ECIS electrode with two separate electrodes. At low frequencies (< 10 Hz), the impedance magnitude of the bipolar electrodes shows a constant region that is equal to the respective value of $R_\parallel$ used for the simulation (Fig. III-56 A). |Z| approaches infinity for f→0 on ECIS electrodes ($R_\parallel$ = inf). We know that at high frequencies (> about 100 kHz in this case) |Z| is determined by R_{bulk} when a two-electrode setup is used, given there are no parasitic contributions. For bipolar electrodes, this appears to be true only for large $R_\parallel$ (> 10 kΩ). If $R_\parallel$ is smaller, it leads to a reduction of |Z| at high frequencies (> 10 kHz). A general relationship for the impedance magnitude in that high frequency region $|Z|_{hf}$ of the cell-free electrode can be formulated according to Eq. 42 as derived from the equivalent circuit (cf. 1.2.4). At high frequencies, the term of the capacitive electrode-electrolyte interface term becomes negligible and $|Z|_{hf}$ only depends on R_{bulk} and $R_\parallel$. In this equation, the term $1/R_\parallel$ also becomes increasingly insignificant for higher $R_\parallel$.

$$|Z|_{hf} = \left(\frac{1}{R_{bulk}} + \frac{1}{R_{\parallel}} \right)^{-1}$$

Eq. 42

The impedance contribution of the cells is thereby restricted to impedance magnitude values between $|Z|_{hf}$ and $R_{\parallel}$. Therefore, the normalized impedance magnitude, and thus the sensitivity of the electrode, increases with increasing $R_{\parallel}$ (Fig. III-56 B). In addition, the maximum is shifted towards lower frequencies. The resistance spectra are very similar to the impedance magnitude spectra (Fig. III-56 C), except for $R_{\parallel}$ = inf. In this case, the capacitive region of the cell-free electrode spectrum is shifted towards lower frequencies compared to $|Z|$. As a result, the corresponding sensitivity of R is much higher (~ 18 for R in comparison with ~ 6 for $|Z|$). As described in chapter 3.4.2.1, the capacitance of the bipolar electrodes shows a notable property (Fig. III-56 E). Above a certain frequency it behaves like in a normal two-electrode setup, whereas below that frequency an inversion between the cell-free and the cell-covered spectrum occurs. C approaches infinity for f→0, similar to the impedance magnitude when regarding ECIS electrodes. For $R_{\parallel}$ = 10 kΩ, the high frequency capacitance is at the same level as for $R_{\parallel}$ = inf, but becomes gradually higher with decreasing electrode resistance. Concomitantly, the frequency dependent part of the spectra is shifted towards the high frequency end of the spectrum. Accordingly, the normalized capacitance is < 1 at high frequencies, but shows peak maxima for bipolar electrodes at lower frequencies (Fig. III-56 F). The peak height increases with decreasing electrode resistance up to a value of 6.5 for $R_{\parallel}$ = 100 Ω. The maxima of the normalized capacitance thus show an inverse dependence on the electrode resistance, whereas those of the of the normalized impedance magnitude and the normalized resistance exhibit a direct dependence.
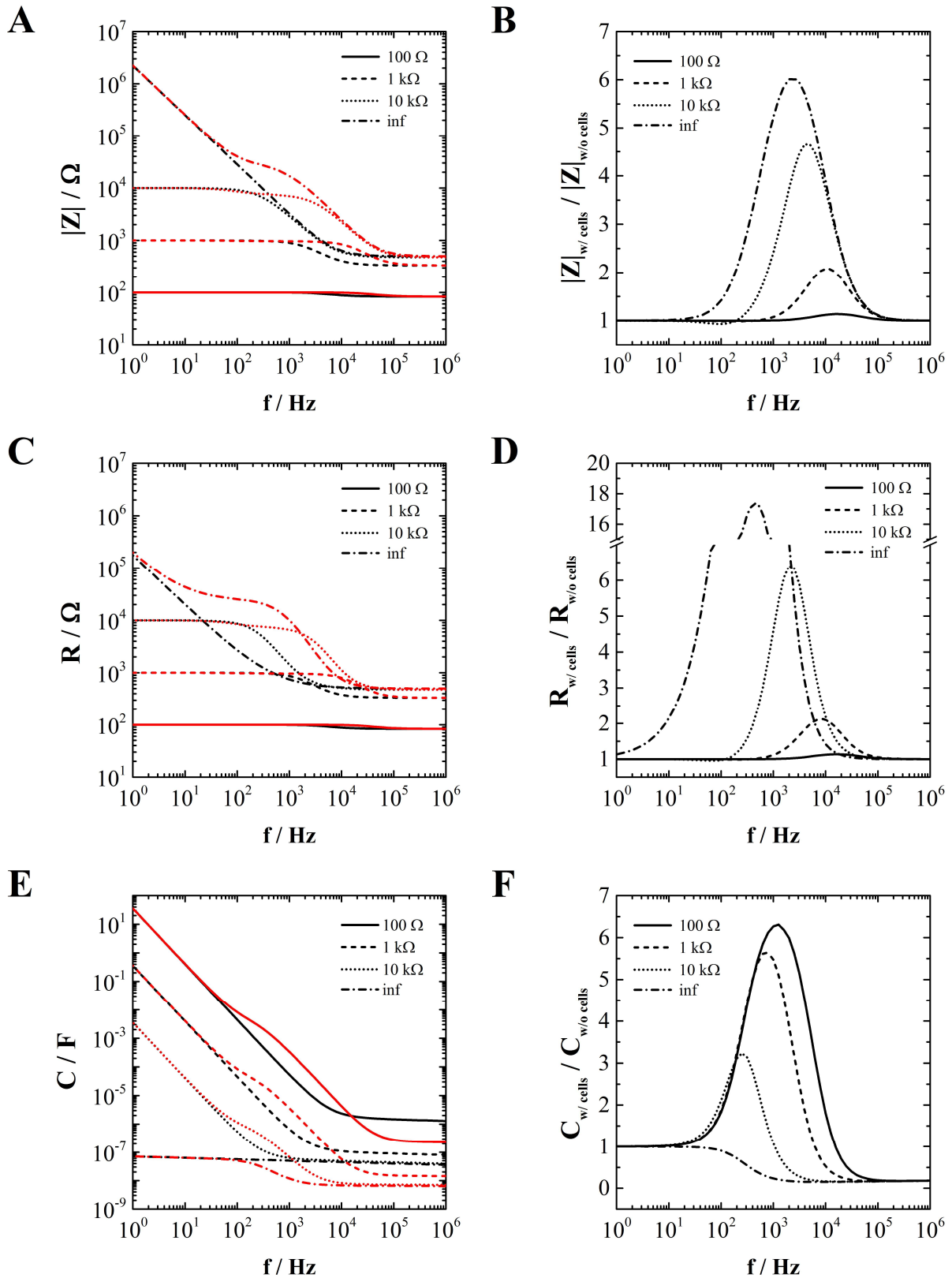
Fig. III-56: Simulation of bipolar electrodes with varying electrode resistances $R_\parallel$ = 100 Ω (*solid*), 1 kΩ (*dashed*), 10 kΩ (*dotted*), and infinity (inf, *dot-dash*). $R_\parallel$ = inf corresponds to a common two-electrode setup. The other simulation parameters were employed as follows: A_{cpe} = 1.5·10⁻⁵ F·s$^{(n-1)}$/cm², n_{cpe} = 0.95, A_{el} = 5.2·10⁻³ cm², R_{bulk} = 500 Ω, C_m = 3 μF/cm², α = 16 Ω$^{0.5}$·cm, R_b = 88 Ω·cm²

3.4.2.5   Simulation of Impedance Spectra of Different Cell Types on Bipolar Electrodes

In this chapter, impedance spectra are simulated for MDCK-I, MDCK-II, and NRK cells growing on bipolar electrodes category 2 to show the effect of different ECIS parameters on the impedance of the bipolar electrodes. The respective ECIS parameters C_m, α and R_b are adapted from the results in chapter 2.2.10 (cf. Fig. III-41). Fig. III-57 A displays the impedance magnitude spectra for all three cell types as well as the cell-free electrode. The spectra of the cell-covered electrodes show very distinct features in a certain frequency range. Below 100 Hz, there is barely any influence of the cells on the spectra and the impedance is only determined by the cell-free electrode. Between 100 Hz and 10 kHz, the impedance increases in the order NRK ($\sim$ 3 kΩ) < MDCK-II ($\sim$ 7 kΩ) < MDCK-I ($\sim$ 9 kΩ) in accordance with their respective R_b and α values. In the capacitive region of the spectrum between 10 kHz and 200 kHz, the impedance of the cell types is shifted towards higher frequencies from MDCK-II to MDCK-I to NRK cells as would be expected from their respective membrane capacitance C_m, which is decreasing in the same order. This behavior is well reflected in the normalized impedance spectra (Fig. III-57 B). The sensitivity between 100 Hz and 10 kHz increases in the order NRK < MDCK-II < MDCK-I, whereas the order is MDCK-II < MDCK-I < NRK between 10 kHz and 200 kHz. The resistance spectra (Fig. III-57 C) are very similar to the impedance magnitude spectra and are only slightly shifted towards lower frequencies. The same is true for the normalized resistance spectra (Fig. III-57 D). However, the spectrum of the cell-free electrode in Fig. III-57 C being shifted towards lower frequencies leads to an increase of the MDCK-I and MDCK-II sensitivity peaks at 4 kHz. While the impedance magnitude and the resistance are almost completely insensitive towards the cells below 100 Hz, the capacitance is affected by the cell types to different degrees in that low-frequency region (Fig. III-57 E). Up to 600 Hz, the capacitance is bigger the higher the respective resistive ECIS parameters R_b and α (NRK < MDCK-II < MDCK-I) are. As described for the impedance magnitude, the capacitance in the high-frequency region (20 kHz – 1 MHz in this case) depends on the membrane capacitance C_m (MDCK-II > MDCK-I > NRK). The intermediate region (600 Hz – 10 kHz) shows a pattern that is inverse to the low frequency region. It is, however, probably affected by all three ECIS parameters.[10] As discussed in the previous chapter (3.4.2.4) the whole frequency region between 600 Hz and 1 MHz is very closely related to classical ECIS measurements[10] (cf. Fig. III-56), while the low-frequency capacitance readings display features specific only for bipolar electrodes. This is well illustrated by the normalized capacitance spectra in Fig. III-57 F, where the intersection point at 600 Hz marks the separation between the low-frequency, bipolar

electrode regime of the spectrum, and the high-frequency, ECIS regime of the spectrum. The NRK cells appear very ECIS-like as they show barely any sensitivity in the 'bipolar region', whereas there is a strong peak for MDCK-I cells at 100 Hz and a less pronounced one for MDCK-II cells at 250 Hz.
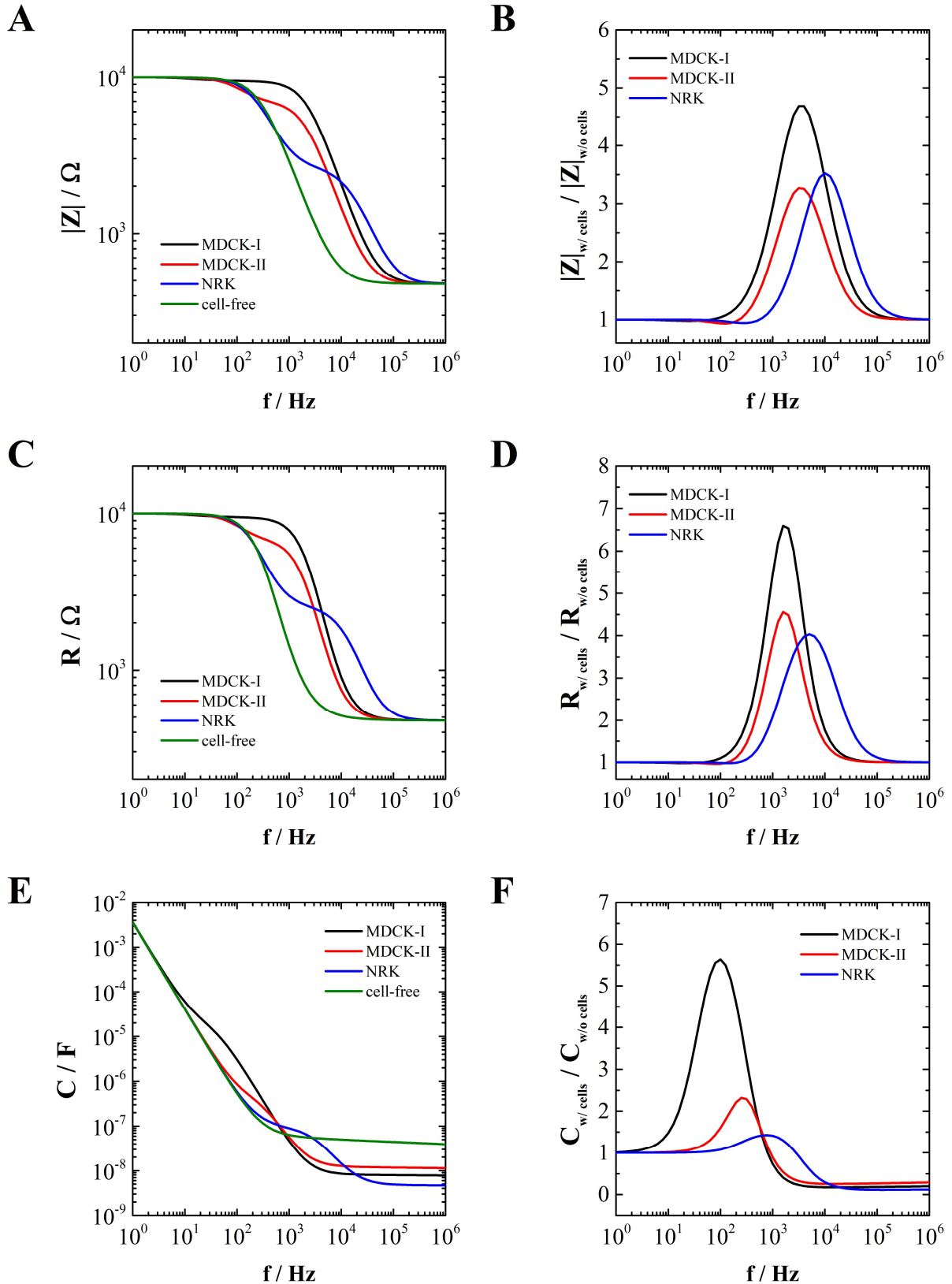
Fig. III-57: Simulation of the frequency-dependent impedance, resistance and capacitance for bipolar electrodes covered with three different cell lines. The characteristic ECIS parameters for each cell line were taken from chapter 2.2.10: MDCK-I (C_m = 3.4 µF/cm², α = 34 $\Omega^{0.5}$·cm, R_b = 600 Ω·cm²), MDCK-II (C_m = 5.6 µF/cm², α = 8 $\Omega^{0.5}$·cm, R_b = 4.8 Ω·cm²), NRK cells (C_m = 1.85 µF/cm², α = 4.8 $\Omega^{0.5}$·cm, R_b = 11 Ω·cm²). The electrode parameters were set as follows: A_{cpe} = 1.5·10⁻⁵ F·s$^{(n-1)}$/cm², n_{cpe} = 0.95, A_{el} = 5.2·10⁻³ cm², R_{bulk} = 500 Ω, $R_{\parallel}$ = 10 kΩ.

3.4.2.6   Discussion

For high enough parallel electrode resistances ($R_\parallel \geq 10$ kΩ), the impedance magnitude of bipolar electrodes corresponds to that of two-electrode setups with the exception of being capped by $R_\parallel$ at low frequencies. It is expected that the sensitivity is capped when measuring cell lines with tight intercellular junctions and correspondingly large impedance contributions like MDCK-I, whereas low-impedance cell lines like NRK are unaffected by the additional parallel conduction pathway. The resistance and capacitance spectra, however, show some more severe differences compared to the regular ECIS electrode arrangement. The resistance of the bipolar electrodes is considerably less sensitive below 1 kHz due to the capping of the electrode resistance. On the other hand, by an inversion of the cell-free and cell-covered spectrum at (for the given simulation parameters) 1 kHz, the capacitance gains sensitivity in a frequency range similar to where the resistance becomes less sensitive. Apparently, using bipolar electrodes, the sensitive component of the complex impedance for monitoring the formation of the barrier forming cell-cell junctions shifts from the real to the imaginary part. This is supported by both experimental evidence (cf. Fig. III-52) and simulations (cf. Fig. III-56) and is relevant for potential future applications of bipolar electrodes as will be discussed below. The observation is also evident by the simulations using cell lines with different ECIS parameters shown in Fig. III-57. The low resistance cell-line NRK appears very ECIS-like in the capacitance spectra as the mean impedance in the R_b and α determined region is much smaller than the parallel electrode resistance $R_\parallel$. On the other hand, the impedance of the high-resistance cell line MDCK-I in that region is very close to $R_\parallel$. The suspected capping in the real part of the impedance R(f) thus leads to a strong cell signal in the imaginary C(f) in the low-frequency region below 100 Hz. The results also suggest that the constant low-frequency part of the impedance magnitude and the resistance spectrum depend only on the parallel resistance of the electrode $R_\parallel$. This may give rise to a combined cell-based and resistive sensor, where the electrode material is sensitive towards a certain analyte or physical quantity like ion concentration or temperature. As an example, PEDOT:PSS has been shown to depend on the cation concentration in the electrolyte.[111] Furthermore, resistive temperature sensors have been integrated in microfluidic devices but have to be controlled separately.[212] Such resistance-type thermometers like the Pt1000 are also used industrially due to their linear temperature dependency.[213] However, achieving the high $R_\parallel$ obligatory for a meaningful sensitivity of |Z| and R to monitor the morphology and barrier function of cells requires either an electrode material with very low conductivity or a long and thin conduction path. The former may prove unfavorable due to a high lead resistance, whereas the latter requires a lot of space and obstructs

miniaturization. It may therefore be a good alternative to design a bipolar electrode with low electrode resistance and use the capacitance for impedance analysis instead of the impedance magnitude or the resistance. This presumes the capacitance to be similarly sensitive for changes in the cell layer, which is yet to be ultimately verified. Aside from the different sensitivities of the impedance components R and C, the cells show similar adhesion and spreading kinetics on both electrode types. Even though certain discrepancies between the cell parameters of MDCK-II cells growing on bipolar and 8W10E electrodes were observed, they are within the range covered by literature (cf. Tab. III-15).[120,202-204] The large error of the electrode parameters suggests that the fabrication process of the electrodes is not yet sufficiently reproducible and requires some improvement. Naturally, the quality of the electrode fabrication performed on a laboratory scale cannot compete with the industrially manufactured 8W10E electrodes. The accuracy of the mean R_b value determined for the bipolar electrodes is thus accordingly low. Considering these errors, the cell parameters lie roughly within the same range on both electrode types.

3.5 Summary and Outlook

In summary, a novel bipolar electrode for the simultaneous impedimetric analysis and manipulation of living cells was developed. The bipolar electrode consisted of a high-resistance conduction path showing a potential gradient that depended on the distance from the contact pads. By appropriate design of an additional passivation layer on top of the electrode, distinct voltages could be tapped, defined by the position of electrode openings in the passivation layer. Upon application of elevated electric fields, the bipolar electrodes were shown to cause a gradient of invasiveness along the conduction path that was caused by an increasing lead resistance with growing distance from the contact pads. We propose this system to be suitable for the optimization of wounding and electroporation experiments as the voltage gradient delineates the optimal voltage amplitude required for the respective application. Two challenges remain to be solved. First, a mathematical model needs to be developed that correlates each position on the electrode with a distinct voltage. Otherwise the results will not be comparable to other electroporation systems like the ECIS setup. Secondly, the distance over which the experimentally relevant voltage gradient occurs is in the range of only a few hundred μm. Therefore, the position with the optimal voltage will be hard to determine with sufficient accuracy. To overcome that problem, the electrode design must be adjusted appropriately.

Another potential application of the bipolar electrodes is the combination of classical impedimetric analysis of living cells with resistive sensors. The low-frequency region of the bipolar electrode is only determined by the electrode resistance and could therefore be used to sense physical or chemical alterations directly beneath the cell layer. The selectivity of the sensor can be adjusted by choice of an appropriate electrode material that changes its resistivity upon exposure to the respective analyte. Due to a shift of the sensitivity from the real part to the imaginary part of the impedance, the electrode design is not restricted to high-resistance electrodes as would be suggested if only |Z| and R were considered. The resulting multi-parametric readout does not require any additional measurement setup and all information can be extracted directly from the impedance spectra.

4   Derivative Impedance Spectroscopy (DIS)

4.1 Introduction

Derivative spectroscopy – or derivative spectrophotometry – (DS) is a method commonly used in UV/VIS spectroscopy for qualitative analysis and quantification. It uses the first or higher order derivatives to enhance the signal, eliminate background or matrix effects, or increase the separation efficiency of peaks arising from different analytes.[214-215] An important property of DS is that the derivative value of a mixture of several components is the sum of the derivative values of each one of them.[216] Therefore, considering a two-component system, the derivative value at one wavelength directly represents one component quantitatively if the derivative of the other component crosses the zero line at that wavelength. This is called the *zero-crossing* method and is used to discriminate analytes in a mixture with closely overlapping spectral bands. So far, this principle has barely found any applications in other analytical methods. Kurzweil et al. used derivatives of impedance spectra to analyze electrochemical cells with respect to the optimum operating state in terms of humidity and temperature.[217] They reported that changes in the capacitance became more obvious when evaluating the derivative spectra thereof. The method was termed derivative impedance spectroscopy (DIS). DIS has to date not been applied to the analysis of living cells.

One issue that will be addressed in this chapter is the discrimination of the cell parameters C_m, α, and R_b. The simulations shown in Fig. III-58, based on MDCK-II cells growing on 8W10E electrodes, will be used to illustrate the problem. While C_m can be clearly estimated from the linear high frequency region with a slope of about -1, the differentiation between α and R_b is more complex as the spectral ranges, in which they are determined, overlap. A change in the membrane capacitance C_m leads to a horizontal shift in the capacitive region of the impedance spectrum above 10 kHz (Fig. III-58 A). This shift is hardly influenced by the resistive parameters α and R_b, which only contribute to the low to medium frequency range of the spectrum (Fig. III-58 B and C). Even though the main impact of α is at slightly lower frequencies than that of R_b, there are still considerable similarities, which impairs an independent quantification. Especially between 100 Hz and 1 kHz there is a strong overlap in the direction and intensity of the signal change for physiologically relevant variations of α and R_b. This may cause problems during modeling when there are several local minima in the SSE hyperplane close to one another. In other words, one particular impedance spectrum may be described by different combinations of α and R_b with similar mathematical accuracy, without

representing the physiological situation equally well. It is therefore crucial for the correct interpretation of the data to be able to clearly discriminate the influences of both parameters.
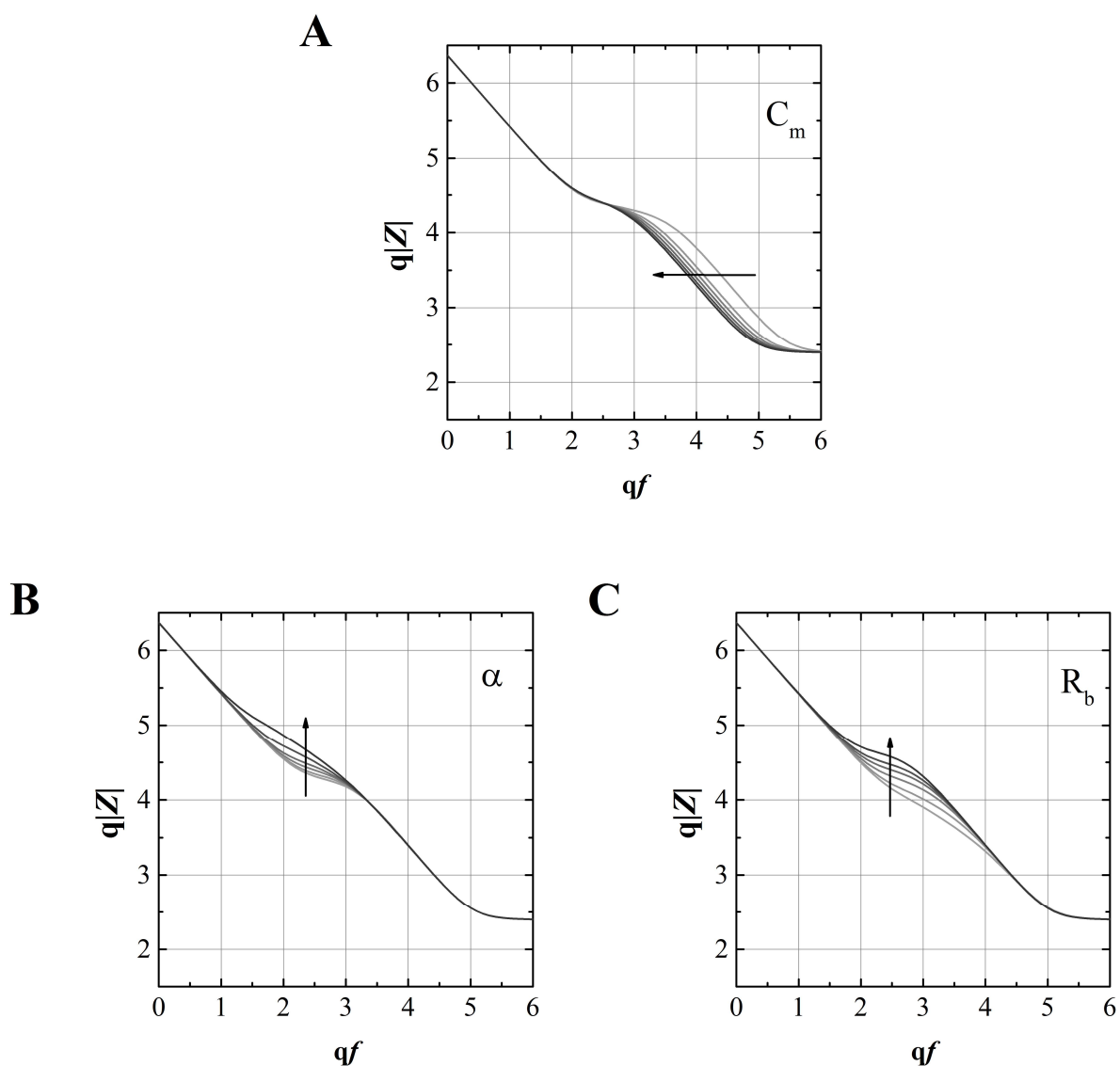

Fig. III-58: Simulations of impedance spectra with varying cell parameters using the transfer function of the ECIS model ($q|Z| = \log(|Z| / \Omega)$ and $qf = \log(f / Hz)$, cf. 4.2.1.). The arrows indicate the direction of increasing cell parameter values from light grey to black curves. The electrode parameters were chosen to resemble 8W10E electrodes: $A_{cpe} = 1.5 \cdot 10^{-5}$ F·s^{n-1}/cm², $n_{cpe} = 0.95$, $A_{el} = 5 \cdot 10^{-3}$ cm², $R_{bulk} = 250$ Ω. In each graph two cell parameters were kept constant as base values and one was varied. The base values, based on MDCK-II cells, are shown in underlined numbers: **(A)** $C_m = 1, 2, 2.5, \underline{3}, 3.5$, and 4 µF·cm^{-2}. **(B)** $\alpha = 5, 10, \underline{15}, 20, 30$, and 50 $\Omega^{0.5}$·cm. **(C)** $R_b = 10, 25, 50, \underline{75}, 100$, and 150 Ω·cm².

4.2 Objective

As it is known from DS, the first and higher order derivatives are able to pronounce subtle peaks and inflection points in the impedance curves. DIS as an analysis tool will therefore be evaluated with respect to its suitability to enhance the modeling accuracy of ECIS data and particularly the discrimination between α and R_b. In a semi-empirical approach, the data analysis was to be carried out on simulated data in order to have an objective reference for the real parameters, compared to those obtained by parameter fitting. Furthermore, controlling the experimental conditions in an *in vitro* experiment, so that only one of the parameters changes and the other ones remain constant, is virtually impossible to achieve and verify. One aim of this work was to run a fitting algorithm on the derivative data and compare the results to the parameters used to simulate the spectra. In this case, artificial noise should be added to the simulated spectra as the quality of the fit, especially of the derivatives, crucially depends on the noise level.[216] The steps involved in the fitting evaluation comprise (a) the simulation of impedance spectra using the cell parameters P_i, (b) the generation of artificial 'raw data' by superposition of computer-generated noise, (c) calculation of the logarithms of the frequency and impedance magnitude, (d) a smoothing algorithm, and (e) subsequent differentiation (Fig. III-59). The last two steps were repeated up to the third derivative (f). Each derivative was fitted using the corresponding numerical derivative of the ECIS model as transfer function (g). Eventually, the fit results X_i were compared to the cell parameters of the original simulated data P_i. For this purpose, the parameter Q_{rel} was introduced that can be regarded as a quality measure of the respective fit. The different steps will be explained in detail in the Materials and Methods section of this chapter (4.3.1).
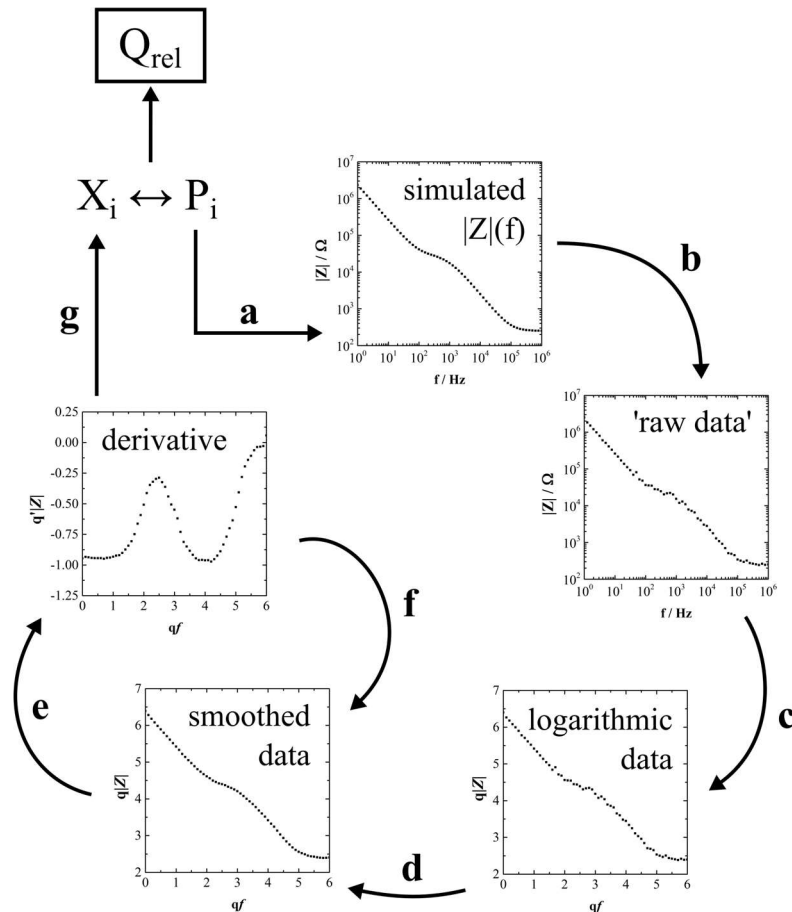
Fig. III-59: Overview of the procedure to evaluate the performance of the DIS in the context of impedance-based cellular assay. (a) Simulation of impedance spectra $|Z|(f)$ using the cell parameters P_i. (b) Generation of artificial raw data by addition of noise. (c) The decadic logarithms of $|Z|$ ($q|Z|$) and f (qf) are calculated. (d) The spectra are smoothed using a Savitzky-Golay filter. (e) The smoothed data are differentiated ($q'f$). (f) After differentiation, the spectra are smoothed again before calculating the second and third order derivative, respectively. (g) Comparison of the fit results X_i to the cell parameters P_i originally used for the simulation gives a measure for the quality of the fit Q_{rel}. (cf. 4.3.1).

In relation to the zero-crossing method used in DS, another goal was to find frequencies in any of the derivative spectra that are sensitive towards only one of the cell parameters α or R_b, and insensitive to the other. In a similar fashion, migration of the zero positions on the frequency axis of the higher derivative orders were to be analyzed with respect to correlations specific for either one of the parameters.

4.3 Materials and Methods

4.3.1   *Regression Analysis of Derivatives*

4.3.1.1   Simulation and Differentiation of Impedance Spectra

Artificial raw data impedance spectra were simulated employing the ECIS model described in II.1.4 using a LabVIEW software (cf. 1.5.1). The impedance values for each spectrum were generated at 61 frequencies from 1 Hz to 1 MHz equally spaced on a logarithmic scale. Only the impedance magnitude spectra |Z|(f) of the impedance were used in this chapter. In order to obtain spectra that resemble actual raw data more closely an artificial noise was added to the smooth simulations. The nature of this noise will be explained in detail in chapter 4.3.1.2. Before any further calculations were made, the decimal logarithms of the impedance magnitude |Z| and the frequency f were calculated (Eq. 43 and Eq. 44). The obtained dimensionless values q|Z| and qf were used for fitting and differentiation.[g] The first, second, and third derivative are defined as shown in Eq. 45, Eq. 46, and Eq. 47, respectively.

$$q|Z| = \log(|Z| \: / \: \Omega) \qquad\qquad\qquad \text{Eq. 43}$$

$$qf = \log(f \: / \: Hz) \qquad\qquad\qquad \text{Eq. 44}$$

$$q|Z|' = \frac{dq|Z|}{dqf} \qquad\qquad\qquad \text{Eq. 45}$$

$$q|Z|'' = \frac{dq|Z|'}{dqf} = \frac{d^{\,2}q|Z|}{dqf^{\,2}} \qquad\qquad\qquad \text{Eq. 46}$$

$$q|Z|''' = \frac{dq|Z|''}{dqf} = \frac{d^{\,3}q|Z|}{dqf^{\,3}} \qquad\qquad\qquad \text{Eq. 47}$$

Part of this work was to fit the derivatives of the ECIS model to the derivatives of the raw data spectra by iteratively varying the cell parameters. Therefore, both the model and the raw data had to be differentiated. The derivatives of the model spectra can be easily calculated by

---

[g] In this work the qX value was defined as the positive decimal logarithm of X in opposition to the commonly used pX value (e.g. the pH value), the negative decimal logarithm of X.

numerical differentiation (Eq. 48). Since the boundary conditions are not defined, the first and last data point are lost after each differentiation of a spectrum.

$$y_i = \frac{x_{i+1} - x_{i-1}}{2dt}$$

Eq. 48

with: y_i as the differentiation at frequency i

x_i as the data point at frequency i

dt as the discrete data point distance ($dt = 0.1$ in this case)

Differentiation is highly sensitive towards noise in a way that the noise level increases with the derivative order. Therefore, the raw data spectra were smoothed with a Savitzky-Golay filter and then differentiated numerically.[218] Savitzky-Golay (SG) filters significantly increase the signal-to-noise ratio (SNR) while still maintaining the shape of the original signal. The method applies a least squares polynomial fit with polynomial order n_{sg} through a window of $2 \cdot s_{sg} + 1$ points, where s_{sg} is the number of side points to a central data point in x. This is repeated for every data point x_i in a spectrum. The obtained x_i' of the polynomial at that frequency i are the smoothed values. A polynomial order of $n_{sg} = 5$ and $s_{sg} = 9$ side points turned out to give the best smoothing results.

4.3.1.2   Noise Simulation

The noise added to the simulated impedance data was assumed to be Gaussian white noise. Gaussian noise is statistical noise with a normal – or *Gaussian* – probability density function (PDF), which is given by Eq. 49.[219]

$$g(x \mid \mu, \sigma^2) = \frac{1}{\sqrt{2 \cdot \pi \cdot \sigma^2}} e^{-\frac{(x-\mu)^2}{2 \cdot \sigma^2}}$$

Eq. 49

with: $g(\mu, \sigma^2)$ as the Gaussian PDF

μ as the mean of the PDF

σ^2 as the variance

σ as the standard deviation

Fig. III-60 shows the bell shaped Gaussian PDF for different values of the standard deviation σ. As an inherent property of a PDF, the highest probability density is at the mean μ. The further away a value is from μ, the lower is its probability density. The scatter range depends on σ. For example, a value x has a probability to be within $-\sigma \le x \le \sigma$ of about 68.3%, within $-2\cdot\sigma \le x \le 2\cdot\sigma$ of about 95.5%, and within $-3\cdot\sigma \le x \le 3\cdot\sigma$ of about 97.7%.
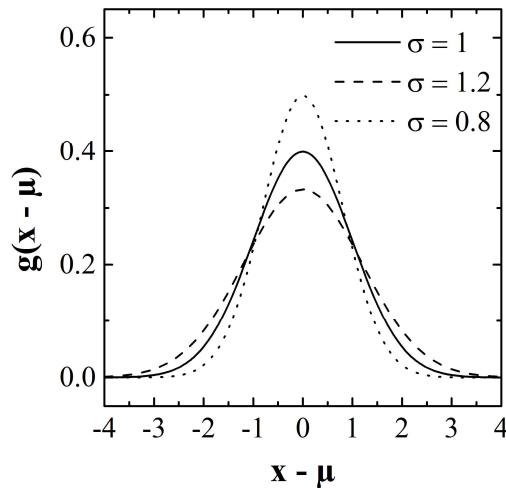

Fig. III-60: Gaussian probability density function for different values of σ when the PDF is plotted as a function of (x-μ) instead of x.

In the case of an impedance magnitude spectrum $|Z|$(f) as used in this work, μ is the simulated transfer function value of $|Z|$ at a certain frequency and σ is the experimentally determined standard deviation at that frequency. Furthermore, x is the randomly assigned value of $|Z|$ after noise addition with a probability defined by the PDF. In order to get a noisy impedance spectrum with normally distributed values around the transfer function, the value of $|Z|$ at each frequency together with its corresponding experimentally determined standard deviation was simply fed into a LabVIEW random number generator coupled with a Gaussian PDF (Fig. III-61). The relative standard deviations σ_{rel} of 8W10E electrodes with confluently grown MDCK-II cells were measured with the SI 1260 setup (cf. 1.2.1). σ_{rel} at each frequency was calculated from 10 consecutive spectra of a single experiment. This was repeated on 5 independent electrodes and the respective σ_{rel} values were averaged (cf. Fig. V-9, supplementary information). The standard deviations σ required for the generation of the Gaussian noise were obtained by multiplication of σ_{rel} with $|Z|$ at each frequency of the spectrum.
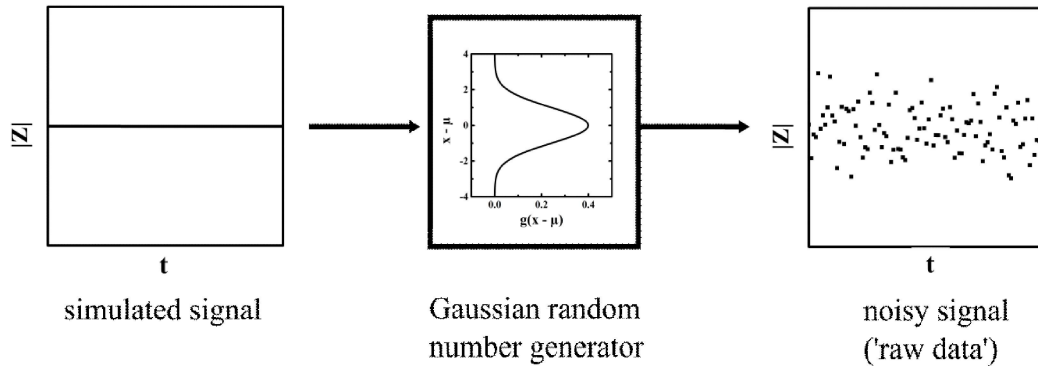
Fig. III-61: Schematic of the generation of 'raw data'. The simulated signal is fed into a LabVIEW random number generator based on a Gaussian probability density function. The noisy signal shows randomly distributed values around the originally simulated values with the difference between both signals occuring with a probability defined by the PDF and the experimentally determined relative standard deviations σ_{rel} at each frequency.

4.3.1.3   Evaluation of the Fit Results

For each derivative order from 0 to 3 the logarithmic and smoothed impedance magnitude spectra $q|Z|_{w/\ cells}$ were fitted with the algorithm described before (cf. *II.3 Regression Analysis*). The same procedure was conducted for the normalized impedance spectra $q|Z|_{norm.}$, defined by Eq. 50.

$$q|Z|_{norm.} = q|Z|_{w/\ cells} - q|Z|_{w/o\ cells} \qquad\qquad \text{Eq. 50}$$

with: $q|Z|_{w/\ cells}$ as the (simulated) $q|Z|$ of the cell-covered electrode

$q|Z|_{w/o\ cells}$ as $q|Z|$ of the cell-free electrode as calculated from the derived CPE parameters and R_{bulk} (cf. 3.2)

Different fitting conditions were employed for every spectrum. While the number of iterations was fixed at 5, the number of increments varied between 5, 7, and 9. Furthermore, the weighting methods unity, statistical, and proportional weighting (cf. II.3.1) were applied consecutively. For the statistical weighting, the empirically determined standard deviations used for the raw data simulations as described in 4.3.1.2 were employed. Because of the different weighting factors, the final SSE_{min} values are not comparable in terms of assessing the best fitting method. Moreover, the raw spectra are smoothed before fitting and are somewhat altered. A smaller SSE value therefore only implies a better fit to the smoothed spectrum, which does not necessarily represent the original data accurately. Consequently, a new dimension Q_{fit} was introduced that

directly compares the final cell parameters obtained from each fit X_i with the cell parameters that were used to simulate the raw data in the first place P_i (Eq. 51). Q_{fit} can be regarded as the inverse, proportionally weighted SSE of the simulated cell parameters and the fit results. A high Q_{fit} value thus implicates that the fit results represent the 'real' cell parameters accordingly well.

$$Q_{fit} = \left(\sum_{i=1}^{3} \frac{(X_i - P_i)^2}{X_i^2} \right)^{-1}$$

Eq. 51

with: X_i as the fit results for C_m, α, and R_b

P_i as C_m, α, and R_b used for the simulations

The maximum value for Q_{fit} depends on the range of the last iteration step, which was set from $0.99 \cdot x_5$ to $1.01 \cdot x_5$ (cf. 3.3). That means every X_i has a relative error of 1% and the summands of the weighted SSE term in Eq. 42 (the squared errors SE) each lie within an interval of at least $\Delta SE = 0.02$. $Q_{fit, max}$, the statistical maximum value for Q_{fit}, is therefore given by Eq. 52.

$$Q_{fit, mav} = \left(\sum_{i=1}^{3} \Delta SE_i \right)^{-1} = (3 \cdot 0.02^2)^{-1} \approx 833$$

Eq. 52

with: $Q_{fit, mav}$ as the maximum average Q_{fit} value for 5 iterations

ΔSE_i as the error interval of the SE summands

Setting Q_{fit} in relation to $Q_{fit, max}$ results in a parameter Q_{rel}, that describes the quality of a fit in relation to the maximum average accuracy for a large sample size, subject to the conditions of the fitting algorithm (Eq. 53).

$$Q_{rel} = \frac{Q_{fit}}{Q_{fit, ave}}$$

Eq. 53

Q_{rel} can take values greater than 1 for single spectra, but should on average be ≤ 1 for a greater number of repetitions. Therefore, the fitting algorithm was performed on 100 impedance spectra with randomly added noise using each of the afore described fitting conditions. This guaranteed sufficient statistical significance. Tab. III-22 and Tab. III-23 show the cell and electrode

parameters of the simulated impedance spectra and the starting values used for fitting, respectively. The electrode parameters were chosen on the basis of 8W10E electrodes and the cell parameters according to the results of Reiß 2004.[202]

Tab. III-22: Parameters used for the simulation of the impedance data. The values were chosen to resemble confluent MDCK-II cells on 8W10E electrodes.[202]

parameter	value
A_{el}	$5 \cdot 10^{-3}$ cm²
A_{cpe}	$1.5 \cdot 10^{-5}$ F·s^{n-1}/cm²
n_{cpe}	0.95
R_{bulk}	250 Ω
C_m	3 µF/cm²
α	16 Ω$^{0.5}$·cm
R_b	88 Ω·cm²

Tab. III-23: Starting values of the cell parameters as used for the fits.

parameter	value
C_m	3.5 µF/cm²
α	20 Ω$^{0.5}$·cm
R_b	100 Ω·cm²

4.3.2   Discrimination of α and R_b in the Impedance Spectrum

As mentioned before, the zero-crossing method is used in derivative spectrophotometry (DS) to determine the concentration of an analyte in multi-component mixtures. The derivative value is measured at a wave length where the derivative of the interfering compound is zero. Due to the additivity of the derivatives of the individual components of a mixture, their concentrations can be measured separately. The same principle was tried on impedance spectra to discriminate between α and R_b. Since the zero-order spectra are monotonically decreasing, only the second and higher order derivatives show zero-crossing (cf. Fig. III-64). However, when either one of the parameters α or R_b was altered while the other one was kept constant, an impact on all relevant zero-crossings was always found. This means that the additivity principle from the DS does not hold true in this case. Instead, two different approaches were made with similar intent. The objective of the first approach was to find any frequencies where a positive or negative change in one parameter affects the derivative value differently than a similar change in the other parameter. For this purpose, alterations in the derivative values at fixed frequencies in response to varying α or R_b values were analyzed (Fig. III-62, red arrows). For the second approach, the migration of the zero-crossing point in x-direction upon changing either α or R_b was investigated with respect to differences in the parameters (Fig. III-62, blue arrow). The two approaches are described in in the chapters 4.3.2.1 and 4.3.2.2, respectively.
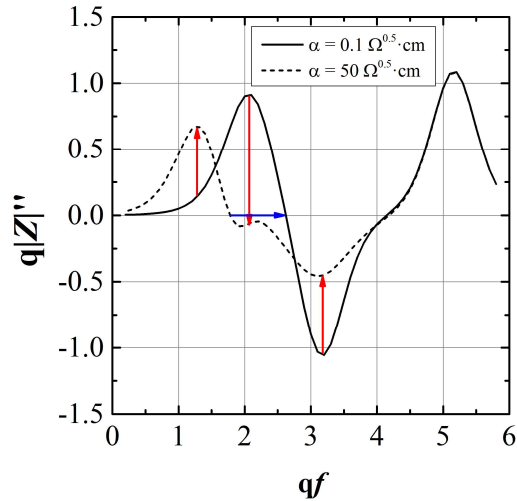
Fig. III-62: Simulated second order derivatives of two magnitude impedance spectra with different values of α. The red and blue arrows indicate the changes in y- and x-direction that are used in the two approaches to discriminate α and R_b as described in the chapters 4.3.2.1 and 4.3.2.2, respectively.

The electrode and cell parameters displayed in Tab. III-24 were used as a basis for all simulations in this chapter. α and R_b were varied according to Tab. III-25, while keeping the other parameter constant at its base value.

Tab. III-24: Base parameters used for the simulation of the impedance data. The values were chosen to resemble confluent MDCK-II cells on 8W10E electrodes.

parameter	value
A_{el}	$5 \cdot 10^{-3}$ cm²
A_{cpe}	$1.5 \cdot 10^{-5}$ F·s^{n-1}/cm²
n_{cpe}	0.95
R_{bulk}	250 Ω
C_m	3 μF/cm²
α	15 $\Omega^{0.5}$·cm
R_b	75 Ω·cm²

Tab. III-25: While keeping one parameter constant at its base value (underlined), the other one was varied as listed here. C_m was kept constant at all times.

α / $\Omega^{0.5}$·cm	R_b / Ω·cm²
0.1	0.1
5	10
10	25
<u>15</u>	50
20	<u>75</u>
30	100
50	150

4.3.2.1   Looking for a Sensitive Frequency

The process of finding a suitable frequency where the difference between the sensitivities towards α or R_b was most pronounced is exemplarily shown in Fig. III-63 for the second order

derivative. First, the most sensitive frequency was determined for each parameter separately. For this purpose, the spectrum with the lowest simulated value of the respective parameter was subtracted from the spectrum with the highest value (Fig. III-63 A and B). This resulted in two differentially normalized spectra $\Delta q|Z|''(\alpha)$ and $\Delta q|Z|''(R_b)$ that indicated the most sensitive frequencies for the respective parameter (Fig. III-63 C and D). Subtracting these spectra from each other shows the highest differences between the sensitivities (Fig. III-63 E and F). The frequencies of the maxima within these spectra were chosen for further analysis. This procedure was performed with zero, first, and second order derivative spectra. The cell parameters were varied as shown in Tab. III-25 and the derivative value was followed at the predetermined frequencies. Since α and R_b covered a different range of values, they were normalized to a common scale between 0 and 1 for better display.
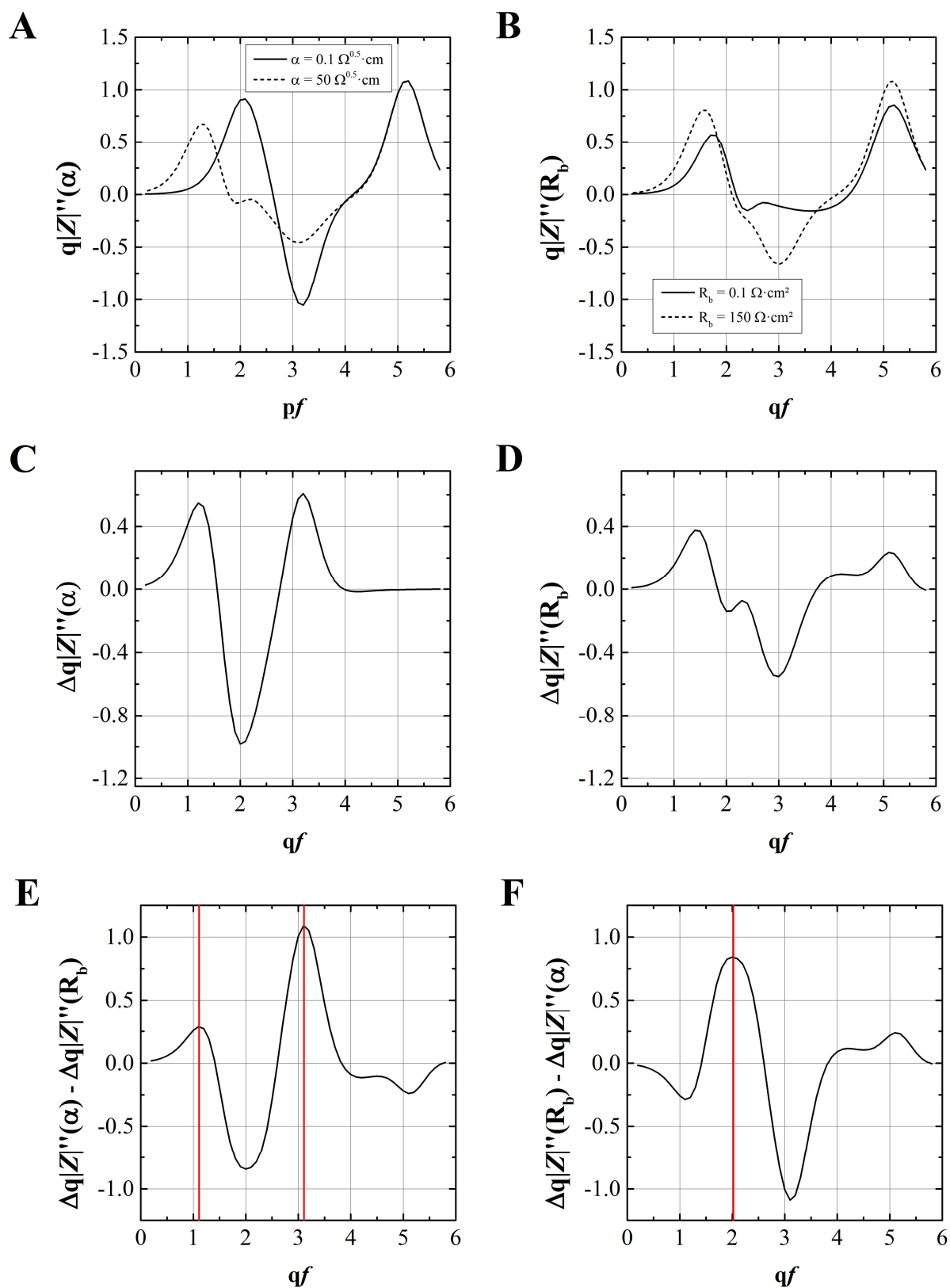
Fig. III-63: Procedure for determining the frequencies where the difference between the effects of α and R_b is most pronounced, exemplarily shown for the second order derivative. **(A)** Second order derivative for the min. and max. α value. **(B)** Second order derivative for the min. and max. R_b value. **(C)** and **(D)** Differences $\Delta q|Z|''$ between the max. and the min. spectra. **(E)** Subtracting $\Delta q|Z|''(R_b)$ from $\Delta q|Z|''(\alpha)$ shows the strongest increase of α compared to R_b at the maxima (see red line). **(F)** The inverse calculation yields the highest increase of R_b compared to α. The maxima of this spectrum correspond to the minima in (E).

4.3.2.2   Zero Migration

The migration of the zero-crossing points along the x-axis was followed upon variation of either α or R_b according to the values listed in Tab. III-25, while keeping the other parameter constant. The zero points pf_0 in each second order derivative spectrum were determined by linear interpolation of every two adjacent data points with different signs (Eq. 54).

$$pf_0 = -\frac{b}{a} \qquad\qquad \text{Eq. 54}$$

with: pf_0 as the zero point

   b as the intercept of the interpolation

   a as the slope of the interpolation

Like in the previous chapter, the values of α and R_b were normalized to a common scale between 0 and 1 for improved portrayal.

4.4 Results and Discussion

4.4.1 Simulation of Derivative Spectra

This chapter describes qualitatively the effects of varying cell parameters on the impedance magnitude spectra of different derivative order by means of simulated data. Fig. III-64 shows the simulated spectra $q|Z|_{w/\ cells}$ with varying α and R_b values from derivative order 0 to 3. The simulations demonstrate that the spectra become more complex with increasing derivative order. The zero-order spectrum is monotonically decreasing (Fig. III-64 A and B) and variations in α and R_b cause spectral changes in a similar frequency range and in the same direction. However, higher order derivatives are differently affected by α and R_b. As indicated by the arrows, changes in the first order derivative spectrum $q'|Z|$ still go into the same direction for both parameters, but occur in a different frequency range (Fig. III-64 C and D). By trend, changes caused by R_b occur at higher frequencies than those induced by α. The second order derivative spectra $q''|Z|$ show more distinct differences (Fig. III-64 E and F). Here, the direction of the spectral changes differs considerably between the parameters, particularly between 1 kHz ($qf = 3$) and 10 kHz ($qf = 4$). Moreover, two zero-crossing points occur in these spectra, one around $pf_0 \approx 2.5$ and one at about $pf_0 \approx 4$. The position of the first one is affected by both

parameters, whereas the second one is only caused to move along the x-axis by R_b. The same tendencies apply for third order derivative spectra $q'''|Z|$. Furthermore, additional zero-crossing points appear for high α ($\geq 50~\Omega^{0.5}\cdot$cm) as well as for low R_b values ($\leq 10~\Omega\cdot$cm²).
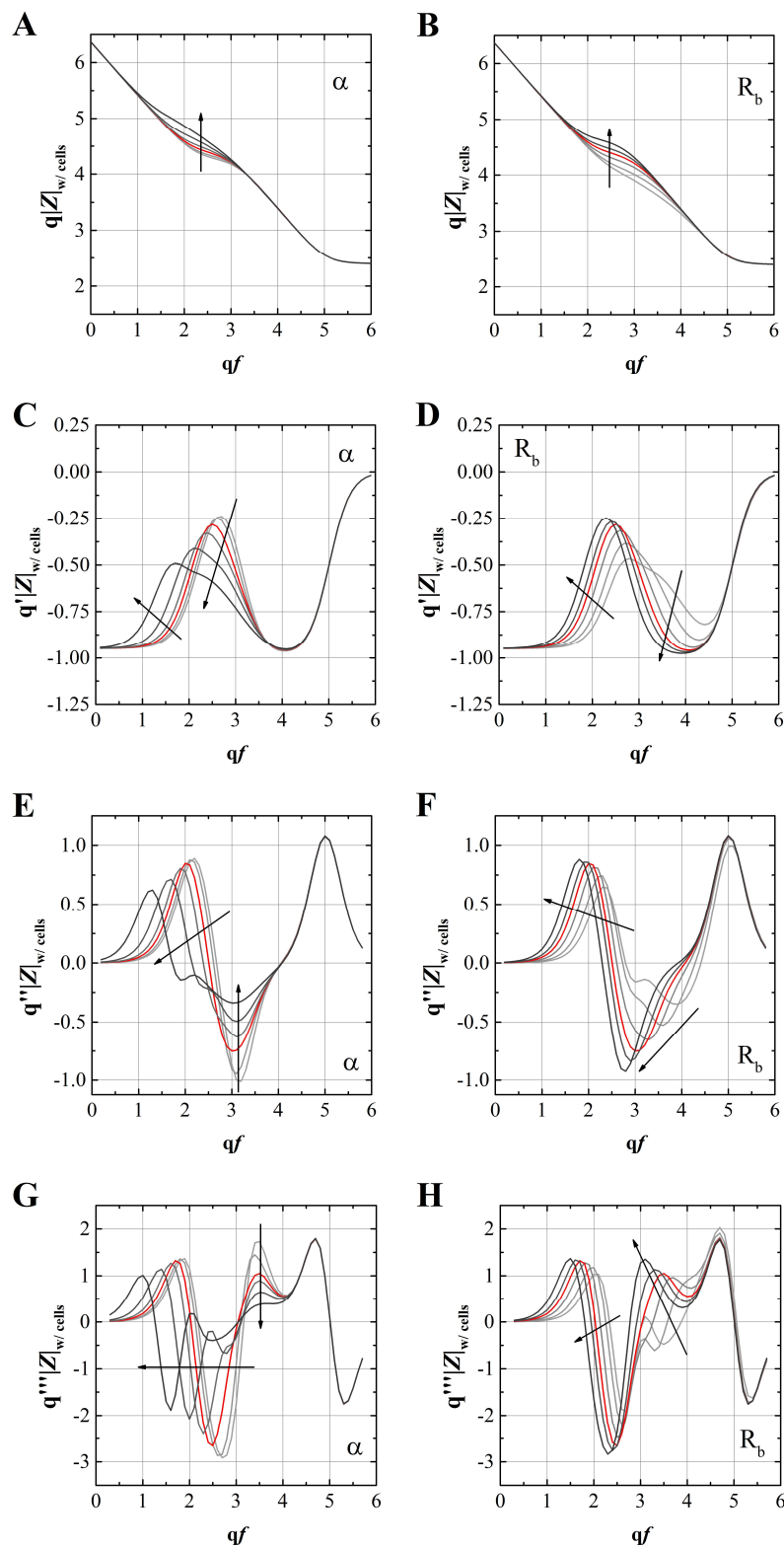

Fig. III-64: Simulations of impedance magnitude spectra with varying cell parameters using the transfer function of the ECIS model (cf. 4.2.1.). The derivatives are shown from zero to 3rd order. The arrows indicate the direction of increasing cell parameter values from light grey to black curves. The electrode parameters were chosen to resemble 8W10E electrodes: $A_{cpe} = 1.5\cdot10^{-5}$ F·s^{n-1}/cm², $n_{cpe} = 0.95$, $A_{el} = 5\cdot10^{-3}$ cm², $R_{bulk} = 250~\Omega$. In each graph two cell parameters were kept constant as base values and one was varied. The base values, based on MDCK-II cells, are shown as underlined numbers and are represented by red lines in the graph: $C_m = 3~\mu$F·cm^{-2}. **(A, C, E, G)** α = 5, 10, <u>15</u>, 20, 30, and 50 $\Omega^{0.5}\cdot$cm. **(B, D, F, H)** R_b = 10, 25, 50, <u>75</u>, 100, and 150 $\Omega\cdot$cm².

4.4.2   Regression Analysis of Derivatives

This chapter covers the results of the regression analysis that was performed with simulated raw data of impedance magnitude spectra of derivative order 0 to 3, using various fitting conditions (cf. 4.3.1). The results are presented in different compilations in Fig. III-65, Fig. III-66, and Fig. III-67, each figure pointing out different aspects. However, some of the data occur in two or all three figures.

Fig. III-65 illustrates a comparison between the different numbers of increments employed during fitting (5, 7, and 9) using the quality indicator Q_{rel}. The results are sorted and split by the weighting methods unity weighting (equates to no weighting, Fig. III-65 A), statistical weighting (Fig. III-65 B), and proportional weighting (Fig. III-65 C). The Q_{rel} values representing the spectra of cell-covered electrodes $q|Z|_{w/\ cells}$ are depicted with single-colored columns and those representing the normalized spectra $q|Z|_{norm}$ are shown in striped columns. Concerning the number of increments, i.e. in every three consecutive bars, there is a clear trend that is apparent for all fitting conditions. Regardless of derivative order or weighting method, the quality of the fits increases in the order 5 increments $\leq$ 7 increments $\leq$ 9 increments. Throughout all fitting conditions, the fits using only 5 increments are below a value of $Q_{rel} =$ 0.3 (black bars), whereas those obtained with 7 or 9 increments (grey and white bars) are in parts considerably higher. Using only 5 increments probably leads to a contraction of the fitting algorithm around local minima and thus to inaccurate fit results. For the higher order derivatives, there is no difference between 7 and 9 increments within the error margin. However, all weighting methods show considerable improvement with 9 increments for zero-order derivative. In order to reduce the amount of data, only the results obtained with 9 increments will be compared below, thereby taking into account only the best results for every derivative order and weighting method.
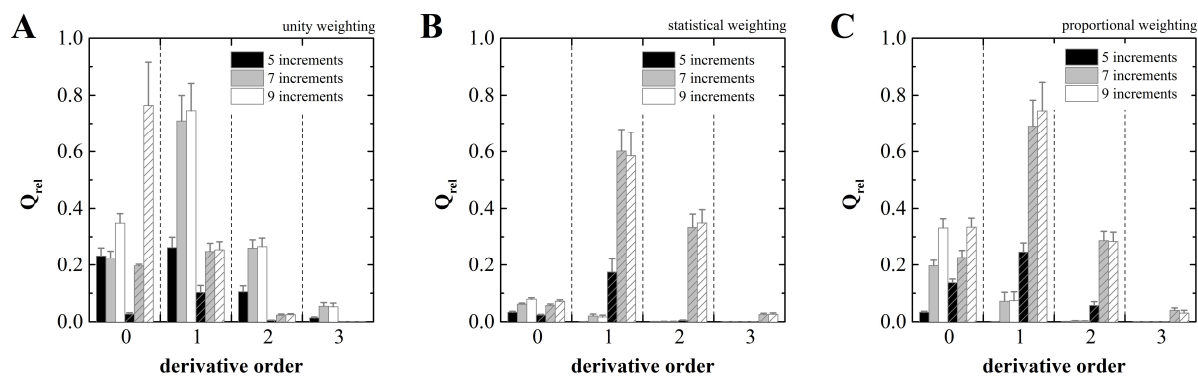
Fig. III-65: Quality of the fits for derivative orders 0 to 3 and fitting conditions, comparing the different number of increments. **(A)** Unity weighting (no weighting). **(B)** Statistical weighting. **(C)** proportional weighting. (N = 100, ± SEM)

Fig. III-66 compares the fits of two different data types of zero-order derivative, the linear and the logarithmic spectra. The linear spectra are the simulated raw data $|Z|(f)$ and the logarithmic spectra $q|Z|(qf)$ are generated by calculating the decadic logarithms of $|Z|$ and f (cf. 4.3.1.1). For both data types, the Q_{rel} values for the impedance of the cell-covered electrode (w) as well as the normalized impedance (n) are shown, each fitted with unity (u), statistical (s), and proportional (p) weighting. There is no significant difference between the fit qualities of the logarithmic and the linear spectra when comparing identical fitting conditions, except for the unweighted cell-covered electrodes (w-u). Here, the logarithmic spectra yield a Q_{rel} value of 0.36 ± 0.03, whereas the linear spectra only show a value of $Q_{rel} = 0.0076 \pm 0.0006$. The impedance magnitude covers a range of several orders of magnitude in the linear data (~100 Ω to 10 MΩ). This leads to an over-accentuation of the higher values and an accordingly bad fit result. By contrast, the values of the corresponding logarithmic data range from 2 to 7 on the y-axis. The data points are thus in the same order of magnitude and can be fitted without difficulty. Normalizing, differentiation, and weighting have the same effect. Since the logarithmic spectra yield overall better results, only those are used for further analysis.
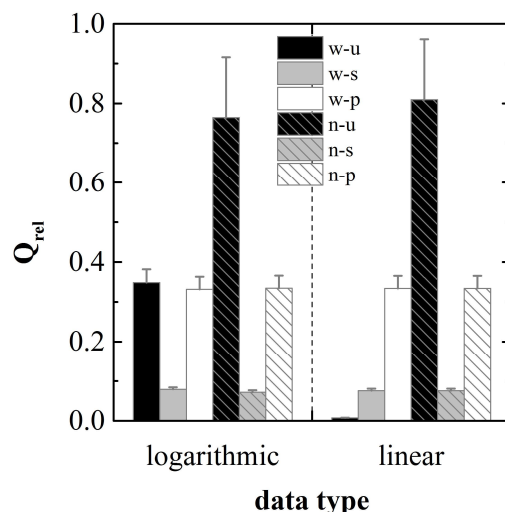
Fig. III-66: Comparison of the fit quality of the linear ($|Z|(f)$) and logarithmic data type ($q|Z|(qf)$). In all spectra 9 increments were used for the fitting algorithm. Fitting conditions: $|Z|$ of the cell-covered electrode (w, *single-colored columns*), normalized $|Z|$ (n, *striped columns*), unity (u, *black*), statistical (s, *grey*), and proportional (p, *white*) weighting. (N = 100, ± SEM)

In order to analyze the dependence of the fit quality on the derivative order, the Q_{rel} values of all fit results using 9 increments are summarized in Fig. III-67. The results for the impedance magnitude of the cell-covered electrodes $q|Z|_{w/\ cells}$ are shown in Fig. III-67 A and those of the normalized impedance magnitude $q|Z|_{norm}$ in Fig. III-67 B. There are two overall trends that depend on the weighting method and on whether $q|Z|_{w/\ cells}$ or $q|Z|_{norm}$ was employed. The first trend shows a decreasing fit quality with increasing derivative order. This applies for $q|Z|_{w/\ cells}$ when using statistical or proportional weighting as well as for $q|Z|_{norm}$ without weighting (unity weighting). In the second trend, the first order derivatives exhibit better fit results than the zero-order spectra but declining fit quality for higher orders. This is true for $q|Z|_{w/\ cells}$ without weighting and for $q|Z|_{norm}$ if the fits are weighted with either statistical or proportional factors. Generally, the third order derivatives exhibit poor Q_{rel} values, the highest being 0.05 ± 0.02 for $q|Z|_{w/\ cells}$ without weighting. The best fit results are obtained with the first derivative of $q|Z|_{w/\ cells}$ without weighting ($Q_{rel} = 0.75 \pm 0.09$), $q|Z|_{norm}$ without differentiation and weighting ($Q_{rel} = 0.76 \pm 0.15$), and the first derivative of $q|Z|_{norm}$ with proportional weighting ($Q_{rel} = 0.74 \pm 0.10$). The three values are not significantly different.
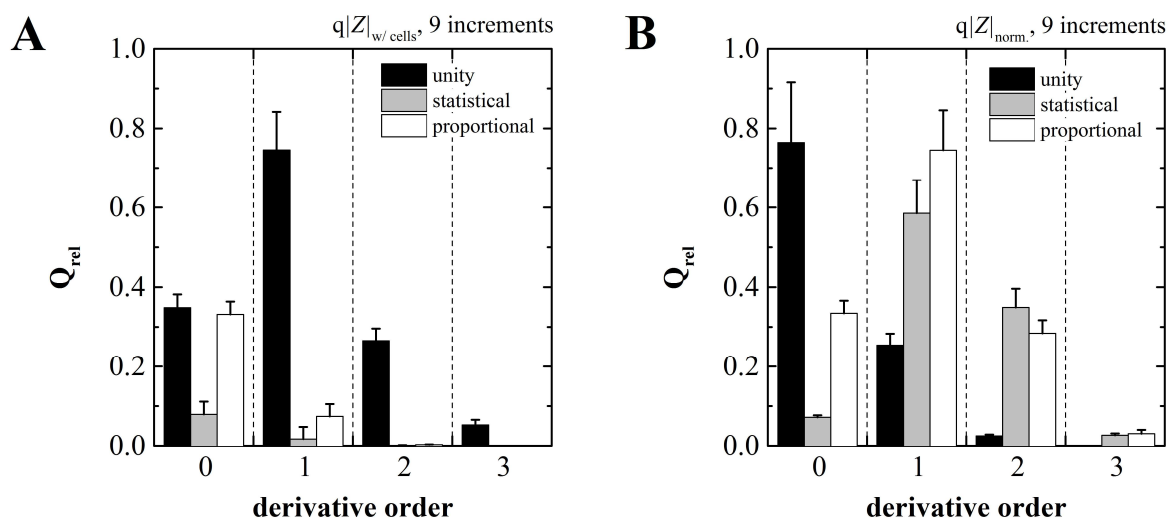
Fig. III-67: Results for all fits performed with 9 increments, using unity, statistical, and proportional weighting for all derivative orders from 0 to 3. **(A)** Impedance magnitude of the cell-covered electrodes $q|Z|_{w/\,cells}$. **(B)** Normalized impedance magnitude $q|Z|_{norm.}$ (N = 100, $\pm$ SEM)

Taking all results from the regression analysis into account, no significant improvement was observed from using the first or a higher derivative order for fitting instead of the original data. Considering the normalized data, the Q_{rel} values show equal quality for the fits if the respective best weighting method is used. However, there is substantial improvement in the first derivative if for example only the $q|Z|_{w/\,cells}$ data are taken into account (cf. Fig. III-67 A). Thus, the effectiveness of DIS strongly depends on the data structure and the shape of the spectrum to be analyzed. Despite the higher fit quality in some of the first order derivatives, the strong decline in Q_{rel} for all higher orders challenges the applicability of DIS in that area. This indicates the presence two opposing trends, one that promotes and one that counteracts the use of derivatives with considerable dependence on the derivative order.

In order to further elucidate this problem, the residuals between the ideally smooth spectra and the noisy spectra were determined for all derivative orders with and without the use of the SG filter (Fig. III-68). A number of data points that corresponds to the side points of the SG filter has been removed on both ends of the frequency spectrum. The typical residual spectra show an increasing noise level that gets more pronounced with every derivative order as reported for derivative spectrophotomety. It appears less severe and is clearly dampened when the SG filter is applied.
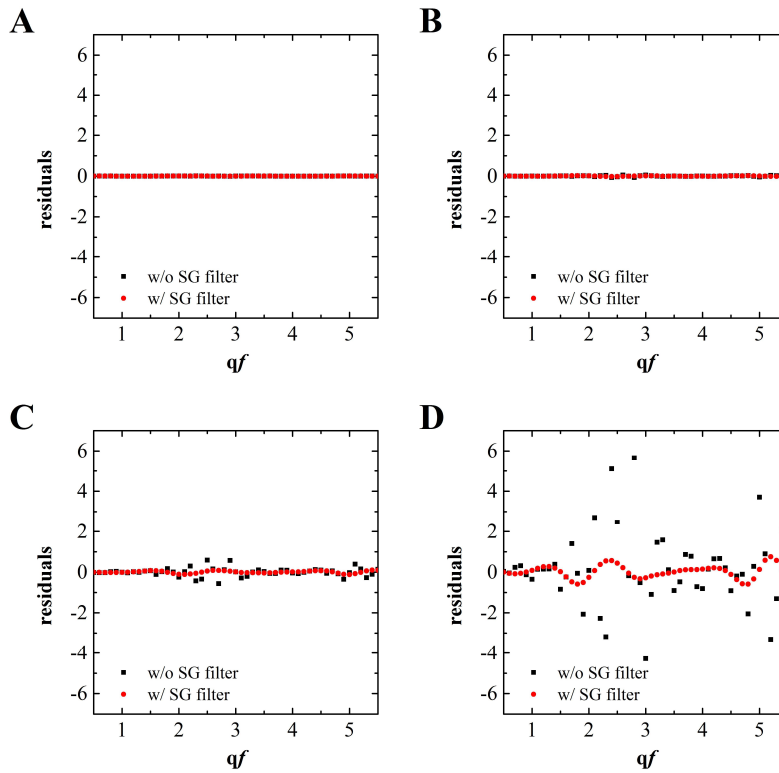
A

B

Fig. III-68: Typical residual spectra, calculated from the difference between the smooth spectra without noise and the simulated raw data with noise. The residuals were determined from spectra with (●) and without (■) the application of a SG filter.
(A) Zero-order spectrum.
(B) First order derivative.
(C) Second order derivative.
(D) Third order derivative.

C

D

A more quantitative analysis was performed by calculating the SSE between the smooth and the noisy data, using the transfer function as $f(x_i)$ and the data points of the noise spectra as Y_i (cf. Eq. 26, II.3.1). A low SSE value means that the noise data represent the smooth spectra well and vice versa. Thereby, it was possible to determine the effectiveness of the SG filter and the degree to which the noise causes deviations from the ideal smooth spectra. The results are shown in Fig. III-69 with logarithmically plotted SSE on the y-axis and the derivative order on the x-axis. The SSE cover a range of several orders of magnitude for both with and without SG filter. In the logarithmic plot, the SSE are linearly correlated with the derivative order. The intercept of the linear fit as well as its slope are significantly lower when applying the SG filter after each differentiation. The slope can be interpreted as the degree to which the approximation to the ideally smooth data changes with the derivative order. Without SG filter, the SSE increase on average by 1.82 ± 0.04 orders of magnitude per derivative order. By comparison, using the SG filter after each differentiation, the SSE changes only by 1.51 ± 0.04 orders of magnitude per derivative order. That means, the SG filter reduces the deviation between smooth and noisy data and its effectiveness slightly improves with increasing derivative order. Despite this improvement, the deviations for higher derivative orders are quite substantial and are assumed to have a severe impact on the fit quality. If the original spectrum is not well represented after differentiation, even a good fit cannot compensate this error.
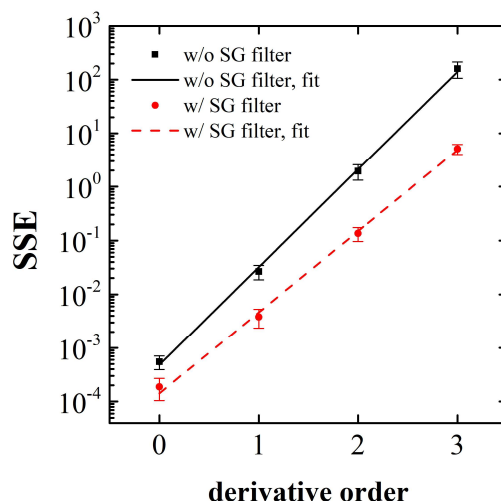
Fig. III-69: SSE calculated from the differences between the smooth and the noisy data of the simulated data set, plotted against the derivative order. Without filter the linear fit shows an intercept of (-3.32 ± 0.06) Ω^2 and a slope of (1.82 ± 0.04) Ω^2. Application of an SG filter reduces the intercept to (-3.85 ± 0.09) Ω^2 and the slope to (1.51 ± 0.04) Ω^2. (N = 100, $\pm$ SEM)

Based on these findings, the following conclusions were drawn. Using DIS had a positive effect on the fit quality for some fitting conditions, whereas there was no general improvement. The applicability thus strongly depended on the shape of the spectrum and the applied weighting method. Convincing results were only obtained with first order derivatives while higher orders showed a strong decline in the fit quality. This was shown to be caused by the ineffectiveness of the SG filter that did not sufficiently reduce the noise amplification caused by the differentiations. Ideally, the slope of an SSE plot like in Fig. III-69 should be zero, meaning that the noise level does not change with increasing derivative order. It is therefore essential for the practicality of DIS to find suitable smoothing algorithms that retain the original spectrum as accurately as possible. Several methods have been described by Knowles et al.[220] and Chartrand[221] for the first derivative. Comparing these methods in an SSE plot and repeating the regression analysis for the data set presented here with the method comprising the lowest slope would be a potential step to further advance the use of DIS in impedimetric analysis. Another option would be to average several spectra recorded in a row and run the fitting algorithm on this averaged spectrum. Thereby, statistical noise deviating from the 'ideal' spectrum should be smoothed out and the spectra should appear less noisy as long as the system is perfectly stationary. That is probably not true for living systems like adherent cells.

4.4.3   Discrimination of α and R_b in the Impedance Spectrum

4.4.3.1   Looking for a Sensitive Frequency

Employing the method described in chapter 4.3.2.1, the frequencies listed in Tab. III-26 emerge as either only sensitive to one of the parameters α and R_b, or to both with signal changes in opposite directions. The respective changes of the signal in correlation with the cell parameters are shown in Fig. III-70. These values only apply for MDCK-II cells using the herein presented cell parameters and may vary significantly for other cell lines.

Tab. III-26: Frequencies and the corresponding derivative orders of signal changes considered useful for the discrimination between α and R_b. These values only apply for MDCK-II cells.

derivative order	q*f*	frequency	designation
0	3.3	2 kHz	$q\|Z\|_{2\ kHz}$
1	2.6	400 Hz	$q'\|Z\|_{400\ Hz}$
1	3.8	6.3 kHz	$q'\|Z\|_{6.3\ kHz}$
2	3.0	1 kHz	$q''\|Z\|_{1\ kHz}$

The most pronounced difference between changes in both parameters for the zero-order spectrum was found for a frequency of 2 kHz ($q\|Z\|_{2\ kHz}$). Here, a variation in α does not affect the impedance signal, whereas there is a noticeable impact upon altering R_b (Fig. III-70 A). However, when R_b gets higher than about 75 Ω·cm² (norm. $R_b = 0.5$), the two curves become barely distinguishable. The same principles apply for the first derivative at 6.3 kHz ($q'\|Z\|_{6.3\ kHz}$) except that increasing R_b leads to a decline of the signal at that frequency (Fig. III-70 C). Following the signal of the first derivative at 400 Hz ($q'\|Z\|_{400\ Hz}$) gives more distinct results. In this case, altering either parameter results in opposing tends over the complete range of parameter values (Fig. III-70 B). Increasing the respective cell parameter leads to a decrease of the signal at 400 Hz for α and to an increase for R_b. Likewise, contrasting tendencies are observed for the second derivative at 1 kHz ($q''\|Z\|_{1\ kHz}$). Here, the signal declines for increasing R_b and increases with higher α values. However, the curve describing an alteration of α is not monotonically increasing as it shows a minimum for $\alpha = 10\ \Omega^{0.5}\cdot cm$ (norm. $\alpha = 0.2$).
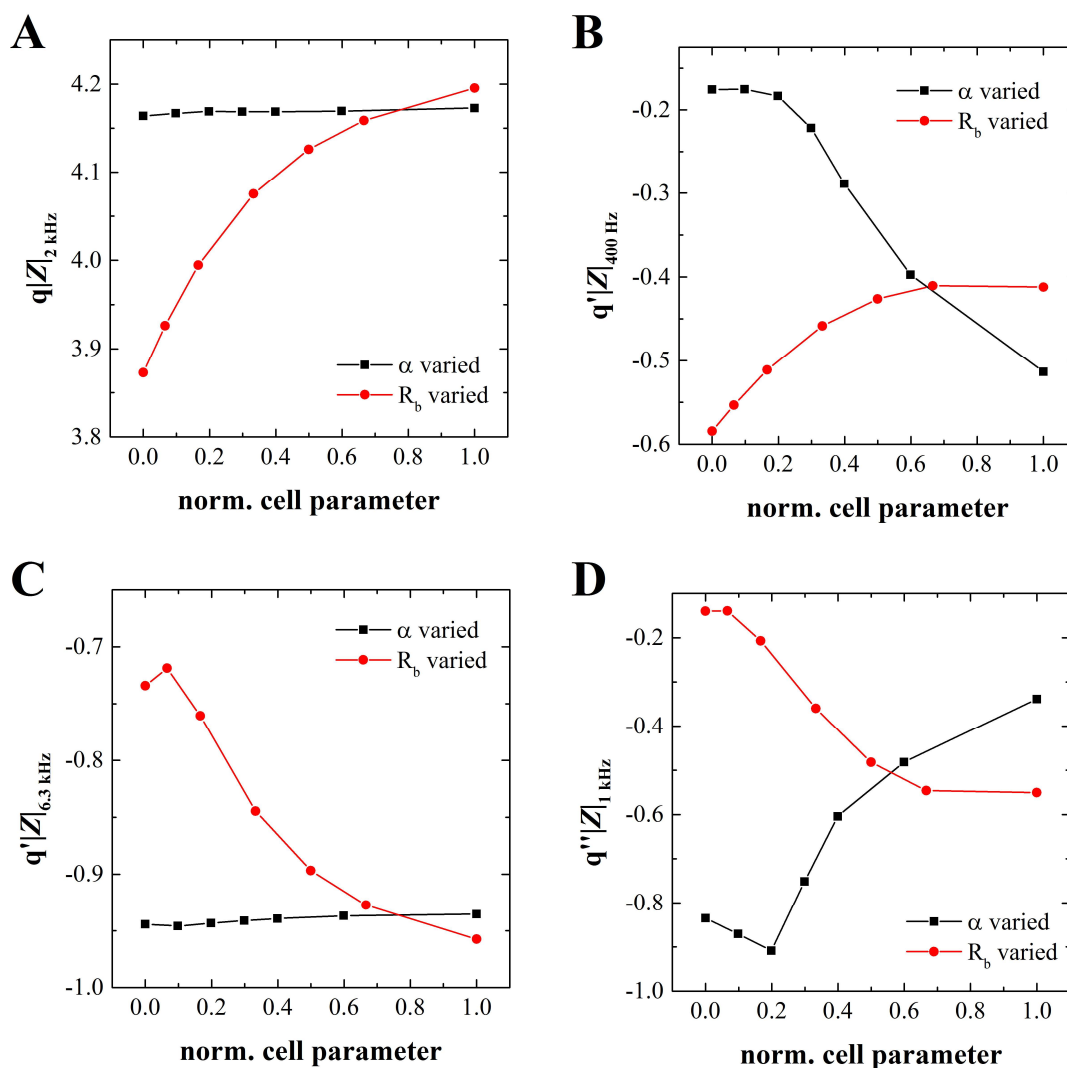
Fig. III-70: Changes of the impedance at various frequencies in spectra of different orders upon altering either cell parameter α or R_b. The cell parameters were normalized to the covered ranges between 0.1 $\Omega^{0.5}\cdot$cm and 50 $\Omega^{0.5}\cdot$cm (α) and between 0.1 $\Omega\cdot$cm² and 150 $\Omega\cdot$cm² (R_b), respectively (cf. Tab. III-25). While one parameter was varied, the others were kept constant at $C_m = 3$ µF/cm², $\alpha = 15$ $\Omega^{0.5}\cdot$cm, and $R_b = 75$ $\Omega\cdot$cm² **(A)** Zero-order spectrum at 2 kHz. **(B)** First derivative at 400 Hz. **(C)** First derivative at 6.6 kHz. **(D)** Second derivative at 1 kHz.

The results show that using the first order second order derivatives allows for a clearer discrimination between α and R_b than when only the zero-order derivative impedance is considered. The opposing tendencies of how both parameters affect $q'|Z|_{400\ Hz}$ can be exploited for that matter. Since in reality the curve progressions may not be as clear-cut as in the simulations it is advisable to additionally follow $q|Z|_{2\ kHz}$, $q'|Z|_{6.3\ kHz}$, and $q''|Z|_{1\ kHz}$ over time in order to be able countercheck the findings. The sensitive frequencies in the different derivative orders depend on the shape of the impedance spectra and need to be determined for each cell line separately. In laboratory experiments, it is possible that both parameters are affected by a certain analytical compound. This was for example observed for cytochalasin B by Opp et al.[139]

and for cytochalasin D in this work (cf. chapters 2.3.4 and 3.4.2.3). Therefore, it is essential to verify the *in silico* results and evaluate the applicability of the DIS for the discrimination of α and R_b with *in vitro* experiments.

4.4.3.2   Zero Migration

As mentioned in chapter 4.4.1 the second derivative of the impedance shows two zero points qf_0, one around $qf_0 \approx 2.5$ (~ 320 Hz) and one at about $qf_0 \approx 4$ (~ 10 kHz). Their exact positions on the x-axis depends on α and R_b as displayed in Fig. III-71. The lower-frequency zero point exhibits similar dependence on both parameters. It is shifted towards lower frequencies with increasing parameter value, α showing a slightly stronger impact in the parameter range under study. Since both parameters cause the zero point to migrate in the same direction, it can be hardly used to discriminate between α and R_b. The higher-frequency zero point is more promising in that sense as its position is only sensitive towards changes in R_b, whereas being largely unaffected by α. Except for $R_b = 0.1 \ \Omega \cdot cm^2$, the curve describing the variation of R_b is monotonically decreasing from $qf_0 = 4.4$ to $qf_0 = 3.9$. By contrast to simply following the zero-order derivative impedance magnitude at 2 kHz (cf. 4.4.3.1, Fig. III-70 A), there is a clear difference between both curves even for high cell parameters. Thus, following the migration of the second zero point shows potential to help discriminating between variations in the spectrum caused by compounds affecting either the subcellular space or the cell-cell contacts. However, *in vitro* experiments are necessary to evaluate the practicability of this method.
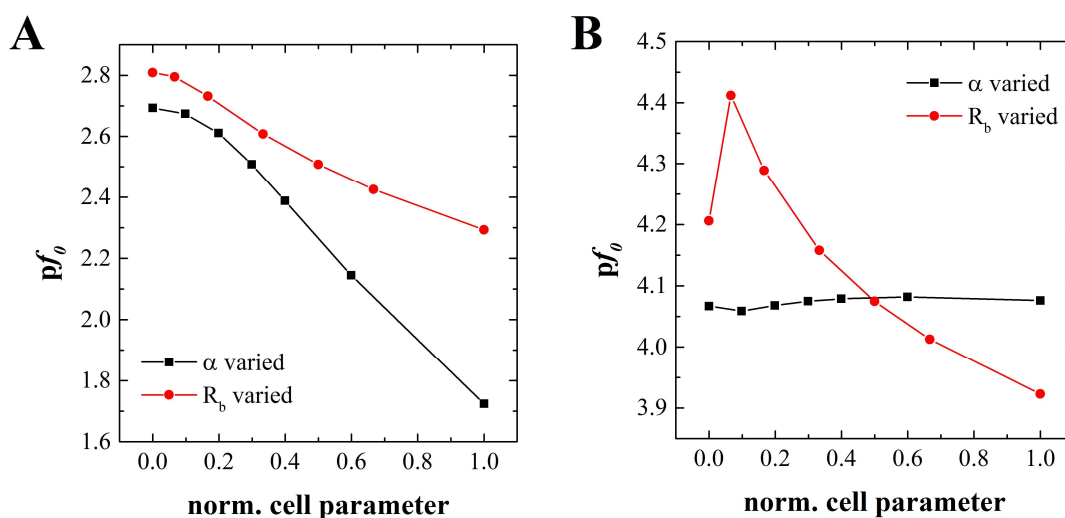
Fig. III-71: Zero migration of the two zero-crossings in the second derivative spectrum of the impedance magnitude q"|Z| upon altering either cell parameter α or R_b. The cell parameters were normalized to the covered ranges between 0.1 $\Omega^{0.5} \cdot$cm and 50 $\Omega^{0.5} \cdot$cm (α) and between 0.1 $\Omega \cdot$cm² and 150 $\Omega \cdot$cm² (R_b), respectively (cf. Tab. III-25). While one parameter was varied, the others were kept constant at C_m = 3 µF/cm², α = 15 $\Omega^{0.5} \cdot$cm, and R_b = 75 $\Omega \cdot$cm² **(A)** Low-frequency zero point p$f_0 \approx$ 2.5 (~ 320 Hz). **(B)** High-frequency zero point p$f_0 \approx$ 4 (~ 10 kHz).

4.5 Summary and Outlook

In summary, a set of methods was developed to analyze the applicability of derivative impedance spectroscopy (DIS) for the analysis of impedance-based cellular assays. For that matter, artificial raw data were generated by overlaying simulated impedance spectra with computer-generated noise. The derivative orders zero to three of these spectra were fitted using different fitting conditions and weighting methods. For a quantitative evaluation, the parameter Q_{rel} was introduced, which is a direct measure for the quality of a fit. For certain fitting conditions the first derivative displayed some improvement compared to fitting the zero-order spectrum. However, the overall tendency was a strong decline of the fit quality with increasing derivative order. This was found to be due to an increasingly inaccurate representation of the original data after each differentiation. Therefore, a suitable filter has to be found that effectively reduces the noise while maintaining the shape of the original spectrum as accurately as possible. In a second approach, DIS was used to discriminate between alterations in the spectrum caused by alterations of either one of the cell parameters α or R_b. Fixed frequencies were found, where simulations showed more distinct differences in the first or second derivative than in the zero-order spectrum. In particular, the first and second derivative exhibited opposing tendencies at 400 Hz and 1 kHz, respectively Moreover, the zero-point migration of the second

derivative was used in a similar fashion. The high-frequency zero point (~ 10 kHz) was shown to migrate only upon alteration of R_b and was unaffected by α. All results from this chapter remain to be verified with *in vitro* experiments.

5 Summary

5.1 English Summary

This thesis focused on the advancement of impedance-based cellular assays using the electric cell-substrate impedance sensing (ECIS) approach. Three linchpins of ECIS were addressed: electrode material, electrode design, and data analysis. Typically, ECIS measurements are performed by application of ac currents with low amplitude between coplanar gold-film electrodes with adherent cell monolayers growing on top. Different chapters of this work discussed the replacement of the electrode material gold by a conducting polymer, the use of a single bipolar electrode instead of two separate electrodes, and the data analysis by means of the derivatives of impedance spectra.

The first part of this work dealt with the fabrication and characterization of screen printed polymer electrode arrays. The arrays, called PDT, were based on the conducting polymer PEDOT:PSS as electrode material, silver leads to reduce the lead resistance, and a silicone passivation layer to delineate the electrode dimensions. The electrodes showed high adhesion stability in aqueous environment at 37 °C, electrical stability in the analytically relevant voltage range between 10 mV and 300 mV, and long-term stability when stored in ambient air in the dark. In comparison with gold electrodes, PEDOT:PSS exhibited a greatly enhanced interface capacitance due to its hydrogel properties. This improved the sensitivity of the impedance magnitude |Z| and the real component of the impedance R at lower frequencies for cell analysis, which is relevant for the analysis of the barrier function and the cell-substrate interaction of adherent cell monolayers. Cell proliferation and adhesion assays are commonly conducted by monitoring the capacitance at 32 kHz or 40 kHz. In this frequency range, the sensitivity of the polymer electrodes surpassed the gold electrodes. A disadvantage of PEDOT:PSS was its high resistivity and thus the high lead resistance, reducing the sensitivities for the parameters |Z| and R at higher frequencies. Alterations in the cell-substrate contact as well as the adhesion and spreading kinetics compared to commercial gold electrodes were discussed with respect to the lower substrate stiffness of PEDOT:PSS compared to gold. Several common analytical assays investigating the micromotion, proliferation, cytotoxicity, and electroporation performance of the PEDOT:PSS electrodes were successfully conducted on both electrode materials, yielding overall similar results. Nevertheless, several differences were established. Due to the high interface capacitance, the PEDOT:PSS electrodes showed an extremely low noise level during

micromotion experiments compared to the gold electrodes. This resulted in accordingly high signal-to-noise ratio and sensitivity. The proliferation assay provided more data scattering on PEDOT:PSS electrodes, which could be either attributed to the smaller electrode size or an inhomogeneous distribution of the substrate stiffness across the electrode surface. Due to a reduced generation of cytotoxic species at the electrode surface, the electroporation at lower frequencies (1.5 kHz) was found to be less invasive on PDT electrodes. Different cell lines with individual cell parameters were shown to retain their specific characteristics concerning barrier function, cell-substrate contact, and membrane capacitance on PEDOT:PSS. A remaining challenge is the electrode drift that occurred over the course of several days during the measurement. The drift was less pronounced in the impedance magnitude and appeared more prominently in the capacitance.

In the second part of this work, a novel bipolar electrode for impedimetric analysis and manipulation of living cells was developed. The bipolar electrode consisted of a high-resistance conduction path showing a potential gradient along its length. The potential at the respective position on the electrode surface depended on its distance from the contact pads. Thus, upon application of elevated electric fields of 5 V for 60 s, the bipolar electrodes caused a gradient of increasing electric field strength along the conduction path. This property of the bipolar electrodes was explained by an increasing lead resistance with growing distance from the contact pads. The system is suggested to be suitable for the optimization of wounding and electroporation experiments as the position on the electrode indicates the optimal voltage amplitude required for the respective application. In a second approach, bipolar electrodes were fabricated comprising a passivation layer with a small working and a large counter electrode like in the ECIS layout. For this layout, a mathematical model based on the ECIS model was developed. Using this model, it was shown that the low frequency part of the impedance magnitude spectrum was determined by the inherent resistance of the bipolar electrode. Compared to ECIS electrodes, the bipolar electrodes showed a sensitivity shift from the real part to the imaginary part of the complex impedance.

The third part of this work aimed to improve the accuracy of data analysis for impedance spectroscopy by calculating the derivatives of the spectra. Therefore, a set of methods was developed to analyze the applicability of derivative impedance spectroscopy (DIS) for the analysis of impedance-based cellular assays. Artificial raw data with known electrode and cell parameters were created by overlaying simulated impedance spectra with computer-generated

noise. The derivative orders zero to three of these spectra were fitted using different settings of the fitting conditions and weighting methods. For a quantitative evaluation, the parameter Q_{rel} was introduced, which is a direct measure for the quality of a fit. For certain fitting conditions the first derivative displayed some improvement compared to the zero-order spectrum. However, the overall tendency was a strong decline of the fit quality with increasing derivative order. This was found to be due to insufficient reduction of the noise, which is amplified after each differentiation. In a second approach, DIS was used to discriminate between spectral changes caused by alterations of either one of the cell parameters, α or R_b. Fixed frequencies were found, where simulations showed more distinct differences in the first or second derivative than in the zero-order spectrum. In particular, the first and second derivative exhibited opposing tendencies for the two cell parameters at 400 Hz and 1 kHz, respectively. Moreover, the migration of the zero-points of the second derivative when varying the cell parameters might become useful in a similar fashion. The high-frequency zero-point (~ 10 kHz) was shown to migrate only upon alteration of R_b and was unaffected by α. The results presented in this chapter are only valid for the investigated system and are not applicable to other cell lines.

5.2 Deutsche Zusammenfassung

Das Ziel dieser Arbeit war die Weiterentwicklung der impedimetrischer Verfahren zur Analyse lebender adhärenter Zellen *in vitro* mittels *Electric Cell-Substrate Impedance Sensing* (ECIS). Dabei standen drei zentrale Themenbereiche dieses Ansatzes im Fokus: das verwendete Elektrodenmaterial, das Elektrodendesign und die Datenanalyse. Typischerweise werden ECIS-Messungen durch Anlegen niedriger Wechselspannungen zwischen coplanaren Goldfilmelektroden, auf welchen monolagige Zellschichten wachsen, durchgeführt. In den einzelnen Kapiteln dieser Arbeit werden der Ersatz von Gold als Elektrodenmaterial durch ein leitfähiges Polymer, die Verwendung einer einzelnen bipolaren Elektrode an Stelle zweier getrennter Elektroden, sowie die Datenauswertung mittels der Ableitungen von Impedanzspektren diskutiert.

Der erste Teil dieser Arbeit behandelte die Herstellung von Polymerelektrodenarrays mittels des Siebdruckverfahrens und deren Charakterisierung. Das leitfähige Polymer PEDOT:PSS diente als Elektrodenmaterial. Ferner wurden Silber-Zuleitungen verdruckt um den Zuleitungswiderstand zu reduzieren, sowie eine Passivierungsschicht aus Silikon, welche die Größe und Form der Elektroden festlegte. Die Elektroden zeigten hohe Adhäsionsstabilität in

wässriger Umgebung bei 37 °C, elektrische Stabilität im analytisch relevanten Spannungsbereich zwischen 10 mV und 300 mV und Langzeitstabilität bei Lagerung unter Lichtausschluss. Aufgrund seiner Hydrogel-Eigenschaften wies PEDOT:PSS eine wesentlich größere Grenzflächenkapazität als Gold auf. Dadurch wurde die Sensitivität des Betrags |Z| sowie des Realteils R der Impedanz bei niedrigen Frequenzen beträchtlich gesteigert, was für die Analyse der Barrierefunktion und der Zell-Substrat-Wechselwirkung adhärenter Zellschichten von Bedeutung ist. Zelluläre Proliferations- und Adhäsionsassays werden normalerweise durch zeitaufgelöste Messung der Kapazität bei 32 kHz oder 40 kHz verfolgt. In diesem Frequenzbereich überstieg die Sensitivität der Polymerelektroden die der Goldelektroden. Der hohe spezifische Widerstand von PEDOT:PSS sowie der sich daraus ergebende Zuleitungswiderstand führte jedoch zu einer verminderten Sensitivität der Messgrößen |Z| und R bei hohen Frequenzen im Vergleich zu den Goldfilm-Elektroden als Benchmark. Unterschiede am Zell-Substrat-Kontakt und in der Adhäsions- und Spreitkinetik der Zellen im Vergleich zu kommerziellen Goldelektroden wurden im Zusammenhang mit dem geringeren Härtegrad von PEDOT:PSS im Vergleich zu Gold diskutiert. Verschiedene etablierte, zell-basierte Assays wie Micromotions-, Proliferations-, Zytotoxizitäts- und Elektroporationsstudien wurden erfolgreich mit beiden Elektrodenmaterialien durchgeführt und führten im Allgemeinen zu ähnlichen Ergebnissen. Dennoch konnten einige Unterschiede festgestellt werden. Die PEDOT:PSS-Elektroden zeigten bei Micromotion-Messungen verglichen mit Goldelektroden ein hohes Signal-Rausch-Verhältnis und dadurch eine verbesserte Sensitivität. Dies lag in der hohen Grenzflächenkapazität begründet, welche mit einem niedrigen Rauschpegel einhergeht. Der Proliferationsassay ergab unregelmäßigere Kurvenverläufe mit PEDOT:PSS-Elektroden, was mit der geringeren Elektrodengröße oder einer inhomogenen Verteilung der Substrathärte über die Elektrodenfläche erklärt werden könnte. Durch eine reduzierte Produktion zytotoxischer Spezies an der Elektrodenoberfläche unter Einwirkung invasiver Spannungen zeigte sich die Elektroporation bei niedrigen Frequenzen (1.5 kHz) weniger invasiv bei der Verwendung von PEDOT:PSS-Elektroden. Verschiedene Zelllinien mit individuellenZellparametern behielten ihre spezifischen Eigenschaften bezüglich Barrierefunktion, Zell-Substrat-Kontakt und Membrankapazität auf PEDOT:PSS bei. Eine Herausforderung für zukünftige Anwendungen ist der Elektrodendrift, welcher bei Impedanzmessungen über mehrere Tage hinweg auftrat. Der Drift war beim Betrag der Impedanz nur schwach ausgeprägt, trat bei der Kapazität jedoch stärker in den Vordergrund.

Im zweiten Teil der Arbeit wurde eine neuartige bipolare Elektrode gleichermaßen für die impedimetrische Analyse und Manipulation lebender Zellen entwickelt. Die beschriebene bipolare Elektrode bestand aus einem Leitungspfad mit hohem Eigenwiderstand, woraus sich ein Potentialgradient entlang des Leitungspfades entwickelt. Untersuchungen zeigten, dass das Potential an der jeweiligen Position auf der Elektrode vom Abstand von den Kontaktabgriffen am Ende der Leiterstruktur abhing. Durch Anlegen starker elektrischer Felder von 5V über 60 s verursachten die bipolaren Elektroden dadurch einen Spannungsgradienten entlang des Leitungspfades, der mit zunehmender Invasivität des elektrischen Feldes einherging. Diese Eigenschaft der bipolaren Elektroden wurde durch den ansteigenden Zuleitungswiderstand mit zunehmendem Abstand von den Kontakten an den Enden der Leiterstruktur erklärt. Ein mögliches Anwendungsgebiet stellt die Optimierung von Verwundungs- und Elektroporationsexperimenten dar, da anhand der Position auf der Elektrode die optimale Spannung, welche für die jeweilige Anwendung benötigt wird, erkennbar ist. Weiterhin wurden bipolare Elektroden hergestellt, welche wie beim ECIS-Layout eine Passivierungsschicht mit Öffnungen für eine kleine Arbeitselektrode und eine größere Gegenelektrode enthielten. Für dieses Elektrodendesign konnte ein auf dem ECIS-Modell basierendes physikalisches Modell entwickelt werden. Durch Anwendung dieses Modells wurde gezeigt, dass der niederfrequente Bereich in den Spektren des Betrags der Impedanz und des Realteils allein durch den Eigenwiderstand der bipolaren Elektrode bestimmt wird. Darüber hinaus wiesen die bipolaren Elektroden im Vergleich zu den ECIS-Elektroden eine Verschiebung der Sensitivität vom Realteil zum Imaginärteil der komplexen Impedanz auf.

Der dritte Teil dieser Arbeit hatte das Ziel, die Genauigkeit der Datenanalyse bei der Durchführung impedanz-basierter Assays durch Berechnung der Ableitungen der Impedanzspektren zu erhöhen. Dafür wurde eine Methode entwickelt, um die Derivativimpedanzspektroskopie (DIS) auf die Verwendbarkeit bei der impedimetrischen Untersuchung lebender Zellen hin zu untersuchen und zu charakterisieren. Künstliche Rohdaten mit bekannten Elektroden- und Zellparametern wurden erstellt, indem simulierte Impedanzspektren mit computergeneriertem Rauschen überlagert wurden. Um eine quantitative Evaluierung zu ermöglichen, wurde der Parameter Q_{rel} eingeführt, welcher ein direktes Maß für die Qualität eines Fits ist. Für bestimmte Einstellungen des Fit-Algorithmus zeigte die erste Ableitung Verbesserungen im Vergleich zum Spektrum nullter Ordnung. Allerdings wurde allgemein ein starker Abfall der Fitqualität mit zunehmender Ordnung der Ableitung beobachtet. Dies wurde auf eine ungenügende Glättung des sich mit jeder Ableitung

verstärkenden Rauschens zurückgeführt. In einem zweiten Ansatz wurde die DIS verwendet, um zwischen spektralen Veränderungen zu unterscheiden, die durch die Zellparameter α oder R_b verursacht wurden. An bestimmten Frequenzen stellten die erste und zweite Ableitung die Unterschiede deutlicher heraus als das Spektrum nullter Ordnung. Insbesondere zeigten die erste und zweite Ableitung für Änderungen der Zellparameter gegenläufige Trends bei 400 Hz bzw. 1 kHz. Darüber hinaus konnte die Migration der Nullstellen in der zweiten Ableitung auf ähnliche Weise verwendet werden. Die hochfrequente Nullstelle bei etwa 10 kHz verschob sich nur durch Veränderungen von R_b, blieb aber unbeeinflusst durch α. Die in diesem Kapitel gezeigten Ergebnisse gelten ausschließlich für das hier untersuchte System und sind nicht auf andere Zelllinien übertragbar.

IV   REFERENCES

1.   So entsteht ein neues Medikament. https://www.vfa.de/de/arzneimittel-forschung/so-funktioniert-pharmaforschung/so-entsteht-ein-medikament.html (accessed 19.09.2016).
2.   Paul, S. M.; Mytelka, D. S.; Dunwiddie, C. T.; Persinger, C. C.; Munos, B. H.; Lindborg, S. R.; Schacht, A. L., How to improve R&D productivity: the pharmaceutical industry's grand challenge. *Nat. Rev. Drug Discov.* **2010,** *9* (3), 203-214.
3.   de Jong, L. A. A.; Uges, D. R. A.; Franke, J. P.; Bischoff, R., Receptor–ligand binding assays: Technologies and Applications. *J. Chromatogr. B* **2005,** *829* (1–2), 1-25.
4.   Sittampalam, G. S.; Kahl, S. D.; Janzen, W. P., High-throughput screening: advances in assay technologies. *Curr. Opin. Chem. Biol.* **1997,** *1* (3), 384-391.
5.   Swinderman, A., Label-free: The way to be? *DDNEWS* 2011.
6.   Ciambrone, G. J.; Liu, V. F.; Lin, D. C.; McGuinness, R. P.; Leung, G. K.; Pitchford, S., Cellular dielectric spectroscopy: a powerful new approach to label-free cellular analysis. *J. Biomol. Screen.* **2004,** *9* (6), 467-80.
7.   Hartigan, J.; Liu, C.; Downey, W., Moving forward with label-free technology. *Drug Discovery World* 2010.
8.   Zang, R.; Li, D.; I-Ching; Tang; Wang, J.; Yang, S.-T., Cell-Based Assays in High-Throughput Screening for Drug Discovery. *International Journal of Biotechnology for Wellness Industries* **2012,** *1* (1), 31-51.
9.   Deprez-Poulain, R.; Deprez, B., Facts, figures and trends in lead generation. *Curr. Top. Med. Chem.* **2004,** *4* (6), 569-80.
10.   Stolwijk, J. A. Electric Manipulation and Impedance Analysis of Adherent Cells on Gold-Film Electrodes. Universität Regensburg, 2011.
11.   Homola, J., Surface Plasmon Resonance Sensors for Detection of Chemical and Biological Species. *Chem. Rev.* **2008,** *108* (2), 462-493.
12.   Fang, Y.; Ferrie, A. M.; Fontaine, N. H.; Mauro, J.; Balakrishnan, J., Resonant Waveguide Grating Biosensor for Living Cell Sensing. *Biophys. J.* **2006,** *91* (5), 1925-1940.
13.   Wegener, J.; Seebach, J.; Janshoff, A.; Galla, H. J., Analysis of the composite response of shear wave resonators to the attachment of mammalian cells. *Biophys. J.* **2000,** *78* (6), 2821-33.
14.   Wegener, J.; Janshoff, A.; Galla, H. J., Cell adhesion monitoring using a quartz crystal microbalance: comparative analysis of different mammalian cell lines. *Eur. Biophys. J.* **1998,** *28* (1), 26-37.
15.   Bergveld, P., Thirty years of ISFETOLOGY: What happened in the past 30 years and what may happen in the next 30 years. *Sensors Actuators B: Chem.* **2003,** *88* (1), 1-20.
16.   Weis, R.; Fromherz, P., Frequency dependent signal transfer in neuron transistors. *Physical Review E* **1997,** *55* (1), 877-889.
17.   Voelker, M.; Fromherz, P., Nyquist Noise of Cell Adhesion Detected in a Neuron-Silicon Transistor. *Phys. Rev. Lett.* **2006,** *96* (22), 228102.
18.   Zeitler, R.; Fromherz, P., The Thermal Voltage Fluctuations in the Planar Core-Coat Conductor of a Neuron-Semiconductor Interface. *Langmuir* **2013,** *29* (20), 6084-6090.
19.   Giaever, I.; Keese, C. R., Micromotion of mammalian cells measured electrically. *Proceedings of the National Academy of Sciences of the United States of America* **1991,** *88* (17), 7896-7900.
20.   Giaever, I.; Keese, C. R., Monitoring fibroblast behavior in tissue culture with an applied electric field. *Proceedings of the National Academy of Sciences of the United States of America* **1984,** *81* (12), 3761-3764.
21.   Solly, K.; Wang, X.; Xu, X.; Strulovici, B.; Zheng, W., Application of real-time cell electronic sensing (RT-CES) technology to cell-based assays. *Assay Drug Dev. Technol.* **2004,** *2* (4), 363-72.

22.   Xi, B.; Wang, T.; Li, N.; Ouyang, W.; Zhang, W.; Wu, J.; Xu, X.; Wang, X.; Abassi, Y. A., Functional Cardiotoxicity Profiling and Screening Using the xCELLigence RTCA Cardio System. *Journal of the Association for Laboratory Automation* **2011,** *16* (6), 415-421.

23.   Onat, D.; Brillon, D.; Colombo, P. C.; Schmidt, A. M., Human Vascular Endothelial Cells: A Model System for Studying Vascular Inflammation in Diabetes and Atherosclerosis. *Current Diabetes Reports* **2011,** *11* (3), 193-202.

24.   Shah, P.; Jogani, V.; Bagchi, T.; Misra, A., Role of Caco-2 cell monolayers in prediction of intestinal drug absorption. *Biotechnol. Prog.* **2006,** *22* (1), 186-98.

25.   Irvine, J. D.; Takahashi, L.; Lockhart, K.; Cheong, J.; Tolan, J. W.; Selick, H. E.; Grove, J. R., MDCK (Madin-Darby canine kidney) cells: A tool for membrane permeability screening. *J. Pharm. Sci.* **1999,** *88* (1), 28-33.

26.   Lin, Z.; Will, Y., Evaluation of drugs with specific organ toxicities in organ-specific cell lines. *Toxicol. Sci.* **2012,** *126* (1), 114-27.

27.   Alberts, B., *Molecular Biology of the Cell: Hauptbd*. Garland: 2002.

28.   Wegener, J., Cell Surface Interactions. In *Wiley Encyclopedia of Biomedical Engineering*, John Wiley & Sons, Inc.: 2006.

29.   Alberts, B., *Essential Cell Biology*. Garland Science: 2010.

30.   Wegener, J., Cell Junctions. In *eLS*, John Wiley & Sons, Ltd: 2001.

31.   Rehahn, M., Elektrisch leitfähige Kunststoffe: Der Weg zu einer neuen Materialklasse. *Chem. unserer Zeit* **2003,** *37* (1), 18-30.

32.   Ito, T.; Shirakawa, H.; Ikeda, S., Simultaneous polymerization and formation of polyacetylene film on the surface of concentrated soluble Ziegler-type catalyst solution. *Journal of Polymer Science: Polymer Chemistry Edition* **1974,** *12* (1), 11-20.

33.   Shirakawa, H.; Louis, E. J.; MacDiarmid, A. G.; Chiang, C. K.; Heeger, A. J., Synthesis of electrically conducting organic polymers: halogen derivatives of polyacetylene, (CH). *J. Chem. Soc., Chem. Commun.* **1977,** (16), 578-580.

34.   Menon, R., Conducting polymers: Nobel Prize in Chemistry, 2000. *Curr. Sci.* **2000,** *79* (12), 1632-1635.

35.   Nalwa, H. S., *Handbook of Advanced Electronic and Photonic Materials and Devices: Conducting polymers. Vol. 8*. 2001.

36.   Lenz, A.; Kariis, H.; Pohl, A.; Persson, P.; Ojamäe, L., The electronic structure and reflectivity of PEDOT:PSS from density functional theory. *Chem. Phys.* **2011,** *384* (1–3), 44-51.

37.   Kingsborough, R. P.; Swager, T. M., Polythiophene Hybrids of Transition-Metal Bis(salicylidenimine)s: Correlation between Structure and Electronic Properties. *J. Am. Chem. Soc.* **1999,** *121* (38), 8825-8834.

38.   Bharathan, J. M.; Yang, Y., Polymer/metal interfaces and the performance of polymer light-emitting diodes. *J. Appl. Phys.* **1998,** *84* (6), 3207-3211.

39.   Liao, J. Y.; Ho, K. C., A photoelectrochromic device using a PEDOT thin film. *J. New Mater. Electrochem. Syst.* **2005,** *8* (1), 37-47.

40.   Groenendaal, L.; Jonas, F.; Freitag, D.; Pielartzik, H.; Reynolds, J. R., Poly(3,4-ethylenedioxythiophene) and Its Derivatives: Past, Present, and Future. *Adv. Mater.* **2000,** *12* (7), 481-494.

41.   Elschner, A.; Kirchmeyer, S.; Lovenich, W.; Merker, U.; Reuter, K., *PEDOT: Principles and Applications of an Intrinsically Conductive Polymer*. CRC Press: 2010.

42.   Lange, U., Electrochemical transistor and chemoresistor based sensors: Measurement technique, materials and applications. 2010.

43.   Hao, Q., Development of conductometric polymer sensor for gaseous hydrogen chloride. 2005.

44.   Heywang, G.; Jonas, F., Poly(alkylenedioxythiophene)s—new, very stable conducting polymers. *Adv. Mater.* **1992,** *4* (2), 116-118.

45.   Jonas, F.; Morrison, J. T., 3,4-polyethylenedioxythiophene (PEDT): Conductive coatings technical applications and properties. *Synth. Met.* **1997,** *85* (1), 1397-1398.

46.   Ghosh, S.; Inganäs, O., Conducting Polymer Hydrogels as 3D Electrodes: Applications for Supercapacitors. *Adv. Mater.* **1999,** *11* (14), 1214-1218.

47.   Griffiths, D. J., *Introduction to Electrodynamics*. Pearson: 2013.

48.   Lide, D. R., *CRC Handbook of Chemistry and Physics, 85th Edition*. Taylor & Francis: 2004.

49.   Hartnagel, H., *Semiconducting Transparent Thin Films*. Taylor & Francis: 1995.

50.   Worfolk, B. J.; Andrews, S. C.; Park, S.; Reinspach, J.; Liu, N.; Toney, M. F.; Mannsfeld, S. C. B.; Bao, Z., Ultrahigh electrical conductivity in solution-sheared polymeric transparent films. *Proceedings of the National Academy of Sciences* **2015,** *112* (46), 14138-14143.

51.   Kim, J. Y.; Jung, J. H.; Lee, D. E.; Joo, J., Enhancement of electrical conductivity of poly(3,4-ethylenedioxythiophene)/poly(4-styrenesulfonate) by a change of solvents. *Synth. Met.* **2002,** *126* (2–3), 311-316.

52.   Guimard, N. K.; Gomez, N.; Schmidt, C. E., Conducting polymers in biomedical engineering. *Prog. Polym. Sci.* **2007,** *32* (8–9), 876-921.

53.   Gerard, M.; Chaubey, A.; Malhotra, B. D., Application of conducting polymers to biosensors. *Biosens. Bioelectron.* **2002,** *17* (5), 345-359.

54.   Ahuja, T.; Mir, I. A.; Kumar, D.; Rajesh, Biomolecular immobilization on conducting polymers for biosensing applications. *Biomaterials* **2007,** *28* (5), 791-805.

55.   Hayat, A.; Marty, J., Disposable Screen Printed Electrochemical Sensors: Tools for Environmental Monitoring. *Sensors* **2014,** *14* (6), 10432.

56.   Istamboulie, G.; Sikora, T.; Jubete, E.; Ochoteco, E.; Marty, J.-L.; Noguer, T., Screen-printed poly(3,4-ethylenedioxythiophene) (PEDOT): A new electrochemical mediator for acetylcholinesterase-based biosensors. *Talanta* **2010,** *82* (3), 957-961.

57.   Wong, J. Y.; Langer, R.; Ingber, D. E., Electrically conducting polymers can noninvasively control the shape and growth of mammalian cells. *Proceedings of the National Academy of Sciences of the United States of America* **1994,** *91* (8), 3201-3204.

58.   Cui, X.; Lee, V. A.; Raphael, Y.; Wiler, J. A.; Hetke, J. F.; Anderson, D. J.; Martin, D. C., Surface modification of neural recording electrodes with conducting polymer/biomolecule blends. *Journal of Biomedical Materials Research* **2001,** *56* (2), 261-272.

59.   Cui, X.; Martin, D. C., Electrochemical deposition and characterization of poly(3,4-ethylenedioxythiophene) on neural microelectrode arrays. *Sensors Actuators B: Chem.* **2003,** *89* (1–2), 92-102.

60.   Collazos-Castro, J. E.; Polo, J. L.; Hernández-Labrado, G. R.; Padial-Cañete, V.; García-Rama, C., Bioelectrochemical control of neural cell development on conducting polymers. *Biomaterials* **2010,** *31* (35), 9244-9255.

61.   Richardson-Burns, S. M.; Hendricks, J. L.; Foster, B.; Povlich, L. K.; Kim, D.-H.; Martin, D. C., Polymerization of the conducting polymer poly(3,4-ethylenedioxythiophene) (PEDOT) around living neural cells. *Biomaterials* **2007,** *28* (8), 1539-1552.

62.   Ostrakhovitch, E. A.; Byers, J. C.; O'Neil, K. D.; Semenikhin, O. A., Directed differentiation of embryonic P19 cells and neural stem cells into neural lineage on conducting PEDOT-PEG and ITO glass substrates. *Arch. Biochem. Biophys.* **2012,** *528* (1), 21-31.

63.   Green, R. A.; Lovell, N. H.; Wallace, G. G.; Poole-Warren, L. A., Conducting polymers for neural interfaces: challenges in developing an effective long-term implant. *Biomaterials* **2008,** *29* (24-25), 3393-9.

64.   Kiilerich-Pedersen, K.; Poulsen, C. R.; Jain, T.; Rozlosnik, N., Polymer based biosensor for rapid electrochemical detection of virus infection of human cells. *Biosens. Bioelectron.* **2011,** *28* (1), 386-92.

65.   Karimullah, A. S.; Cumming, D. R. S.; Riehle, M.; Gadegaard, N., Development of a conducting polymer cell impedance sensor. *Sensors Actuators B: Chem.* **2013,** *176*, 667-674.

66.   White, H. S.; Kittlesen, G. P.; Wrighton, M. S., Chemical derivatization of an array of three gold microelectrodes with polypyrrole: fabrication of a molecule-based transistor. *J. Am. Chem. Soc.* **1984,** *106* (18), 5375-5377.

67.   Khodagholy, D.; Rivnay, J.; Sessolo, M.; Gurfinkel, M.; Leleux, P.; Jimison, L. H.; Stavrinidou, E.; Herve, T.; Sanaur, S.; Owens, R. M.; Malliaras, G. G., High transconductance organic electrochemical transistors. *Nat Commun* **2013,** *4*.

68.   Ramuz, M.; Hama, A.; Huerta, M.; Rivnay, J.; Leleux, P.; Owens, R. M., Combined Optical and Electronic Sensing of Epithelial Cells Using Planar Organic Transistors. *Adv. Mater.* **2014,** *26* (41), 7083-7090.

69.   Bogatin, E., *Signal Integrity: Simplified*. Prentice Hall: 2004.

70.   Lasia, A., *Electrochemical Impedance Spectroscopy and its Applications*. Springer New York: 2014.

71.   Barsoukov, E.; Macdonald, J. R., *Impedance Spectroscopy: Theory, Experiment, and Applications*. Wiley: 2005.

72.   Sheet resistance. https://en.wikipedia.org/wiki/Sheet_resistance (accessed 24.08.2016).

73.   4192A LF Impedance Analyzer Operating and Service Manual. Agilent Technolgies: 2000.

74.   Mukherjee, A. K.; Thakur, A. K.; Takashima, W.; Kaneto, K., Minimization of contact resistance between metal and polymer by surface doping. *J. Phys. D: Appl. Phys.* **2007,** *40* (6), 1789.

75.   Weis, M.; Lin, J.; Taguchi, D.; Manaka, T.; Iwamoto, M., Insight into the contact resistance problem by direct probing of the potential drop in organic field-effect transistors. *Appl. Phys. Lett.* **2010,** *97* (26), 263304.

76.   Kuphaldt, T. R. Kelvin (4-wire) Resistance Measurement. http://www.allaboutcircuits.com/textbook/direct-current/chpt-8/kelvin-resistance-measurement (accessed 01.06.2016).

77.   Helmholtz, H., Studien über electrische Grenzschichten. *Annalen der Physik* **1879,** *243* (7), 337-382.

78.   Helmholtz, H., Ueber einige Gesetze der Vertheilung elektrischer Ströme in körperlichen Leitern mit Anwendung auf die thierisch-elektrischen Versuche. *Annalen der Physik* **1853,** *165* (6), 211-233.

79.   Gouy, M., Sur la constitution de la charge électrique à la surface d'un électrolyte. *J. Phys. Theor. Appl.* **1910,** *9* (1), 457-468.

80.   Chapman, D. L., LI. A contribution to the theory of electrocapillarity. *Philosophical Magazine Series 6* **1913,** *25* (148), 475-481.

81.   Stern, O., Zur Theorie der elektrischen Doppelschicht. *Zeitschrift für Elektrochemie und angewandte physikalische Chemie* **1924,** *30* (21-22), 508-516.

82.   Wang, H.; Pilon, L., Accurate Simulations of Electric Double Layer Capacitance of Ultramicroelectrodes. *The Journal of Physical Chemistry C* **2011,** *115* (33), 16711-16719.

83.   Grimnes, S.; Martinsen, O. G., *Bioimpedance and Bioelectricity Basics*. Elsevier Science: 2000.

84.   Burt, R.; Birkett, G.; Zhao, X. S., A review of molecular modelling of electric double layer capacitors. *PCCP* **2014,** *16* (14), 6519-6538.

85.   Rodgers, B. Diffusion: Calculating D from a Warburg Impedance. http://www.consultrsr.net/resources/eis/warburg2.htm (accessed 23.06.2016).

86.   Cuervo-Reyes, E.; Scheller, C. P.; Held, M.; Sennhauser, U., A Unifying View of the Constant-Phase-Element and Its Role as an Aging Indicator for Li-Ion Batteries. *J. Electrochem. Soc.* **2015,** *162* (8), A1585-A1591.

87.   Mulder, W. H.; Sluyters, J. H.; Pajkossy, T.; Nyikos, L., Tafel current at fractal electrodes. *Journal of Electroanalytical Chemistry and Interfacial Electrochemistry* **1990,** *285* (1), 103-115.

88.   Kim, C.-H.; Pyun, S.-I.; Kim, J.-H., An investigation of the capacitance dispersion on the fractal carbon electrode with edge and basal orientations. *Electrochim. Acta* **2003,** *48* (23), 3455-3463.

89.   Schiller, C. A.; Strunz, W., The evaluation of experimental dielectric data of barrier coatings by means of different models. *Electrochim. Acta* **2001,** *46* (24–25), 3619-3625.

90.   Jorcin, J.-B.; Orazem, M. E.; Pébère, N.; Tribollet, B., CPE analysis by local electrochemical impedance spectroscopy. *Electrochim. Acta* **2006,** *51* (8–9), 1473-1479.

91.   Pajkossy, T., An International Journal Devoted to All Aspects of Electrode Kinetics, Interfacial Structure Properties of Electrolytes, Colloid and Biological ElectrochemistryImpedance of rough capacitive electrodes. *J. Electroanal. Chem.* **1994,** *364* (1), 111-125.

92.   Randles, J. E. B., Kinetics of rapid electrode reactions. *Discussions of the Faraday Society* **1947,** *1* (0), 11-19.

93.   Rodgers, B. FittingEIS Dat - Diffusion Elements – Warburg. http://www.consultrsr.net/resources/eis/diffusion.htm (accessed 30.07.2016).

94.   Michaelis, S. Non-Invasive Biosensors to Characterize the Cell-Material Interface. Westfälische Wilhelms-Universität Münster, 2010.

95.   Reddy, J., *An Introduction to the Finite Element Method*. McGraw-Hill Education: 2005.

96.   Lo, C. M.; Keese, C. R.; Giaever, I., Impedance analysis of MDCK cells measured by electric cell-substrate impedance sensing. *Biophys. J.* **1995,** *69* (6), 2800-2807.

97.   Bredas, J. L.; Street, G. B., Polarons, bipolarons, and solitons in conducting polymers. *Acc. Chem. Res.* **1985,** *18* (10), 309-315.

98.   Ouyang, J.; Xu, Q.; Chu, C.-W.; Yang, Y.; Li, G.; Shinar, J., On the mechanism of conductivity enhancement in poly(3,4-ethylenedioxythiophene):poly(styrene sulfonate) film through solvent treatment. *Polymer* **2004,** *45* (25), 8443-8450.

99.   Ouyang, J., "Secondary doping" methods to significantly enhance the conductivity of PEDOT:PSS for its application as transparent electrode of optoelectronic devices. *Displays* **2013,** *34* (5), 423-436.

100.   Skotheim, T. A.; Reynolds, J., *Conjugated Polymers: Processing and Applications*. CRC Press: 2006.

101.   Lang, U.; Müller, E.; Naujoks, N.; Dual, J., Microscopical Investigations of PEDOT:PSS Thin Films. *Adv. Funct. Mater.* **2009,** *19* (8), 1215-1220.

102.   Zuppiroli, L.; Bussac, M. N.; Paschen, S.; Chauvet, O.; Forro, L., Hopping in disordered conducting polymers. *Physical Review B* **1994,** *50* (8), 5196-5203.

103.   Crispin, X.; Marciniak, S.; Osikowicz, W.; Zotti, G.; van der Gon, A. W. D.; Louwet, F.; Fahlman, M.; Groenendaal, L.; De Schryver, F.; Salaneck, W. R., Conductivity, morphology, interfacial chemistry, and stability of poly(3,4-ethylene dioxythiophene)–poly(styrene sulfonate): A photoelectron spectroscopy study. *J. Polym. Sci., Part B: Polym. Phys.* **2003,** *41* (21), 2561-2583.

104.   Kim, Y. H.; Sachse, C.; Machala, M. L.; May, C.; Müller-Meskamp, L.; Leo, K., Highly Conductive PEDOT:PSS Electrode with Optimized Solvent and Thermal Post-Treatment for ITO-Free Organic Solar Cells. *Adv. Funct. Mater.* **2011,** *21* (6), 1076-1081.

105.   Xia, Y.; Ouyang, J., PEDOT:PSS films with significantly enhanced conductivities induced by preferential solvation with cosolvents and their application in polymer photovoltaic cells. *J. Mater. Chem.* **2011,** *21* (13), 4927-4936.

106.   Shi, H.; Liu, C.; Jiang, Q.; Xu, J., Effective Approaches to Improve the Electrical Conductivity of PEDOT:PSS: A Review. *Advanced Electronic Materials* **2015,** *1* (4), n/a-n/a.

107.   Bobacka, J.; Lewenstam, A.; Ivaska, A., Electrochemical impedance spectroscopy of oxidized poly(3,4-ethylenedioxythiophene) film electrodes in aqueous solutions. *J. Electroanal. Chem.* **2000,** *489* (1–2), 17-27.

108.   Hernández-Labrado, G. R.; Contreras-Donayre, R. E.; Collazos-Castro, J. E.; Polo, J. L., Subdiffusion behavior in poly(3,4-ethylenedioxythiophene): Polystyrene sulfonate (PEDOT:PSS) evidenced by electrochemical impedance spectroscopy. *J. Electroanal. Chem.* **2011,** *659* (2), 201-204.

109.   Stavrinidou, E.; Leleux, P.; Rajaona, H.; Fiocchi, M.; Sanaur, S.; Malliaras, G. G., A simple model for ion injection and transport in conducting polymers. *J. Appl. Phys.* **2013,** *113* (24), 244501.

110.   Bobacka, J., Potential Stability of All-Solid-State Ion-Selective Electrodes Using Conducting Polymers as Ion-to-Electron Transducers. *Anal. Chem.* **1999,** *71* (21), 4932-4937.

111.   Lin, P.; Yan, F.; Chan, H. L. W., Ion-Sensitive Properties of Organic Electrochemical Transistors. *ACS Applied Materials & Interfaces* **2010,** *2* (6), 1637-1641.

112.   Inzelt, G., *Conducting Polymers: A New Era in Electrochemistry*. Springer Berlin Heidelberg: 2012.

113.   Macdonald, J. R.; Garber, J. A., Analysis of Impedance and Admittance Data for Solids and Liquids. *J. Electrochem. Soc.* **1977,** *124* (7), 1022-1030.

114.   Press, W. H., *Numerical Recipes 3rd Edition: The Art of Scientific Computing*. Cambridge University Press: 2007.

115.   OriginLab http://www.originlab.de/doc/Origin-Help/FIt-with-Err-Weight (accessed 04.07.2016).

116.   Almeida, A. M.; Castel-Branco, M. M.; Falcão, A. C., Linear regression for calibration lines revisited: weighting schemes for bioanalytical methods. *J. Chromatogr. B* **2002,** *774* (2), 215-222.

117.   Bewersdorff, J., *Statistik - wie und warum sie funktioniert: Ein mathematisches Lesebuch*. Vieweg+Teubner Verlag: 2011.

118.   Blobel, V.; Lohrmann, E., *Statistische und numerische Methoden der Datenanalyse*. Vieweg+Teubner Verlag: 2013.

119.   Fuller, S.; von Bonsdorff, C. H.; Simons, K., Vesicular stomatitis virus infects and matures only through the basolateral surface of the polarized epithelial cell line, MDCK. *Cell* **1984,** *38* (1), 65-77.

120.   Wegener, J.; Sieber, M.; Galla, H.-J., Impedance analysis of epithelial and endothelial cell monolayers cultured on gold surfaces. *J. Biochem. Bioph. Methods* **1996,** *32* (3), 151-170.

121.   Le Grimellec, C.; Lesniewska, E.; Cachia, C.; Schreiber, J. P.; de Fornel, F.; Goudonnet, J. P., Imaging of the membrane surface of MDCK cells by atomic force microscopy. *Biophys. J.* **1994,** *67* (1), 36-41.

122.   Poole, K.; Meder, D.; Simons, K.; Müller, D., The effect of raft lipid depletion on microvilli formation in MDCK cells, visualized by atomic force microscopy. *FEBS Lett.* **2004,** *565* (1-3), 53-58.

123.   Limonciel, A.; Wilmes, A.; Aschauer, L.; Radford, R.; Bloch, K. M.; McMorrow, T.; Pfaller, W.; van Delft, J. H.; Slattery, C.; Ryan, M. P.; Lock, E. A.; Jennings, P., Oxidative stress induced by potassium bromate exposure results in altered tight junction protein expression in renal proximal tubule cells. *Arch. Toxicol.* **2012,** *86* (11), 1741-51.

124.   Prozialeck, W. C.; Edwards, J. R.; Lamar, P. C.; Smith, C. S., Epithelial barrier characteristics and expression of cell adhesion molecules in proximal tubule-derived cell lines commonly used for in vitro toxicity studies. *Toxicol. In Vitro* **2006,** *20* (6), 942-53.

125.   Danielsson, P.; Bobacka, J.; Ivaska, A., Electrochemical synthesis and characterization of poly(3,4-ethylenedioxythiophene) in ionic liquids with bulky organic anions. *J. Solid State Electrochem.* **2004,** *8* (10), 809-817.

126.   Parry, T.; Parrott, A., *Statistics in Clinical Research*. Institute of Clinical Research: 2004.

127.   Wegener, J.; Keese, C. R.; Giaever, I., Recovery of adherent cells after in situ electroporation monitored electrically. *BioTechniques* **2002,** *33* (2), 348, 350, 352 passim.

128.   Teissie, J.; Golzio, M.; Rols, M. P., Mechanisms of cell membrane electropermeabilization: A minireview of our present (lack of ?) knowledge. *Biochimica et Biophysica Acta (BBA) - General Subjects* **2005,** *1724* (3), 270-280.

129.   Zimmermann, U.; Pilwat, G.; Riemann, F., Dielectric Breakdown of Cell Membranes. *Biophys. J.* **1974,** *14* (11), 881-899.

130.   Kinosita, K.; Tsong, T. Y., Voltage-induced conductance in human erythrocyte membranes. *Biochim. Biophys. Acta* **1979,** *554* (2), 479-497.

131.   Pliquett, F.; Wunderlich, S., Relationship between cell parameters and pulse deformation due to these cells as well as its change after electrically induced membrane breakdown. *Bioelectrochem. Bioenerg.* **1983,** *10* (5), 467-475.

132.   Keese, C. R.; Wegener, J.; Walker, S. R.; Giaever, I., Electrical wound-healing assay for cells in vitro. *Proc Natl Acad Sci U S A* **2004,** *101* (6), 1554-9.

133.   Pinco, K. A.; He, W.; Yang, J. T., α4β1 Integrin Regulates Lamellipodia Protrusion via a Focal Complex/Focal Adhesion-independent Mechanism. *Molecular Biology of the Cell* **2002,** *13* (9), 3203-3217.

134.   Wegener, J., *Measuring Biological Impacts of Nanomaterials*. Springer International Publishing: 2016.

135.   Lo, C. M.; Keese, C. R.; Giaever, I., Monitoring motion of confluent cells in tissue culture. *Exp. Cell Res.* **1993,** *204* (1), 102-9.

136.   Lovelady, D. C.; Richmond, T. C.; Maggi, A. N.; Lo, C. M.; Rabson, D. A., Distinguishing cancerous from noncancerous cells through analysis of electrical noise. *Physical review. E, Statistical, nonlinear, and soft matter physics* **2007,** *76* (4 Pt 1), 041908.

137.   Tarantola, M.; Marel, A. K.; Sunnick, E.; Adam, H.; Wegener, J.; Janshoff, A., Dynamics of human cancer cell lines monitored by electrical and acoustic fluctuation analysis. *Integrative biology : quantitative biosciences from nano to macro* **2010,** *2* (2-3), 139-50.

138.   Peng, C. K.; Havlin, S.; Stanley, H. E.; Goldberger, A. L., Quantification of scaling exponents and crossover phenomena in nonstationary heartbeat time series. *Chaos* **1995,** *5* (1), 82-87.

139.   Opp, D.; Wafula, B.; Lim, J.; Huang, E.; Lo, J. C.; Lo, C. M., Use of electric cell-substrate impedance sensing to assess in vitro cytotoxicity. *Biosens. Bioelectron.* **2009,** *24* (8), 2625-9.

140.   Sapper, A.; Wegener, J.; Janshoff, A., Cell Motility Probed by Noise Analysis of Thickness Shear Mode Resonators. *Anal. Chem.* **2006,** *78* (14), 5184-5191.

141.   An Introduction to Noise Signals. http://www.ni.com/white-paper/3006/en/ (accessed 16.10.2016).

142.   Sejdić, E.; Lipsitz, L. A., Necessity of noise in physiology and medicine. *Comput. Methods Programs Biomed.* **2013,** *111* (2), 459-470.

143.   Campos, D.; Méndez, V.; Llopis, I., Persistent random motion: Uncovering cell migration dynamics. *J. Theor. Biol.* **2010,** *267* (4), 526-534.

144.   https://de.mathworks.com/help/dsp/ref/dsp.colorednoise-class.html (accessed 14.10.2016).

145.   Colors of noise. https://en.wikipedia.org/wiki/Colors_of_noise#Blue_noise (accessed 16.10.2016).

146.   Hildebrand, J. A., Anthropogenic and natural sources of ambient noise in the ocean. *Mar. Ecol. Prog. Ser.* **2009,** *395*, 5-20.

147.   Peng, C. K.; Buldyrev, S. V.; Havlin, S.; Simons, M.; Stanley, H. E.; Goldberger, A. L., Mosaic organization of DNA nucleotides. *Physical review. E, Statistical physics, plasmas, fluids, and related interdisciplinary topics* **1994,** *49* (2), 1685-9.

148.   Kantelhardt, J. W.; Koscielny-Bunde, E.; Rego, H. H. A.; Havlin, S.; Bunde, A., Detecting long-range correlations with detrended fluctuation analysis. *Physica A: Statistical Mechanics and its Applications* **2001,** *295* (3–4), 441-454.

149.   Buldyrev, S. V.; Goldberger, A. L.; Havlin, S.; Mantegna, R. N.; Matsa, M. E.; Peng, C. K.; Simons, M.; Stanley, H. E., Long-range correlation properties of coding and noncoding DNA sequences: GenBank analysis. *Physical Review E* **1995,** *51* (5), 5084-5091.

150.   https://de.mathworks.com/help/matlab/ref/besseli.html (accessed 12.11.2016).

151.   Abramowitz, M.; Stegun, I. A., *Handbook of Mathematical Functions: with Formulas, Graphs, and Mathematical Tables*. Dover Publications: 2012.

152.   http://dlmf.nist.gov/10.30#ii (accessed 12.11.2016).

153.   Bao, Z.; Feng, Y.; Dodabalapur, A.; Raju, V. R.; Lovinger, A. J., High-Performance Plastic Transistors Fabricated by Printing Techniques. *Chem. Mater.* **1997,** *9* (6), 1299-1301.

154.   Shaheen, S. E.; Radspinner, R.; Peyghambarian, N.; Jabbour, G. E., Fabrication of bulk heterojunction plastic solar cells by screen printing. *Appl. Phys. Lett.* **2001,** *79* (18), 2996-2998.

155.   Lee, D. H.; Choi, J. S.; Chae, H.; Chung, C. H.; Cho, S. M., Screen-printed white OLED based on polystyrene as a host polymer. *Current Applied Physics* **2009,** *9* (1), 161-164.

156.   Xu, J. M., Plastic electronics and future trends in microelectronics. *Synth. Met.* **2000,** *115* (1–3), 1-3.

157.   Khan, S.; Lorenzelli, L.; Dahiya, R. S., Technologies for Printing Sensors and Electronics Over Large Flexible Substrates: A Review. *IEEE Sens. J.* **2015,** *15* (6), 3164-3185.

158.   Wegener, J.; Keese, C. R.; Giaever, I., Electric Cell–Substrate Impedance Sensing (ECIS) as a Noninvasive Means to Monitor the Kinetics of Cell Spreading to Artificial Surfaces. *Exp. Cell Res.* **2000,** *259* (1), 158-166.

159.   Madou, M. J., *Fundamentals of Microfabrication: The Science of Miniaturization, Second Edition*. Taylor & Francis: 2002.

160.   Zehnder, Steven M.; Suaris, M.; Bellaire, Madisonclaire M.; Angelini, Thomas E., Cell Volume Fluctuations in MDCK Monolayers. *Biophys. J.* **2015,** *108* (2), 247-250.

161.   Janshoff, A.; Lorenz, B.; Pietuch, A.; Fine, T.; Tarantola, M.; Steinem, C.; Wegener, J., Cell Adhesion to Ordered Pores: Consequences for Cellular Elasticity. *J. Adhes. Sci. Technol.* **2010,** *24* (13-14), 2287-2300.

162.   Xia, Y.; Sun, K.; Ouyang, J., Solution-Processed Metallic Conducting Polymer Films as Transparent Electrode of Optoelectronic Devices. *Adv. Mater.* **2012,** *24* (18), 2436-2440.

163.   Price, D. T.; Rahman, A. R.; Bhansali, S., Design rule for optimization of microelectrodes used in electric cell-substrate impedance sensing (ECIS). *Biosens. Bioelectron.* **2009,** *24* (7), 2071-6.

164.   Nyikos, L.; Pajkossy, T., Fractal dimension and fractional power frequency-dependent impedance of blocking electrodes. *Electrochim. Acta* **1985,** *30* (11), 1533-1540.

165.   Srinivasan, S., *Fuel Cells: From Fundamentals to Applications*. Springer US: 2006.

166. Ujvári, M.; Gubicza, J.; Kondratiev, V.; Szekeres, K. J.; Láng, G. G., Morphological changes in electrochemically deposited poly(3,4-ethylenedioxythiophene) films during overoxidation. *J. Solid State Electrochem.* **2015,** *19* (4), 1247-1252.

167. Láng Gyözö, G.; Ujvári, M.; Vesztergom, S.; Kondratiev, V.; Gubicza, J.; Szekeres Krisztina, J., The Electrochemical Degradation of Poly(3,4-ethylenedioxythiophene) Films Electrodeposited from Aqueous Solutions. In *Z. Phys. Chem.*, 2016; Vol. 230, p 1281.

168. Wegener, J., Impedance Analysis of Cell Junctions. In *Nanotechnology*, Wiley-VCH Verlag GmbH & Co. KGaA: 2010.

169. Eisenberg, J. L.; Safi, A.; Wei, X.; Espinosa, H. D.; Budinger, G. R. S.; Takawira, D.; Hopkinson, S. B.; Jones, J. C. R., Substrate stiffness regulates extracellular matrix deposition by alveolar epithelial cells. *Research and reports in biology* **2011,** *2011* (2), 1-12.

170. Hassarati, R. T.; Goding, J. A.; Baek, S.; Patton, A. J.; Poole-Warren, L. A.; Green, R. A., Stiffness quantification of conductive polymers for bioelectrodes. *J. Polym. Sci., Part B: Polym. Phys.* **2014,** *52* (9), 666-675.

171. Crispin, X.; Jakobsson, F. L. E.; Crispin, A.; Grim, P. C. M.; Andersson, P.; Volodin, A.; van Haesendonck, C.; Van der Auweraer, M.; Salaneck, W. R.; Berggren, M., The Origin of the High Conductivity of Poly(3,4-ethylenedioxythiophene)−Poly(styrenesulfonate) (PEDOT−PSS) Plastic Electrodes. *Chem. Mater.* **2006,** *18* (18), 4354-4360.

172. Nardes, A. M.; Kemerink, M.; Janssen, R. A. J.; Bastiaansen, J. A. M.; Kiggen, N. M. M.; Langeveld, B. M. W.; van Breemen, A. J. J. M.; de Kok, M. M., Microscopic Understanding of the Anisotropic Conductivity of PEDOT:PSS Thin Films. *Adv. Mater.* **2007,** *19* (9), 1196-1200.

173. Brown, X. Q.; Ookawa, K.; Wong, J. Y., Evaluation of polydimethylsiloxane scaffolds with physiologically-relevant elastic moduli: interplay of substrate mechanics and surface chemistry effects on vascular smooth muscle cell response. *Biomaterials* **2005,** *26* (16), 3123-3129.

174. Engler, A. J.; Griffin, M. A.; Sen, S.; Bönnemann, C. G.; Sweeney, H. L.; Discher, D. E., Myotubes differentiate optimally on substrates with tissue-like stiffness. *pathological implications for soft or stiff microenvironments* **2004,** *166* (6), 877-887.

175. Tilghman, R. W.; Cowan, C. R.; Mih, J. D.; Koryakina, Y.; Gioeli, D.; Slack-Davis, J. K.; Blackman, B. R.; Tschumperlin, D. J.; Parsons, J. T., Matrix rigidity regulates cancer cell growth and cellular phenotype. *PloS one* **2010,** *5* (9), e12905.

176. Klein, E. A.; Yin, L.; Kothapalli, D.; Castagnino, P.; Byfield, F. J.; Xu, T.; Levental, I.; Hawthorne, E.; Janmey, P. A.; Assoian, R. K., Cell-cycle control by physiological matrix elasticity and in vivo tissue stiffening. *Curr. Biol.* **2009,** *19* (18), 1511-8.

177. Wells, R. G., The role of matrix stiffness in regulating cell behavior. *Hepatology (Baltimore, Md.)* **2008,** *47* (4), 1394-400.

178. Cooper, J. A., Effects of cytochalasin and phalloidin on actin. *J. Cell Biol.* **1987,** *105* (4), 1473-8.

179. Flanagan, M. D.; Lin, S., Cytochalasins block actin filament elongation by binding to high affinity sites associated with F-actin. *J. Biol. Chem.* **1980,** *255* (3), 835-8.

180. Waschke, J.; Curry, F. E.; Adamson, R. H.; Drenckhahn, D., Regulation of actin dynamics is critical for endothelial barrier functions. *American Journal of Physiology - Heart and Circulatory Physiology* **2005,** *288* (3), H1296-H1305.

181. Matthews, J. B.; Tally, K. J.; Smith, J. A.; Awtrey, C. S., F-actin differentially alters epithelial transport and barrier function. *J. Surg. Res.* **1994,** *56* (6), 505-9.

182. Stevenson, B. R.; Begg, D. A., Concentration-dependent effects of cytochalasin D on tight junctions and actin filaments in MDCK epithelial cells. *J. Cell Sci.* **1994,** *107* (3), 367-375.

183. Gottlieb, T. A.; Ivanov, I. E.; Adesnik, M.; Sabatini, D. D., Actin microfilaments play a critical role in endocytosis at the apical but not the basolateral surface of polarized epithelial cells. *J. Cell Biol.* **1993,** *120* (3), 695-710.

184. Humphries, J. D.; Wang, P.; Streuli, C.; Geiger, B.; Humphries, M. J.; Ballestrem, C., Vinculin controls focal adhesion formation by direct interactions with talin and actin. *The Journal of Cell Biology* **2007,** *179* (5), 1043-1057.

185. Friederich, E.; Kreis, T. E.; Louvard, D., Villin-induced growth of microvilli is reversibly inhibited by cytochalasin D. *J. Cell Sci.* **1993,** *105* (3), 765-775.

186. Podolak, I.; Galanty, A.; Sobolewska, D., Saponins as cytotoxic agents: a review. *Phytochem. Rev.* **2010,** *9* (3), 425-474.

187. Bangham, A. D.; Horne, R. W.; Glauert, A. M.; Dingle, J. T.; Lucy, J. A., Action of saponin on biological cell membranes. *Nature* **1962,** *196*, 952-5.

188. Haridas, V.; Higuchi, M.; Jayatilake, G. S.; Bailey, D.; Mujoo, K.; Blake, M. E.; Arntzen, C. J.; Gutterman, J. U., Avicins: triterpenoid saponins from Acacia victoriae (Bentham) induce apoptosis by mitochondrial perturbation. *Proc Natl Acad Sci U S A* **2001,** *98* (10), 5821-6.

189.   Gauthier, C.; Legault, J.; Girard-Lalancette, K.; Mshvildadze, V.; Pichette, A., Haemolytic activity, cytotoxicity and membrane cell permeabilization of semi-synthetic and natural lupane- and oleanane-type saponins. *Biorg. Med. Chem.* **2009,** *17* (5), 2002-2008.

190.   Wang, H.-B.; Dembo, M.; Wang, Y.-L., Substrate flexibility regulates growth and apoptosis of normal but not transformed cells. *American Journal of Physiology - Cell Physiology* **2000,** *279* (5), C1345-C1350.

191.   Heneghan, C.; McDarby, G., Establishing the relation between detrended fluctuation analysis and power spectral density analysis for stochastic processes. *Physical review. E, Statistical physics, plasmas, fluids, and related interdisciplinary topics* **2000,** *62* (5 Pt A), 6103-10.

192.   Lovelady, D. C.; Friedman, J.; Patel, S.; Rabson, D. A.; Lo, C. M., Detecting effects of low levels of cytochalasin B in 3T3 fibroblast cultures by analysis of electrical noise obtained from cellular micromotion. *Biosens. Bioelectron.* **2009,** *24* (7), 2250-4.

193.   Sapper, A.; Reiss, B.; Janshoff, A.; Wegener, J., Adsorption and Fluctuations of Giant Liposomes Studied by Electrochemical Impedance Measurements. *Langmuir* **2006,** *22* (2), 676-680.

194.   Hassibi, A.; Navid, R.; Dutton, R. W.; Lee, T. H., Comprehensive study of noise processes in electrode electrolyte interfaces. *J. Appl. Phys.* **2004,** *96* (2), 1074-1082.

195.   Krol, A.; Grinfeldt, M. G.; Levin, S. V.; Smilgavichus, A. D., Local mechanical oscillations of the cell surface within the range 0.2-30 Hz. *Eur. Biophys. J.* **1990,** *19* (2), 93-9.

196.   Mittelman, L.; Levin, S.; Verschueren, H.; De Baetselier, P.; Korenstein, R., Direct correlation between cell membrane fluctuations, cell filterability and the metastatic potential of lymphoid cell lines. *Biochem. Biophys. Res. Commun.* **1994,** *203* (2), 899-906.

197.   Tuvia, S.; Almagor, A.; Bitler, A.; Levin, S.; Korenstein, R.; Yedgar, S., Cell membrane fluctuations are regulated by medium macroviscosity: Evidence for a metabolic driving force. *Proceedings of the National Academy of Sciences of the United States of America* **1997,** *94* (10), 5045-5049.

198.   Gascoyne, P. R. C.; Shim, S.; Noshari, J.; Becker, F. F.; Stemke-Hale, K., Correlations between the Dielectric Properties and Exterior Morphology of Cells Revealed by Dielectrophoretic Field-Flow Fractionation. *Electrophoresis* **2013,** *34* (7), 1042-1050.

199.   Cole, K. S., *Membranes, Ions and Impulses: A Chapter of Classical Biophysics*. University of California Press: 1972.

200.   Hansson, G. C.; Simons, K.; van Meer, G., Two strains of the Madin-Darby canine kidney (MDCK) cell line have distinct glycosphingolipid compositions. *The EMBO Journal* **1986,** *5* (3), 483-489.

201.   von Bonsdorff, C. H.; Fuller, S. D.; Simons, K., Apical and basolateral endocytosis in Madin-Darby canine kidney (MDCK) cells grown on nitrocellulose filters. *The EMBO Journal* **1985,** *4* (11), 2781-2792.

202.   Reiß, B. Mikrogravimetrische Untersuchung des Adhäsionskontakts tierischer Zellen: Eine biophysikalische Studie. Westfälische Wilhelms-Universität Münster, 2004.

203.   Stevenson, B. R.; Anderson, J. M.; Goodenough, D. A.; Mooseker, M. S., Tight junction structure and ZO-1 content are identical in two strains of Madin-Darby canine kidney cells which differ in transepithelial resistance. *J. Cell Biol.* **1988,** *107* (6 Pt 1), 2401-8.

204.   Lo, C. M.; Keese, C. R.; Giaever, I., Cell-substrate contact: another factor may influence transepithelial electrical resistance of cell layers cultured on permeable filters. *Exp. Cell Res.* **1999,** *250* (2), 576-80.

205.   Naciri, M.; Kuystermans, D.; Al-Rubeai, M., Monitoring pH and dissolved oxygen in mammalian cell culture using optical sensors. *Cytotechnology* **2008,** *57* (3), 245-250.

206.   Arndt, S.; Seebach, J.; Psathaki, K.; Galla, H. J.; Wegener, J., Bioelectrical impedance assay to monitor changes in cell shape during apoptosis. *Biosens. Bioelectron.* **2004,** *19* (6), 583-94.

207.   Stolwijk, J. A.; Hartmann, C.; Balani, P.; Albermann, S.; Keese, C. R.; Giaever, I.; Wegener, J., Impedance analysis of adherent cells after in situ electroporation: non-invasive monitoring during intracellular manipulations. *Biosens. Bioelectron.* **2011,** *26* (12), 4720-7.

208.   Granot, Y.; Rubinsky, B., Methods of optimization of electrical impedance tomography for imaging tissue electroporation. *Physiol. Meas.* **2007,** *28* (10), 1135-47.

209.   Kim, J. A.; Cho, K.; Shin, Y. S.; Jung, N.; Chung, C.; Chang, J. K., A multi-channel electroporation microchip for gene transfection in mammalian cells. *Biosens. Bioelectron.* **2007,** *22* (12), 3273-3277.

210.   Wu, M.; Zhao, D.; Wei, Z.; Zhong, W.; Yan, H.; Wang, X.; Liang, Z.; Li, Z., Method for Electric Parametric Characterization and Optimization of Electroporation on a Chip. *Anal. Chem.* **2013,** *85* (9), 4483-4491.

211.   Wu, M.; Zhao, D.; Hao, Y.; Liang, Z.; Li, Z. In *A symmetrical hyperbolic formatted microchip for rapid optimization of electroporation*, The 8th Annual IEEE International Conference on Nano/Micro Engineered and Molecular Systems, 7-10 April 2013; 2013; pp 312-315.

212.   Petronis, S.; Stangegaard, M.; Christensen, C. B.; Dufva, M., Transparent polymeric cell culture chip with integrated temperature control and uniform media perfusion. *BioTechniques* **2006,** *40* (3), 368-76.

213.   Jones, D. P., *Biomedical Sensors*. Momentum Press: 2010.

214.   Murillo, J. A.; Lemus, J. M.; Garcia, L. F., Simultaneous determination of the binary mixtures of cefsulodin and clavulanic acid by using first-derivative spectrophotometry. *J. Pharm. Biomed. Anal.* **1995,** *13* (6), 769-76.

215.   Bosch Ojeda, C.; Sanchez Rojas, F., Recent applications in derivative ultraviolet/visible absorption spectrophotometry: 2009–2011: A review. *Microchem. J.* **2013,** *106*, 1-16.

216.   Kus, S.; Marczenko, Z.; Obarski, N., Derivative UV-VIS spectrophotometry in analytical chemistry. *Chem. Anal* **1996,** *41* (6).

217.   Kurzweil, P.; Fischle, H. J., A new monitoring method for electrochemical aggregates by impedance spectroscopy. *J. Power Sources* **2004,** *127* (1–2), 331-340.

218.   Savitzky, A.; Golay, M. J. E., Smoothing and Differentiation of Data by Simplified Least Squares Procedures. *Anal. Chem.* **1964,** *36* (8), 1627-1639.

219.   Feher, K.; Hewlett-Packard, E. o., *Telecommunications Measurements, Analysis, and Instrumentation*. Noble Publishing: 1997.

220.   Knowles, I.; Renka, R. J., Methods for numerical differentiation of noisy data. *Electron. J. Differ. Equ.* **2014,** *21*, 235-246.

221.   Chartrand, R., Numerical differentiation of noisy, nonsmooth data. *ISRN Applied Mathematics* **2011,** *2011*.

V   APPENDIX

1   List of Abbreviations

AC	alternating current
ACN	acetonitrile
CaAM	calcein acetoxymethylester
CE	counter electrode
CLSM	confocal laser scanning microscope
CNLS	complex nonlinear least-squares
CPE	constant phase element
CytD	cytochalasin D
DC	direct current
DFA	detrended fluctuation analysis
DIS	derivative impedance spectroscopy
DMSO	dimethyl sulfoxide
DS	derivative spectroscopy
DUT	device under test
DVA	detrended variance analysis
ECIS	electric cell-substrate impedance sensing
EDL	electric double layer
EG	ethylene glycol
EIS	electrical impedance spectroscopy
EIS	electrochemical impedance spectroscopy
EthD-1	ethidium homodimer-1
EtOH	ethanol
FCS	fetal calve serum
FEM	finite element method

FFT	fast Fourier transform
FITC	fluorescein isothiocyanate
GDA	glutardialdehyde
HOMO	highest occupied molecular orbital
ISFET	ion selective field-effect transistor
LAPS	light-addressable potentiometric sensor
LOD	limit of detection
LUMO	lowest unoccupied molecular orbital
MDCK	Madin-Darby canine kidney
MeOH	methanol
NRK	normal rat kidney
OECT	organic electrochemical transistor
OLED	organic light emitting diode
OSC	oscillator
PDF	probability density function
PDMS	polydimethylsiloxane
PDT	PEDOT:PSS electrode array
PEDOT	polyethylene(3,4)dioxythiophene
PSD	power spectral density
PSS	polystyrene sulfonate
QCM	quartz crystal microbalance
RT	room temperature
RWG	resonant waveguide grating
SD	standard deviation
SE	squared errors
SEM	standard error of the mean
SG	Savitzky-Golay
SNR	signal-to-noise ratio
SPR	surface plasmon resonance
SSE	sum of squared errors
TsO	tosylate
UV/VIS	ultraviolet/visible light
WE	working electrode

2   Supplementary Information
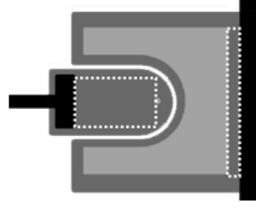
Fig. V-1: Drawing of a PDT well. The white dotted lines mark the areas that were used for the calculation of the lead resistance (cf. Eq. 55). *Black:* silver leads, *light grey:* PEDOT:PSS exposed to the electrolyte, *dark grey:* PEDOT:PSS covered by a silicone passivation layer. For an image of the complete PDT array refer to Fig. III-11.

$$R_{lead} = 700 \ \Omega/sq \cdot \frac{100}{60} + 700 \ \Omega/sq \cdot \frac{13}{80} \approx 1200 \ \Omega \qquad\qquad \text{Eq. 55}$$
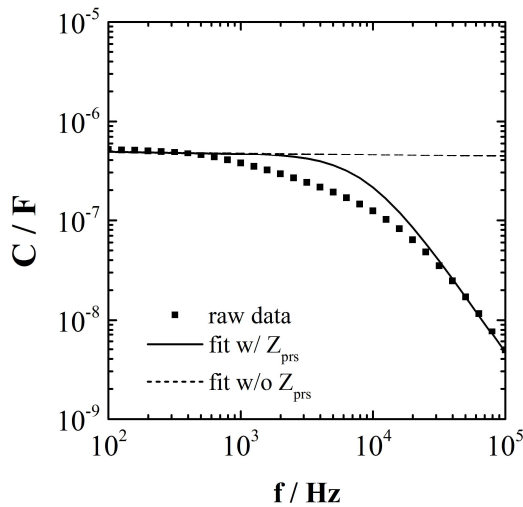
Fig. V-2: Capacitance spectrum of a cell-free PDT electrode after MDCK-II cells were permeabilized with saponin. The raw data were fitted with and without an experimentally determined value for the parasitic impedance Z_{prs}. Parameters used for the fits: $R_{bulk} = 2400 \ \Omega$, $A_{cpe-c} = 4.15 \cdot 10^{-4} \ F \cdot s^{n-1}/cm^2$, $n_{cpe-c} = 0.985$, $A_{el} = 1.3 \cdot 10^{-4} \ cm^2$, $A_{prs} = 2 \cdot 10^{-10} \ F \cdot s^{n-1}/cm^2$, $n_{prs} = 0.945$, $A_{cpe-r} = 0.002 \ F \cdot s^{n-1}/cm^2$, $n_{cpe-c} = 0.2$.
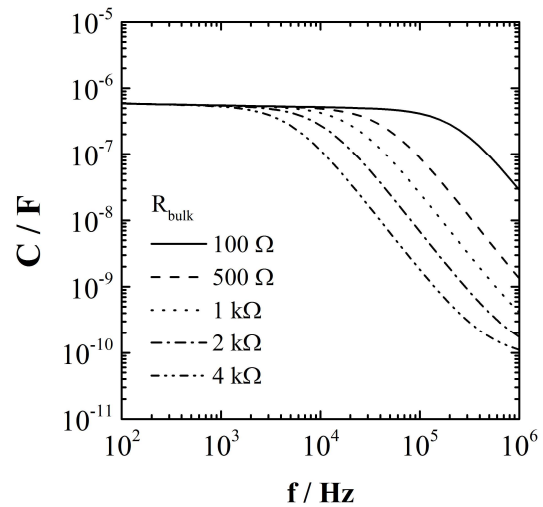
Fig. V-3: Simulated capacitance spectra of cell-free electrodes with different values of R_{bulk}. Parameters used for the simulation: $A_{cpe-c} = 5.26 \cdot 10^{-4} \ F \cdot s^{n-1}/cm^2$, $n_{cpe-c} = 0.975$, $A_{el} = 1.3 \cdot 10^{-4} \ cm^2$, $A_{prs} = 2 \cdot 10^{-10} \ F \cdot s^{n-1}/cm^2$, $n_{prs} = 0.945$, $A_{cpe-r} = 0.002 \ F \cdot s^{n-1}/cm^2$, $n_{cpe-c} = 0.2$.
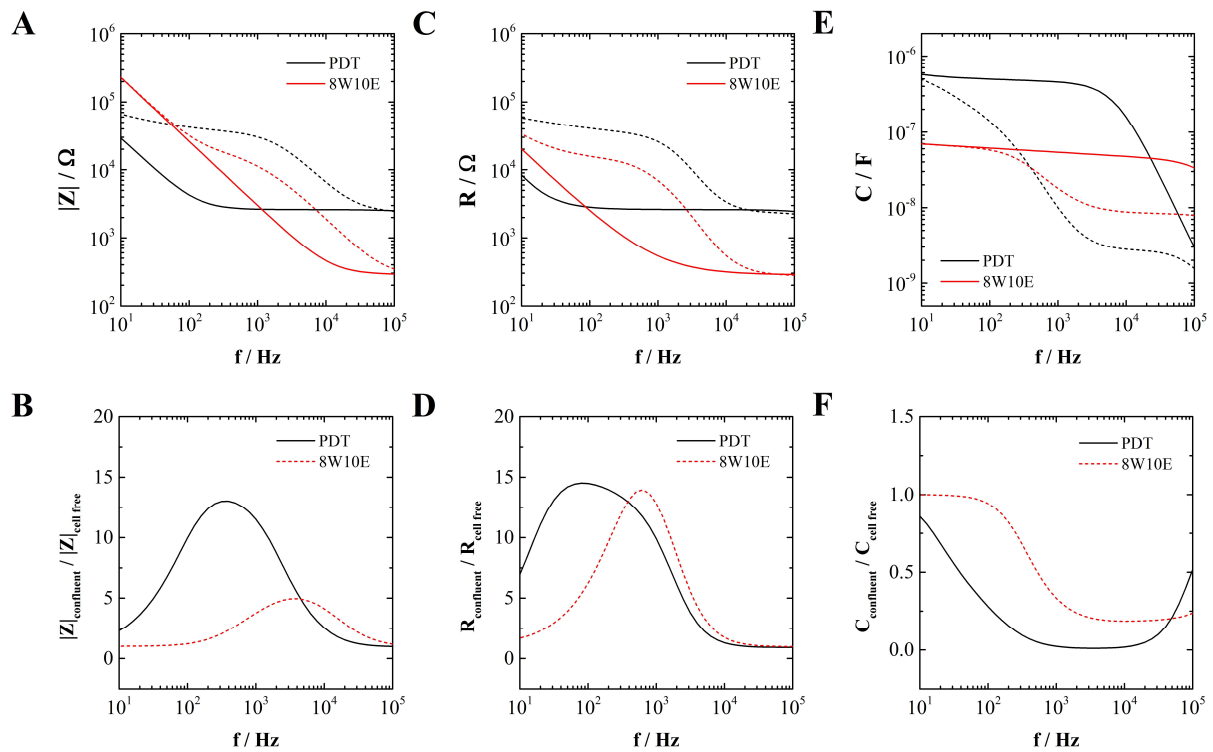
Fig. V-4: Simulated frequency spectra of different impedance components. **(A)** Impedance magnitude |Z|, **(B)** normalized impedance magnitude, **(C)** resistance R, **(D)** normalized resistance, **(E)** capacitance C, **(F)** normalized capacitance. In (A), (C), and (E), solid lines correspond to cell-free electrodes and dashed lines to cell-covered electrodes. Parameters used for the simulations: *(PDT)* R_{bulk} = 2610 Ω, A_{cpe-c} = $4.4 \cdot 10^{-4}$ F·s^{n-1}/cm², n_{cpe-c} = 0.975, A_{el} = $1.3 \cdot 10^{-4}$ cm², A_{prs} = $2 \cdot 10^{-10}$ F·s^{n-1}/cm², n_{prs} = 0.945, A_{cpe-r} = 0.002 F·s^{n-1}/cm², n_{cpe-c} = 0.2. *(8W10E)* R_{bulk} = 288 Ω, A_{cpe} = $1.73 \cdot 10^{-5}$ F·s^{n-1}/cm², n_{cpe} = 0.945, A_{el} = $5 \cdot 10^{-4}$ cm², A_{prs} = $2.4 \cdot 10^{-10}$ F·s^{n-1}/cm², n_{prs} = 0.981.
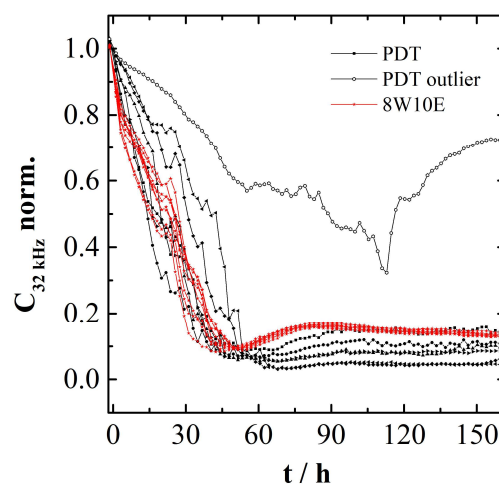
Fig. V-5: Proliferation raw data of MDCK-II cells on PDT and 8W10E electrodes. The time course is presented by the normalized capacitance at 32 kHz. The cells were seeded at a density of 20000 cells/cm² at time point t = 0 h.
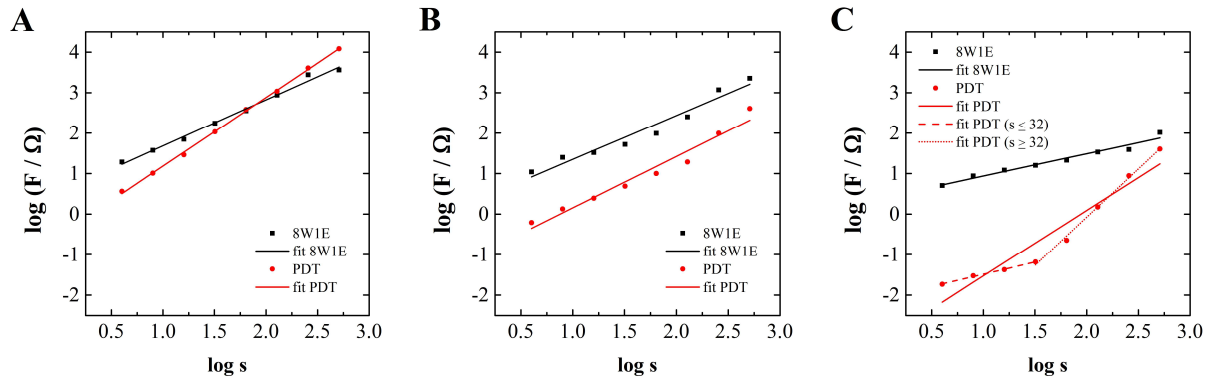
Fig. V-6: Typical data of the DFA analysis of MDCK-II cells growing on 8W1E and PDT electrodes including the segment size s dependent fluctuations F(s) and the corresponding linear fits. **(A)** Living cells. **(B)** Fixed cells. **(C)** Cell-free electrode. For the analysis, only the last 512 of the overall 612 data points of the time series were used. The measurements were recorded at 400 Hz. This figure contains the same data as Fig. V-7.
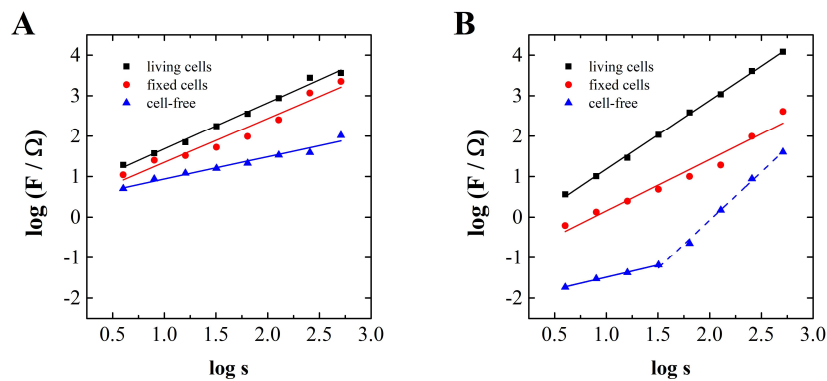
Fig. V-7: Typical data of the DFA analysis of MDCK-II cells growing on 8W1E and PDT electrodes including the segment size s dependent fluctuations F(s) and the corresponding linear fits. **(A)** 8W1E electrodes. **(B)** PDT electrodes. For the analysis, only the last 512 of the overall 612 data points of the time series were used. The measurements were recorded at 400 Hz. This figure contains the same data as Fig. V-6.
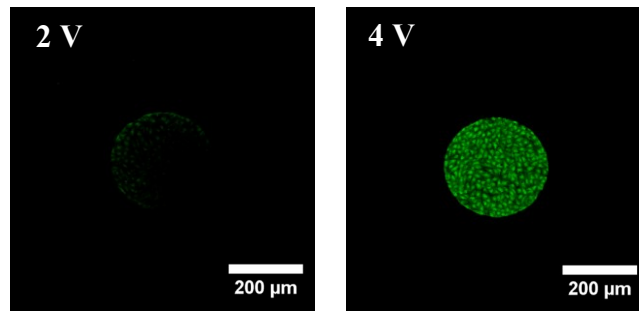
Fig. V-8: Typical micrograph of electroporated NRK cells grown on 8W1E electrodes using a 4 kDa FITC dextran as model compound (pulse duration: 200 ms, pulse frequency: 1.5 kHz; CLSM settings: pinhole size s, gain 105, laser excitation: 488 nm). The electroporation was performed two days after confluent seeding. At 1.5 kHz the electroporation pulses with the given conditions were fatal for the cells (cf chapter II.2.3.8).
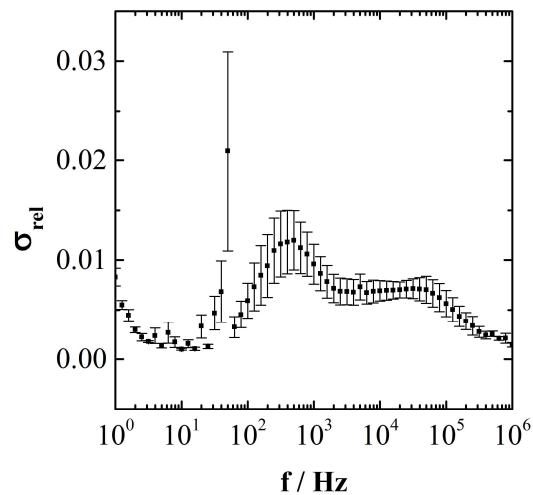
Fig. V-9: Noise spectrum used for the simulation of artificial raw data. The relative standard deviation σ_{rel} was calculated from 10 consecutive impedance magnitude spectra. (N = 5, ± SEM)

3 LabView Programs

3.1 Simulation and Manual Fitting of Impedance Spectra
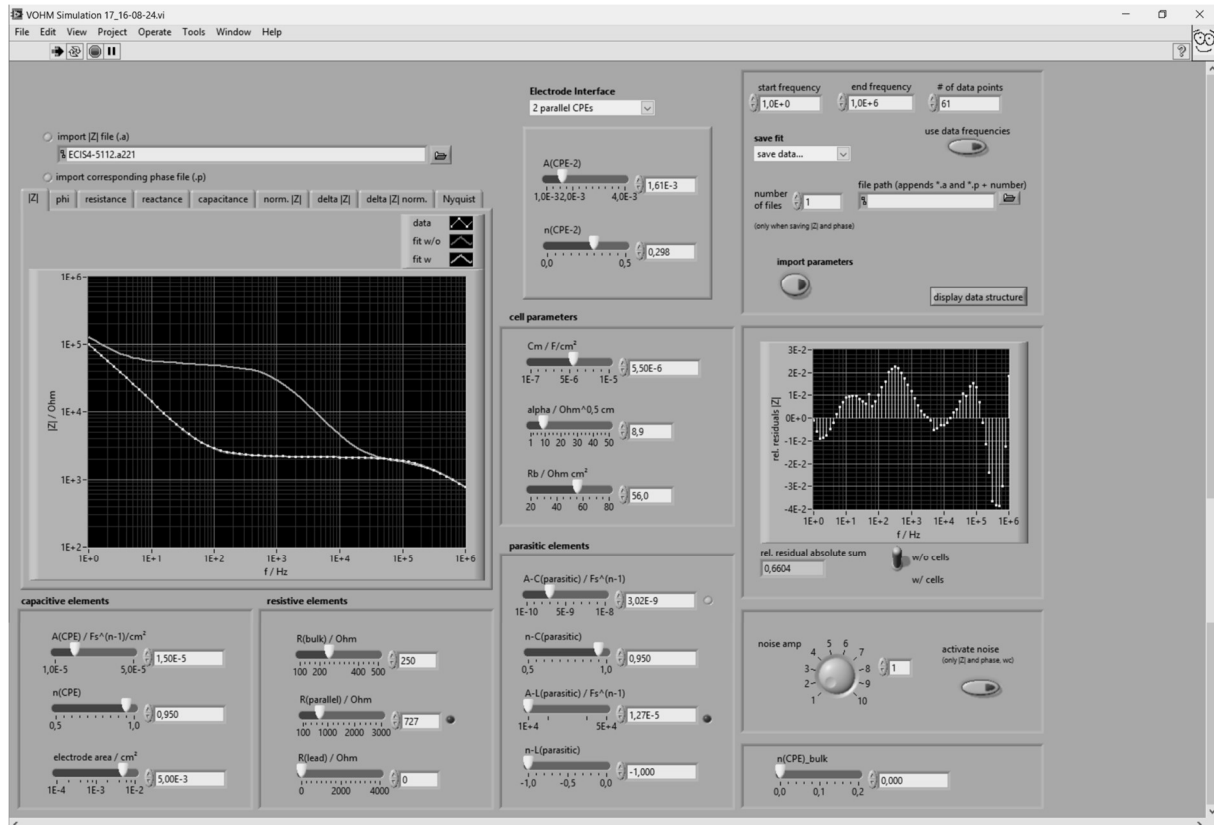
File name:	VOHM Simulation 17_16-08-24.vi
Description:	Simulates impedance spectra according to the ECIS model, including the option to add artificial noise. Impedance spectra can also be fitted manually by loading the raw data into the GUI.
Used in chapters:	III.2.3.1.3, III.2.3.1.4, III.2.3.2, III.2.3.3.2, III.3.4.2.3, III.3.4.2.4, III.3.4.2.5, III.4.4.2

3.2   Simulation of Time Series with Different Noise Colors
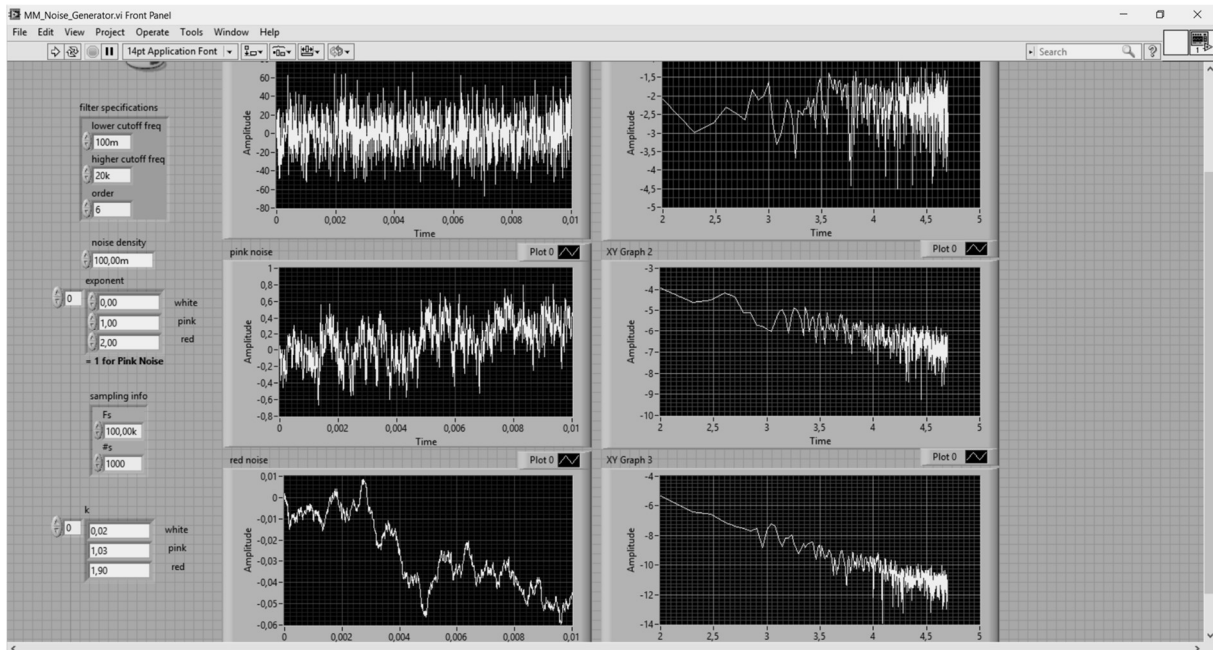
File name:	MM_Noise_Generator.vi
Description:	Simulates random noise time series with different noise colors. PSD spectra are calculated as well as the respective slopes of the linear fits.
Used in chapter:	III.1.4.1

3.3 Micromotion Analysis
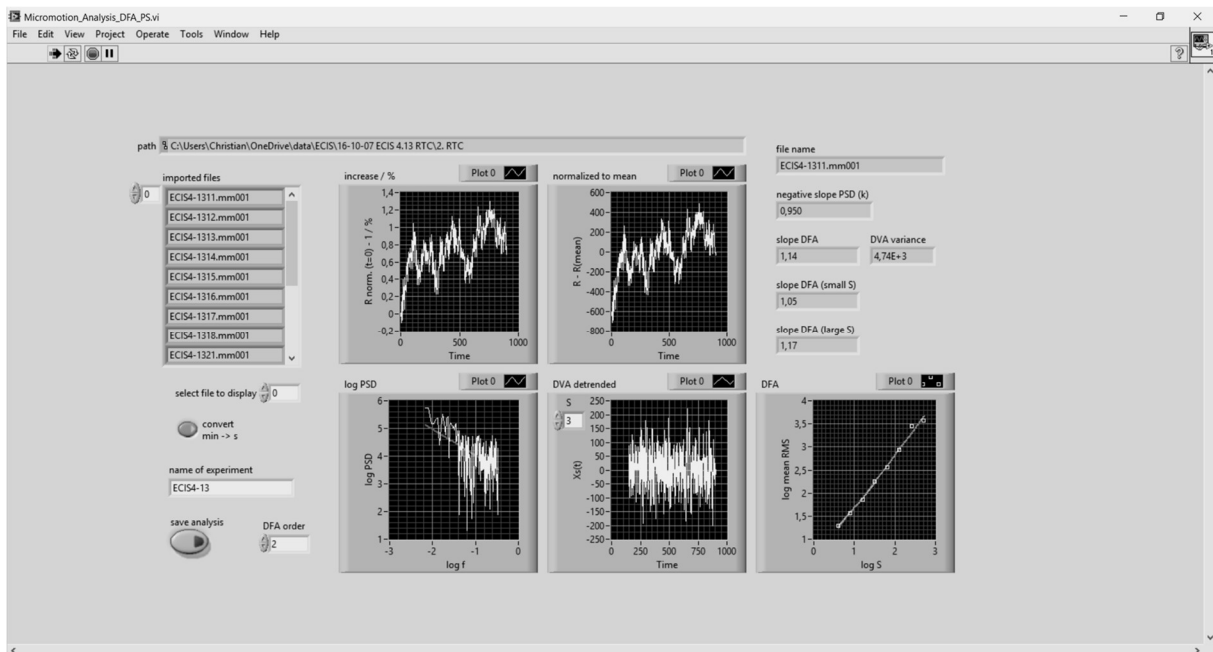
File name: Micromotion_Analysis_DFA_PS.vi

Description: Analyzes micromotion time series using PSD analysis, DVA, and DFA.

Used in chapter: III.1.4.1

3.4   Simulation of Derivative Impedance Spectra
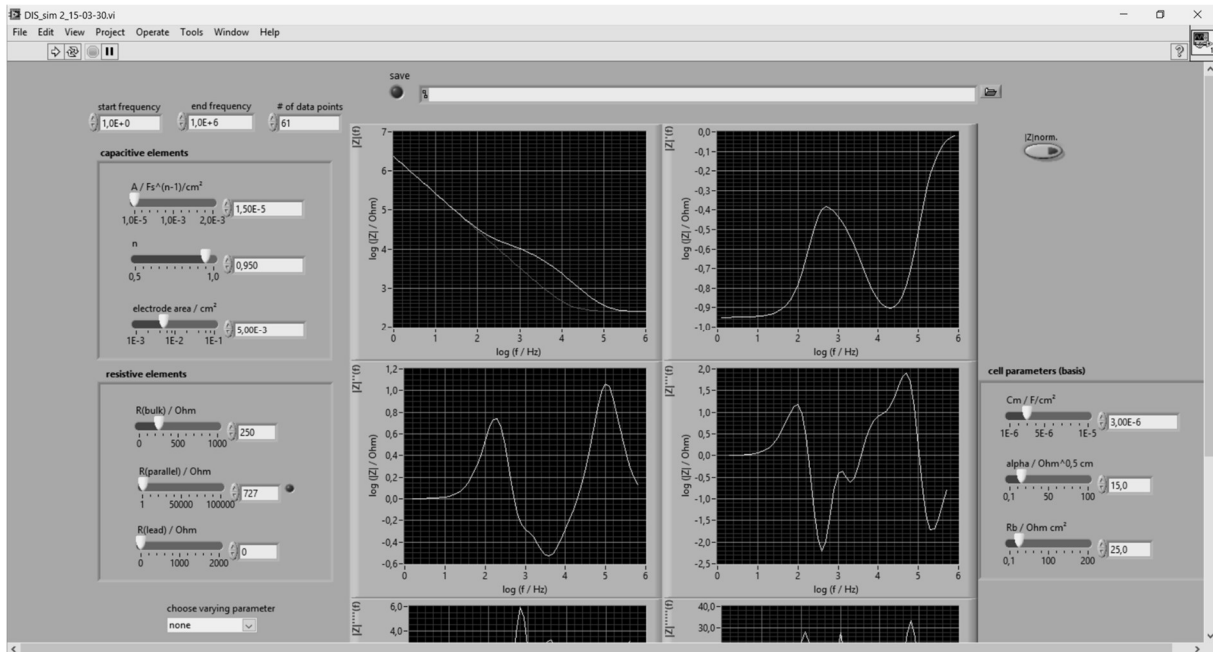
File name: DIS_sim 2_15-03-30.vi

Description: Simulates impedance spectra and its derivatives with varying cell parameters.

Used in chapters: III.4.4.1, III.4.4.3

3.5 Fitting of Impedance Spectra

3.5.1   Fitting of Single Spectra Using the Hyperfunnel Algorithm
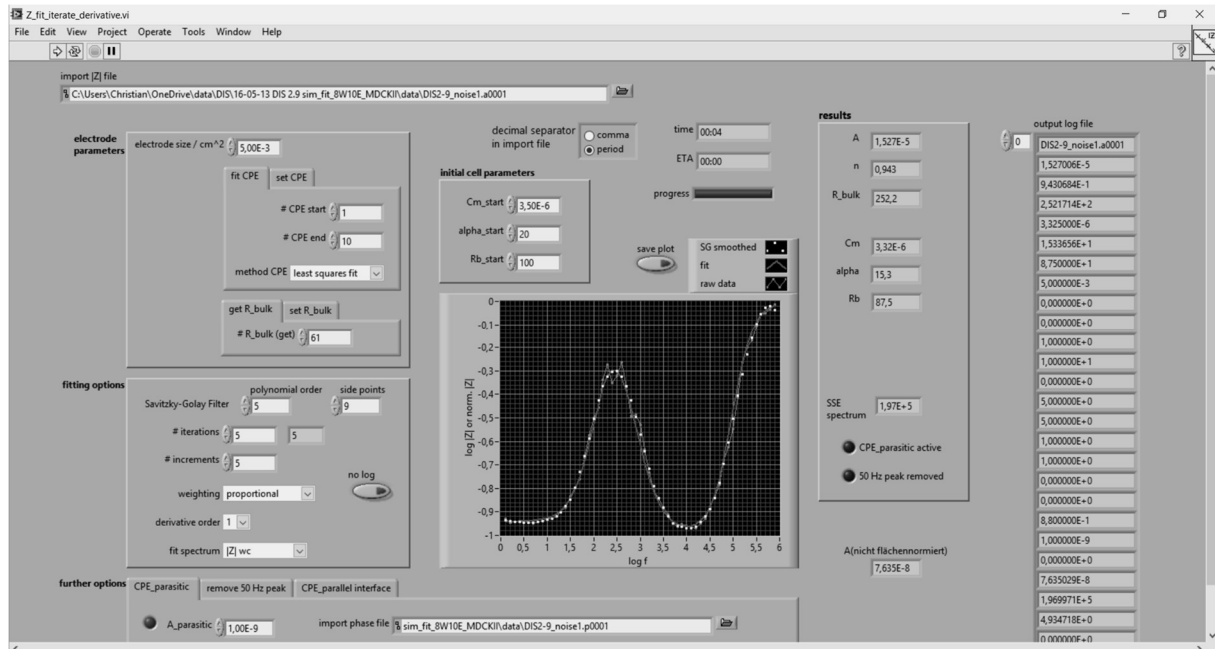
File name:	Z_fit_iterate_derivative.vi
Description:	Capable of fitting single impedance spectra and its derivative orders using the hyperfunnel algorithm (cf. II.3.3).
Used in chapter:	III.4.4.2

3.5.2 Batch Fitting using the Hyperfunnel Algorithm

File name:	Z_iterate_batch.vi
Description:	Capable of fitting multiple impedance spectra and its derivative orders using the hyperfunnel algorithm (cf. II.3.3) by batch processing.
Used in chapter:	III.4.4.2

3.5.3   Analysis of the Results Generated by Batch Fitting
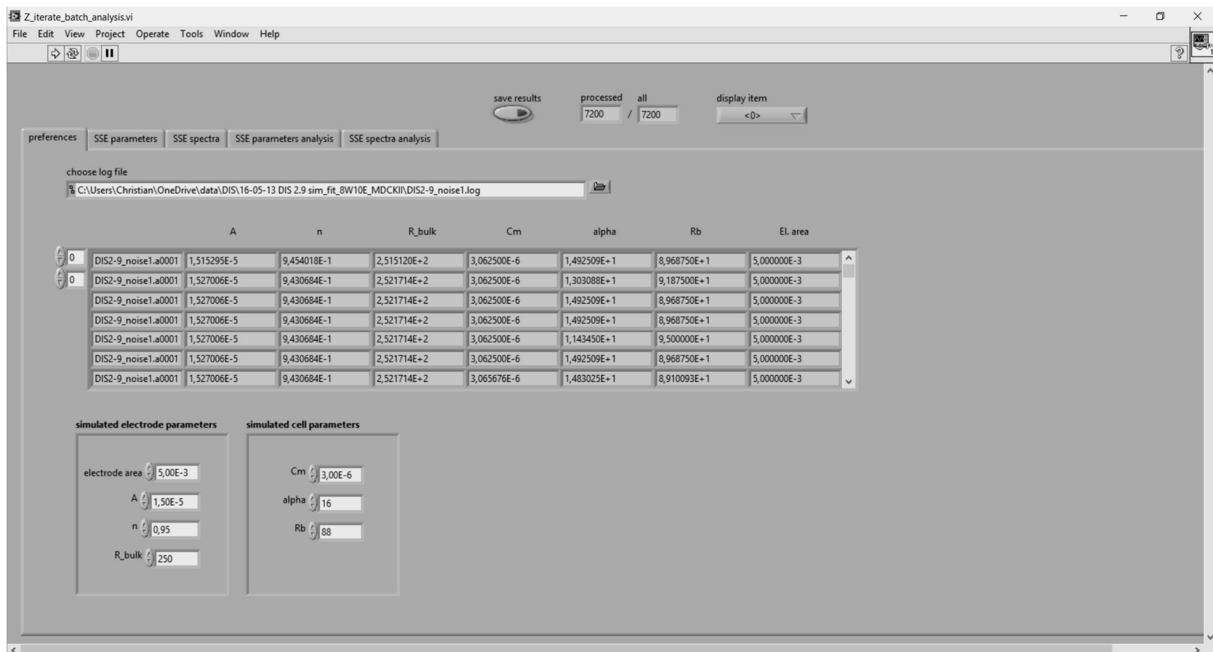
File name:	Z_iterate_batch_analysis.vi
Description:	Analyzes the results generated by batch processed fitting.
Used in chapter:	III.4.4.2

4   Publications and Presentations

4.1 Patents

12/2016   „Bipolare Elektrode zur impedimetrischen Untersuchung und Manipulation lebender Zellen *in vitro*", patent pending

4.2 Conferences

08/2016   **3rd Conference on Impedance-Based Cellular Assays**, Regensburg, talk and poster presentation

09/2015   **11th Workshop on Biosensors & Bioanalytical Microtechniques in Environmental, Food & Clinical Analysis**, Regensburg, talk and poster presentation

03/2015   **Fraunhofer EMFT Annual Event**, Munic, talk

02/2015   **9th Interdisciplinary Doctoral Seminar,** Berlin, talk and poster presentation

04/2014   **XII International Conference on Optical Chemical Sensors and BioSensors EUROPT(R)ODE,** Athens, Greece, poster presentation

09/2013   **13th Conference on Methods and Applications of Fluorescence**, Genoa, Italy, poster presentation

08/2013   **2nd Conference on Impedance-Based Cellular Assays**, Budapest, Hungary, poster presentation

5 Acknowledgements